NYS000565
Submitted: September 9, 2015

Technical Letter Report on Literature Review and Assessment of Potential Seismic Effects on Ongoing Material Degradation – Tensile Strength, Fracture Toughness and Physical Properties

Manuscript Completed: March 2015
Manuscript Published: June 2015

Prepared by Omesh Chopra,[1] Dwight Diercks,[2] David Ma,[1] and Bruce Biwer[1]
[1] Environmental Science Division
[2] Nuclear Engineering Division
Argonne National Laboratory, Argonne, IL 60439

Dr. Makutesswara Srinivasan, NRC Contracting Officer's Representative
Dr. Appajosula Rao, NRC Alternate Contracting Officer's Representative

Prepared for
Division of Engineering
Office of Nuclear Regulatory Research
U.S. Nuclear Regulatory Commission
Washington, DC 20555
NRC Job Code V6370

Abstract

All structures, systems, and components (SSCs) in nuclear power plants (NPPs) are subjected to aging degradation during reactor operation because of chemical and mechanical effects and interactions with the service environment. The objective of this program is to evaluate the potential cumulative effects of repeated and sudden, below design basis earthquake (DBE) loading on progressing degradation of NPP structural materials. Structural damage to NPPs occurs when the cumulative effects of ground acceleration (i.e., seismically induced vibrations) exceed a certain threshold. The ASME Code Section III design rules and U.S. Nuclear Regulatory Commission regulatory guidance concerning seismic design are summarized, and the postulated and anticipated seismic loads and response spectra for NPP SSCs are discussed. Seismic loading rate effects on the cyclic deformation behavior (including microstructural effects), tensile properties, fracture behavior, and elastic properties of structural alloys used in the primary coolant pressure boundary and other safety-related systems are reviewed in detail. A detailed knowledge of the evolution of material microstructure during service is essential for understanding the fundamental mechanisms of crack initiation and failure. Six specific information gaps related to cumulative seismic damage analysis are identified.

Table of Contents

Figures

Tables

Executive Summary

All structures, systems, and components (SSCs) in nuclear power plants (NPPs) are subjected to aging degradation during reactor operation because of chemical and mechanical effects and interactions with the service environment. The objective of this program is to evaluate the potential cumulative effects of repeated and sudden, below safe shutdown earthquake (SSE) loading on progressing degradation of NPP structural materials. The program addresses knowledge gaps in a fundamental manner, considering the mechanical response of degraded material to establish their basic properties under various stages of degradation and determine whether repeated below design basis earthquake (DBE) events could adversely affect ongoing material and component degradation. Included is a literature review to evaluate the effects of repeated and sudden below-SSE loading on specific degradation mechanisms. This research addresses the U.S. Nuclear Regulatory Commission's (NRC's) long-term research project related to determining the effects of repeated and cumulative below-DBE loading on progressive nuclear reactor material degradation

The SSCs important to safety are designed to meet consensus codes and standards for NPPs to help ensure that a sufficient design margin is maintained throughout the plant's operating life to ensure that premature failure of such SSCs does not result in unacceptable consequences. In particular, these SSCs are designed to withstand the effects of the DBE, which is also termed as the safe shutdown earthquake (SSE). The SSC design takes into account historical experiences of ground motion at the site and SSE, and this ensures that in the event of an occurrence of an earthquake of concern, the safety systems will function and the plant will shut down in an orderly manner. However, it is not clear if and how this design approach is applicable to reactor coolant pressure boundary (RCPB) components that have ongoing degradation.

A number of analytical and experimental studies have been conducted to better understand the structural response of NPPs considering the presence of cracks in piping components. Many of these studies use seismic hazard analysis in evaluating failure response to SSE conditions, based on the frequency and the size of seismic load and using original material properties, though at elevated operating temperatures. The NRC has also sponsored research on the concept of a "cracked-pipe element" as a "degraded condition" and tested simple and component tests of girth welds. The results of these studies are summarized here.

Seismic Design

Structural damage to NPPs occurs when the cumulative effects of ground acceleration exceed a certain threshold. Design codes typically include an analysis of seismic fatigue degradation based on one SSE and 5 to 20 operating basis earthquakes (OBEs) with 10 to 20 cycles per event, depending on the location. However, seismic events less than the OBE are not considered in the analysis. The fatigue damage from all design transients is evaluated for the period of reactor operation to determine a characteristic-derived property known as the cumulative usage factor (CUF). Strain-rate effects are also an important consideration in seismic damage analysis, and the stress-strain behavior under short-term high strain rate loading may be quite different than that under normal loading conditions.

The present investigation includes a review of NPP design criteria and standards for seismic design, as contained in 10 CFR 50 regulations, the ASME Boiler and Pressure

Vessel Code, and NRC Regulatory Guides. In general, designs of NPPs during the 1960s and 1970s used a deterministic approach to seismic design based on site-specific examinations of local and regional seismic, geological, and geotechnical soil conditions to determine the maximum credible earthquake. After 2000, there were attempts to standardize the design of NPPs to include not only a standardized reactor coolant system but also a standardized balance-of-plant. Furthermore, as more data became available on actual recorded earthquake activities, a better understanding developed regarding the shape of the design basis ground response spectra recorded at various sites around the world. However, the analytical techniques and procedures necessary to convert input earthquake motions to resultant seismic forces, moments, or stresses in components need to be examined, considering the current material condition of the components and high-frequency, cyclic elastic straining, to evaluate potential impact on component design.

The seismic loads on a structure are inertial loads generated by the deformation of the structure as it vibrates, and the seismic forces depend on the distribution of mass and stiffness throughout the structure. Because structures are typically designed to respond inelastically under vibration, the seismic forces also depend on the manner by which plasticity spreads through the structure, and these forces are typically amplified by resonance effects. In addition, the maximum vibratory accelerations of the SSE must take into account the characteristics of the underlying soil material in transmitting the earthquake-induced motions. Finally, damping effects within the structure must be taken into account.

The information needed for a seismic design includes (a) design ground response spectra, (b) in-structure response spectra, (c) acceleration time history, and (d) seismic anchor movements. The seismic design specifications include (a) the scope and boundaries of components to be seismically designed; (b) the applicable design and construction code; (c) the required seismic function (e.g., operability, leak tightness, and position retention) on the component or piping system; (d) the free-field seismic input for the design basis earthquake; (e) the in-structure seismic response spectra; and (f) the operating and design loading conditions concurrent with the seismic load.

The requirements for the acceptability of a component design by analysis are described in ASME Section III, Division 1 Subarticle NB-3210, “Design Criteria.” Alternatively, a design by rule approach as described in Subarticle NB/NC-3600, may be used for piping and piping components. The design methods in Section III Subarticle NB, NC, or NG for ASME Class 1, 2, and CS components also require a fatigue analysis as well as a fracture mechanics evaluation to prevent the likelihood of nonductile failure. The ASME Code fatigue analysis considers all transient loads, and for each load-cycle or load-set pair, an individual fatigue usage factor is determined by the ratio of the number of cycles anticipated during the lifetime of the component to the allowable cycles.

Seismic Loading Rate Effects

The imposed loading rate has been found to be a significant variable in the response of large structures to seismic events. The strain rate imposed during an earthquake is variable, but a range of 0.1 to 10 s^{-1} appears to be typical of strong earthquakes. The effect of loading rate on the cyclic deformation behavior, tensile properties, and fracture behavior of NPP structural alloys is reviewed in detail.

Cyclic Deformation Behavior

Existing fatigue strain-versus-life (ε–N) data indicate that in the temperature range of dynamic strain aging (200–370°C), some heats of carbon and low-alloy steels are sensitive to strain rate even in an inert environment; with decreasing strain rate, the fatigue life may be either unaffected, decrease for some heats, or increase for others. The cyclic stress–strain response of these steels varies with steel type, temperature, and strain rate. In general, they show initial cyclic hardening, followed by cyclic softening or a saturation stage at all strain rates. At high strain amplitudes, a secondary hardening stage is observed prior to fracture.

For the wrought austenitic stainless steels (SSs), the fatigue life is generally independent of strain rate at temperatures up to 400°C. During cyclic straining, austenitic SSs exhibit rapid hardening during the first 50–100 cycles, and the extent of hardening increases with increasing strain amplitude and decreasing temperature and strain rate. The cast austenitic stainless steels (CASS) CF-3, CF-8 and CF-8M generally show behaviors similar to the wrought austenitic SS, though the cyclic-hardening behavior may be influenced by aging in some cases.

For ferritic steels at low constant cyclic strain amplitudes, the dislocation bundles produced during the rapid hardening stage shake down into bundles of fragmented dislocations, whereas a cell structure is developed at higher strain ranges. The saturation cell size generally increases with either a decrease in strain amplitude or an increase in temperature. For the austenitic SSs, initial cyclic hardening is associated with the formation of an increased dislocation density in a uniform planar structure. During subsequent cyclic softening and stabilization, the dislocations eventually evolve into a well-defined cell structure.

Under variable strain fatigue, the dislocation cell structure formed under initial higher strain amplitude can change gradually upon subsequent cycling at lower amplitude, with the cell size increasing by the disintegration of some of the existing cell walls. Depending upon the microstructure that had developed at the high strain amplitude, decreasing the strain amplitude may not lead to the behavior observed for cycling a virgin specimen at the low strain amplitude; some memory of prior strain cycling may remain in the material.

Tensile Properties

Literature data indicate that the yield and ultimate tensile strengths of A508 Cl 3 and A533 Gr B steel generally increase with increasing strain rate, while the ductility decreases or shows little effect. However, some data suggest a reversal in the yield and tensile strength behavior with strain rate in the region of the normal light-water reactor (LWR) operating temperatures. Dynamic strain aging appears to play a role in this strain rate sensitivity, with serrated flow observed in the temperature range of 140 to 350°C, depending upon temperature and strain rate.

For Type 304, 304L, 304N and 304LN SSs, the yield stress and flow stress are generally found to increase with increasing strain rate, the ultimate tensile strength tends to decrease, and the ductility decreases or shows little change. However, a study on Type 304L SS showed an unexpected decrease in flow stress with increasing strain rate at 427 and 538°C.

For Type 316 SS, the yield and ultimate tensile strengths were found to increase with increasing strain rate at 650°C, while the effect on the ductility was relatively small. Subsequent research indicated variable results, with an increase in ductility with increasing strain rate observed at 700°C. Most researchers report an increase in flow stress with increasing strain rate for Types

316L and 316LN SSs, but there is some indication of a reversal in the strain rate effect on the ultimate tensile strength at temperatures on the order of 300 to 500°C. Elongation and reduction of area also appear to increase somewhat with increasing strain rate, though the opposite effect has been observed for cold-worked material.

The tensile data for Type 304/308 welds and Type 308 SS weld metal show mixed results. Some researchers observe a marked increase in flow stress with increasing strain rate, while others observe only a small effect. The elongation appears to decrease with increasing strain rate for the weld metal and remain roughly constant or increase slightly for the base metal. However, none of these data were obtained in the temperature range of interest for LWRs.

The limited data on the strain-rate effect on the flow stress of Alloy 600 indicate little effect of strain rate on flow stress and ductility at temperatures up to 760°C and marked increase in flow stress with increasing strain rate at higher temperatures. The tensile data for Alloy 690 indicate an increase in flow stress with increasing strain rate over the entire temperature range from −100°C to 1,200°C, though the magnitude of the effect appears to be temperature dependent.

Fracture Behavior

The Charpy impact data for A508 Cl 3 and A533 Gr B pressure vessel steels indicate either little effect or an increase in the ductile-to-brittle transition temperature (DBTT) with increasing loading rate. An increased loading rate also appears to increase the upper shelf energy somewhat for both steels. Neutron irradiation clearly increases the DBTT, and Type 308 SS weld filler metal appears to be increasingly susceptible to brittle fracture with elevated-temperature aging.

The fracture toughness of A508 Cl 3 and A533 Gr B steels generally increases with increasing loading rate, and the fracture toughness-versus-temperature curves shift to higher temperatures. However, a decrease in the crack initiation toughness, J_{IC}, with increasing strain rate has been observed by some researchers in the temperature range of interest for LWR applications. The J–R curves generally show an increase in cracking resistance with increasing loading rate.

The fracture toughness data for Types 304 and 316 SSs generally suggest a beneficial effect of increasing loading rate on the crack resistance. However, the variability in the data indicates that the loading conditions of interest must be well defined before these results can be reliably applied to a specific loading situation. The limited data in the literature on the effect of loading rate on the fracture toughness properties of the CASS materials are somewhat inconsistent, and as-cast and aged material show different behaviors. Recent work on low-temperature crack propagation for aged CASS CF-8 material in pressurized water reactor (PWR) environments investigated the potential synergy between thermal and hydrogen embrittlement associated with decomposition of the ferrite at reactor temperatures, and a large effect of the coolant environment on fracture toughness was observed.

For Alloy 600, a dramatic degradation in fracture toughness is observed in hydrogenated water at temperatures below 149°C, an effect attributed to hydrogen-induced intergranular cracking. This behavior is similar to that observed for aged CF-8 material in LWR shutdown water chemistry. At higher temperatures in the same environment, the fracture toughness increases with increasing loading rate. A qualitatively similar behavior occurs for Alloy 690.

Elastic Properties

No strain-rate dependence is observed for the elastic properties of NPP structural alloys.

Information Gaps

Five information gaps were identified in this work, as follows:

1. The possible impact of (a) current material condition, (b) loading rates associated with typical seismic events and with low-level seismic fatigue cycles (e.g., magnitudes associated with seismic accelerations between 0.01 g and OBE) on reactor component design needs to be investigated for at least two components, one from reactor core internal components and the other from primary pressure boundary piping.
2. The cumulative effect of elastic strain cycling on material microstructure and the resulting effect on fracture properties of reactor structural materials needs to be examined.
3. The reason for the reversed strain rate dependence (i.e., decrease in yield and flow stress with increase in strain rate) at 400°C and its potential impact on seismic design of safety-related structures and components needs to be determined.
4. The possible decrease in fracture toughness of CASS materials and austenitic SS welds thermally aged at 300 to 370°C and tested under dynamic loading conditions at temperatures between room temperature and 100°C needs to be investigated.
5. The potential effect of reduced fracture toughness of Alloys 600 and 690, aged CASS CF-3 and CF-8 materials, and austenitic SS welds in LWR SWC on the seismic design of reactor safety-related components needs to be determined.

Acronyms and Abbreviations

AEC	Atomic Energy Commission
AMP	aging management program
Argonne	Argonne National Laboratory
ASB	adiabatic shear banding
ASME	American Society of Mechanical Engineers
ASTM	American Society for Testing and Materials
BAC	boric acid corrosion
BCC	body -centered cubic
BPV	boiler and pressure vessel
BWR	boiling water reactor
CASS	cast austenitic stainless steels
CAV	cumulative absolute velocity
CC	concrete containment
CEUS	central and eastern United States
CGR	crack growth rate
CT	compact tension
CUF	cumulative usage factor
DBE	design basis earthquake
DBTT	ductile-brittle transition temperature
DRS	Design Response Spectra
DSA	dynamic strain aging
DSHA	deterministic seismic hazards analysis
EBR-II	Experimental Breeder Reactor-II
EPRI	Electric Power Research Institute
FAC	flow-accelerated corrosion
FCC	face-centered cubic
GALL	Generic Aging Lessons Learned
GDC	general design criteria
GMRS	ground motion response spectrum
GTA	gas tungsten arc
IAEA	International Atomic Energy Agency
IASCC	irradiation-assisted stress corrosion cracking
IGSCC	intergranular stress corrosion cracking
ISI	in-service inspection
J-R	J-integral resistance
JSPS	Japan Society for Promoting Science
LRT	leak rate test
LWR	light water reactor
MC	metal containment

MIC	microbiologically induced corrosion
MMI	Modified Mercalli Intensity
Mn	manganese
Mo	molybdenum
Nb	niobium
Ni	nickel
NPP	nuclear power plant
NRC	Nuclear Regulatory Commission
OBE	operating basis earthquake
PGA	peak ground acceleration
PSB	persistent slip band
PSHA	probabilistic seismic hazard analysis
PWR	pressurized water reactor
PWSCC	primary water stress corrosion cracking
RCPB	reactor coolant pressure boundary
RG	regulatory guide
RIS	radiation-induced segregation
SA	submerged arc
SCC	stress corrosion cracking
SFE	stacking fault energy
SMA	shielded metal arc
SRSS	square root of the sum of squares
SS	stainless steel
SSC	structure, system, and component
SSE	safe shutdown earthquake
SSI	soil structure interaction
SWC	shutdown water chemistry
TGSCC	transgranular stress corrosion cracking
WUS	western United States

Nomenclature

a	crack length; in some cases it represents acceleration
a_g	maximum rock acceleration
C	coefficient of the power-law J-R curve
C_V	room temperature "normalized" Charpy-impact energy, i.e., Charpy-impact energy per unit fracture area, at any given service and aging time (J/cm^2). The fracture area for a standard Charpy V-notch specimen (ASTM Specification E 23) is 0.8 cm^2. The value of impact energy in J has been divided by 0.8 to obtain "normalized" impact energy in J/cm^2.
da	increment in crack length
dJ	increment in fracture toughness J
e_f	elongation at fracture
e_u	uniform elongation
E	elastic modulus, in some cases it represent Charpy V-notch impact energy in joules
g	acceleration equal to the acceleration of gravity (980.665 cm s^{-2} or 32.2 ft/s)
f_J	J^{th} mode of frequency
f_{Jn}	J^{th} mode of frequency associated with parameter number n
J	J integral, a mathematical expression used to characterize the local stress-strain field at the crack tip region (parameter J represents the driving force for crack propagation)
J_{Ic}	value of J near the onset of crack extension
K	stress intensity factor
K_c	critical stress intensity factor
K_{IA}	critical stress intensity factor for crack arrest
K_{Ic}	critical stress intensity factor for crack extension
K_{ID}	critical stress intensity factor for crack extension under dynamic loading
K_J	J-integral critical stress intensity factor
K_{Jc}	equivalent critical stress intensity factor for crack extension
n	exponent of the power-law J-R curve, and for fatigue usage factor determination it represents number of applied fatigue cycles
N	number of fatigue cycles to failure
P	number of significant parameters considered in structural frequency broadening
R	load ratio
S	spectral acceleration
S_m	maximum value of stress intensity
T	tearing modulus or temperature
U	usage factor
ε	strain
$\dot{\varepsilon}$	strain rate or $d\varepsilon/dt$
ε_a	applied strain
ε_f	fracture strain
ε_t	total strain

ε_u	uniform strain
υ	Poisson ratio
σ	stress
$\bar{\sigma}$	Von Mises effective stress
σ_1 & σ_2	principal stresses in or parallel to the mid plane of the wall of a component
σ_3	principal stress perpendicular to the mid plane of the wall of a component
σ_a	applied stress
σ_f	flow stress, defined as the average of yield and ultimate stress
σ_u	ultimate stress
σ_y	yield stress

SI units of measurements have been used in this report. Conversion factors for measurements in British units are as follows:

To convert from	to	multiply by
in.	mm	25.4
J	Ft-lb	0.7376
kJ/m^2	$in.\text{-}lb/in.^2$	5.71015
kJ/mole	kcal/mole	0.239

Acknowledgments

This work is sponsored by the Office of Nuclear Regulatory Research, U.S. Nuclear Regulatory Commission, under Job Code V6370; Program Manager, Dr. Makutesswara Srinivasan.

1. Introduction

All structures, systems, and components (SSCs) in nuclear power plants (NPPs) are subjected to aging degradation during reactor operation because of chemical and mechanical effects and interactions with the service environment, all of which are influenced by such factors as reactor coolant chemistry, material condition, temperature, neutron irradiation, and mechanical loading.[1–11] The effects of these environmental variables are typically addressed by the plant-specific design and operational technical specifications. Operational experience has shown that depending up on the operating conditions, general corrosion,[12–15] pitting,[16,17] crevice corrosion, cavitation,[18] boric acid corrosion (BAC),[19–25] microbiologically-induced corrosion (MIC),[26] flow accelerated corrosion (FAC),[27–31] erosion corrosion,[32] wear,[1,4] mechanical and thermal fatigue,[1,4,33] and loss of material due to selective leaching of some of the constituent of material[1,4] are the most commonly observed aging degradation processes for NPPs. Furthermore, various mechanisms operate, in synergy with temperature, stress state, strain rate and material condition, resulting in intergranular stress corrosion cracking (IGSCC), transgranular stress corrosion cracking (TGSCC), or primary water stress corrosion cracking (PWSCC) in light water reactors (LWRs).

In addition, exposure to neutron irradiation for extended periods changes the microstructure (radiation hardening) and microchemistry (radiation-induced segregation, or RIS)[34–38] of reactor core support structures and internal components. Neutron irradiation results in damage at the atomistic and microstructural scale, which is manifested by an increase in the tensile strength and hardness of the material and a decrease in fracture toughness or resistance to brittle fracture,[39–53] commonly known as embrittlement. Neutron irradiation also increases the susceptibility of structures and components to irradiation-assisted stress corrosion cracking (IASCC).[52–61]

Time-dependent material degradation can lead to formation of voids, and micro- and macro-cracks, which can then slowly grow because of chemical and mechanical interactions of the material at the tip of the progressing crack. Metallurgical aspects also control the growth of such cracks. Dissimilar-metal welds in particular are vulnerable regions in the component because of (a) different microstructure and the redistribution of alloying and interstitial elements compared to base metal and (b) high residual stress resulting from welding. During operation, such cracks can propagate through the component wall resulting in observable coolant leakage. Furthermore, for core internal components, neutron irradiation enhances the growth rates of these cracks.

This research addresses the U.S. Nuclear Regulatory Commission's (NRC's) long-term research project related to determining the effects of repeated and cumulative below design basis earthquake (DBE) loading on progressing nuclear reactor material degradation. The proposed study considers specific aging degradation mechanisms that, from previous operating experience, have been found to be operative for structures and components important to safety and require an aging management program (AMP) to ensure structural and functional integrity. These aging degradation mechanisms include corrosion, FAC, MIC, thermal and neutron embrittlement, and crack growth rates (CGRs) for IGSCC, TGSCC, PWSCC, fatigue loading, and irradiation-assisted stress corrosion cracking (IASCC). The structures and components affected by these aging degradation mechanisms include Class 1 pressure boundary components and those whose functionality is safety-related.

The SSCs important to safety are designed to consensus codes and standards for NPPs such that sufficient design margin is maintained throughout the life of the plant operation to ensure that premature failure of such SSC does not result in unacceptable consequences. The SSCs important to safety are those that are necessary to ensure (a) the integrity of the reactor coolant pressure boundary, (b) the capability to shut down the reactor and maintain it in a safe-shutdown condition, or (c) the capability to prevent or mitigate the consequences of accidents that could result in potential offsite exposures comparable to the guideline exposure of Title 10, Part 50, of the Code of Federal Regulations (10 CFR 50), "Domestic Licensing of Production and Utilization Facilities,"[62] Section 50.34(a)(1). General design criteria (GDC)[63] 2, "Design Bases for Protection Against Natural Phenomena," of Appendix A,[64] to 10 CFR Part 50, "Seismic and Geological Siting Criteria for Nuclear Power Plants," requires that NPP SSCs important to safety be designed to withstand the effects of natural phenomena such as earthquakes, tornados, hurricanes, floods, tsunamis, and seiches without loss of capability to perform their safety function.

All SSCs important to safety are designed to withstand the effects of the DBE, which is also termed as the safe-shutdown earthquake (SSE). A DBE or SSE is the largest possible earthquake at the site, considering the regional and local geology and seismology and specified characteristics of local and subsurface material. Ground shaking of a DBE might be exceeded, but the probability of this happening is considered small. The SSE represents the vibratory ground motion for which SSCs important to safety must be designed to remain functional and within applicable stress, strain, and deformation limits. The SSC design takes into account historical experiences of ground motion at the site and SSE and ensures that in the event of an occurrence of an earthquake of concern, the safety systems will function and the plant will shut down in an orderly manner so that no radionuclides are released to harm the public and the environment.

An operating basis earthquake (OBE) is the largest earthquake that reasonably could be expected to affect the plant site during the operating life of the plant. It is typically a third or half of the SSE. All NPPs are designed to withstand the OBE and still operate without undue risk to the health of the public. Furthermore, various NPP structures and components vibrate at different frequencies during a seismic event. Vibrations in the range of 1-10 Hz are of particular concern, because they correspond to damaging response frequencies for most structures and components. Earthquakes below 15 Hz predominate in the western United States (WUS). All NPPs in the WUS are designed to withstand low frequencies. Although NPPs in central and eastern United States (CEUS) are also designed to withstand low frequencies, the typical earthquakes in CEUS are associated with higher frequencies. Higher frequencies are less damaging to large structures, but may adversely affect small components.

For concrete and other building structures, the concept of "cumulative absolute velocity" (CAV) exists as an index for the onset of structural damage from cumulative effects of ground acceleration.[65,66] However, it is not clear if and how such concept is applicable to reactor coolant pressure boundary (RCPB) components with ongoing degradation. For example, in the NRC Generic Aging Lessons Learned (GALL) report,[3] it is required that the effects of concrete degradation be considered after an earthquake event. However, no such consideration is required for metallic materials degradation in the GALL report.

In the GALL report, the "Detection of Aging Effects" program element of AMP XI S4, 10 CFR Part 50, Appendix J,[67] states that a containment LRT (leak rate test) program is effective in detecting leakage rates of the containment pressure boundary components, including seals and

gaskets. While the calculation of leakage rates and satisfactory performance of containment leakage rate testing demonstrates the leak tightness and structural integrity of the containment, it does not by itself provide information that would indicate that aging degradation has begun or that the capacity of the containment may have been reduced for other types of loads, such as seismic loading. This would be achieved with the additional implementation of an acceptable containment in-service inspection program as described in American Society of Mechanical Engineers (ASME) Boiler and Pressure Vessel (BPV) Code, Section XI,[68] Subsections IWE (AMP XI.S1) and IWL (AMP XI.S2).[3] Similar management program, including any associated inspection requirements, regarding material degradation due to seismic loading effects on the metallic pressure boundary components, have currently not been proposed. All operating nuclear power reactors in the United States are listed in Table 1. The locations of these plants and a few others that have been shutdown are shown in Fig. 1.

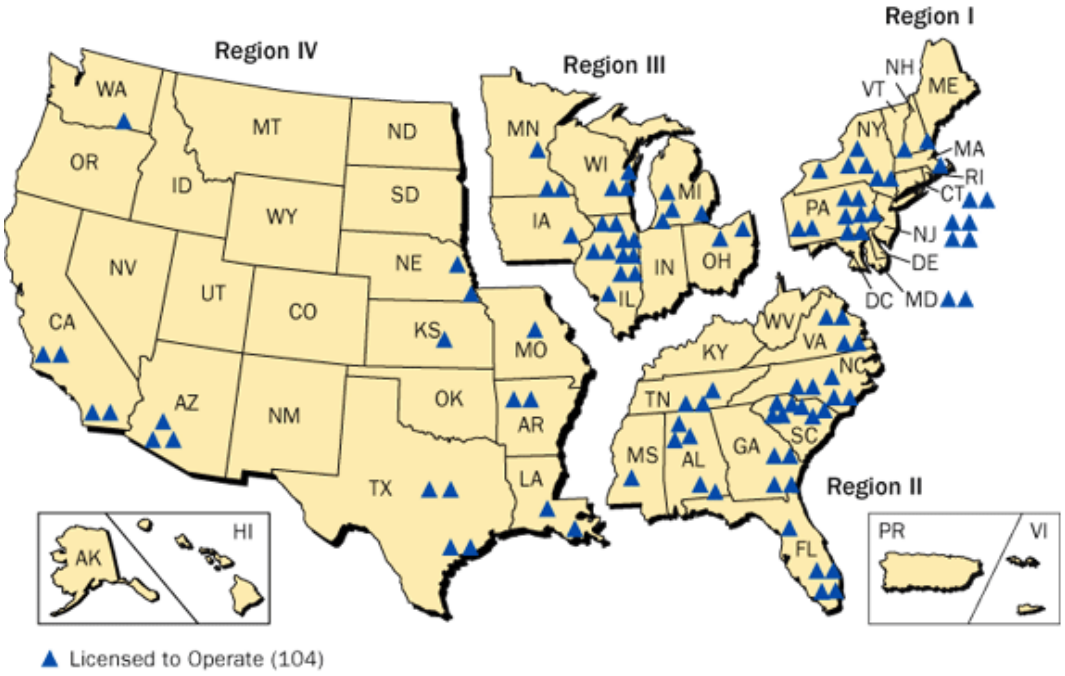

Figure 1. Location of nuclear power reactors in the United States of America. Only 99 plants out of these are operating at present.

A number of studies have been conducted recently to better understand the structural response of NPPs to the presence of cracks in piping components, both analytically[69,70] and experimentally, for example. Many of these studies use seismic hazard analysis in evaluating failure response to SSE conditions, based on the frequency and the size of seismic load and with original material properties, though at the elevated operating temperatures. In experimental studies,[71] well-defined cracks of various morphologies and depths were introduced into both experimental coupons and component mockup assemblies, which were then subjected to loads on a shaking table to simulate earthquake loading. The piping component tests included static and dynamic cycling tests of pressurized elbows, tees, nozzles and reducers. The tests were carried out at high-strain amplitudes, and the results illustrated the accumulation of ratcheting strain.* The specimens

*Ratcheting represents elastic shakedown behavior in which plastic deformation takes place while due to material strain hardening the steady-state is perfectly elastic. It is an open elastic-plastic hysteresis loop where the material accumulates a net strain during each cycle.

Table 1. List of operating nuclear power reactors in the United States and their type, vendor, location, and date of license.

Unit	Type	MW	Vendor	State	License	Unit	Type	MW	Vendor	State	License
Arkansas Nuclear 1	PWR	843	B&W	AK	1974	Millstone 3	PWR	1227	W4L	CT	1986
Arkansas Nuclear 2	PWR	995	CE	AK	1974	Monticello	BWR	579	GET3	MN	1970
Beaver Valley 1	PWR	892	W3L	PA	1976	Nine Mile Point 1	BWR	621	GET2	NY	1974
Beaver Valley 2	PWR	846	W3L	PA	1987	Nine Mile Point 2	BWR	1140	GET5	NY	1987
Braidwood 1	PWR	1178	W4L	IL	1987	North Anna 1	PWR	981	W3L	VA	1978
Braidwood 2	PWR	1152	W4L	IL	1988	North Anna 2	PWR	973	W3L	VA	1980
Browns Ferry 1	BWR	1065	GET4	AL	1973	Oconee 1	PWR	846	B&WLL	SC	1973
Browns Ferry 2	BWR	1104	GET4	AL	1974	Oconee 2	PWR	846	B&WLL	SC	1973
Browns Ferry 3	BWR	1115	GET4	AL	1976	Oconee 3	PWR	846	B&WLL	SC	1974
Brunswick 1	BWR	938	GET4	NC	1976	Oyster Creek	BWR	619	GET2	NJ	1991
Brunswick 2	BWR	937	GET4	NC	1974	Palisades	PWR	778	CE	MI	1971
Byron 1	PWR	1164	W4L	IL	1985	Palo Verde 1	PWR	1335	CES80	AZ	1985
Byron 2	PWR	1136	W4L	IL	1987	Palo Verde 2	PWR	1335	CES80	AZ	1986
Callaway 1	PWR	1236	W4L	MO	1984	Palo Verde 3	PWR	1335	CES80	AZ	1987
Calvert Cliffs 1	PWR	873	CE	MD	1974	Peach Bottom 2	BWR	1112	GET4	PA	1973
Calvert Cliffs 2	PWR	862	CE	MD	1976	Peach Bottom 3	BWR	1112	GET4	PA	1974
Catawba 1	PWR	1129	W4L	SC	1985	Perry 1	BWR	1261	GET6	OH	1986
Catawba 2	PWR	1129	W4L	SC	1986	Pilgrim 1	BWR	685	GET3	MA	1972
Clinton 1	BWR	1065	GET6	IL	1987	Point Beach 1	PWR	512	W2L	WI	1970
Columbia Gen. Station	BWR	1190	GET5	WA	1984	Point Beach 2	PWR	514	W2L	WI	1973
Comanche Peak 1	PWR	1200	W4L	TX	1990	Prairie Island 1	PWR	551	W2L	MN	1974
Comanche Peak 2	PWR	1150	W4L	TX	1993	Prairie Island 2	PWR	551	W2L	MN	1974
Cooper Station	BWR	830	GET4	NE	1974	Quad Cities 1	BWR	867	GET3	IL	1972
Davis-Besse	PWR	893	B&WLL	OH	1977	Quad Cities 2	BWR	869	GET3	IL	1972
Diablo Canyon 1	PWR	1151	W4L	CA	1984	R. E. Ginna	PWR	498	W2L	NY	1969
Diablo Canyon 2	PWR	1149	W4L	CA	1985	River Bend 1	BWR	989	GET6	LA	1985
Donald C. Cook 1	PWR	1009	W4L	MI	1974	Salem 1	PWR	1174	W4L	NJ	1976
Donald C. Cook 2	PWR	1060	W4L	MI	1977	Salem 2	PWR	1130	W4L	NJ	1981
Dresden 2	BWR	867	GET3	IL	1991	Seabrook 1	PWR	1295	W4L	NH	1990
Dresden 3	BWR	867	GET3	IL	1971	Sequoyah 1	PWR	1148	W4L	TN	1980
Duane Arnold	BWR	640	GET4	IA	1974	Sequoyah 2	PWR	1126	W4L	TN	1981
Fermi 2	BWR	1122	GET4	MI	1985	Shearon Harris 1	PWR	900	W3L	NC	1986
Fitzpatrick	BWR	852	GET4	NY	1974	South Texas 1	PWR	1410	W4L	TX	1988

Unit	Type	MW	Vendor	State	License	Unit	Type	MW	Vendor	State	License
Fort Calhoun	PWR	500	CE	NE	1973	South Texas 2	PWR	1410	W4L	TX	1989
Grand Gulf 1	BWR	1297	GET4	MS	1984	St. Lucie 1	PWR	839	CE	FL	1976
Hatch 1	BWR	876	GET4	GA	1974	St. Lucie 2	PWR	839	CE	FL	1983
Hatch 2	BWR	883	GET4	GA	1978	Surry 1	PWR	799	W3L	VA	1972
Robinson 2	PWR	710	W3L	SC	1970	Surry 2	PWR	799	W3L	VA	1973
Hope Creek 1	BWR	1061	GET4	NJ	1986	Susquehanna 1	BWR	1149	GET4	PA	1982
Indian Point 2	PWR	1023	W4L	NY	1973	Susquehanna 2	BWR	1140	GET4	PA	1984
Indian Point 3	PWR	1025	W4L	NY	1975	Three Mile Island 1	PWR	786	B&WLL	PA	1974
Joseph M. Farley 1	PWR	851	W3L	AL	1977	Turkey Point 3	PWR	720	W3L	FL	1972
Joseph M. Farley 1	PWR	860	W3L	AL	1981	Turkey Point 4	PWR	720	W3L	FL	1973
LaSalle County 1	BWR	1118	GET5	IL	1982	VC Summer	PWR	966	W3L	SC	1982
LaSalle County 2	BWR	1120	GET5	IL	1983	Vogtle 1	PWR	1109	W4L	GA	1987
Limerick 1	BWR	1134	GET4	PA	1985	Vogtle 2	PWR	1127	W4L	GA	1989
Limerick 2	BWR	1134	GET4	PA	1989	Waterford 3	PWR	1250	CE	LA	1985
McGuire 1	PWR	1100	W4L	NC	1981	Watts Bar 1	PWR	1123	W4L	TN	1996
McGuire 2	PWR	1100	W4L	NC	1983	Wolf Creek 1	PWR	1166	W4L	KS	1985
Millstone 2	PWR	884	CE	CT	1975						

Notes: No commercial NPPs operate in Alaska or Hawaii. B&W: Babcock and Wilcox 2-Loop Lower; CE: Combustion Engineering; CE80: Combustion Engineering System 80; W2L: Westinghouse 2-Loop; W3L: Westinghouse 3-Loop; W4L: Westinghouse 4-Loop; GET2: General Electric Type 2; GET3: General Electric Type 3; GET4: General Electric Type 4; GET5: General Electric Type 5; GET6: General Electric Type 6.

were cycled until a through-wall crack occurred. The simplified (small) piping system tests were designed to excite the systems to seismic levels well above the typical design earthquake levels in order to induce elasto-plastic response in the system's components. The results have shown that the cracked components were able to sustain such loading and that premature failure did not occur. The results thus provided added confidence that the component design margin is adequate to prevent catastrophic failure during a simulated SSE loading.

Shao et al.[72] have also documented a study of dynamic response due to seismic loading of degraded NPP structures and components, but not the reactor pressure boundary material and components. They observed that the degraded structures or components could be more vulnerable to seismic loads because aging or degradation may affect dynamic properties, structural response, resistance or capacity, failure modes, and locations of failure initiation.

This NRC-sponsored research also examined the concept of "cracked-pipe element," as a "degraded condition" and tested simple and component tests of girth welds.[73] These tests were conducted at room temperature, and the results showed that the pipe test failures were due to low-cycle fatigue with small-scale yielding, and that there were large margins on the acceleration needed to cause failure in a single large seismic event compared to the input acceleration in the tests. Based on extrapolated results to full-scale behavior, the authors concluded that a large margin exists for the acceleration to cause failure relative to the typical design peak ground acceleration (PGA) values for U.S. plants.

The PGA values for operating NPPs in the United States are listed in Table 2. The four plants on the West Coast are listed separately at the end of the table. PGA is a measure that has been widely used in developing NPP "fragility estimates." It represents the sensitivity of NPP structures and components to the inertial effects of acceleration during a seismic event. Two PGA values are listed in the table, namely, the value used in the original design and the updated value proposed by the NRC for each NPP in response to the earthquake that occurred near the North Anna NPP on August 23, 2011. The updated PGA value was to be used for the revalidation of the seismic analysis for all operating plants and for the seismic design of new reactors. For some plants, the original analysis was considered overly conservative, and therefore the proposed PGA value was lower than the original. The August 23 earthquake caused the plant to automatically shut down and resulted in loss of offsite power. This event was followed by a 4.5 magnitude aftershock on August 25. The plant experienced several other aftershocks for several weeks after the main event.

Structural damage to NPPs occurs when the cumulative effects of ground acceleration (i.e., seismically induced vibrations) exceed a certain threshold. The Electric Power Research Institute (EPRI), in 1988, developed the concept of CAV as an index for indicating the onset of structural damage due to cumulative effect of ground acceleration.[65] The NRC Regulatory Guide (RG) 1.208 states that the threshold between damaging and nondamaging earthquakes (for buildings of good design and construction) conservatively occurs at ground motions with CAVs greater than 0.16 g-seconds.[74]

Fatigue is another major form of degradation that has been considered in design codes. In general the design transients considered in the fatigue analysis of the reactor pressure boundary components include among others, heat-up, cooldown, pressurizer heat-up and cooldown [for pressurized water reactors (PWRs)], reactor trip, turbine trip, leak test, hydrostatic test, and seismic load. The plant start-up and shutdown conditions are considered to impose the major cyclic

loads of concern. The seismic loading considered in the fatigue analysis includes one SSE

Table 2. PGA values for U.S. NPPs.

NPP Facility	SSE PGA (g units)		NPP Facility	SSE PGA (g units)	
	Original	Updated		Original	Updated
Arkansas Nuclear One (ANO) 1/2	0.200	0.0240	North Anna 1/2	0.120	0.570
Beaver Valley 1/2	0.150	0.167	Oconee 1/2/3	0.100	0.400
Belefonte 1/2	0.180	0.344	Oyster Creek 1	0.180	0.174
Braidwood 1/2	0.200	0.208	Palisades 1	0.200	0.283
Browns Ferry 1/2/3	0.180	0.378	Peach Bottom 2/3	0.120	0.400
Brunswick 1/2	0.160	0.194	Perry 1	0.150	0.188
Byron 1/2	0.200	0.270	Pilgrim 1	0.150	0.500
Callaway 1	0.200	0.500	Point Beach 1/2	0.120	0.140
Calvert Cliffs 1/2	0.150	0.112	Prairie Island 1/2	0.120	0.060
Catawba 1/2	0.150	0.330	Quad Cities 1/2	0.240	0.160
Clinton 1	0.260	0.260	River Bend 1	0.100	0.105
Comanche Peak 1/2	0.120	0.058	H B Robinson 2	0.200	0.470
Cooper 1	0.200	0.137	St Lucie 1/2	0.100	0.056
Davis-Besse 1	0.150	0.167	Salem 1/2	0.200	0.150
DC Cook 1/2	0.200	0.137	Seabrook 1	0.250	0.500
Dresden 2/3	0.200	0.246	Sequoyah 1/2	0.180	0.380
Duane Arnold 1	0.120	0.088	South Texas 1/2	0.100	0.056
Joseph M Farley 1/2	0.100	0.068	Surry 1/2	0.150	0.110
Fermi 2	0.150	0.180	Susquehanna 1/2	0.100	0.130
James A FitzPatrick 1	0.150	0.120	Three Mile Island 1	0.120	0.227
Fort Calhoun 1	0.170	0.204	Turkey Point 3/4	0.150	0.040
R E Ginna 1	0.150	0.122	Virgil C Summer 1	0.150	0.368
Grand Gulf 1	0.150	0.093	Vermont Yankee 1	0.120	0.570
Shearon Harris 1	0.150	0.110	Vogtle 1/2	0.100	0.400
Edwin I Hatch 1/2	0.150	0.142	Waterford 3	0.180	0.174
Hope Creek 1	0.200	0.170	Watts Bar 1/2	0.200	0.283
Indian Point 2/3	0.150	0.412	Wolf Creek 1	0.120	0.400
LaSalle County1/2	0.200	0.317			
Limerick 1/2	0.150	0.193	Columbia 1	0.250	a
William B MgGuire 1/2	0.150	0.305	Diablo Canyon 1/2	0.750	a
Millstone 2/3	0.170	0.190	San Onofre 2/3	0.670	b
Monticello 1	0.120	0.153	Palo Verde 1/2/3	0.250	a
Nine Mile Point 1/2	0.150	0.200			

a: Data will be available in 2015.
b: Plant has been shut down.

and 5 to 20 OBEs with 10 to 20 cycles per event, depending on the location. Paragraph IV(a)(2)(i) of Appendix S to 10 CFR 50 requires that the value of the OBE ground motion must be set to one of the following choices:

(A) One-third or less of the SSE ground motion design response spectra, and the requirements associated with the OBE ground motion in 10 CFR 50 Appendix S, Paragraph IV(a)(2)(i)(B)(I), can be satisfied without performing explicit response or design analyses; or

(B) A value greater than one-third of the SSE ground motion design response spectra and analysis and design must be performed to demonstrate that the requirements associated with the OBE ground motion in 10 CFR 50 Appendix S, Paragraph

IV(a)(2)(i)(B)(I), are satisfied. The design must consider soil-structure interaction effects and the duration of vibratory ground motion.

Paragraph IV(a)(2)(i)(B)(I) of Appendix S[75] to 10 CFR 50 states that when subjected to the effects of OBE ground motion in combination with normal operating loads, all SSCs necessary for continued operation without undue risk to the health and safety of the public must remain functional and within applicable stress, strain, and deformation limits. In addition, Paragraph IV(a)(3) of Appendix S to 10 CFR 50 requires that if vibratory ground motion exceeds the OBE ground motion or if significant plant damage occurs, the NPP must shut down.

In all fatigue design analyses, any seismic events less than the OBE are not considered in the analysis. The fatigue damage from all transients above OBE, also known as design transients, is evaluated for the period of reactor operation to determine a characteristic derived property known as the cumulative usage factor (CUF).[69] Therefore, this study is focused only on the potential effects of repeated, below OBE loadings.

The information generated thus far for modeling has generally used the original and as-fabricated material properties and has not considered the potential effects of both the degradation on material properties and the repeated and cumulative effects of repeated below-OBE loadings. The earthquake loading studies conducted thus far have not considered the effects of seismic loading on progressing material degradation with respect to the potential enhancement of such degradation under repeated seismic loading, particularly for below-OBE loading.

Repeated and sudden below-OBE loadings may impose sudden high-strain-rate deformation on reactor materials. The deformation mechanisms of a material may vary with the rate of strain from creep to wave propagation influences and thermal effects, e.g., adiabatic shear banding (ASB).[76] Adiabatic shear banding is a major dynamic deformation and failure mechanism of metals and alloys and refers to abrupt localization of plastic deformation into narrow bands, typically 5–500 μm wide. It occurs in metal-forming and -cutting processes, various types of ballistic impact, and vehicle crashes. The strain rates are typically in the range of 1,000 to 7,000 s^{-1}. However, these strain rates are more than two orders of magnitude higher than the strain rates associated with a seismic event. Zener and Hollomon[77] proposed that the inherent temperature increase of the material during dynamic loading could cause material softening, which may overcome strain-hardening effects, eventually leading to strain localization. However, for most materials the temperature rise prior to strain location is relatively small and insufficient to significantly soften a uniformly deforming material.[78,79]

Recently, Rittel et al.[80,81] proposed that part of the cold work energy that is not dissipated as heat and is stored in the material causes microstructural changes characterized by the formation of nano-size grains by dynamic recrystallization. They also showed that dynamic recrystallization is not the outcome of shear localization, as commonly believed, but precedes shear localization. The role of dynamic stored energy of cold work on microstructural changes due to dynamic recrystallization and eventual failure by adiabatic shear localization has been further verified by Osovski et al.[82–84] These authors also showed that twinning plays an important role in the onset of dynamic recrystallization. They argued that twinning does not store significant amounts of energy even in material that exhibits strain hardening. Therefore, because of the lack of stored energy, twins may act a retarding factor for dynamic recrystallization, thereby reducing its susceptibility to

shear localization. For example, a Ti6Al4V alloy, without twins, was found to recrystallize dynamically approximately at mid-range of the strain to failure, whereas pure α-Ti, which exhibits massive twinning, showed dynamic recrystallization at the late stages of deformation (close to 0.9 of failure strain).[82] These differences were rationalized in terms of the difference in stored energy in the materials.

Thus, the stress-strain behavior under short-term high-strain-rate loading may be quite different than that under normal loading conditions. Furthermore, it has been postulated[85] that to understand the seismic effects on fatigue better, fatigue tests may need to be performed both under load- and displacement-controlled modes. Since the current ASME Code fatigue design curves for NPP structural materials are based on fatigue data obtained from completely reversed, strain-controlled fatigue tests, the design curves may not be appropriate for high-strain-rate seismic loading.

The objective of this program is to evaluate the potential cumulative effects of repeated and sudden below-SSE loading on progressing degradation of NPP structural materials. The program will address knowledge gaps in a fundamental manner, considering the mechanical response (stress-strain behavior) of degraded material to establish basic properties of degraded materials under various stages of degradation and determine whether such below-DBE events that occur repeatedly during plant operation could adversely affect ongoing material and component degradation and become a safety concern.

A literature review of both domestic and international sources of technical information of generic nature will be conducted to review and evaluate the effects of repeated and sudden below-SSE loading on specific degradation mechanisms. This review will consider possible scenarios in which seismic shock loading (severe or lower level/more frequent) could accelerate degradation in passive component materials of construction. Because of aging degradation of reactor structural materials, the available margin and useful life of components are also reduced.

This scoping study is expected to provide reactor material degradation fundamental insights, information addressing potential technical issues, or identified gaps to support anticipated future NRC needs. The aging degradation mechanisms included in this study are uniform and pitting corrosion; FAC; MIC; IASCC; IGSCC; TGSCC; PWSCC; loss of fracture toughness; and fatigue crack initiation and growth. The structures and components affected by these aging degradation mechanisms include Class 1 pressure boundary components and those whose functionality is safety-related. Concrete structures, other NPP structures and components of such structures, or spent nuclear fuel pools and structures within the cooling pool, cable, and storage casks, are not within the scope of this study.

2. Background Information

GDC 1, “Quality Standards and Records,” in Appendix A “General Design Criteria of Nuclear power Plants,”[64] to 10 CFR 50, “Domestic Licensing of Production and Utilization Facilities,” requires, in part, that SSCs important to safety be designed, fabricated, erected, and tested to quality standards commensurate with the importance of the safety functions to be performed. Where recognized codes and standards are used, Criterion 1 requires that they be identified and evaluated to determine their applicability, adequacy, and sufficiency and be supplemented or modified as necessary to ensure a quality product in keeping with the required function.

In addition, Criterion 30, “Quality of Reactor Coolant pressure Boundary,” of Appendix A to 10 CFR 50 requires, in part, that components that are part of the RCPB be designed, fabricated, erected, and tested to the highest practical standards. Appendix B, “Quality Assurance Criteria for Nuclear Power Plants and Fuel Processing Plants,”[86] to 10 CFR 50 requires, in part, that measures be established for the control of special processing of materials and that proper testing be performed. Provisions of ASME BPV Code have been used since 1971 as part of the framework to establish the necessary design, fabrication, construction, testing, and performance requirements for SSCs important to safety. Among other things, ASME standards committees develop improved methods for the construction and in-service inspection (ISI) of ASME Class 1, 2, 3, MC (metal containment) and CC (concrete containment) NPP components.

The regulation in 10 CFR 50.55a, “Codes and Standards,” Subsection 50.55a(c) “Reactor Pressure Boundary,”[87] requires, in part, that components of the RCPB must be designed, fabricated, erected, and tested in accordance with the standards for Class 1 components of Section III, “Rules for Construction of Nuclear Power Plant Components,” of the BPV Code[89] or equivalent quality standards. The regulations in 10 CFR 50.55a(d) “Quality Group B components,” and 50.55a(e) “Quality Group C components,” require that the components classified Quality Group B and C must meet the requirements for Class 2 and 3, respectively, in Section III of ASME BPV Code. The NRC RG 1.26[90] establishes an acceptable method for complying with the applicable 10 CFR 50 requirements by classifying fluid systems and components important to safety and applying corresponding quality codes and standards to such systems and components.

The ASME Section III, Division 1 Class 1 components of LWRs are part of the RCPB. Class 2 components are part of the various important-to-safety systems such as emergency core cooling, and Class 3 components are part of the various systems needed for plant operation. These Class 1, 2, and 3 components are designated in RG 1.26 as Quality Groups A, B, and C, respectively. Application of 10 CFR 50.55a and GDC 1 provides assurance that established standard practices of proven or demonstrated effectiveness are used to achieve a high likelihood that these safety functions will be performed and that the codes and standards applied are commensurate with the importance to safety of these functions.

Nuclear power plant ASME Code Class 1 and 2 components are designed by either ASME Section III, Division 1 "Design by Analysis" (NB-3200 and NC-3200, respectively) or "Design by Rule" (NB-3600 and NC-3600, respectively) to ensure structural integrity of the safety-related reactor pressure boundary components and core support structures and core internals. ASME Code Class CS (core support structures) components are designed in accordance with Section III Subarticle NG-3200.

ASME publishes a new edition of the BPV Code, which includes Section III, every three years and new addenda every year. ASME BPV Code is incorporated by reference into 10 CFR

50.55a. The latest editions and addenda of Section III that the NRC has approved for use are referred to in 10 CFR 50.55a(a)(1)(i). ASME also publishes Code Cases quarterly. Code Cases provide alternatives to existing Code requirements that the ASME has developed and approved. The new Code Cases and revisions to existing Code Cases are incorporated by reference into 10 CFR 50.55a. NRC RG 1.84, "Design, Fabrication, and Materials Code Cases Acceptability, ASME Section III," lists all Section III Code Cases approved by the NRC. Currently, there are 80 acceptable Section III Code Cases and 12 conditionally acceptable Section III Code Cases.

The approved Code Cases may be used voluntarily by licensees as an alternative to compliance with ASME Code provisions that have been incorporated by reference in 10 CFR 50.55a. The requirements addressing implementation of approved Code Cases are contained in 10 CFR 50.55a(b)(4). It is the responsibility of the user to make certain that the provisions of the Code Case do not conflict with licensee commitments or regulatory requirements. Code Cases that the NRC has determined to be unacceptable are listed in NRC RG 1.193.[92] Code Cases may be annulled because the provisions have been incorporated into the Code, the application for which it was specifically developed no longer exists, or experience has shown that the design analysis or construction method is no longer adequate.

2.1 Service Conditions

The various components and support structures of a nuclear power system are subjected to plant and system operating and test conditions that are required to be considered in the design basis of the components to satisfy the applicable systems safety criteria. The pressures, temperatures, and mechanical loads to which reactor components and support structures are subjected as a result of plant or system operating or test conditions are referred as component and support structure design, service, and test loadings. These loadings are established from the anticipated or postulated plant or system operating and test conditions during the intended service life of the component and support structure. The ASME Code defines four levels of service conditions (A, B, C, and D) for various load combinations and stress limits.

- Level A service conditions (normal conditions) include operating pressure during system start-up, normal operation, hot standby, and shutdown, and weight loads.

- Level B service conditions (upset conditions, incidents of moderate frequency) consist of fluid transients (e.g., water hammer or relief valve discharge) and OBE seismic loads.

- Level C service conditions (emergency conditions, infrequent conditions, low probability) are those that may necessitate the removal of the components from service for inspection or repair for damages. Therefore, they require reactor shutdown for corrective action and repair of damages.

- Level D service conditions (faulted conditions, extremely low probability of postulated events) permit gross general deformations with some consequent loss of dimensional stability and damages requiring repair, which may require removal of the component. An example of level D loading is a combination of loss of coolant accident and SSE.

Examples of reversing and nonreversing dynamic loads are shown in Fig. 2. Reversing dynamic loads are loads that cycle about a mean value and include building filtered and earthquake loads. Nonreversing dynamic loads are loads that do not cycle about a mean value and include the inertial thrust force due to sudden opening or closing of valves and water

hammer resulting from entrapped water in two-phase flow systems. Reflected waves in a piping system due to flow transients are classified as nonreversing dynamic loads.

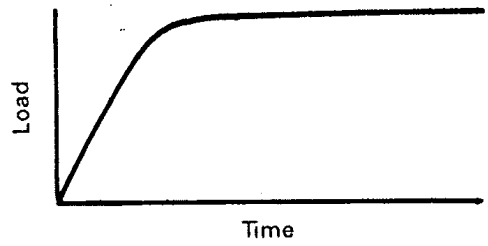

(a) Nonreversing dynamic load (relief/safety valve open-end discharge).

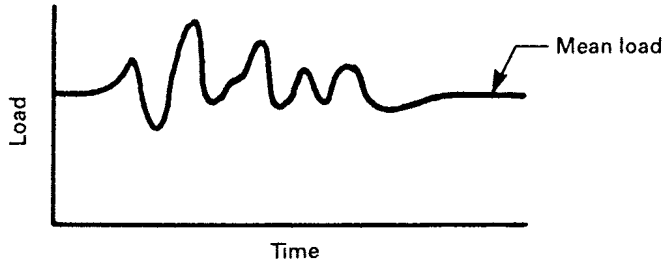

(b) Reversing dynamic load (earthquake load cycling about normal operating conditions).

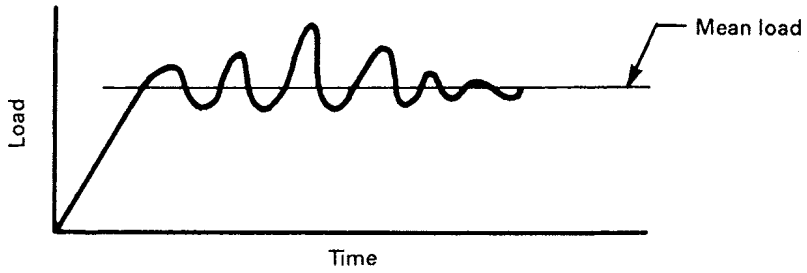

(c) Nonreversing dynamic load (initial water slug followed by reflected waves).

Figure 2. Examples of reversing and nonreversing dynamic loads (ASME Section III, Division 1, Subsection NB-3200, Figure NB-3213-1).

The stress levels in the components are calculated for various load combinations from applied internal pressure, dead weight, thermal expansion, earthquake loading, pipe rupture, and plant operational thermal and pressure transients. The basis for the classification of the various stresses is as follows:

(a) Primary stresses are caused by primary loads, and the primary stress limits are intended to prevent plastic deformation.

(b) Secondary stresses are caused by secondary loads, and the primary plus secondary stress limits are intended to prevent excessive plastic deformation leading to incremental collapse.*

* In limit analysis, collapse load is the maximum load or combinations of loads that a structure made of ideally plastic (non-strain-hardening) material can carry. In such cases the deformations increase without bound at this load.

(c) Peak stresses are the highest stresses in a local region and are the source for causing fatigue failure. The peak stress limit is intended to prevent failure due to cyclic loading.

In addition, when assurance of operability is required, the following design, service, and test limits are also defined for specific components and support structures:

- Level A service limits must be satisfied for all level A service loadings to which the component or support structure may be subjected in performance of its specific function (ASME Section III, Division 1 NB/NG-3222).

- Level B service limits must be satisfied for all level B service loadings for which these service limits have been designated, and the component or support structure must withstand these loadings without damage requiring repair (ASME Section III, Division 1 NB/NG-3223).

- Level C service limits must be satisfied for all level C service loadings for which these service limits have been designated. These limits permit large deformations in areas of large discontinuity that may necessitate the removal of the component or support structure from service for inspection or repair of damage (ASME Section III, Division 1 NB/NG-3224).

- Level D service limits must be satisfied for all level D service loadings for which these limits have been designated. These limits permit gross general deformations with some consequence loss of dimensional stability and damage requiring repair that may require removal of the component from service (ASME Section III, Division 1 NB/NG-3225).

- Alternating service limits are also defined, which may be more restrictive service limits than defined in the component design specification. Components and support structures may be designed using these more restrictive service limits.

If these service stress limits are too restrictive, ASME Section III, Division 1 NB-3228 provides guidance for using plastic analyses, which allow some relaxation of the basic stress limits (ASME Section III, Division 1 NB/NG-3228). The applied loads are classified as follows:

(a) Primary loads (sustained loads), which include loads caused by internal pressure, dead weight, and the like, and failure due to these loads results in catastrophic failure; and

(b) Secondary loads (expansion loads), which are caused by displacements that arise from thermal expansion, hot- and cold-piping-fluid cyclic loads, seismic anchor movements, and building settlement.

In addition, “alternating stress” is defined as one-half of the calculated peak stress. In fatigue analyses, fatigue failure can be prevented by ensuring that the number of load cycles associated with a specific alternating stress is less than the number of load cycles allowed in the design fatigue curve (S-N curve).

2.2 Seismic Design

The seismic design of commercial NPPs has evolved significantly since the 1960s.[93] The initial design of NPPs was based on static analysis in which the seismic loads were applied laterally with an acceleration of 0.05g, 0.10g, and 0.20g in low-, moderate-, and high-seismic-intensity

areas, respectively. However, the analytical procedures used to develop the forces and moment,- and resultant seismic loadings in structures and components were controlled by computational limitations. In addition, the acceptance criteria were typically limited to one-third increase in normal allowable stresses when seismic stresses were combined with normal dead and live load stresses. The normal allowable stresses were between 0.6 and 0.67 times the specified minimum yield stress.

In 1963, the concepts of dynamic response spectra analysis were introduced in seismic design of NPP structures and components with the publication of the U.S. Atomic Energy Commission report TID-7024.[94] Initially, these concepts were limited to building structures but, by 1971, were gradually extended to include the load definition for mechanical and electrical distribution systems and components. A response spectrum is a plot of the maximum acceleration, velocity, or displacement of a family of oscillations associated with the ground or structures. Each earthquake produces its own unique spectrum of ground motions, which vary in frequency and acceleration and may last several seconds or longer. The record of ground motion recorded on an accelerograph appears as a jagged line that represents the peak values of acceleration/deceleration (Fig. 3). The ground motion response spectrum (GMRS) represents the range of multiple earthquake records shown in Fig. 4; it appears as an irregular graph of peaks and valleys that combines a number of individual response spectra from past earthquakes.[95]

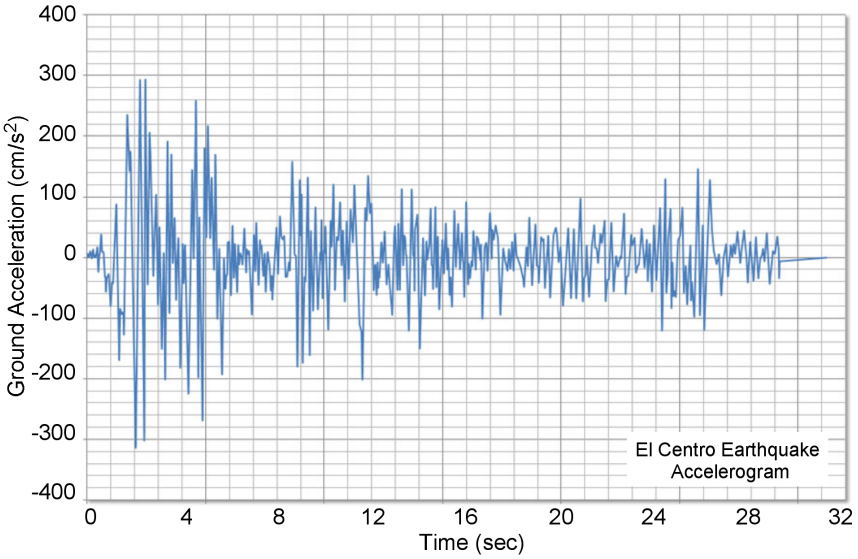

Figure 3. Ground acceleration record of the Imperial Valley Aftershock May 19, 1940 at El Centro, CA.

The seismic spectra important to NPP design have PGAs in the range of 5 to 10 Hz. The NRC has developed Design Response Spectra (DRS) statistically from response spectra of past strong-motion earthquakes. In 1973, the former Atomic Energy Commission (AEC), the NRC's predecessor, published RG 1.60, DRS for Seismic Design of Nuclear Power Plants,[96] to provide spectral shapes for horizontal and vertical ground movements. It was based on a mean plus one standard design basis response based on a normal probability density function as shown in the horizontal design response spectra in NRC RG 1.60. Furthermore, floor or in-structure response spectra also began to be used in design of structures and components located at other than the free-field surface ground levels of buildings.

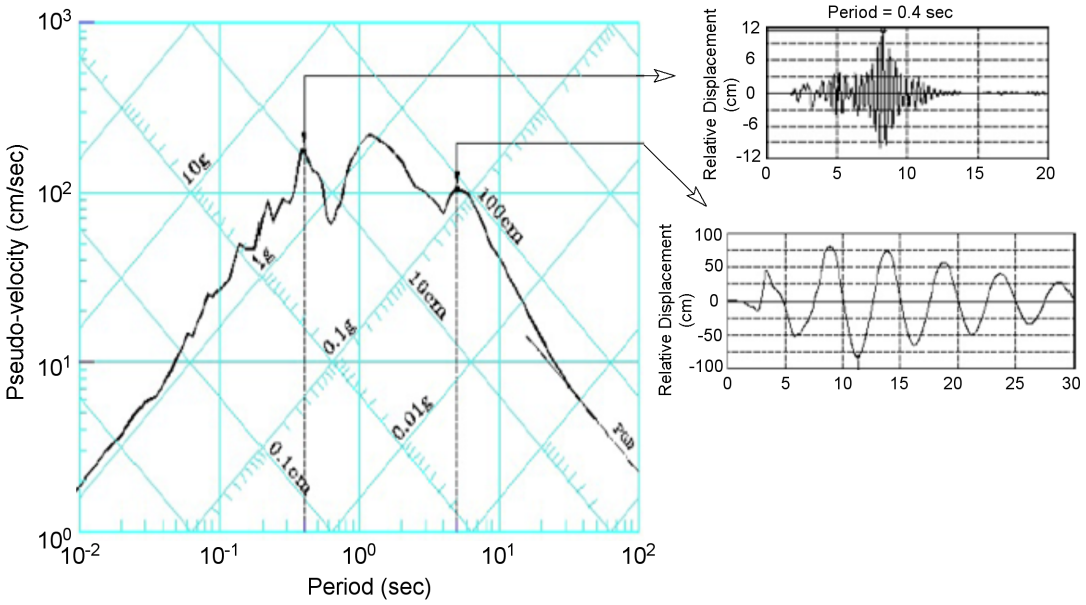

Figure 4. Site-specific ground motion response spectrum (Ref. 95).

In general, designs of NPPs during the 1960s and 1970s used a deterministic approach to seismic design based on site-specific examinations of local and regional seismic, geological, and geotechnical soil conditions to determine the maximum credible earthquake. Deterministic seismic hazard analyses (DSHA) quantified the effects of a maximum credible earthquake based on known seismic sources sufficiently near the site as well as available historical seismic and geological data to estimate ground motion at the NPP site. Appendix A to 10 CFR 100 requires an evaluation of fault and earthquake occurrences to provide the basis for determining an SSE.[64] It describes the limitations for basing seismic design criteria on literature reviews of geographical and geological information and requires supplementing the assessment with studies for vibratory ground motion, evidence of surface faulting, and evidence of seismically induced floods and water waves that could affect the site. In 10 CFR 100 Appendix A, SSE is defined by response spectra corresponding to the maximum vibratory accelerations as outlined in paragraph (a) of section VI; and where the maximum vibratory accelerations of the SSE at the foundations of the NPP structures are determined to be less than one-tenth the acceleration of gravity (0.1 g) as a result of the steps required in paragraphs (a)(1)(i) through (iv) of section V, it shall be assumed that the maximum vibratory accelerations of the SSE at these foundations are at least 0.1 g.

After 2000, there were attempts to standardize the design of NPPs to include not only a standardized reactor coolant system, but also a standardized balance of plant. This resulted in the development of standardized ground response spectra and floor or in-structure response spectra used in the present day seismic analyses of NPP structures and components. In the design of new NPPs, the SSE is established on the basis of Probabilistic Seismic Hazard Analysis (PSHA) performed in accordance with 10 CFR 100.23 "Geologic and Seismic Siting Criteria." Whereas DSHA-based PGA values on a single earthquake source, PSHA utilized the most recent information related to earthquake sources and occurrences and ground motion estimates to establish the probability of exceeding various levels of earthquake-induced ground motion at a specific location during a specific period in the future. The PSHA quantifies the seismic hazard characteristics of a site from seismic hazard curves or “response spectra” developed in part by identifying and characterizing each seismic source in terms of maximum magnitude, magnitude recurrence relationship, and source geometry.

Furthermore, as more data became available on actual recorded earthquake activities, a better understanding developed regarding the shape of the design basis ground response spectra recorded at various sites around the world. For example, data recorded at sites with relatively high seismic activity (e.g., California, Japan, Chile) with a significant amount of faulting and other geographical characteristics indicated that the peak or dominant site response spectra occurred between 2.5 and 9 Hz. However, earthquake motion recorded at sites associated with moderate or low seismic activity show that the associated free-field ground acceleration response spectra peak occurred at much higher frequencies (e.g., between 10 and 25 Hz). As a result, the standard plant free-field ground response spectra have tended to have higher acceleration spectrum amplitudes than the spectra used in the past, particularly on rock sites. In addition, the acceptance criteria have also been updated.

A seismic hazard map of the United States showing 2% probability of exceedance of the design basis PGA in 50 years is presented in Fig. 5. Documented earthquake activity in the United States since 1568, is shown in Fig. 6. Seismic risk is determined from an assessment of historical earthquake activity and a seismic hazard map of a specific region showing the likely PGA values to be experienced during an earthquake with a probability of exceedance.

In general, the seismic design of civil, mechanical, electrical, instrumentation, and control structures and components of NPPs involves three activities:

1. Quantification of seismic load and other concurrent applicable loads and specification of their load combinations;

2. Analysis methods and procedures necessary to convert input earthquake motions normally expressed in the form of acceleration, to resultant seismic forces, moments, or stresses in structures and components; and

3. Codes and Standards acceptance criteria used to determine the adequacy of the analysis performed in no. 2.

The first and third activities are defined by applicable national codes, standards, and regulatory requirements. The second activity depends on the experience and training of the engineers performing the analysis and their understanding of dynamic analysis of structures using finite element methods to incorporate any specific analytical techniques.

ASME BPV Code Section III does not require dynamic analysis. However, the design of NPP structures and components requires consideration of seismic and other dynamic inputs, which are defined in the design specifications of the structures and components. The requirements and recommendations for seismic analysis of NPP piping systems that are important to safety are detailed in ASME Code Non-mandatory Appendices N, “Dynamic Analysis Methods,” and F, “Rules for Evaluation of Service Loading with Level D Service Limits.” The earthquake engineering criteria for construction permits, operating licenses, design certifications, combined licenses, design approvals, or manufacturing licenses of NPPs are given in Appendix S to 10 CFR 50. In addition, the NRC periodically issues special guidance documents specifying requirements for equipment classification and procedures for combination of loads and describing new analytical techniques. Examples of such documents include RG 1.29, “Seismic Design Classification”[97]; RG 1.61 “Damping Values for Seismic Design of Nuclear Power Plants;”[98] and RG 1.92 “Combining Modal Responses and Spatial Components in Seismic Response Analysis.”[99]

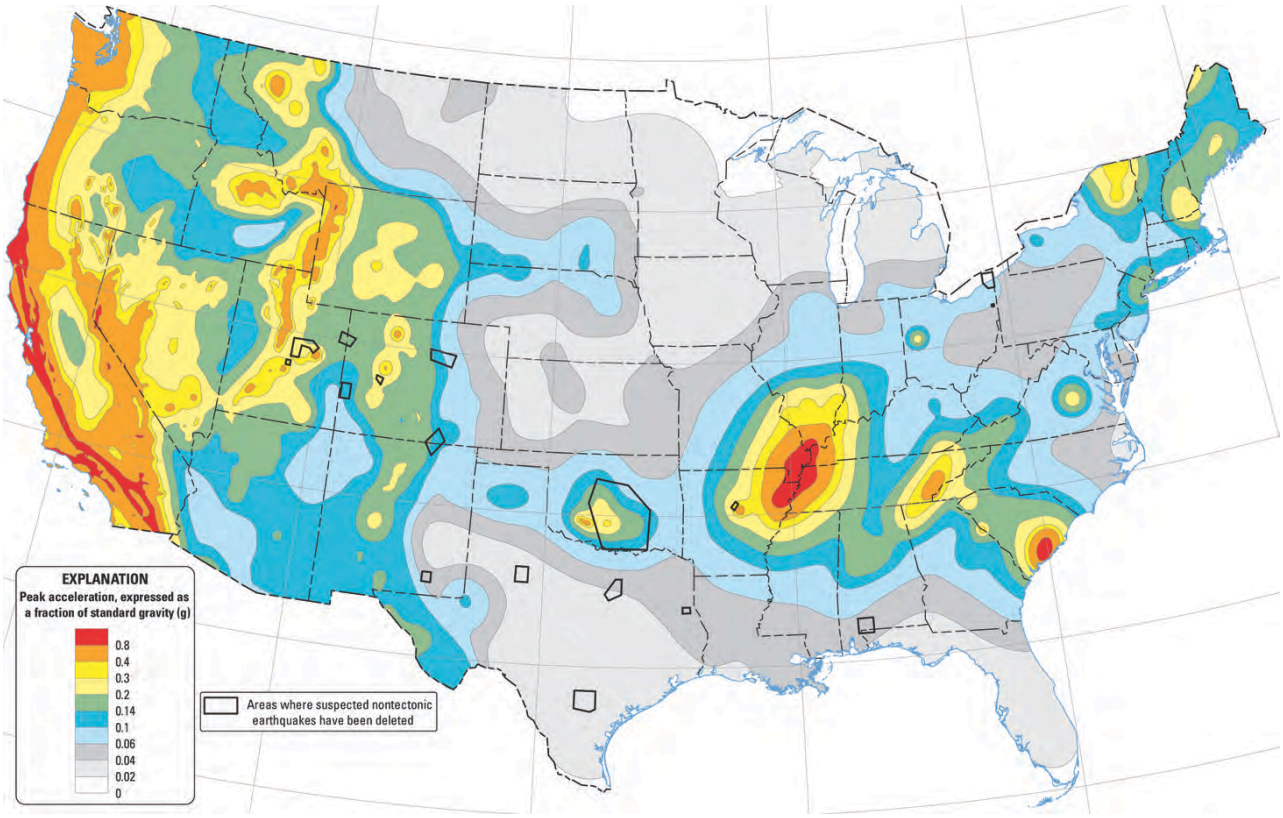

Figure 5. A seismic hazard map showing 2% probability of exceedance of design-limit PGA in 50 years.

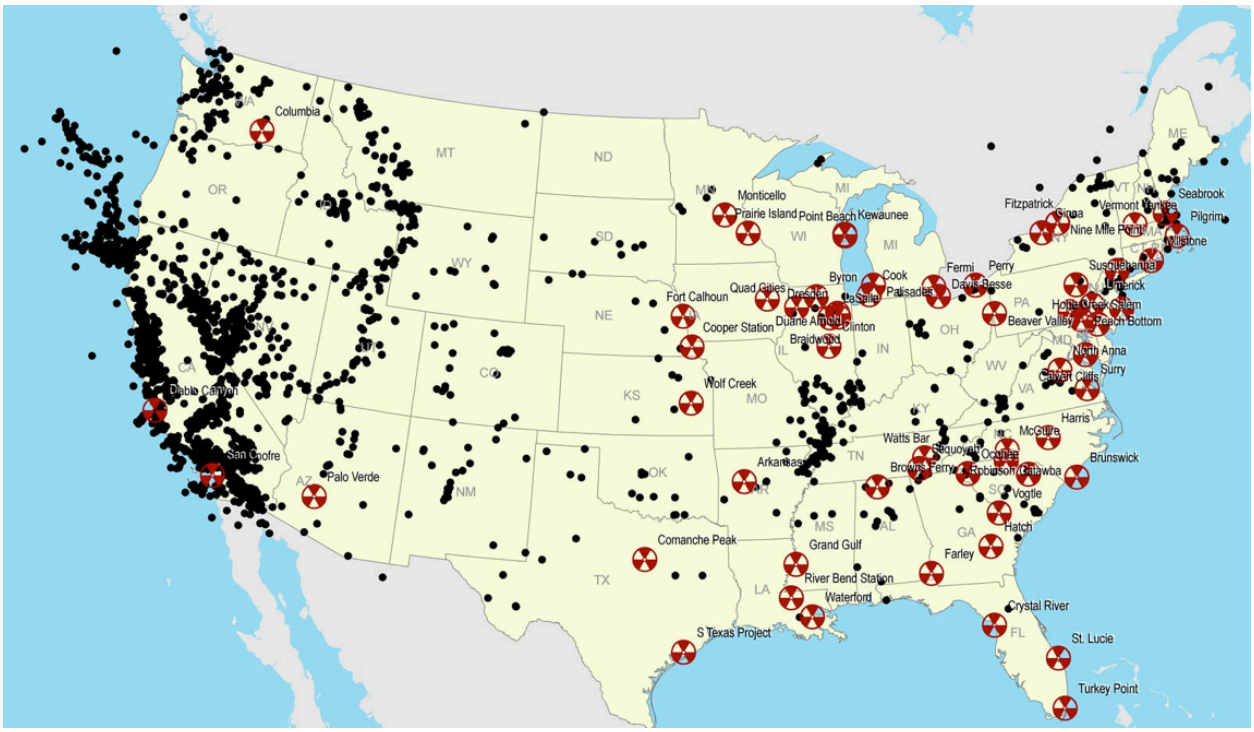

Figure 6. Documented earthquake activity in the United States since 1568.

Component design may be based on the use of static forces resulting from equivalent earthquake acceleration acting at the center of gravity of the extended masses, or a dynamic system analysis may be used to show how seismic loading is transmitted from the defined ground motions to all parts of the buildings and SSCs. Subarticles N-1100 and N-1200 of Non-mandatory Appendix N[100] Article N-1000, "Dynamic Analysis Methods," describe one or more acceptable steps for seismic analysis. However, because the seismic dynamic analysis involves a series of steps, and some of the steps have acceptable alternative methods, these are not the only acceptable methods. Appendix N Subarticles N-1300 through N-1700 describe areas of dynamic analysis that are used in the design of NPP components, such as flow-induced vibration and dynamics of coupled fluid-shells, but are not specifically required in seismic analysis.

2.3 Selection of Seismic Loads

As discussed earlier, all nuclear facilities are designed so that earthquakes and other external events will not jeopardize the safety of the plant, particularly the safe shutdown of the reactor. The selection of the intensities of the OBE and DBE (or SSE) depends on the region of the country where the site is located, its geological conditions, and previous seismic experience and records. The information developed from studies of strong-motion earthquakes can be used to obtain estimates of the structural response of NPP components supported by the ground. However, such information is not available for most of the NPP sites. Seismic design of NPP structures and components requires reasonably good estimates for the motion history of the maximum ground acceleration, the maximum ground velocity, and the maximum ground displacement. Furthermore, a high factor of safety may be required for Class 1 components of NPPs, where damage might involve exposure of large numbers of people to excessive radiation hazard.[101]

The methods currently used for the design of NPP structures and components under postulated and anticipated loads during reactor service include techniques for calculating the structural or mechanical response of the structures and components either in terms of a well-defined time history of motion or some probability intensity associated with a general pattern of motion. Unfortunately, the same degree of certainty in the design calculations for earthquake loadings is possible in only a few areas of the world where observations of strong-motion earthquake intensities have been recorded over long periods.[101] The basis and methodology for establishing seismic loads on a structure or component are summarized below.[102]

The seismic loads on a structure are generated by the deformation of the structure as it vibrates, which is different from the gravitational loads and, in most cases, even wind loads. Therefore, the seismic load is part of the dynamics of the structure and is governed by Newton's Second law (F = ma). However, the gravitational and effective wind loads are governed by Newton's third law (action–reaction). The seismic load is the inertial force on the structure and can be expressed in terms of the acceleration of the structure. However, its magnitude and distribution on the structure continually change with time, t, during the vibration created by the seismic event. The first step in seismic design of structures is to determine the maximum seismic force and its distribution on the structure during the seismic event. Particular attention is paid to the use of equivalent static procedures that attempt to capture the principal effects of the essentially dynamic state.

The seismic force depends on the distribution of mass and stiffness throughout the structure. Therefore, the distribution of mass and stiffness of the structure and the manner in which plasticity spreads through the structure are the two key factors critical in determining the

maximum magnitude and the distribution of seismic force in the structure. These two factors must be considered in any approach that attempts to quantify the seismic force.

The dynamic factor must capture the facts that the seismic force represents an amplification of the vibration of the ground due to resonance effects of the structure and that the maximum amplification depends on the free vibration period of the structure. For an elastic structure, the free vibration period, T, is proportional to $\sqrt{(M/K)}$, where M is the mass and K is the elastic stiffness of the structure. Therefore, for a structure with a uniform or regular mass, the dynamics factor and hence the seismic force depend on the mass and elastic stiffness of the structure.

A response spectrum is simply a plot of the peak or steady-state response, such as displacement, velocity, or acceleration of a series of vibrations of varying natural period (or natural frequency), that are forced into motion by the same base vibration or shock. The resulting plot is used to establish the response of any linear system, given its natural period of vibration. For example, the *acceleration response spectrum*, a graph of the maximum acceleration as a function of the free vibration or natural period, is typically used in assessing the peak response of buildings to earthquakes. Some values from the ground response spectrum (calculated from recordings of surface ground motion from seismographs) are typically used for correlation with seismic damage.

Figure 7 shows a typical acceleration response spectrum of the averaged and smoothed maximum acceleration of elastic structures founded on rock due to an earthquake. In this example, the maximum amplification of the rock acceleration is 2.5. The plot indicates that structures with a small period (i.e., high stiffness or shorter structures) experience higher magnification of the ground acceleration; after the plateau the magnification rapidly decreases for structures with a longer natural period of vibration (i.e. for more flexible or taller structures).

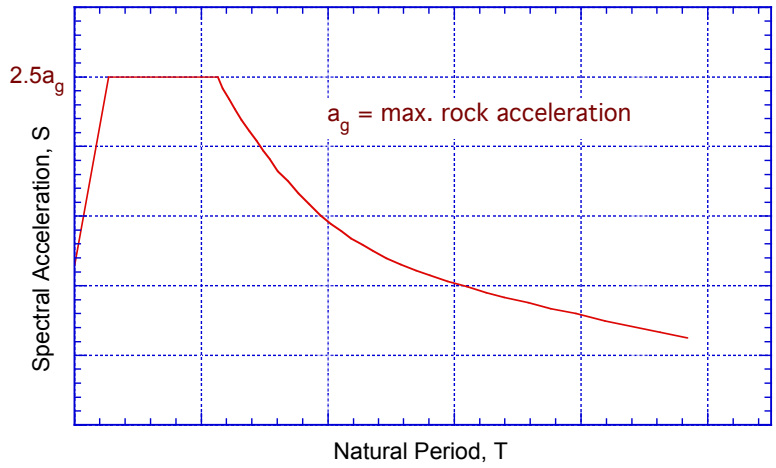

Figure 7. Acceleration response spectrum of elastic structures founded on rock.

However, structures are not typically founded on rock; there is soil between the structure and the rock where the earthquake originated. Structures located some distance from the epicenter of the earthquake experience additional acceleration due to the resonance of the soil. It was initially believed that this soil resonance effect was significant only for structures with higher range of natural period. However, recent experience indicates that the soil resonance effect also occurs in the short period range, particularly on soft sites.

2.3.1 Soil Structure Interaction

The maximum vibratory accelerations of the SSE must take into account the characteristics of the underlying soil material in transmitting the earthquake-induced motions at the various locations of the plant's foundation. Depending on the elevation above the foundation, various NPP structures and components vibrate at different frequencies during a seismic event. Vibrations in the range of 1–10 Hz are particularly of concern, because they correspond to damaging resonance frequencies for most structures and components. These accelerations and the corresponding shaking frequencies are parameters that are considered in PSHA, discussed further in Subsection 2.3.3. The complete seismic spectrum may be characterized by two intervals: PGA and spectral acceleration, averaged between 5 and 10 Hz.

Earthquakes with frequencies below 15 Hz predominate in the western United States (WUS). As discussed before, earthquakes below the 10-Hz frequency range pose the greatest hazard; in WUS, earthquake magnitude is a primary design consideration for NPPs. In central and eastern United States (CEUS), since recording of seismic events are sparse, NPP designs consider both earthquake magnitude and Modified Mercalli Intensity (MMI). The effect of an earthquake on the earth's surface is called the intensity. Various intensity scales have been developed during the past several hundred years; the MMI scale is currently used in the United States. The scale, designated by Roman numerals, comprises increasing levels of intensity ranging from imperceptible shaking (designated by number I) to catastrophic destruction (designated by number X). Although NPPs in the CEUS are designed to withstand low-frequency earthquakes, the typical earthquakes in the CEUS are associated with higher frequencies than in the WUS. Higher frequencies are less damaging to large structures but may adversely affect small components.

The response of a structure to earthquake shaking is affected by interactions between three linked systems: the structure, the foundation, and the soil underlying and surrounding the foundation. However, in most analytical methods, the foundation is considered part of the structure. Therefore, the term soil-structure interaction (SSI) is used to describe this effect. The SSI analysis evaluates the collective response of these systems to a specific free-field ground motion. The term "free field" refers to motions not affected by structural vibrations or the scattering of waves at and around the foundation. SSI effects are absent for the theoretical condition of a rigid foundation supported on rigid soil. The SSI effects are categorized as inertial interaction effects, kinematic interaction effects, and soil–foundation flexibility effects.[103] In seismic design analyses, these effects are related to the following:

- *Foundation stiffness and damping*: In a vibrating structure, inertia gives rise to base sheer, moment, and torsion forces, all of which generate displacements and rotations at the soil–foundation interface. These displacements and rotations are possible because of flexibility in the soil–foundation system, and it significantly increases the overall structural flexibility. In addition, these displacements result in energy dissipation due to radiation damping and hysteretic soil damping. These effects are referred to as inertial interaction effects because they are caused by structural inertia.

- *Variation between foundation input motions and free-field ground motions*: The free-field motions and foundation input motions are different for two reasons. First, for stiff foundation elements placed at or below the ground surface, kinematic interactions cause the foundation motions to deviate from the free-field motions because of base slab averaging, wave scattering, and embedment effects, in the absence of both structure

and foundation inertia. Second are the relative displacements and rotations between the foundation and free field associated with both structure and foundation inertia.

- *Foundation deformation*: The forces and displacements imposed by the superstructure and the soil medium lead to flexural, axial, and shear deformation of structural foundation elements. These deformations could be significant, particularly for flexible foundations such as rafts and piles. Therefore, foundation components must be designed to account for deformations.

Two methods, a direct analysis and a substructure approach, are used to evaluate the SSI effects. In a direct analysis, the soil and structure are included within the same model and analyzed as a complete system. However, although direct analyses can address all the SSI effects, incorporation of kinematic interaction is challenging. In addition, because direct solution of the SSI problem is difficult from a computational perspective, particularly for a system that is geometrically complex or contains significant nonlinearities on the soil or structural materials, it is rarely used in practice.

In a substructure approach, the SSI analysis is separated into distinct parts that are combined to obtain the complete solution. In this approach, a proper consideration of SSI effects requires the following:

- An evaluation of free-field soil motions and corresponding soil material properties;
- An evaluation of transfer functions to convert free-field motions to foundation input motions;
- Incorporation of springs and dashpots (or more complex nonlinear elements) to represent the stiffness and damping of the soil–foundation interface; and
- A response analysis of the combined structure-spring/dashpot system with the foundation input motion applied.

2.3.2 Damping Values for Seismic Design

Damping is a measure of the energy dissipation of a material or structural system as it responds to dynamic excitation. The term “damping” is used to assist in mathematical modeling and in solving dynamic equations of motion for a vibratory system in which energy is dissipated. In addition to the energy lost between the structure and its supports on the ground, there are energy losses within the structure itself and at the points of attachment of equipment and components to the structure. One of the ways for damping due to energy losses within a structure, is due to the spread of plasticity or inelasticity throughout the structure.

Structures are typically designed to withstand considerably smaller horizontal forces than those calculated from available earthquake motions that have been recorded. Yet the NPP structures and components do not show any evidence of degradation or damage that one would expect if the design forces reached the levels computed from seismic analysis.[104] For example, the El Centro or Imperial Valley earthquake measuring 7.0 M_W (moment magnitude scale)* in the southwest corner of Southern California on May 18, 1940, represented a maximum ground motion acceleration of 0.32g and a maximum ground velocity of 0.36 m/s (14 in./s). The El

* This is equivalent to 6.4 M_L Richter scale.

Centro earthquake ground motion acceleration record is shown in Fig. 3. The horizontal force coefficient for structures with natural periods of 0.5 s was of the order of 0.6 times the weight, even for critical damping values as high as 10%. Yet structures designed for maximum ground motion acceleration of 0.1g performed well under the El Centro earthquake.

Veletsos and Newmark[104] demonstrated that inelastic behavior can effectively reduce the horizontal force coefficient that may be used in seismic design to values of the order of one-fourth or less than those that would be applicable for elastic systems. They recognized that although other factors such as ground coupling also modify the input motion of a specific structure, the process of inelastic energy absorption is a major consideration in seismic design procedures. Veletsos and Newmark proposed a "ductility factor," defined as the ratio of the maximum deformation and yield point deformation. They concluded that for most materials, including steel and reinforced concrete, plastic deformation of the order of three times the elastic deformation (i.e., corresponding to a ductility factor of 4) does not involve any significant distortions or damage. However, a design based on a ductility factor of 4 would permit the structure to behave elastically or nearly elastically for most earthquakes except those as intense as the SSE. The maximum accelerations in the elasto-plastic systems, and consequently the design load factors of such systems, can be expressed in terms of the corresponding quantities for elastic systems multiplied by a reduction factor related to the degree of plastic deformation, which is permissible.[104]

In an elastic dynamic seismic analysis, the energy that is dissipated is accounted for by specifying the amount of viscous damping (i.e., damping force proportional to the velocity) in the analytical model. The amount of damping in the structural elements and components depends on (a) the intensity of motion, (b) the associated stress levels, and (c) the geometry and energy absorption mechanism within the structural element or component.

The guidance in NRC RG 1.61, Damping Values for Seismic Design of Nuclear Power Plants,[105] provides acceptable damping values to be used in the elastic seismic response analysis and design of seismic Category I NPP structures and components in which energy dissipation is approximated by viscous damping unless otherwise specified. Regulatory positions 1 through 5 of Section C of the RG provide the updated damping values for structures; piping; electrical distribution system; heating, ventilation, and air conditioning duct; and mechanical and electrical components, respectively. Damping values higher than those provided in RG 1.61 may be used if documented test data support the higher values. Damping values associated with SSI analysis are not within the scope of RG 1.61.

As noted in regulatory position 1.2 of RG 1.61, "The SSE damping values specified in Table 3 for linear dynamic analysis of structures have been selected based on the examination that the structural response attributed to load combinations that include SSE will be close to applicable code stress limits, as defined in NUREG-0800[106] Section 3.8." However, there may be cases in which the predicted structural response to load combinations that include SSE is significantly below the applicable code stress level. Although this is not a concern for structural evaluation, for in-structure response spectra it is necessary to use the damping-compatible structural response. Consequently, the following additional guidance is provided for analyses used to determine in-structure response spectra:

1. Use of OBE damping values specified in Table 4, which are acceptable to the staff without further review.

2. Submit a plant-specific technical basis for use of damping values higher than the OBE damping values specified in Table 4, but not greater than the SSE damping values specified in Table 3, subject to staff review on a case-by-case basis.

Table 3. Safe-shutdown earthquake (SSE) damping values.

Structural Material	Damping (% of Critical Damping)
Reinforced concrete	7%
Reinforced masonry	7%
Prestressed concrete	5%
Welded steel or bolted steel with friction connections	4%
Bolted steel with bearing connections	7%
Note: For steel structures with a combination of different connection types, use the lowest specified damping value, or as an alternative, use a "weighted average" damping value based on the number of each type present in the structure.	

Table 4. Operating basis earthquake (OBE) damping values.

Structural Material	Damping (% of Critical Damping)
Reinforced concrete	4%
Reinforced masonry	4%
Prestressed concrete	3%
Welded steel or bolted steel with friction connections	3%
Bolted steel with bearing connections	5%

2.3.3 Design Response Spectra

The NRC staff has used the 1973 edition (i.e., Rev. 1) of RG 1.60, DRS for Seismic Design of Nuclear Power Plants,[96] for numerous siting and licensing activities and it forms part of the licensing basis for NPPs constructed during the 1970s and 1980s. However, in 1997, the role of PSHA led to the establishment of new requirements for siting regulation in 10 CFR 100.23, "Geology and Seismic Siting Criteria." The new siting regulation applies to new reactors as well as NPP construction permit or operating licenses on or after January 10, 1997. The new siting requires, in part, the explicit consideration of the uncertainties associated with geological and seismological characteristics through an appropriate analysis, such as PSHA. The role of PSHA also led to the development initially of NRC RG 1.65,[107] which was subsequently replaced in 2007 with NRC RG 1.208, A Performance-Based Approach to Define the Site-Specific Earthquake Ground Motion.[74] RG 1.208 provides general guidance on methods acceptable to the NRC staff for the following:

1. Conducting geological, geophysical, seismological, and geotechnical investigations;

2. Identifying and characterizing seismic sources;

3. Conducting a PSHA;

4. Determining seismic wave transmission (soil amplification) characteristics of soil and rock sites; and

5. Determining a site-specific, performance-based GMRS), satisfying the requirements of paragraphs (c), (d)(1), and (d)(2) of 10 CFR 100.23, and leading to the establishment of a SSE to satisfy the design requirements of Appendix S to 10 CFR 50.

According to Appendix S to 10 CFR Part 50, the foundation-level ground motion must be represented by an appropriate response spectrum with a peak ground acceleration of at least 0.1g. The steps necessary to develop the final SSE are described in Chapter 3, "Design of Structures, Components, Equipment and Systems," of NUREG-0800, and Regulatory Position 5.4 of NRC RG 1.208 provides a detailed description of the development of the final SSE. Although NRC RG 1.60 is no longer used to characterize the hazard for the seismic design of NPPs, the certified seismic design response spectra for several new reactor designs have been derived from RG 1.60 spectra with modified control points to broaden the spectra in the higher frequency range. The RG 1.60 spectral values are based on deterministic values for WUS earthquakes. However, recent observations have shown that higher frequency motions at CEUS rock sites may be significantly greater than motions recorded in WUS rock sites.

The recorded ground accelerations and response spectra of past earthquakes provide a basis for the design of structures to resist earthquakes. The response spectra developed for a site are known as the DRS, and are developed statistically from response spectra of past strong-motion earthquakes.[108–111] This procedure was considered acceptable by the NRC staff for defining the DRS on sites underlain by either rock or soil deposits and covering all frequencies of interest. However, for unusually soft sites, modification to this procedure will be required.

The horizontal- and vertical-component DRS correspond to a maximum horizontal ground acceleration of 1.0 g, are shown in Figs. 8 and 9, respectively. For sites with different acceleration values specified for the design earthquake, these DRS, without SSI effects should be linearly scaled proportional to the specified maximum horizontal ground acceleration. However, the procedure described above will not apply for sites that (a) are relatively close to the epicenter of an expected earthquake or (b) have physical characteristics that could significantly affect the spectral pattern of input motion, such as being underlain by poor soil deposits. In these cases, the DRS should be developed individually according to the site characteristics.

In Fig. 8, the base diagram consists of three parts: the bottom line on the left part represents the maximum ground displacement; the bottom line on the right part represents the maximum acceleration; and the middle part depends on the maximum velocity. The numerical values of design displacements, velocities, and accelerations for the horizontal component DRS are obtained by multiplying the corresponding values of the maximum ground displacement and acceleration by the factors given in Table 5.

Construction of the spectral shapes in Fig. 9 followed the instructions in references 106 and 107 for the construction of vertical component spectra. Note that the vertical DRS values are two-thirds those of the horizontal DRS for frequencies less than 0.25; for frequencies higher than 3.5, they are the same, while the ratio varies between two-thirds and 1 for frequencies between 0.25 and 3.5. The numerical values of design displacements, velocities, and accelerations in these spectra are obtained by multiplying the corresponding values of the maximum horizontal ground motion [acceleration = 1.0 g and displacement = 0.914 m (36 in.)] by the factors given in Table 6.

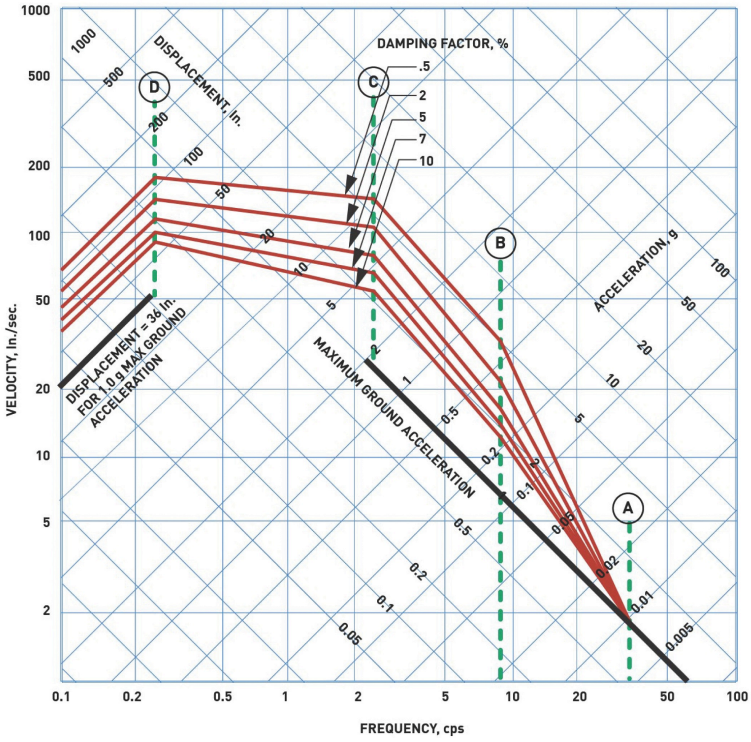

Figure 8. Horizontal design response spectra scaled to 1 g horizontal ground acceleration (NRC RG-1.60 Figure 1).

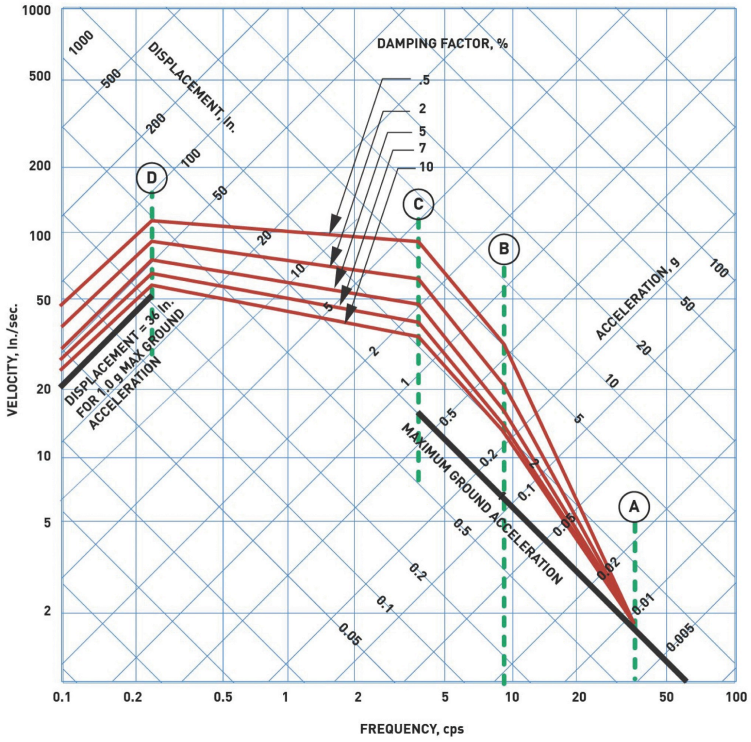

Figure 9. Vertical design response spectra scaled to 1 g horizontal ground acceleration (NRC RG-1.60 Figure 2).

Table 5. Horizontal design response spectra: relative values of spectrum amplification factors for control points (NRC RG 1.60 Table 1).

Percent of Critical Damping	Amplification Factors for Control Points			
	Acceleration[a,b]			Displacement[a,b]
	A (22 cps)	B (9 cps)	C (3.5 cps)	D (0.25 cps)
0.5	1.0	4.96	5.95	3.20
2.0	1.0	3.54	4.25	2.50
5.0	1.0	2.61	3.13	2.05
7.0	1.0	2.27	2.72	1.88
10.0	1.0	1.90	2.28	1.70

[a] Maximum ground displacement is taken proportional to maximum ground acceleration and is 0.914 m (36 in.) for ground acceleration of 1.0 gravity.
[b] Acceleration and displacement amplification factor are taken from recommendations given in Ref. 108.

Table 6. Vertical design response spectra: relative values of spectrum amplification factors for control points (NRC RG 1.60 Table 2).

Percent of Critical Damping	Amplification Factors for Control Points			
	Acceleration[a,b]			Displacement[a,b]
	A (22 cps)	B (9 cps)	C (3.5 cps)	D (0.25 cps)
0.5	1.0	4.96	5.67[c]	2.13
2.0	1.0	3.54	4.05	1.67
5.0	1.0	2.61	2.98	1.37
7.0	1.0	2.27	2.59	1.25
10.0	1.0	1.90	2.17	1.13

[a] Maximum ground displacement is taken proportional to maximum ground acceleration and is 0.914 m (36 in.) for ground acceleration of 1.0 gravity.
[b] Acceleration amplification factors for the vertical design response spectra are equal to those for horizontal design response spectra at a given frequency, whereas displacement amplification factors are 2/3 those for horizontal design response spectra. These ratios, between the amplification factors for the two design response spectra are in agreement with those recommended in Ref. 108.
[c] These values were changed to make this table consistent with the discussions of vertical components in the discussion section of NRC RG 1.60 Rev. 2.

An example of horizontal SSE response spectra with 5% critical damping is shown in Fig. 10. It is anchored in the high frequency range at a specific value of acceleration; in this case, 0.28g. The response spectrum is scaled up or down (or remain unchanged) depending on the PGA of the actual NPP site. The PGA values at various NPP sites in the United States are listed in Table 2.

Establishing the seismic loads for RCPB components and reactor core support structures and core internals typically involves the following steps:

1. Develop the SSE response spectra that define PGA and an acceleration response spectrum that is representative of the specific site.

2. Generate two horizontal and one vertical ground acceleration time histories. A single set of three mutually orthogonal, statistically independent, synthetic acceleration time histories, is used as the input in the dynamic analysis of seismic Category I structures.

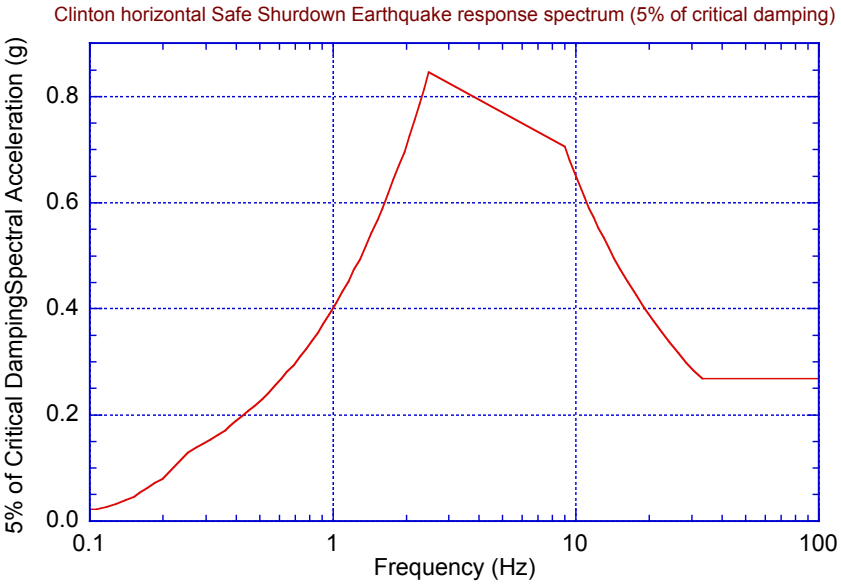

Figure 10. Horizontal SSE response spectrum with 5% critical damping.

The synthetic time histories are generated by modifying a set of actual recorded earthquake time histories and the following NRC guidelines:

- The response spectra of the time histories must envelop the design response spectra.
- The time histories must last at least 20 seconds.
- The time histories must contain at least 6 seconds of strong motion.

3. Develop acceleration time histories and in-structure response spectra (also called floor response spectra) at various locations (such as supports of piping, reactor vessel) of the reactor building, incorporating SSI analysis.

The third step provides seismic loads in the form of in-structure response spectra or time-histories for RCPB components and reactor core internals or any other components within the reactor building. Time-history analysis is required if the system has small clearances (gaps) between the components (e.g., reactor internals).

An example of design horizontal time histories, H2 acceleration, velocity, and displacement is shown in Fig. 11. Design horizontal time history, H1, is applied in the north south (global x or 1) direction; design horizontal time history, H2, is applied in the east west (global Y or 2) direction; and design vertical time history is applied in the vertical (global Z or 3) direction.

2.3.4 In-Structure Response Spectra

NRC RG 1.122, Development of Floor DRS for Seismic Design of Floor-Supported Equipment or Components[112] describes methods that are acceptable to NRC staff for developing the two horizontal and one vertical in-structure response spectra (e.g., floor response spectra) from the time history motions resulting from the dynamic analysis of the supporting structure. Because a large number of degrees of freedom would be necessary if the complete plant was treated in a single mathematical model, the plant is usually divided into several separate systems. Thus, usually there are one or more mathematical models of supporting structures. Each supporting structure normally supports one or more systems or pieces of equipment. Because most

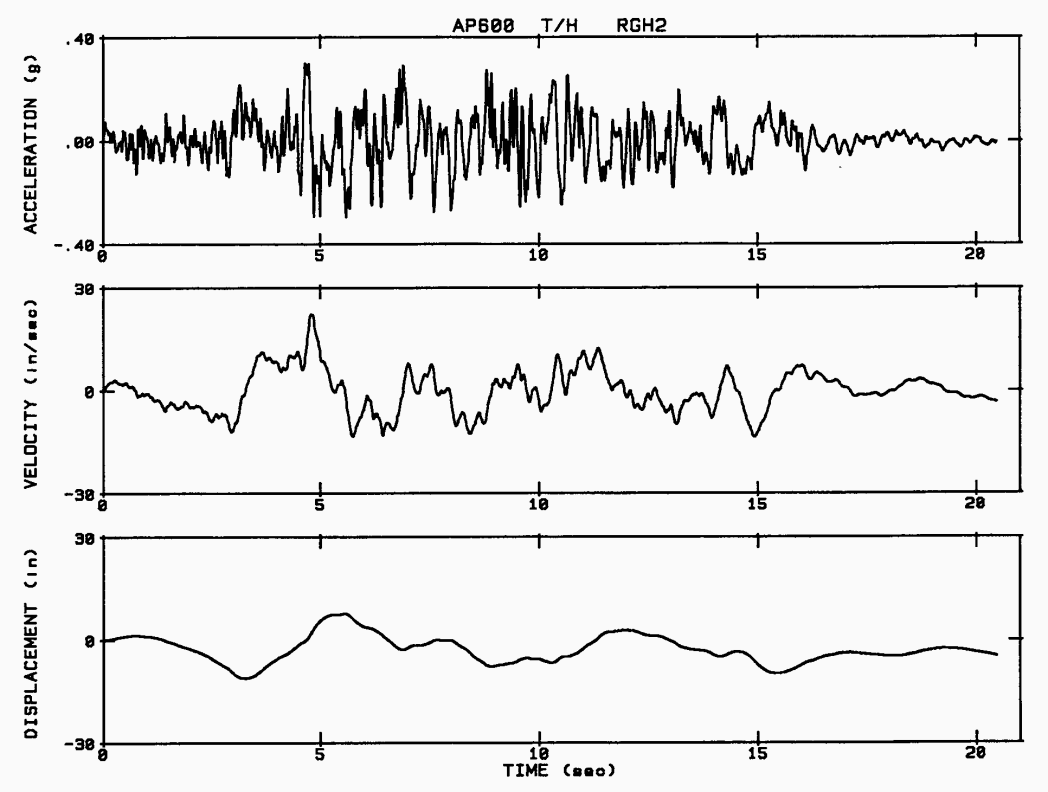

Figure 11. Horizontal SSE response spectrum with 5% critical damping.

equipment that has a small mass relative to the supporting structure, it would also have negligible interaction effects on the support structure. Therefore, such equipment needs to be included only in the mass distribution of the mathematical model for that structure. However, for other major equipment systems such as the reactor coolant system, its stiffness, mass, and resulting frequency range should be included in the model for the supporting structure to account for potential dynamic interaction effects.

The two horizontal and the vertical in-structure response spectra can be calculated from the time history motions of the supporting structure at the various floors or other equipment-support locations of interest. It is important that the spectrum ordinates are calculated at the natural frequencies of the supporting structure and at frequencies sufficiently close to produce accurate response spectra.

In seismic analysis performed separately for each of the three directions, the ordinates of the floor design response spectrum for a given direction, at the location of interest, are obtained by combining the ordinates of the three floor response spectra for that direction, according to the SRSS criterion. The same procedure is used for seismic analysis for un-symmetric structures. The resulting response spectrum is smoothed with peaks broadened. In the case of symmetric structures, the floor design response spectrum for a given direction will be the smoothed floor response spectrum for that direction.

In addition, uncertainties in the structural frequencies can arise because of uncertainties in parameters such as the material properties of the structure and soil, damping values, soil-structure interaction techniques, and the approximations in the modeling techniques used in seismic analysis. To account for these uncertainties, the computed floor response spectra from

the floor time history motions is smoothed, and peaks associated with each of the structural frequencies are broadened (see Fig. 12) by a frequency, Δf_J expressed as

$$\Delta f_J = \left[\left(0.05 f_J\right)^2 + \sum_{n=1}^{P} \left(\Delta f_{Jn}\right)^2 \right]^{1/2} \quad \text{(not less than } 0.1 f_J\text{)}, \tag{1}$$

where Δf_{Jn} denotes the variation in the J-th mode frequency, f_J, due to variation in parameter number n, and P is the number of significant parameters considered. A value of $0.1 f_J$ is used if the actual computed value of Δf_J is less than $0.1 f_J$. If the above procedure is not used, Δf_J is taken as $0.1 f_J$.

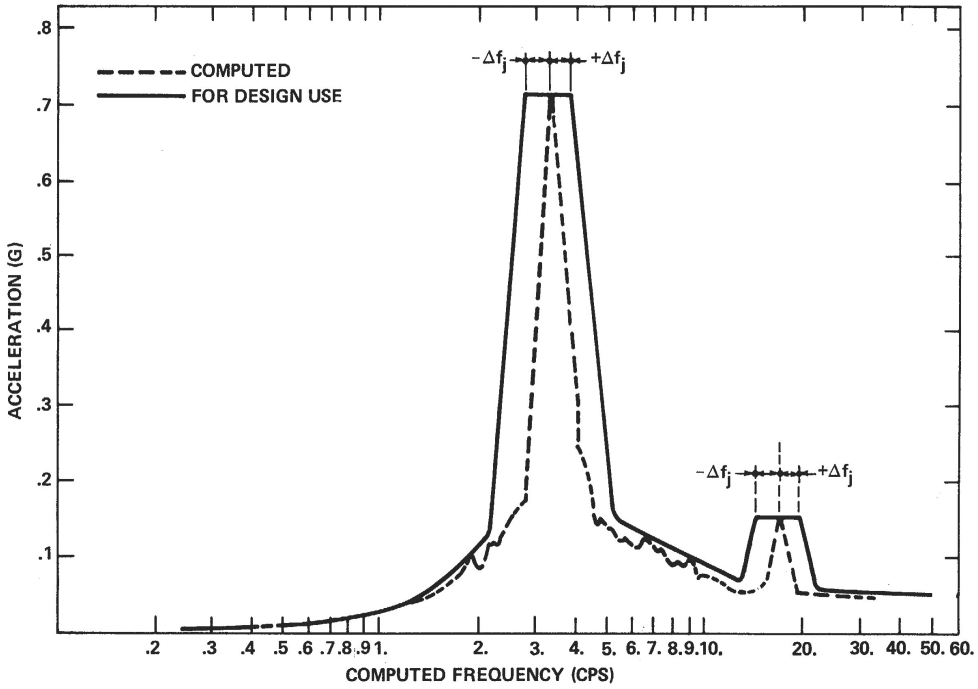

Figure 12. Vertical design response spectra scaled to 1-g horizontal ground acceleration.

When the mathematical model of the supporting structure is subjected simultaneously to the action of three spatial components of an earthquake, the calculated response spectrum in a given direction with peaks broadened and smoothed is considered the floor design response spectrum in that direction.

2.4 Seismic Design and Qualification

The information needed for a seismic design includes

(a) design ground response spectra,

(b) in-structure response spectra,

(c) acceleration time history, and

(d) seismic anchor movements.

The seismic design specifications include

(a) the scope and boundaries of components to be seismically designed,

(b) the applicable design and construction code,

(c) the required seismic function (e.g., operability, leak tightness, and position retention) of the component or piping system,

(d) the free-field seismic input for the design basis earthquake,

(e) the in-structure seismic response spectra, and

(f) the operating and design loading conditions concurrent with the seismic load.

Operability is the ability of the component to deliver, control, or shut off flow during or after the SSE. The seismic qualification of the components that must remain operable during the SSE must be established by static or dynamic analysis or by testing. Leak tightness is the ability of the component to prevent leakage to the environment during or following SSE. The requirements for seismic qualification of components such as piping systems depend on the pipe size and the magnitude of the seismic input. The requirements for pipe larger than 50.8 mm (2 in.) nominal pipe size and for an earthquake with a PGA value larger than 0.3 g are the same as the operability requirements. For smaller size pipes or when PGA values are less than 0.3 g, the position retention rules apply for leak tightness, with additional requirements that the loads imposed on nonwelded and nonflanged pipe joints are within specified limits. Position retention is the ability of the component not to fall or collapse in case of an earthquake. The seismic qualification of systems and components that must retain position but need not perform a function or be leak-tight may be established by installing bracing using the standard support and restraint spacing criteria. The adequacy of the component supports and their attachment to the building should be established. Seismic design analysis should be used to establish the seismic load on each component support, and the adequacy of the supports and anchorage for position retention should be demonstrated against failure modes that could cause loss of position.

Seismic qualification of existing components should consider the current material condition of the component. Maintenance records of the equipment or components should be examined to assess their adequacy, operability, and structural integrity. The quality of the construction and the maintenance condition of the components should be established by inspection. If corrosion or environmentally assisted cracking is postulated, the component should be examined by nondestructive volumetric techniques such as radiographic, ultrasonic, or eddy current examinations to indicate the presence of discontinuities /flaws in the material or wall thinning.

The seismic design of a system or component should also consider interaction of seismic-induced failure of a SSC that affects the function of the system or component being qualified. These interactions are of four types:

1. A falling interaction involves an overhead or adjacent structure or component falling on a critical component.
2. A sway or swing interaction occurs when an adjacent or suspended structure or component swings or rocks during a seismic event and affects a critical component.

3. A spray interaction involves spraying or flooding of a critical component due to leakage or rupture of an overhead or adjacent system or component.
4. A system interaction is an accidental signal resulting in unanticipated operating conditions, such as an unintended closure of a valve or startup of a pump. A significant interaction results in damage of the component or equipment being targeted.

However, because the original design of reactor structures and components is based on the original material properties, does not consider the current condition of the material, and does not consider loading rate effects and also because fatigue cycles below OBE are excluded from the fatigue analyses, their possible impacts on reactor component design need to be evaluated. Such evaluations should be performed in the next phase of this program for a two components—one from the reactor core support structure and core internal components and the other from the primary pressure boundary piping **(Information Gap 1).**

2.5 Component Design

2.5.1 ASME Section III, Division 1 NB/NC/NG-3200 Design by Analysis

In accordance with Section III Subarticle NB-3210 "Design Criteria," the requirements for the acceptability of a design by analysis are as follows:

(a) The design shall be such that stress intensities will not exceed the limits described in Subarticle NB-3211 and Subarticle NB-3100 tabulated in Section II, Part D, Subpart 1, Tables 2A, 2B, and 4.

(b) The design details shall conform to the rules given in NB-3100 and those given in the Subarticle applicable to the specific component.

(c) For configurations where compressive stresses occur, in addition to the requirements of (a) and (b) above, the critical buckling stress shall be taken into account. For the special case of external pressure, NB-3133 applies.

(d) Protection against nonductile fracture shall be provided by satisfying one of the following provisions:
   (1) performing an evaluation of service and test conditions by method similar to those contained in Appendix G; or
   (2) for piping, pump, and valve material thickness greater than 64 mm (2.5 in.) establishing a lowest service temperature that is not lower than RT_{NDT} (NB-2331) + 100°F (56°C); or
   (3) for piping, pump, and valve material thickness equal to or less than 64 mm (2.5 in.), the requirements of NB-2332(a) shall be met at or below the lowest service temperature as established in the design specifications.

The NB/NG/NC-3200 design is based on the maximum shear theory (NB-3212). The maximum shear stress at a given location is equal to one-half the difference between the algebraically largest and the algebraically smallest of the three principal stresses at that location. Failure or gross distortion of a component occurs when the normal stress or shear stress developed due to the imposed loading exceeds the yield strength of the material. The design loading conditions are typically evaluated by linear elastic methods, rules for stress categorization, and appropriate design limits. However, the NB/NC-3200 method also allows plastic analysis,

elastic-plastic analysis, and experimental stress analysis. The basis for the classification of the various stresses was discussed in Section 2.1.

In the linear elastic method, the design stresses are considered as stress intensities, S_m, rather than longitudinal or hoop stresses or σ_1, σ_2, or σ_3 principal stresses. The stress intensity is defined as twice the maximum shear stress defined above. Thus, for Class 1 components and piping, the stress intensity is determined by using the Tresca criteria as the maximum value of the following:

$$S_m = \max \begin{matrix} |\sigma_1 - \sigma_2| \\ |\sigma_2 - \sigma_3| \\ |\sigma_3 - \sigma_1| \end{matrix}$$

where σ_1 and σ_2 are the principal stresses in or parallel to the mid-plane of the wall of the component and σ_3 is the principal stress perpendicular to the mid-plane of the component wall. The principal stresses are taken to be positive when tensile and negative when compressive. In the latter case, the stress intensity increases. The allowable stress, S_m, is taken as the lesser of the material ultimate tensile stress at temperatures determined from the tables in ASME Code Section II Part D divided by 3, or 2/3 times the yield stress at temperatures also determined from ASME Division 1 Section II Part D.

The stress limits that must be satisfied for design loadings under Service Levels A, B, C, and D, test loads, and special stresses, are described in ASME BPV Code Section III Subarticles 3222 through 3227. Guidance for the applications of plastic analysis is discussed in Section III Subarticle NB-3228.

2.5.2 ASME Section III, Division 1 NB/NC-3600 Design by Rule

ASME BPV Code Section III, Division 1 Subarticle NB/NC-3600 design is based on a set of simple formulas to determine either the maximum thickness or the maximum allowable working pressure for pressure load conditions. It applies only to piping and piping components. The expressions provided in ASME Section III Code are based on maximum stress theory. The NB/NC-3600 method provides a quick, simple, and acceptable method for the design and construction of piping and vessel for high-pressure systems. The NB/NC-3200 method requires a higher degree of stress analysis than the NB/NC-3600 method, because in NB-3200 all aspects of loading are considered and evaluated. In the NB-3600 approach, piping components are represented by a beam element in the model, and the calculated stresses are multiplied by a stress index factor to account for the actual component geometry. ASME Section III, Division 1 Subarticle NB-3656(b)(4) specifies the stress limits for stresses due to seismic anchor motion caused by SSE and other reversing dynamic loading in level D service loads. Seismic anchor motion is the differential motion between piping support (e.g., support at a higher elevation would be subjected to larger motion than those at a lower elevation) or the differential motion between equipment nozzles and piping support. The seismic anchor motion loads are deformation-based and, like thermal expansion, are considered as secondary stress and should satisfy the primary plus secondary stress limits. Other special requirements for piping support design and strength analysis are contained in Subarticle NF-3600 “Design Rules for Piping Supports.”

For Class 1 nuclear piping, detailed modeling is required to calculate primary stresses, primary plus secondary stresses, and peak stress, which include effects of local stress concentrations

and discontinuities to meet the ASME Code stress intensity limits at the service temperature for various service conditions. However, the size, number, and complexity in a typical NPP make such detailed modeling of all piping components (e.g., elbow, tee, reducer, nozzle, and so on) impractical. Instead, the overall piping stresses are calculated at discrete points (of maximum stress) using simple beam-type finite element models. Local stress concentrations due to non-uniformity in the piping cross sections are accounted for through use of stress intensity factors (stress indices) for specific piping components.

By developing a set of stress indices, the stress in NPP piping can be calculated easily and conservatively. In the NB-3600 methodologies, the stress orientations are ignored and only the resultant moment is used in the stress calculation. For those pipe components that do not satisfy the simplified analysis approach, Section III Subarticle NB-3600 allows detailed stress analysis as specified in Subarticle NB-3200, "Design by Analysis." In the NB-3200 analysis, a detailed finite element model is developed and all the stress orientations are considered; the resulting stress values are based on actual component dimensions. In general, the nuclear industry has found that it is more economical to replace or modify a piping component that does not meet the simplified design-by-rule approach than it is to perform the detailed analysis.

The stress intensity limits in ASME Section III, Division 1 Subarticle NB-3600 piping analysis by design by rule approach are Subarticle NB-3652 for primary stress, NB-3653.1 for primary plus secondary stress, and NB-3653.2 for peak stress (fatigue analysis). Three main stress indices are used in these analyses: B-indices for primary stress evaluation, C-indices for primary plus secondary stress evaluation, and K-indices for peak stress fatigue evaluation. The B1 and B2 stress indices are intended to protect the piping without gross plastic deformation and against catastrophic failure. The stress indices are used to modify nominal stress equations for straight pipes so that the behavior of piping components such as elbows can be controlled using the same basic stress limits as for straight pipe. Values for the B, C, and K stress indices are given in Table NB-3681(a)-1 for a variety of piping components. The methods for determining flexibility factors for some commonly used piping products are given in Subarticle NB-3686.

Piping stress due to seismic loads includes seismic inertia effects and anchor movements. Both should be considered in the NB-3600 piping design analysis. Anchor motion due to earthquake and other reversing-type dynamic loading is the differential motion between (a) two pipe supports (e.g., piping support at higher elevation would have a larger support motion than supports at lower elevation) or (b) an equipment nozzle and a pipe support. Earthquake anchor motion loads are deformation-based and, like the thermal expansion load, are considered as secondary stress and should satisfy the primary plus secondary stress intensity limit when combined with other loads. Earthquake anchor movements are generally input as relative displacements at piping supports in performing a static analysis, and the resulting stresses are combined with the piping stresses due to inertia effect. ASME BPV Code Section III Subarticle NB-3656(b)(4) specifies the following stress limits for stresses due to earthquake anchor motions and other reversing type dynamic loading in level D service loads. Note that service level D loads involve SSE only; OBE is considered as a service level B load.

NB-3600 does not contain any equations for deflection limits. NB-3654.2(b) specifies that any deflection limits prescribed by the design specification must be satisfied for service level B service loads. NB-3655.5 specifies that any deformation or deflection limits prescribed by the design specifications must be considered with respect to level C service limits.

2.5.3 ASME Section III, Division 1 Subarticle NB/NC/NG Fatigue Analysis

The design methods in ASME Code Section III, Division 1 Subarticle NB, NC, or NG for ASME Class 1, 2, and CS components require a fatigue analysis as well as a fracture mechanics evaluation to prevent the likelihood of nonductile failure. The ASME Code fatigue analysis considers all transient loads based on the anticipated number of thermal and pressure transients, and for each load-cycle or load-set pair, an individual fatigue usage factor is determined by the ratio of the number of cycles anticipated during the lifetime of the component to the allowable cycles. Figs. I-9.1 through I-9.6 of ASME BPV Code Section III Mandatory Appendix I, specify fatigue design curves for various materials that define the allowable number of cycles as a function of applied stress amplitude. The CUF is the sum of the individual usage factors for all load-set pairs. ASME Code Section III requires that at each location the CUF, calculated based on Miner's rule, must not exceed unity for acceptable fatigue design. Thus,

$$CUF = \Sigma U_i = \Sigma(n_i/N_i) \quad (2)$$

where U_i is the usage factor; n_i is the number of operating cycles at stress level i; and N_i is the number of cycles to failure at stress level i determined from the ASME Code Section III, Division 1 fatigue design curve.

Although ASME Code Section III rules apply to Class 1 components, those fatigue design rules are sometimes applied to other classes of components to provide a robust fatigue design in situations in which known fatigue issues exist or fatigue duty is high [e.g., Class 2 PWR feedwater nozzles]. In addition, an environmental correction factor, F_{en}, is also applied to these components if they are exposed to an LWR coolant environment. The methodology for estimating F_{en} is described in detail in NUREG/CR-6909 Rev. 1.[33] The fatigue analyses for U.S. NPPs typically consider 5 OBEs and 1 SSE with 10 cycles for each event. However, some analyses consider 20 cycles for each event.

3. Seismic Loading Rate Effects

3.1 Material Performance Parameters

The SSCs in an NPP are required to dissipate a considerable amount of energy in an earthquake event. These SSCs are typically designed to absorb this energy through local elastic deformation and, in more severe seismic events, plastic deformation within the ductility limits of the affected material. For many years, it was generally held that loading rate was not a significant variable in the response of a large structure to earthquakes.[113] However, more recent events with very high ground-motion velocities, such as the 1994 Northridge and 1995 Kobe earthquakes (maximum recorded horizontal ground velocities of 177 and 176 cm/s^{-1}, respectively), have convinced most researchers that the loading rate effects are important and, in particular, a possible explanation for the unexpectedly poor behavior of large steel structures during these events.[114 –116]

Strain rate effects during earthquakes are important for several reasons. First, as discussed below, the imposed strain rate affects the tensile properties of most structural alloys; increasing strain rate generally produces a corresponding increase in the yield and tensile strengths and a decrease in ductility. However, this increase in strength is not as beneficial as one might think, because under seismic loading conditions, the maximum strain, ε, is typically achieved when the strain rate is zero (i.e., $d\varepsilon/dt = 0$ when ε is a maximum). More importantly, the fracture toughness of these same materials generally decreases with increasing strain rate, and because most structural components (and almost all weldments) inevitably contain flaws, this property more than tensile strength controls the behavior of these materials under dynamic loading conditions.

A number of attempts have been made to define the strain rate imposed on structural materials during an earthquake. Chang and Lee[117] estimated that strain rates between 10^{-6} and 10^{-1} s^{-1} might be experienced by steel building frames during earthquake ground motions. Similarly, Uang and Bondad[118] and Nakashima et al.[120] placed an upper limit of 10^{-1} s^{-1} on the strain rate anticipated during an earthquake. However, Antaki[120] estimated that for pipelines subject to plastic loading during seismic events, strain rates as high as 8 s^{-1} were possible. Wiesner and MacGillivray[121] state that typical loading rates under earthquake conditions lie in the range of 0.1 to 10 s^{-1}. Similarly, Gioncu[116] has calculated anticipated strain rates on structural components as high as 2.5 s^{-1} for a single-degree-of-freedom structural system and 10 s^{-1} for a multiple-degree-of-freedom system, and he identifies imposed strain rates of 0.1 to 10 s^{-1} to be typical of strong earthquakes.

As shown in Fig. 2(b), a seismic load is reversing dynamic load about a normal (or mean) operating load. In some incidences, the latter may include some other off-normal or accident load condition. Both the frequency and magnitude of the seismic load vary during a seismic event and include up to a few hundred cycles. Therefore, the cyclic deformation behavior of structural materials used in the construction of the reactor coolant pressure boundary components is reviewed first. Typically, the structural materials include A106–Gr B and A333–Gr 6 ferritic steels; A 508 Cl. 3, A533–Gr B, and A302–Gr B low-alloy steels; and low- and high-carbon grades of Type 304 and 316 SSs, as well as nuclear-grade Type 316NG SS, and their associated weld metals.

3.1.1 Cyclic Deformation Behavior

3.1.1.1 Cyclic Stress-Strain Curves

Ferritic Steels

The existing fatigue strain versus life (ε–N) data indicate that in the temperature range of dynamic strain aging (200–370°C), some heats of carbon and low-alloy steels are sensitive to strain rate even in an inert environment; with decreasing strain rate, the fatigue life may be either unaffected,[122–124] decrease for some heats,[125] or increase for others.[126] In the Argonne studies,[124] at 288°C, a decrease in strain rate by 2 orders of magnitude has little or no effect on fatigue lives of A106–Gr B and A533–Gr B steel whereas fatigue lives of A302–Gr B steel in radial orientation decreased by a factor of ≈5. A decrease in life with decreasing strain rate was also observed for the A333–Gr 6 CS. Inhomogeneous plastic deformation can result in localized plastic strains; this localization retards blunting of propagating cracks that is usually expected when plastic deformation occurs and can result in higher crack growth rates.[127] The increases in fatigue life have been attributed to retardation of crack growth rates due to crack branching and suppression of plastic zone. Formation of cracks is easy in the presence of dynamic strain aging.[126]

The cyclic stress–strain response of carbon and low-alloy steels varies with steel type, temperature, and strain rate. In general, these steels show initial cyclic hardening, followed by cyclic softening or a saturation stage at all strain rates. At high strain amplitudes, a secondary hardening stage is observed prior to fracture. The carbon steels, with a pearlite and ferrite structure and low yield stress, exhibit significant initial hardening. The low-alloy steels, which consist of tempered ferrite and a bainitic structure, have a relatively high yield stress, and show little or no initial hardening, may exhibit cyclic softening during cyclic straining. For both steels, maximum stress increases with increase in applied strain and decreases with increase in temperature. However, in the temperature range of dynamic strain aging (200–370°C), these steels exhibit enhanced cyclic hardening, a secondary hardening stage, and negative strain rate sensitivity.[125,126] The temperature range and extent of dynamic strain aging vary with composition and structure. Under conditions of dynamic strain aging, cyclic-stress increases with decreases in strain rate.

The effect of strain rate and temperature on the cyclic stress response of A106–Gr B, A333–Gr 6, A533–Gr B, and A302–Gr B steels is shown in Fig. 13. For both carbon and low-alloy steels, cyclic stresses are higher at 288°C than at room temperature. At 288°C, all steels exhibit greater cyclic and secondary hardening because of dynamic strain aging. The extent of hardening increases as applied strain rate decreases. The cyclic stress–versus–strain curves for carbon and low–alloy steels at 288°C are shown in Fig. 14; cyclic stress corresponds to the value at half-life. At 288°C, the stress–strain curve for carbon steels can be represented with the equation

$$\Delta\varepsilon_t = \frac{\Delta\sigma}{1965} + \left(\frac{\Delta\sigma}{C}\right)^{7.74}, \tag{3}$$

where the constant C is expressed as

$$C = 1080 - 50.9\,\mathrm{Log}\left(\dot{\varepsilon}\right); \tag{4}$$

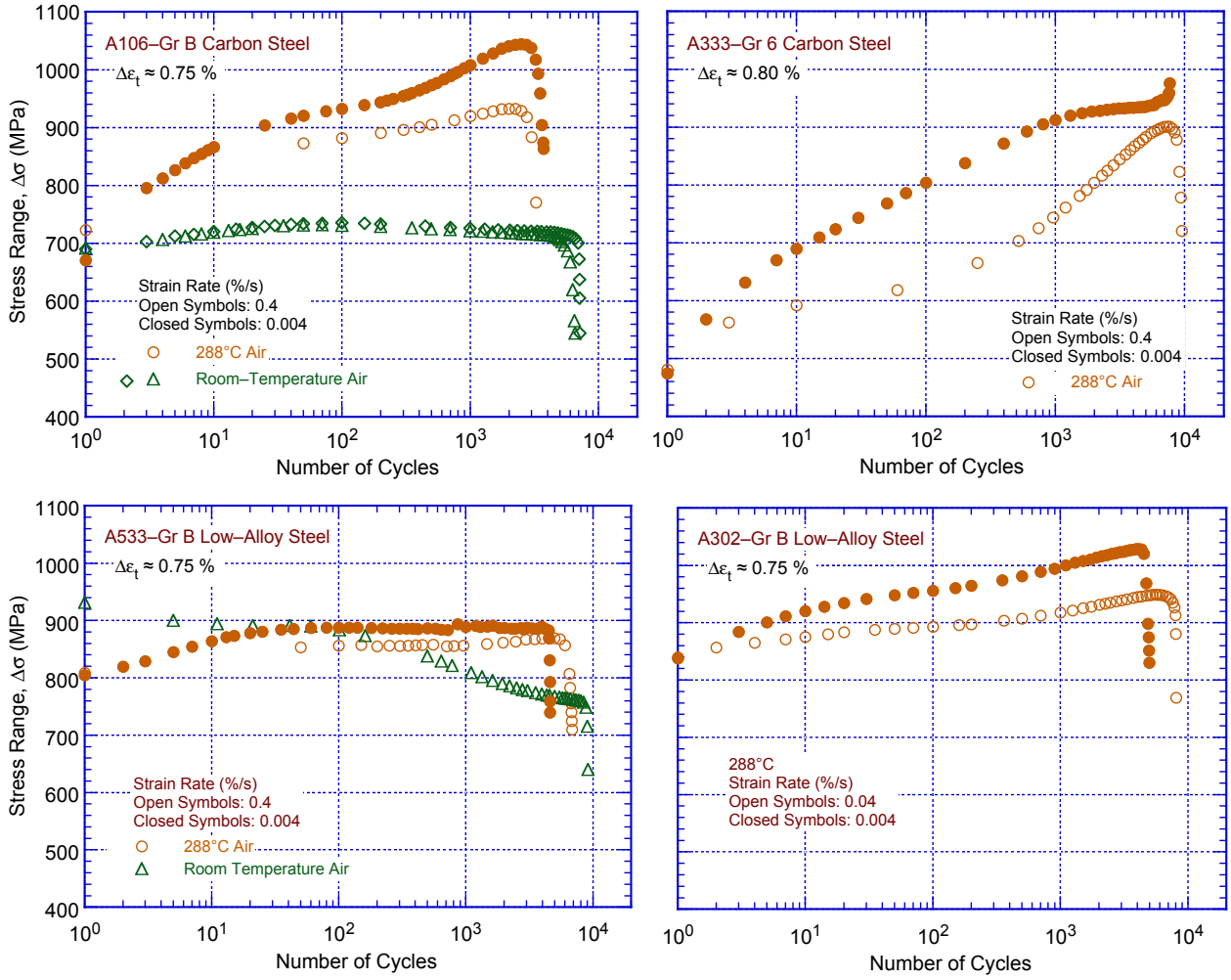

Figure 13. Effect of strain rate and temperature on cyclic stress of carbon and low-alloy steels (Ref. 124).

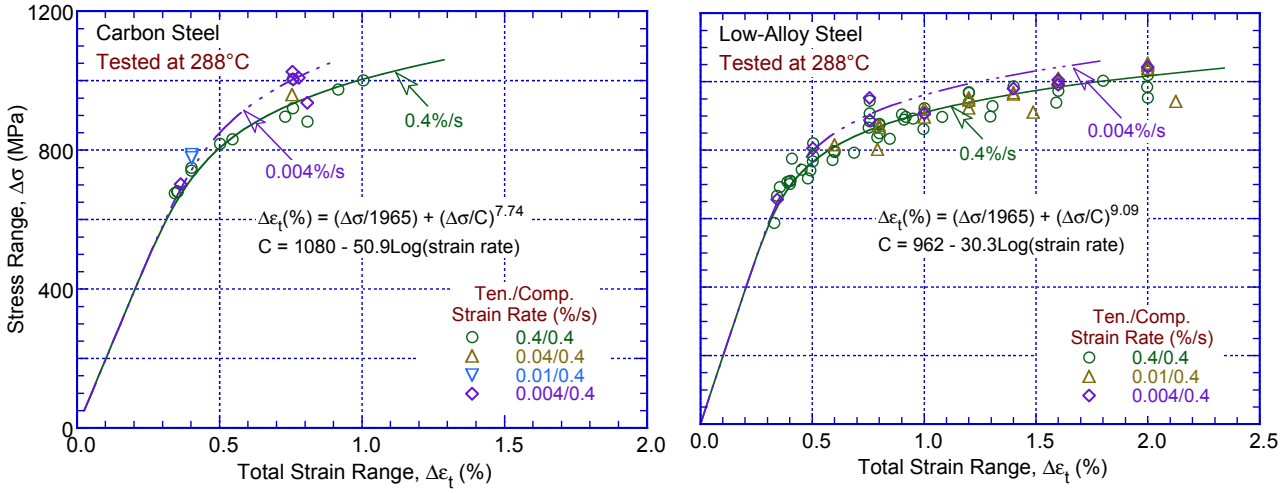

Figure 14. Cyclic stress–strain curve for carbon and low–alloy steels at 288°C in air (Ref. 124).

and for low–alloy steels, with the equation

$$\Delta\varepsilon_t = \frac{\Delta\sigma}{1965} + \left(\frac{\Delta\sigma}{D}\right)^{9.09}, \quad (5)$$

where the constant D is expressed as

$$D = 962 - 30.3\,\mathrm{Log}\left(\dot{\varepsilon}\right), \quad (6)$$

where $\Delta\sigma$ is the cyclic stress range (MPa) and $\dot{\varepsilon}$ is applied total strain rate (%/s). The cyclic stress response is lower at room temperature than at 288°C.

Wrought Austenitic Stainless Steels

The existing fatigue ε–N data indicate that in air, the fatigue life of typical austenitic SS reactor structural materials (e.g., Types 304L, 304, 316, 316L, and 316NG SS) is independent of temperature in the range from room temperature to 427°C.[128] In addition, although the effect of strain rate on fatigue life has been observed at 400–430°C, variation in strain rate in the range 0.4–0.008%/s has no effect on the fatigue lives of these materials at temperatures up to 400°C.[128–131] The fatigue ε–N behavior of cast austenitic SSs (CASS materials), such as grades CF-3, CF–8, and CF–8M, is similar to that of wrought austenitic SSs.[130,131]

During cyclic straining, austenitic SSs exhibit rapid hardening during the first 50–100 cycles; the extent of hardening increases with increasing strain amplitude and decreasing temperature and strain rate.[132–134] The cyclic strain hardening behaviors of Types 304 and 316NG SS tested in air at room temperature and 288°C are shown in Fig. 15. The initial hardening is followed by softening and a saturation stage at 288°C, and by continuous softening at room temperature. For both Types 304 and 316NG SS, cyclic hardening at 288°C is greater at low strain rates (i.e., cyclic stresses are higher at 0.004%/s than at 0.4%/s).

The cyclic stress–versus–strain curves for Types 304, 316, and 316NG SS at room temperature and 288°C are shown in Fig. 16; cyclic stress corresponds to the value at half-life and at a strain rate of 0.4%/s. For the various steels, cyclic stresses increase in magnitude in the following order: Types 316NG, 304, and 316. At room temperature, the strain amplitude, ε_a (%), for Type 316 SS can be expressed in terms of the cyclic stress amplitude σ_a (MPa) by the equation

$$\varepsilon_a = \frac{\sigma_a}{1950} + \left(\frac{\sigma_a}{588.5}\right)^{1.94}; \quad (7)$$

for Type 304 SS, by

$$\varepsilon_a = \frac{\sigma_a}{1950} + \left(\frac{\sigma_a}{503.2}\right)^{2.19}; \quad (8)$$

for Type 316NG SS, by

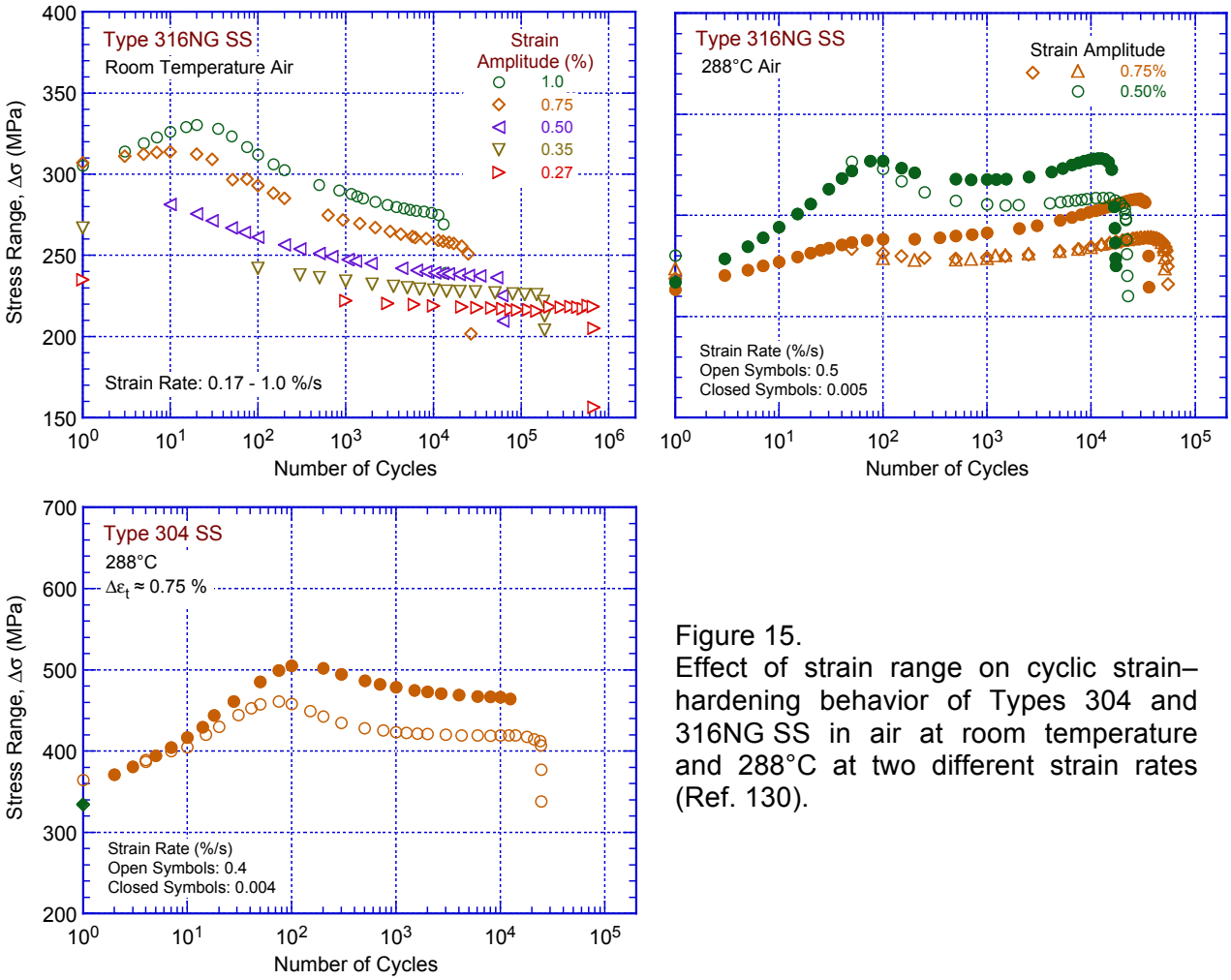

Figure 15.
Effect of strain range on cyclic strain–hardening behavior of Types 304 and 316NG SS in air at room temperature and 288°C at two different strain rates (Ref. 130).

$$\varepsilon_a = \frac{\sigma_a}{1950} + \left(\frac{\sigma_a}{447.0}\right)^{2.59} . \quad (9)$$

At 288-430°C, the cyclic stress versus strain curve for Type 316 SS can be expressed by

$$\varepsilon_a = \frac{\sigma_a}{1760} + \left(\frac{\sigma_a}{496.8}\right)^{2.19} ; \quad (10)$$

for Type 304 SS, by

$$\varepsilon_a = \frac{\sigma_a}{1760} + \left(\frac{\sigma_a}{373.9}\right)^{2.31} ; \quad (11)$$

for Type 316NG SS, by

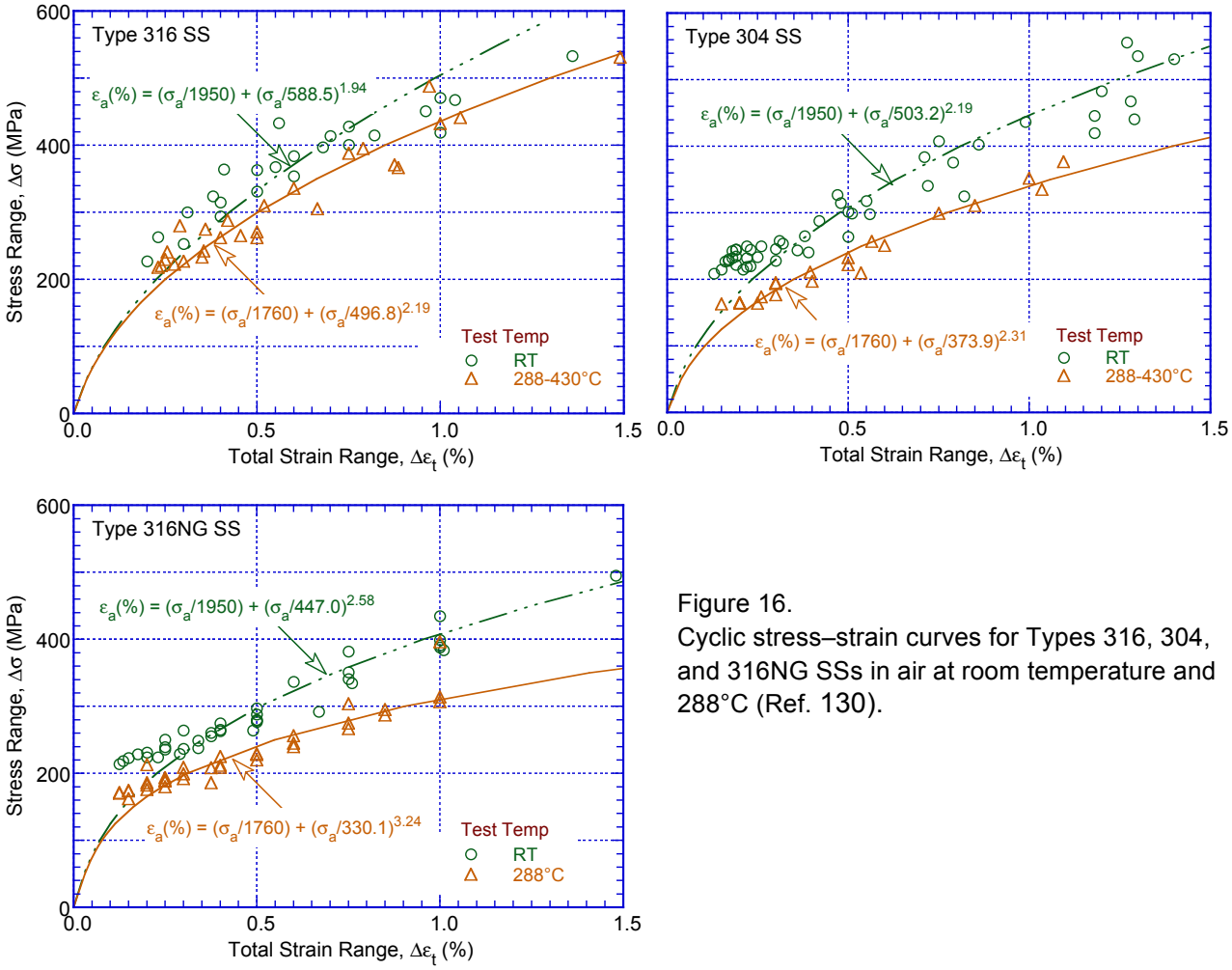

Figure 16.
Cyclic stress–strain curves for Types 316, 304, and 316NG SSs in air at room temperature and 288°C (Ref. 130).

$$\varepsilon_a = \frac{\sigma_a}{1760} + \left(\frac{\sigma_a}{330.1}\right)^{3.24} . \qquad (12)$$

CASS Materials

Available fatigue S–N data[130,135–137] indicate that in air, the fatigue lives of CF-3, CF-8 and CF-8M CASS materials are similar to those of wrought austenitic SSs. It is well known that the Charpy impact and fracture toughness properties of CASS materials decrease significantly after thermal aging at temperatures between 300 and 450°C.[138,139] The cyclic–hardening behavior of two heats of unaged and aged CASS CF-8M material is shown in Fig. 17. The results indicate that the cyclic strain-hardening behavior is also influenced by thermal aging. At 288°C, cyclic stresses of CASS materials aged for 10,000 h at 400°C are higher than for unaged material or wrought SSs. In addition, strain rate effects on cyclic stress are greater for aged than for unaged steel (i.e., cyclic stresses increase significantly with decreasing strain rate). However, existing data are inadequate to establish unequivocally the effect of thermal aging on the fatigue life of these steels. For example, thermal aging for 25,200 h at 465°C exerted no effect on the fatigue life of a CF-8M steel in air at 325°C,[135] whereas, in the present study, aging for 10,000 h at 400°C decreased the fatigue life of Heat 74 at 288°C, particularly in water.[130] These

differences are most likely caused by microstructural differences arising from relatively high temperature of thermal aging (i.e., 465°C). Aging at 400°C results in spinodal decomposition of the ferrite to form Cr–rich regions that very effectively increase tensile strength, whereas aging at 465°C for extended periods results in the formation of Cr–rich α' particles and over-aging.

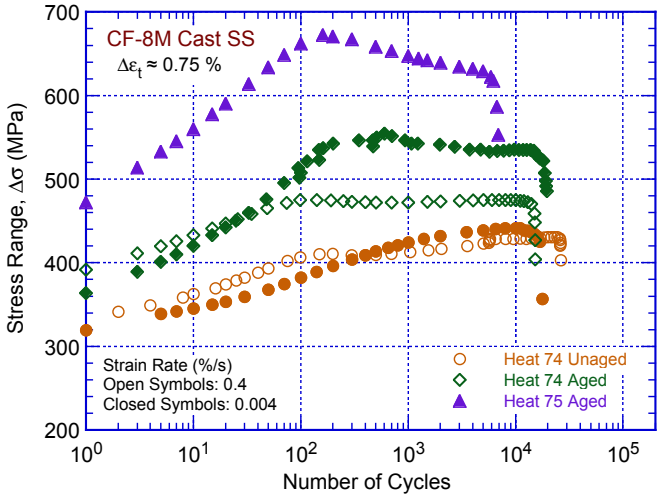

Figure 17.
Effect of strain rate on cyclic–hardening behavior of wrought and cast SSs in air at 288°C (Ref. 130).

3.1.1.2 Microstructural Changes

It is generally believed that surface fatigue cracks nucleate in the regions of localization of plastic strain, known as persistent slip bands (PSBs), which result in the formation of sharp surface slip markings consisting of extrusions and intrusions on the initially flat surface.[140–142] The formation of fatigue cracks is a consequence of the temporary irreversibility of slip activity within the PSBs. Therefore, a detailed knowledge of the evolution of dislocation substructure during cyclic straining is essential for understanding the fundamental mechanisms of surface extrusions/intrusions and fatigue crack initiation.[143]

Dislocations are linear lattice imperfections in a crystalline material. These imperfections are of two types: (a) edge dislocations in which the arrangement of atoms around the dislocation is represented by inserting an extra plane of atoms, and (b) screw dislocations, which are produced by displacing the crystal on one side of a plane relative to the other side and are described as a single-surface helicoid. Dislocations are represented by their Burgers vector, which is the vector required in any atom-to-atom closed-loop path in a dislocation-free crystal, to complete the same atom-to-atom closed-loop path in a crystal containing the dislocation. The Burgers vector of dislocations is always the same and independent of the position of the dislocation. The Burgers vector of an edge dislocation is normal to the line of the dislocation, and the Burgers vector of a screw dislocation is parallel to the line of the dislocation.

Plastic deformation in crystalline materials occurs by movement of the line defects or dislocations. There are two basic types of dislocation movement: “glide,” in which the dislocation moves in the surface defined by its line and Burgers vector, and “climb,” in which the dislocation moves out of the glide surface. Slip is the most common manifestation of glide. In crystalline materials, plastic deformation occurs by the movement or sliding of one plane of atoms over another on specific planes, known as slip planes. In other words, plastic deformation occurs by glide or climb of dislocation along specific slip planes. The slip plane is normally the plane with the highest density of atoms and the direction of slip is the direction is the direction in the slip plane in which the atoms are most closely spaced. In face-centered

cubic (FCC) metals (e.g., austenitic stainless steels), slip occurs on four {111} planes in three ⟨111⟩ directions; total 12 slip systems. In body-centered cubic (BCC) metals (e.g., iron), slip direction is the ⟨111⟩ close packed direction but the slip plane is not well defined. There are no truly closed-packed planes in the BCC crystal. Some BCC materials (e.g., α-iron) can contain 48 slip systems; there are six {110} slip planes, each with two ⟨111⟩ directions (12 systems), 24 {123} and 12 {112} planes each with one ⟨111⟩ direction (36 systems). At low temperatures, it is on {110} plane.

Note that glide is a conservative motion of dislocation, which does not cause any density change in the slip plane. On the other hand, climb is a nonconservative motion of dislocation, which leaves behind a trail of vacancies and interstitials that require mass transport. At low temperatures at which diffusion is difficult, and in the absence of a non-equilibrium concentration of point defects, the movement of dislocations is restricted entirely to glide.[144] However, at high temperatures, dislocation can move out of its slip plane by climb. When dislocation moves up one atom spacing out of its slip plane, it is called positive climb, and when it moves down one atom spacing, it is called negative climb. Positive climb can occur by either diffusion of vacancies to or a creation of an interstitial at the line of the dislocation. Similarly, a negative climb can occur by an interstitial diffusion to or a creation of vacancy at the line of the dislocation. Thus, these processes require mass transport by diffusion and hence thermal activation. During plastic deformation, slip occurs in several slip systems. Thus, dislocations moving along one slip plane will have to intersect the dislocations moving along other slip planes. Such intersections result in jogs in individual dislocations, creation of vacancies and interstitial, multiplication of dislocations, and dislocation tangles, which are all referred as "forest dislocations." At a sufficiently high stress, movement of jogs leaves behind a trail of vacancies or interstitials, depending on the sign of the dislocation and the direction of motion.

The dislocation substructure that develops in the material as well as in the PSBs, therefore, is strongly affected by the nature of "slip" in the material. Dislocation substructures can be divided into three types: wavy slip, planar slip, and a mixture of the two types. The two factors that influence slip and the associated microstructure are stalking fault energy (SFE) and short-range order of dislocations. Planar slip is promoted in low-SFE materials and wavy slip in high-SFE materials because cross slip* of dislocations is easier, which increases dislocation interactions, resulting in an increase in strain hardening of the material.[143] Furthermore, the presence of nitrogen interstitials as alloying elements in austenitic SSs inhibits cross slip and promotes planar slip. The reason is believed to be primarily a short-range order of dislocations although nitrogen does slightly lower the SFE of the material.

However, these discussions indicate that any service or loading conditions that enhance diffusion can greatly influence dislocation motion and therefore the material microstructure during service. Since repeated and sudden, below-SSE loading involves high strain rates and high frequencies, elastic strain cycling of structural materials, which generally generates point defects such as vacancies and interstitials, it is likely to have a strong effect on the material microstructure. Therefore, the cumulative effect of elastic strain cycling on material microstructure and the resulting effect on fracture properties of reactor structural materials need to be evaluated in the next phase of this program **(Information Gap 2)**.

As discussed earlier, at all strain rates, the cyclic deformation behavior of reactor structural materials typically consists of initial cyclic hardening followed by cyclic softening or a saturation or equilibrium stage. At high strain amplitudes, a secondary hardening stage is observed prior to fracture. In addition, at 200–370°C, these steels exhibit enhanced cyclic hardening and a

* When a dislocation moving, for example, in one {111} type plane to another {111} type p lane.

secondary hardening stage because of dynamic strain aging. In the temperature regime of dynamic strain aging, the microstructural changes are significantly altered because of the interactions between mobile dislocations and interstitial carbon or nitrogen atoms. Such interactions are strongly dependent on temperature and strain rate. Several studies on microstructural changes in reactor structural materials under cyclic loading have been conducted during the past several decades to define the microstructure at different stages of strain cycling, and to correlate the microstructure to fatigue ε-N data and fatigue damage. For example, previous studies suggest that the saturation stage is associated with the formation of an equilibrium substructure, which does not change with successive cycling. The results of microstructural studies may be briefly summarized as follows.

During the initial, rapid hardening stage the microstructure consists of clusters or bundles of dislocations, separated by regions free of dislocations.[145] The substructure during the equilibrium stage depends on the applied strain amplitude. At low strain amplitudes, the dislocation bundles produced during the rapid hardening stage shake down into bundles of fragmented dislocations, whereas a cell structure is developed at a high strain range.[146,147] The saturation cell size increases with either a decrease in strain amplitude or an increase in temperature.[148] In the metals studied, the saturation stress is a unique function of the applied strain range, strain rate and temperature.[149] The saturation stress and the corresponding cell size are related and are independent of the prior strain history.[150] This relationship appears typical of all wavy slip mode materials.[151] However, as discussed later in this section, this behavior may not be true in all cases; the saturation stress and substructure may not reverse by decreasing the applied strain amplitudes beyond half-life. The evolution of microstructure during cyclic straining of carbon and low-alloy steels and austenitic SSs is discussed below.

Ferritic Steels

The microstructures that developed in A106–Gr B carbon steel specimens tested at 288°C, 0.375% strain amplitude, and three different strain rates are shown in Figs. 18-21.[124] The results indicate that the dislocation structure varies significantly with strain rate; the lower the strain rate the more mature (i.e. well-established) the dislocation structure. At an 0.4 %/s strain rate (Figs. 18 and 19), there is no well-established dislocation structure, although immature dislocation walls can be observed. A mature microstructure consisting of dislocation cells, walls, and/or veins with high dislocation density is observed in both the ferrite and pearlite

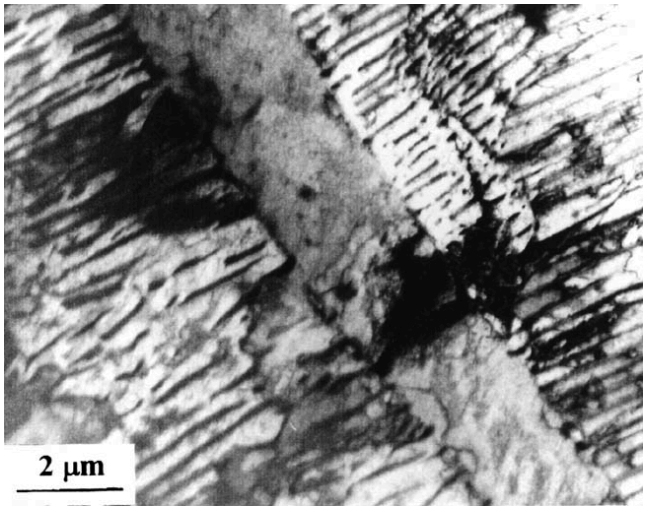

Figure 18.
Typical microstructure in A106–Gr B specimen tested at an 0.4 %/s strain rate showing immature dislocation walls in three pearlite grains consisting of Fe_3C plates in the ferrite matrix (Ref. 124).

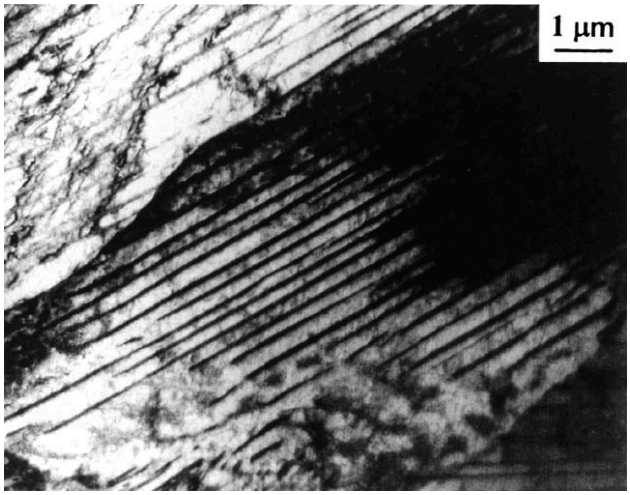

Figure 19.
Ferrite grain between two pearlite grains in A106–Gr B specimen tested at an 0.4 %/s strain rate (Ref. 124).

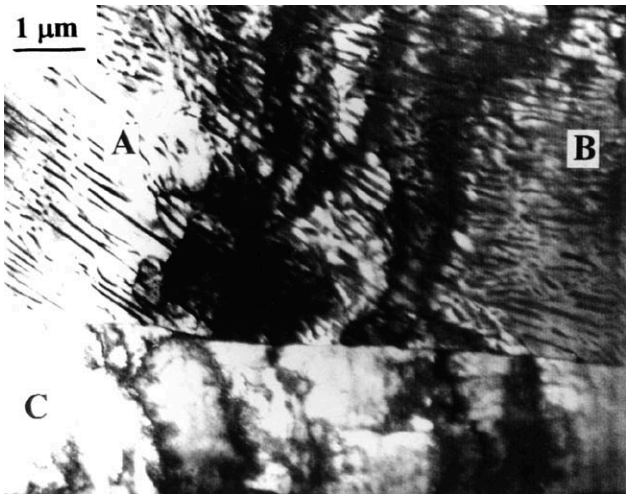

Figure 20.
Typical microstructure in A106–Gr B specimen tested at an 0.04 %/s strain rate showing a cell structure in ferrite (C) and two pearlite grains (A and B) (Ref. 124).

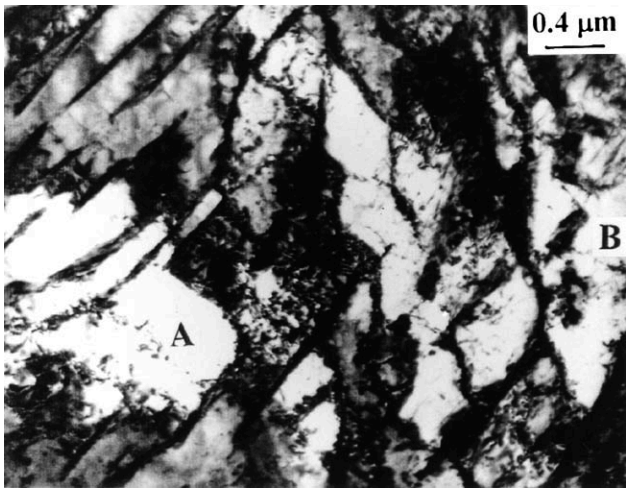

Figure 21.
Formation of dislocation walls in two pearlite grains (A and B) in A106–Gr B specimen tested at an 0.004 %/s strain rate (Ref. 124).

grains at 0.04 and 0.004 %/s strain rates as shown in Figs. 20 and 21. The dislocation walls may cross individual cementite plates or particles within a pearlite grain to keep a consistent crystallographic structure.

Wrought Austenitic Stainless Steels

As shown in Fig. 15, the cyclic stress versus fatigue cycles response of Type 316NG at room temperature consists of a short cyclic hardening stage followed by cyclic softening and ultimately a saturation or stabilized behavior up to failure. A similar behavior is also observed for Type 316L SS.[152] Like the microstructure of most other metals, the microstructure of austenitic SSs also changes significantly during cycling straining. The evolution of dislocation microstructure in Type 316L SS tested at room temperature, 0.7% strain amplitude, and 0.1%/s strain rate, at different stages of fatigue life are shown in Figs. 22–25. The results show that at room temperature, the hardening stage lasts less than 1% of life (only 30 odd cycles). During this stage, dislocations are arranged essentially in a planar structure. The microstructure is similar to that observed in the as-received condition, except it contains a higher dislocation density and the dislocation interactions are more complex (i.e., more tangled dislocation structure).[152] The microstructure that developed at the end of the hardening stage (after ~30 cycles) is shown in Fig. 22. It consists of a uniform distribution of dislocations.

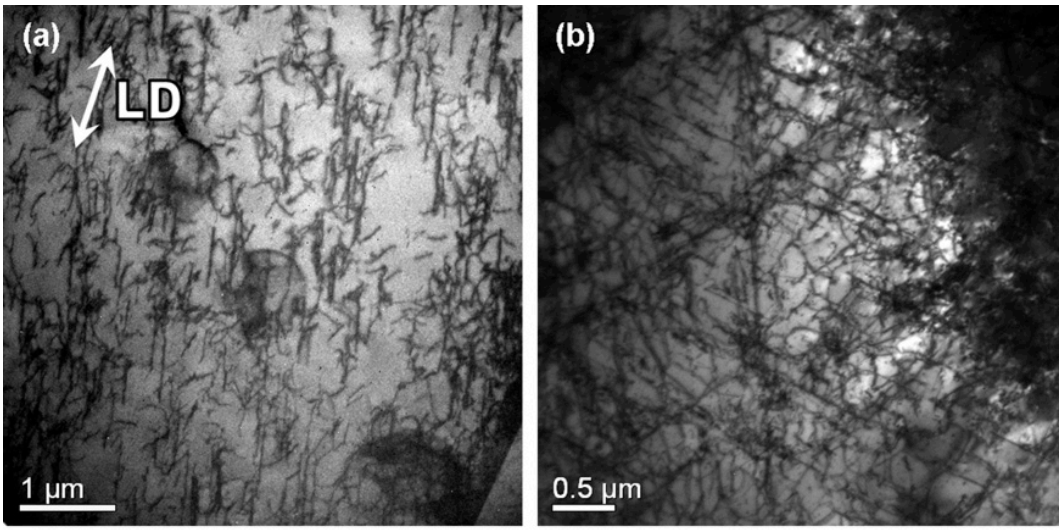

Figure 22. Microstructure in Type 316L after ~30 cycles (hardening stage) (Ref. 152).

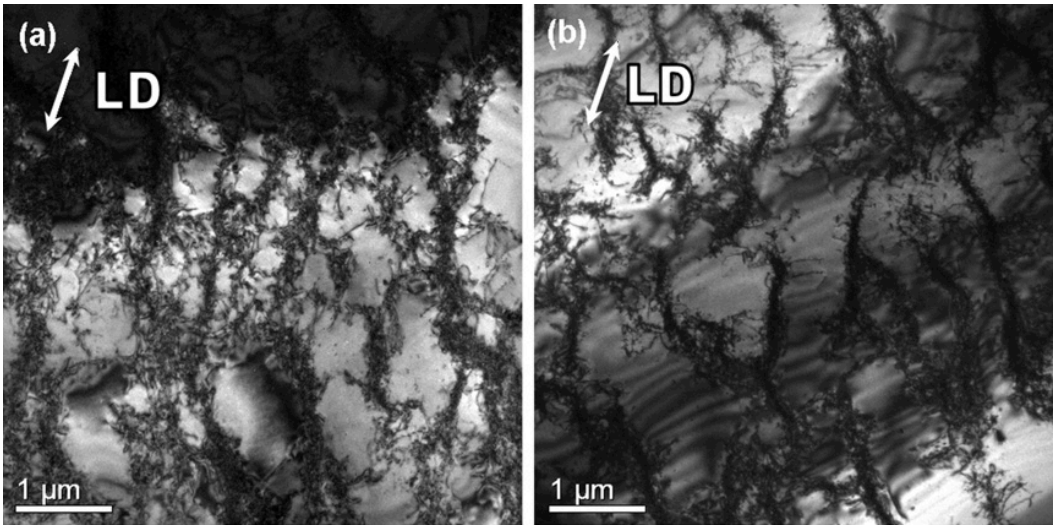

Figure 23. Microstructure in Type 316L after ~90 cycles (softening stage) (Ref. 152).

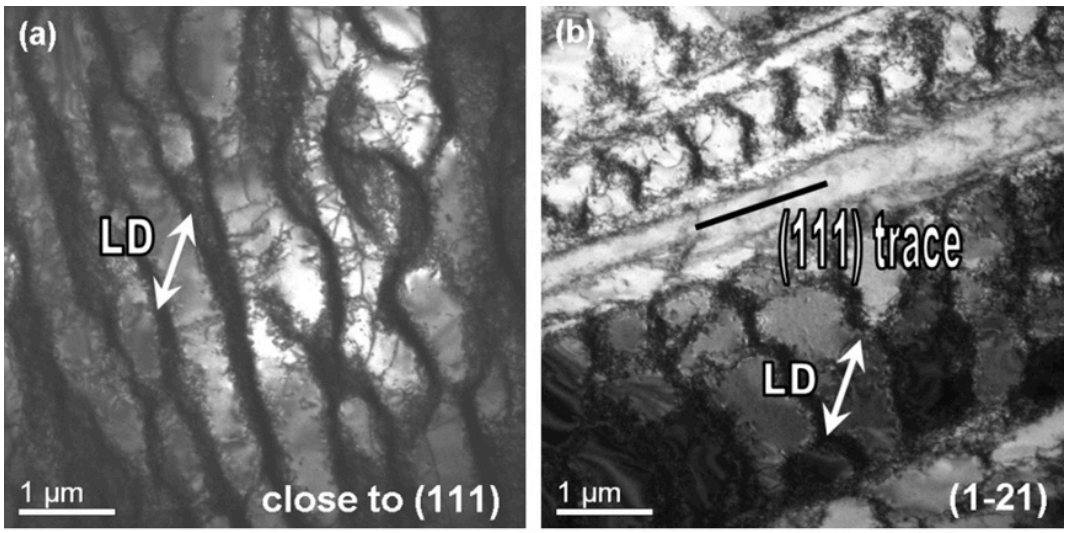

Figure 24. Microstructure in Type 316L after ~1500 cycles (midlife) (Ref. 152).

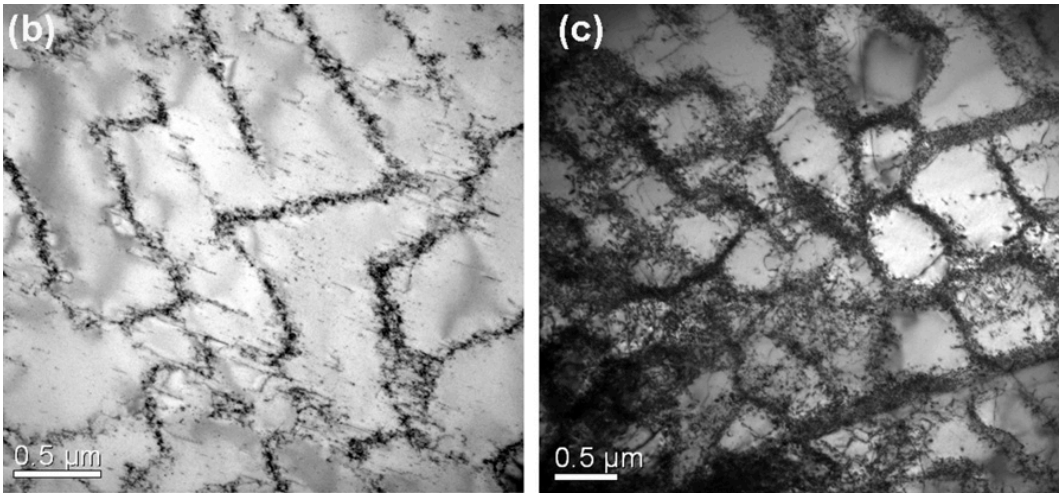

Figure 25. Microstructure in Type 316L after ~3000 cycles (end-of-life) (Ref. 152).

The microstructure observed during the softening stage (after ~90 cycles) is shown in Fig. 23; it consists of thick veins or premature walls of dislocations separated by long dislocation-free regions. With continued straining, these thick dislocation veins/walls further developed into better-defined, dense and thin cell walls.[152] In addition, the results show that labyrinth structures had already developed at the end of the softening stage. Dislocation activity along primary and secondary slip planes can trigger the formation of dislocation walls in different directions, similar to a labyrinth structure.

The microstructures observed at midlife (~1500 cycles) and at end-of-life (~3000 cycles) are shown in Figs. 24 and 25, respectively. At mid-life, the microstructure consists of well-defined dislocation walls separated by dislocation-free regions (Fig. 24a), and persistent slip bands (Fig. 24b). The microstructure at end-of-life consists of labyrinth structure (Fig. 25b) and cells (Fig. 25c). The microstructures represent saturation or steady state, and are almost identical. The main differences are that the cell walls are thinner and the cell size progressively decreased with number of cycles. Finally, the structure consists of round cell walls and shorter channels.

Overall, the results indicate that for Type 316L SS, the cyclic hardening behavior is associated with an increase in the total dislocation density, and the softening behavior is related to the rearrangement of dislocations into a well-defined cell structure. The latter is responsible for the saturation or steady-state cyclic stress versus fatigue cycles behavior of the material.

Effects of Variable Strain Fatigue

The reversibility of the substructure that evolves during cyclic straining when the applied strain range is decreased is reviewed in this section. The goal is to assess (a) the role of microstructure on the stress dependence of the various cyclic loading parameters and (b) relate the substructure to the overall mechanical properties. The cyclic hardening behavior of annealed Ferrovac E material (pure iron) at three different strain ranges is shown in Fig. 26.[153] The curves show a primary rapid hardening stage followed by a saturation or equilibrium stage, during which the cyclic stress remains relatively constant. In all cases, the saturation flow stress is reached in a few cycles (less than 10 cycles). The magnitude of the cyclic stress increases with increasing strain amplitude. Furthermore, at high strain amplitudes, a secondary hardening stage is observed prior to fracture.

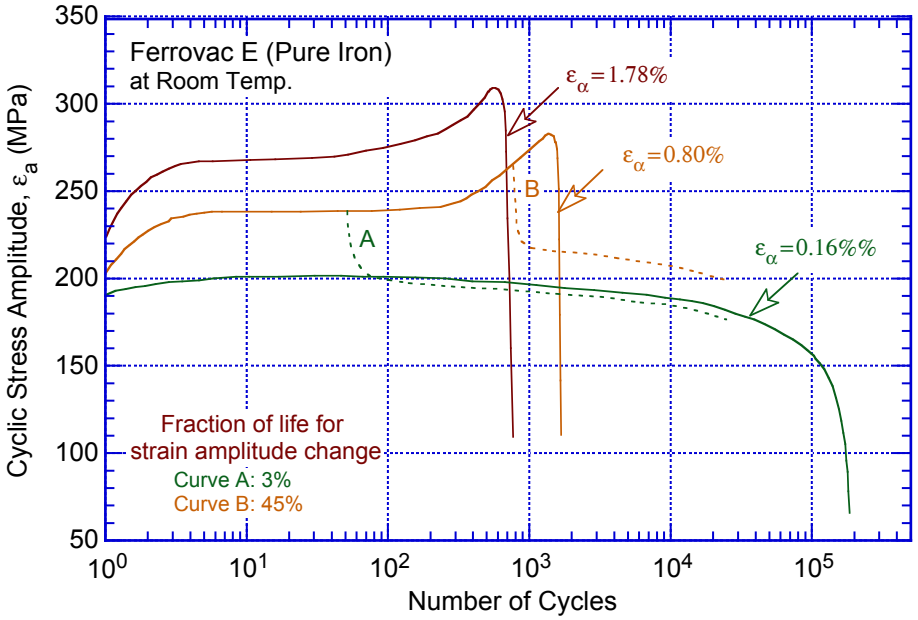

Figure 26. Plots of cyclic stress versus number of cycles for annealed Ferrovac E to demonstrate potential effect of a decrease in strain amplitude on material microstructure and fracture properties (Ref. 153).

The material microstructure generated by cycling at 0.16 and 0.8% strain amplitudes was examined at various fractions of fatigue life, after the completion of the rapid hardening stage. The micrographs of the substructure that developed during cyclic straining at 0.16 and 0,8% strain amplitudes are shown in Figs. 27 and 28, respectively.[153] Although a sharp and well-defined cell structure was generally seen during the later stages, after about 50% of fatigue life, it was not seen during the early stages. The nature of the cell structure and the dislocation arrangements in the cell walls were observed to vary considerably with continued cycling.

At the lower strain amplitude (0.16%), after 10% of fatigue life, the substructure consists of closely spaced bundles of dislocations separated by regions relatively free of dislocations, as

seen in Fig. 27a. The bundles consist of tangled dislocation lines associated with dislocation loops and dipoles. A cell structure starts to form after 40% of fatigue life. The existing bundles of dislocations break up and the dislocations rearrange into a large-cell structure.[153] Some of the cell walls are composed of dislocation tangles and loops. However, the initial structure consisting of bundles of dislocations can still be seen in some areas. With further cycling, these cells become sharp with no apparent change in the cell size. A well-defined cell structure is observed throughout the specimen. Many low-energy subgrain boundaries made up of cross grids of screw dislocations are also observed. Figure 27b shows a typical substructure produced during the later stages of fatigue life. Although no quantitative measurements were made for the misorientations across the cell walls, the sharp contrasts between neighboring cells indicate the presence of appreciable misorientations between them.

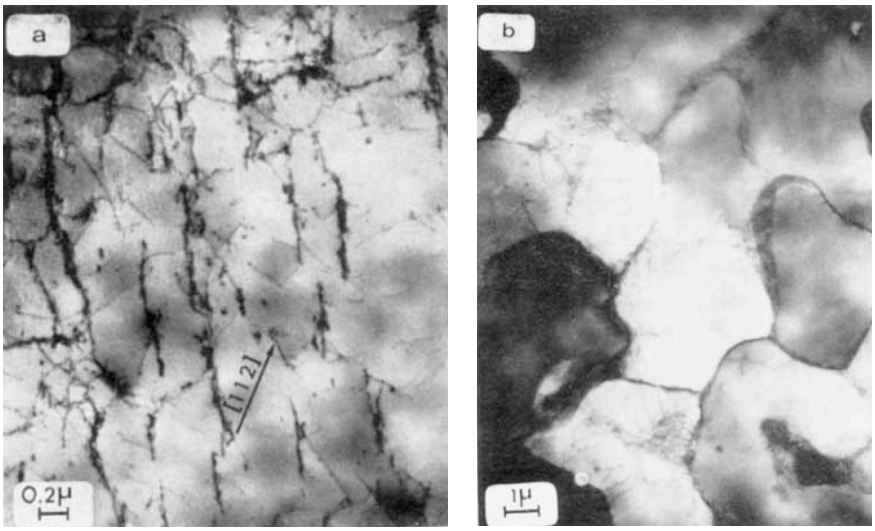

Figure 27. Dislocation structure of annealed iron cycled at 0.16% strain amplitude to different stages of fatigue life: (a) 10% and (b) 100%. (Ref. 153).

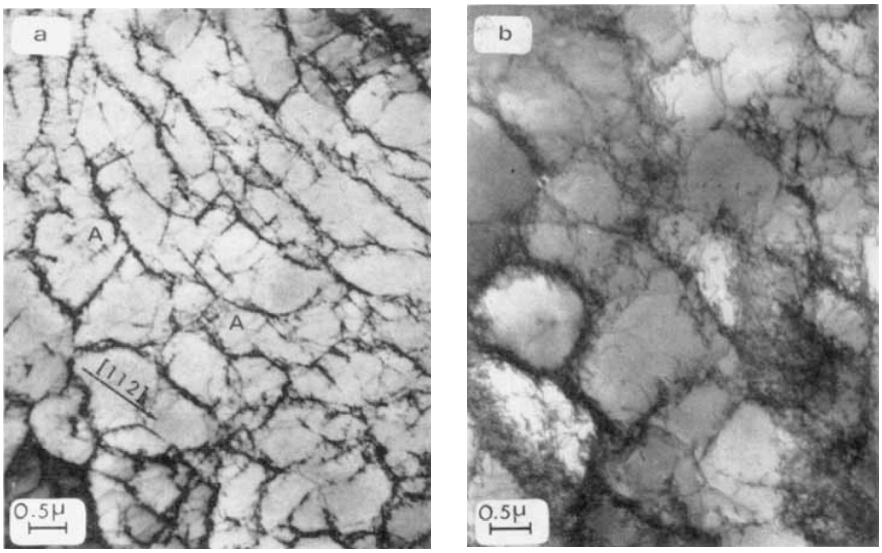

Figure 28. Dislocation structure of annealed iron cycled at 0.8% strain amplitude to different stages of fatigue life: (a) 3%, (b) 10%, (c) 45%, and (d) 100%. (Ref. 153).

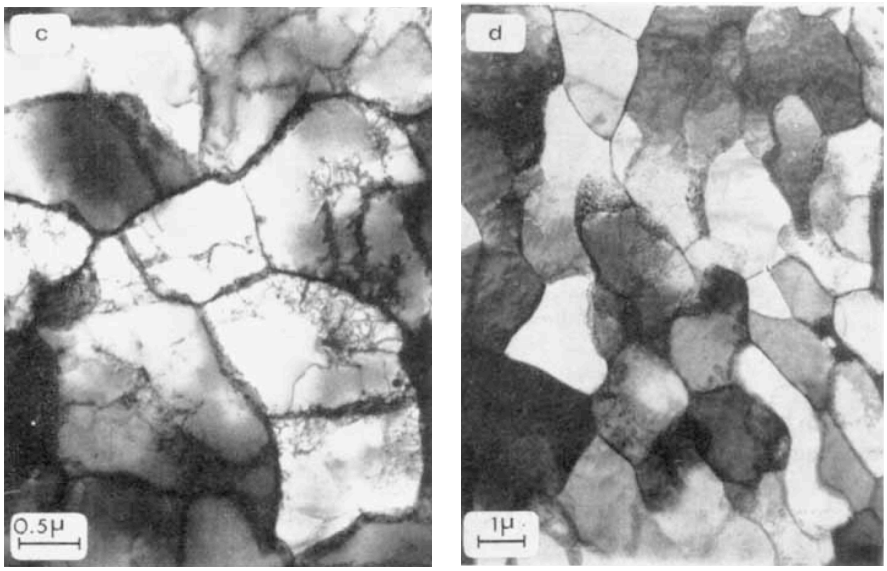

Figure 28. (Continued)

A similar evolution of microstructure is observed during strain cycling at 0.8% strain amplitude. However, a cellular structure forms at an early stage in fatigue life.[153] Figure 28a shows that a semicellular network of dislocations develops at 3% fatigue life. The dislocation walls consist of dislocation tangles with interspersed loops and dipoles. In Fig. 28a, loops appear to be forming from heavily jogged dislocations in the area indicated by A. Since formation of loops is favored at low strain amplitude,[154] the number of loops at 0.8% strain amplitude is smaller than that observed at 0.16%. However, unlike most FCC metals in which dislocation loops are dispersed uniformly throughout the substructure, in the study on Ferrovac E (pure iron), loops were mainly observed in and around the regions of dislocation tangles or cell walls.[153] A more regular cell structure begins to form after 10% of fatigue life (Fig. 28b). No apparent change in the cell size is observed with further cycling, though misorientations develop between groups of cells and the cell walls gradually become sharp and distinct.

Between 10 and 50% fatigue life, the substructure observed in different areas consisted of a cell structure at various degrees of refinement. A homogeneous and well-defined cell structure develops during the later stages of fatigue life. Typical structures observed after 45% of life and after fracture are shown in Figs. 28c and 28d, respectively. Most of the dislocations are present in the cell walls, and the cell size is much smaller than that observed at lower strain amplitude cycling.

The reversal of the substructure was studied by high-strain cycling followed by cycling at low-strain amplitude. The stress response for specimens that were cycled at 0.8% strain amplitude up to 3 and 45% of fatigue life, and then cycled further at 0.16% strain amplitude, are shown as dotted lines (curves A and B, respectively) in Fig. 26. The results show that on decreasing the applied strain amplitude, the cyclic stress decreases rapidly during the first 100 cycles and saturates at a new stress level. The magnitude of the new saturation stress depends on the number of cycles at the higher strain amplitude. For example, the new saturation stress for curve A corresponds to the value observed during cycling of a virgin specimen at the lower strain amplitude alone, whereas it is higher for curve B.

The microstructural observations indicate that the reversal of the substructure developed at the high strain amplitude is very slow and continues over the remaining life. There is little or no

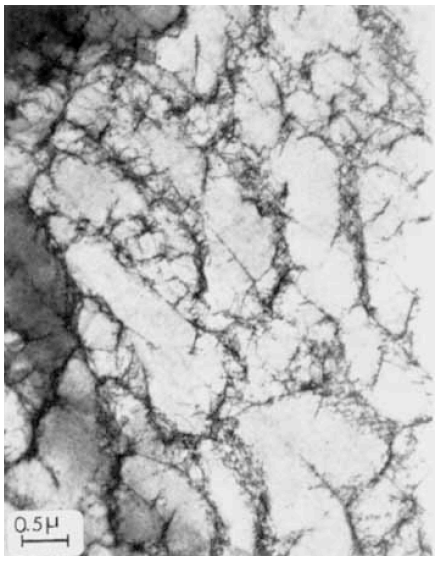

Figure 29.
Dislocation structure of annealed iron cycled initially at 0.80% strain amplitude to 3% of fatigue life followed by cycling at 0.16% strain amplitude for 20,000 cycles.

change in the substructure during the sharp decrease in cyclic stress. Substructures similar to Figs. 28a and c are observed in tests represented by curves A and B, respectively. The only differences atre that the dislocation walls are less dense and that a larger number of dislocation loops are present. With cycling at the lower strain amplitude, the cell size increases by the disintegration of some of the existing cell walls. Figure 29 shows a large semi-cellular structure observed in the test represented by curve A, after 20,000 cycles at the lower strain range. Many discontinuities can be seen in the cell walls. With continued cycling, a distinct cell structure develops, similar to that shown in Fig. 28b. The substructure that corresponds to curve B after 20,000 cycles at the lower strain range is shown in Fig. 30. It is evident that a complete reversal of the structure is not accomplished in the specimen. The substructure is very inhomogeneous and a considerable amount of the previous structure is retained even at fracture. Some regions show large cells surrounded by smaller cells. This can be seen in Fig. 31, which shows the substructure in the specimen subjected to 100 cycles at 0.8% strain amplitude followed by cycling to failure at 0.16% strain amplitude.

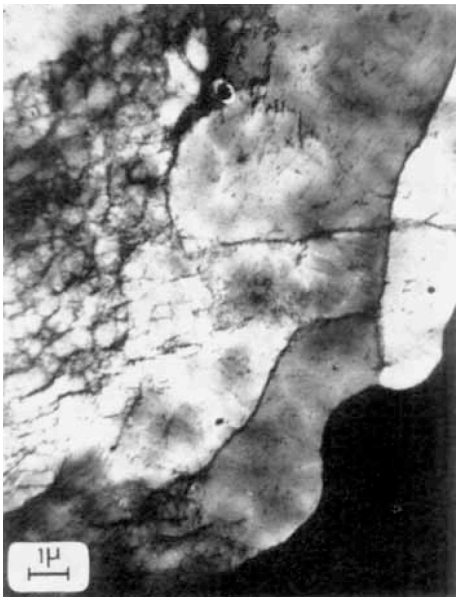

Figure 30.
Dislocation structure of annealed iron cycled initially at 0.80% strain amplitude to 45% of fatigue life followed by cycling at 0.16% strain amplitude for 20,000 cycles.

Figure 31.
Dislocation structure of annealed iron cycled initially at 0.80% strain amplitude to 5% of fatigue life followed by cycling at 0.16% strain amplitude to fracture.

These results indicate that depending on the microstructure that had developed at the high strain amplitude, decreasing the strain amplitude may not lead to the behavior observed for cycling a virgin specimen at the low strain amplitude; some memory of prior strain cycling may remain in the material.

3.1.2 Tensile Properties

Research on the effects of strain rate on the mechanical properties of metals and alloys dates back at least 70 years to the work of Manjoine[155] and Zener and Holloman.[77] Manjoine conducted room-temperature tensile tests on mild steel at 9.5×10^{-7} to 3×10^{2} s^{-1} strain rates, with test durations ranging from 24 h to less than 1 s. A significant increase in yield stress was observed over the strain rates associated with strong earthquakes, with the value increasing from ~270 MPa at a strain rate of 10^{-1} s^{-1} to ~400 MPa at a strain rate of 10 s^{-1}. The ultimate tensile strength increased less dramatically, from ~410 MPa at 10^{-1} s^{-1} to ~450 MPa at 10 s^{-1}. Thus, the yield ratio, defined as the ratio of the yield stress to the ultimate tensile strength, increases with increasing strain rate and the ductility correspondingly decreases.[156–162]

Campbell and Ferguson[163] have observed a similar strain-rate sensitivity for the shear flow stress of mild steel in experiments at temperatures from −78 to 440°C and strain rates from 10^{-3} to 4×10^{4} s^{-1}. The rate sensitivity of the flow stress was found to be a decreasing function of temperature, except at the highest strain rates, at which a large increase in the rate sensitivity was observed, with the flow stress at constant temperature varying approximately linearly with strain rate. The data were interpreted in terms of thermal activation rate theory and the theory of the damping of dislocation motion by phonon viscosity. Qualitatively similar strain-rate sensitivity effects have been observed at room temperature in both torsion and shear loading tests at strain rates up to 3000 s^{-1} on mild steel, copper, and titanium.[164]

The effects of strain rate on the mechanical properties of a number of structural alloys used as pressure boundary materials in NPPs are summarized below. These alloys include low-alloy pressure vessel steels (A508 Cl 3 and A533 Gr B steels), austenitic stainless steel (SS) piping materials (Types 304, 304L, 304LN, 304NG, 316, 316L, 316LN and 316NG SSs), and Alloy 600 and 690 steam-generator tubing material.

3.1.2.1 Carbon and Low-Alloy Steels

A508 Cl 3 and A533 Gr B Ferritic Steels

The influence of dynamic strain aging (DSA) on the deformation and fracture properties of A508 Cl 3 steel has been studied by Kim and Kang.[165] Serrated flow in stress-strain curves was observed between about 140 and 340°C and varied with the strain rate and microstructural condition. The onset temperature of serrated flow for the pearlite-ferrite microstructural condition was lower than that for the as received, tempered martensite condition. The serrated flow range for both the microstructural conditions shifted to higher temperatures with increased strain rates. The results of Kim and Kang on the fracture toughness properties A508 Cl 3 steel are discussed in Section 3.1.2.3.

Tanguy et al. have studied the effects of strain rate and temperature on the tensile properties and fracture behavior of A508 Cl 3 steel.[166,167] As shown in Fig. 32, the yield stress is found to significantly increase with strain rate over a range from 4×10^{-4} s^{-1} to 4×10^{3} s^{-1} and a temperature range from −196°C to +100°C. Wu and Kim[168] (2003) conducted tensile tests on as-received and hydrogen-charged A508 Cl 3 steel at room temperature and 473 to 623K (200 to 350°C) and strain rates of 10^{-5} to 10^{-3} s^{-1}. They found the yield and tensile strengths increased with increasing strain rate at room temperature, while the elongation and reduction in area were essentially unchanged (Fig. 33). At 288°C (Fig. 34), both the ultimate tensile strength and elongation decreased with increasing temperature.

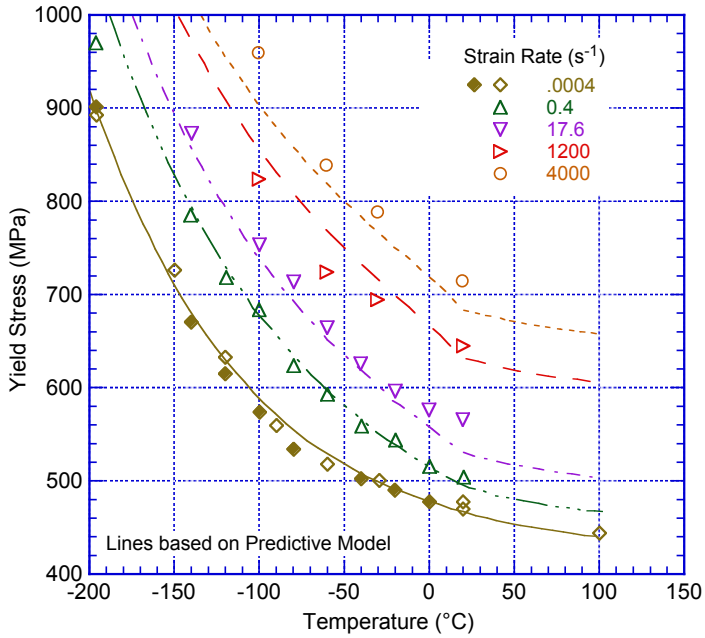

Figure 32.
Yield stress versus temperature at different strain rates for A508 Class 3 pressure vessel steel (Ref. 167).

Xu et al.[169] also investigated the effects of DSA on the tensile behavior of A508 Cl 3 steel. As-received material has been subjected to uniaxial tension tests in the strain-rate range of 6.67×10^{-5} s^{-1} to 1.2×10^{-2} s^{-1} and the temperature range of 25 to 400°C. Their tensile test results are summarized in Fig. 35. It was found that the region of DSA was in the temperature range of 250–350°C at a strain rate of 1.2×10^{-3} s^{-1}, 200–300°C at 1.2×10^{-4} s^{-1}, and 200–300°C at 6.67×10^{-5} s^{-1}. Serrated stress–strain behaviors were observed in these temperatures and strain-rate ranges. The solutes responsible for DSA were identified to be carbon and nitrogen, with nitrogen playing the more important role.

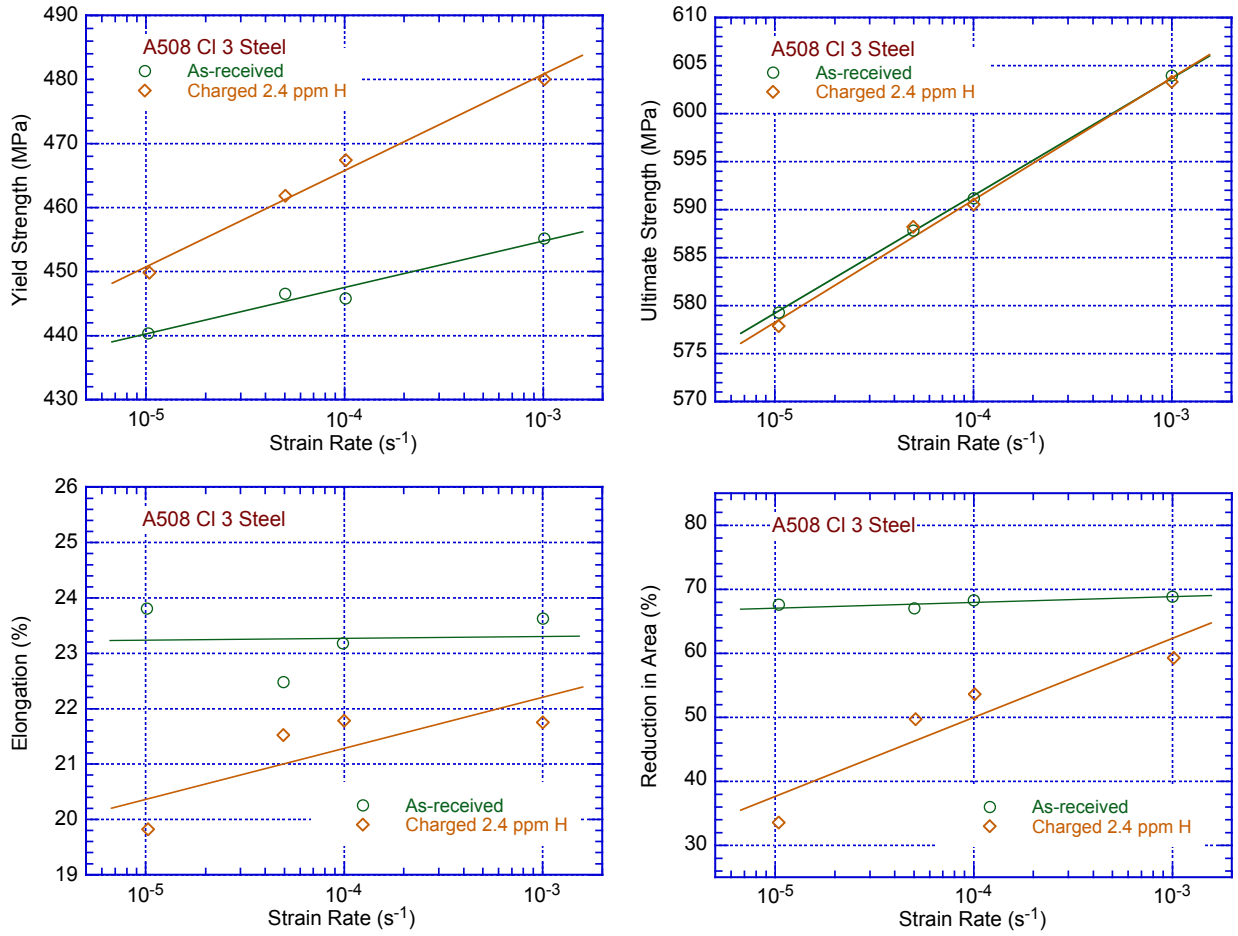

Figure 33. Summary of tensile properties data for A508 Cl 3 pressure vessel steel as a function of strain rate at room temperature in the as-received condition and after being charged with 2.4 ppm H (Ref. 168).

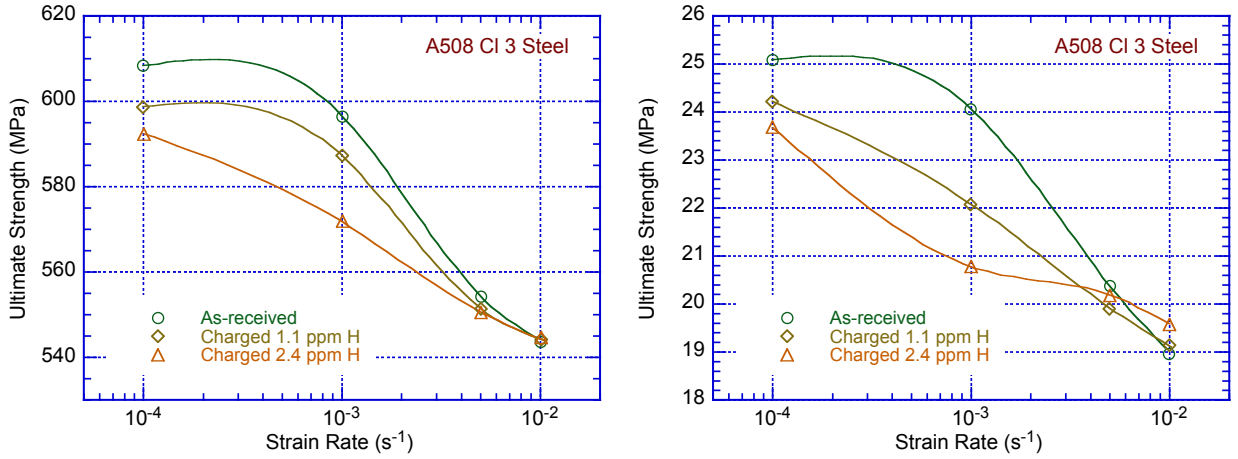

Figure 34. Summary of tensile properties data for A508 Cl 3 pressure vessel steel as a function of strain rate at 561K (288°C) in the as-received condition and after being charged with 1.1 and 2.4 ppm H (Ref. 168).

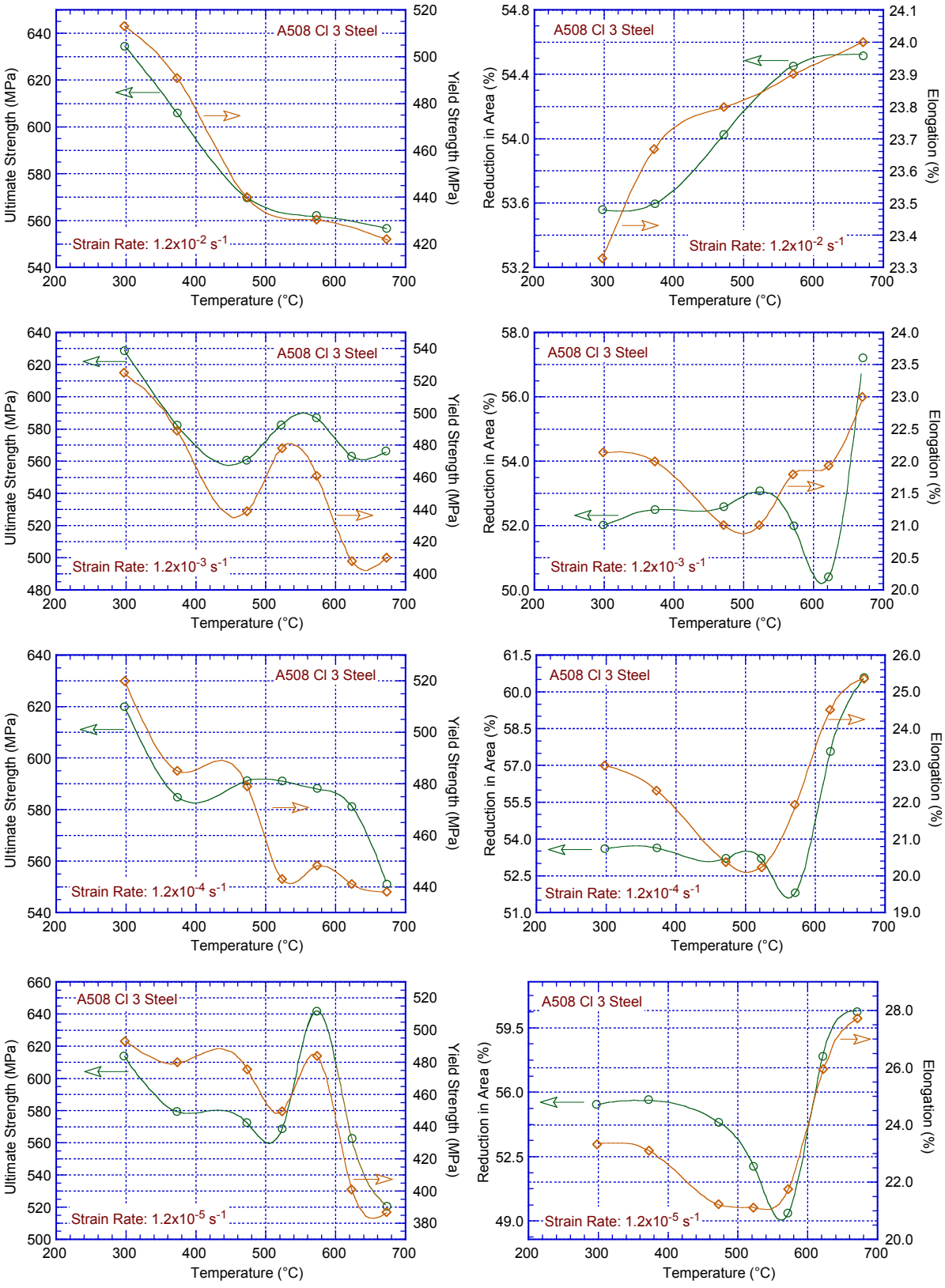

Figure 35. Summary of tensile properties data for A508 Cl 3 pressure vessel steel as a function of temperature at four different strain rates (Ref. 169).

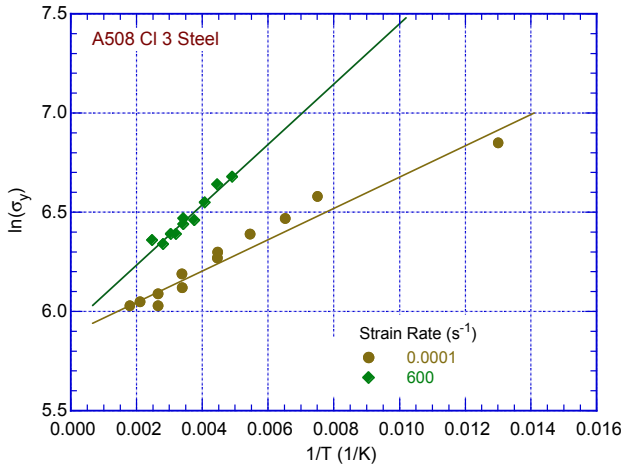

Figure 36.
Plot of of ln(σy) versus 1/T at two different strain rates for A508 Cl 3 steel (Ref. 170).

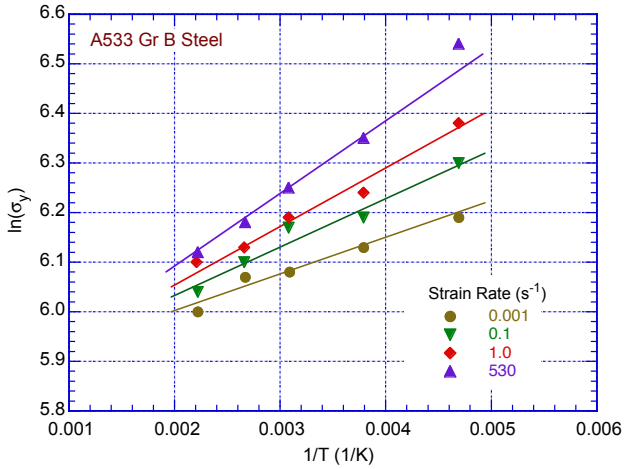

Figure 37.
Plot of of ln(σy) versus 1/T at four different strain rates for A533 Gr B steel (Ref. 170).

Bonora and Milella[170] and Milella[171] analyzed the dependence of yield strength on temperature for both A508 Cl 3 and A533 Gr B steels, using their own data[172] as well as the data of Kanninen.[173] For the A508 steel, the data analyzed extend from approximately −196 to +280°C at a strain rate of 10^{-4} s^{-1} and from approximately −73°C to 127°C at a strain rate of 600 s^{-1}. For the A533 steel, the data extend from -60 to 175°C at strain rates of 10^{-3}, 10^{-1}, 10, and 531-574 s^{-1}. For both materials, an Arrhenius plot of ln(σ_y) versus 1/T (1/K) results in an approximately linear relationship with a positive slope (Figs. 36 and 37). The slope of the plot becomes increasingly positive as the strain rate increases, and, if the curves are extrapolated back toward lower values of 1/T (increasing temperature), they appear to intersect at a common point. This latter observation indicates that the effect of strain rate on yield stress diminishes with increasing temperature and vanishes altogether (and possibly reverses) at sufficiently high temperatures above the test temperatures for the data analyzed. A plot of the slopes of the linear relationships described above versus the natural logarithm of the strain rate results in another linear plot with a positive slope.

Steichen and Williams[174] conducted tensile tests on unirradiated and neutron-irradiated A533 Gr B steel at temperatures of −196 to 260°C and strain rates of 1.3×10^{-4} to 10^{2} s^{-1}. The yield strength of both unirradiated and irradiated material was observed to significantly increase with decreasing temperature and increasing strain rate. At all temperatures, increasing fluence increased the yield strength and decreased the rate sensitivity of the alloy. Cleavage fractures occurred in irradiated specimens when the yield strength was elevated to the effective cleavage stress by fluence, temperature, and strain rate.

These observations on the strain rate dependence of yield stress on strain rate for A533 Gr B steel are supported by data reported by Wiessner and MacGillivray.[121] Figure 38 from their work shows yield stress and ultimate tensile strength values determined in round-robin tests over a range of strain rates for 20MnMoNi55 pressure-vessel steel, which is similar to A533 Gr B. Once again, both the yield and tensile strengths increase with increasing strain rate, with the former increasing more dramatically.

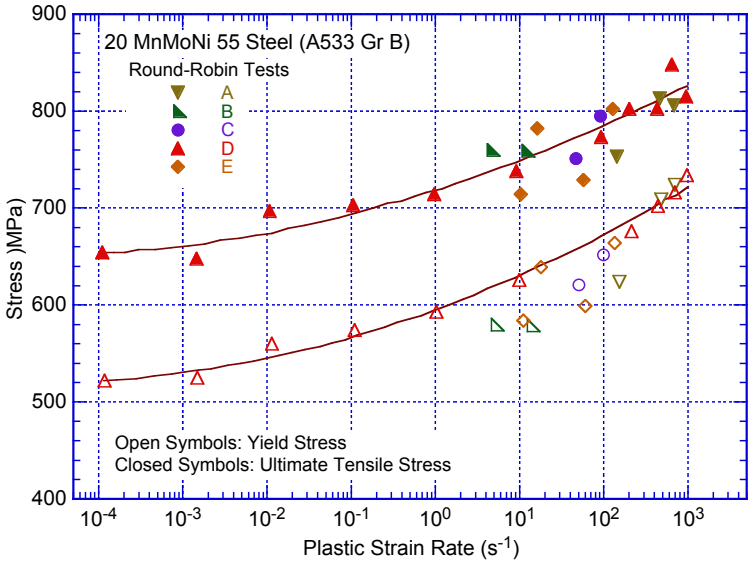

Figure 38. Results of round-robin tensile tests conducted at various strain rates on 20 MnMoNi 55 (similar to A533 Gr B) pressure vessel steel (Ref. 121).

Solomos et al. have also investigated the effects of temperature and strain rate on the yield strengths of three nuclear structural steels, namely 20 MnMoNi 55 (A533 Gr B) ferritic steel, X6 CrNiNb 1810 (Type 347) austenitic SS, and a ferritic 26 NiCrMo 14 6 bolting steel.[175] Tensile tests were conducted at room and elevated temperatures (400–600°C) and strain rates from 10^{-3} to 300 s^{-1}. Once again, they found that the yield strength and flow stress increase with increasing strain rate within the range tested at room temperature. At 400°C, the effect is reversed, with a decrease in both properties with increasing strain rate (Figs. 39 and 40). The reason for the reversed strain rate dependence (i.e., decrease in yield and flow stress with increase in strain rate) at 400°C and its potential impact on seismic design of safety-related structures and components needs to be evaluated in the next phase of this program **(Information Gap 3)**.

Finally, Chaouadi and Puzzolante[176] determined the tensile properties of forged 20MnMoNi55 steel and A533 Gr B steel plate at 25, 100, and 290°C at strain rates of 1×10^{-4} s^{-1} and 10 s^{-1}. The designation 20MnMoNi55 is the German specification for a steel similar to A508 Cl 3 pressure vessel steel, and the JSPS material is a special heat of A533 Gr B steel provided by the Japan Society for Promoting Science (JSPS) Committee 129 for a series of round-robin tests on its ductile-to-brittle transition behavior. Their results, which are summarized in Table 7, indicate an increase in tensile and yield strengths with increasing strain rate at 25 and 100°C but a reverse effect on tensile strength at 290°C. The ductility appears to show little effect of strain rate at all three temperatures.

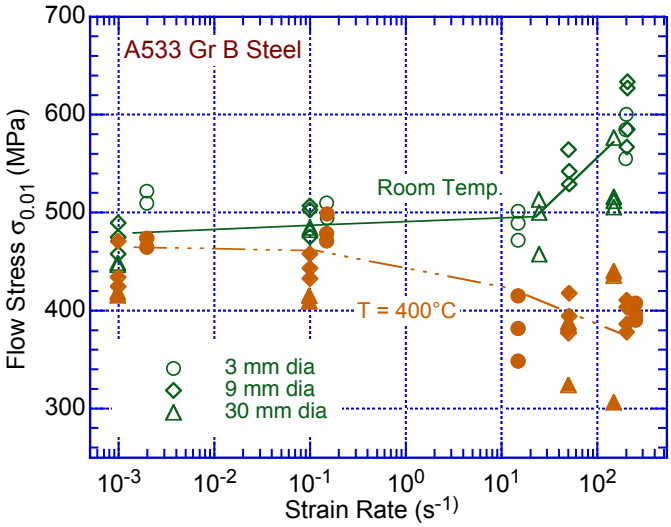

Figure 39.
Variation of yield strength (flow stress at a strain of 0.01) for A533 Gr B pressure vessel steel with strain rate for three specimen sizes and two temperatures (Ref. 175).

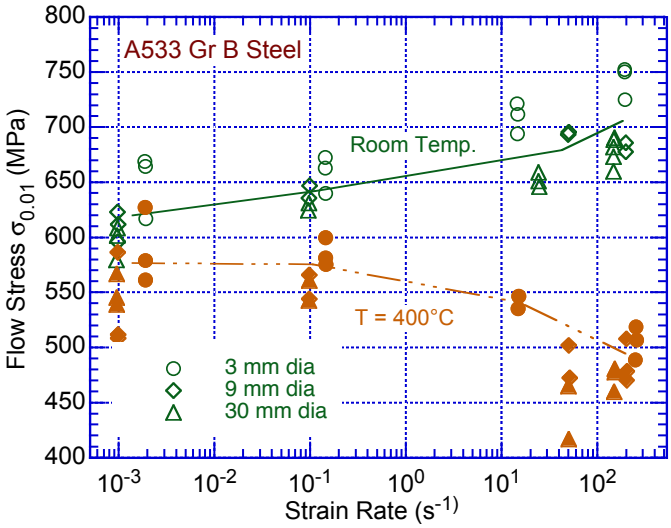

Figure 40.
Variation of ultimate tensile strength of A533 Gr B pressure vessel steel with strain rate for three specimen sizes and two temperatures (Ref. 175).

Table 7. Effect of test temperature and strain rate on the tensile properties of A533 Gr B steel plate and forged 20MnMoNi55 (Ref. 176).

Material	Test Temp. (°C)	Strain Rate (s^{-1})	Yield Stress (MPa)	Tensile Strength (MPa)	Uniform Elongation (%)	Total Elongation (%)	Reduction of Area (%)
A533 Gr B	100	1 x 10^{-4}	438	604	10	18	59
A533 Gr B	100	10	508	668	10	22	64
A533 Gr B	290	1 x 10^{-4}	435	664	11	19	54
A533 Gr B	290	10	433	574	9	19	63
20MnMoNi55	25	1 x 10^{-4}	450	595	10	23	75
20MnMoNi55	25	10	522	666	11	24	75
20MnMoNi55	290	1 x 10^{-4}	403	586	10	23	75
20MnMoNi55	290	10	397	520	8	22	78

In summary, literature data indicate that the yield and ultimate tensile strengths of A508, Cl 3, and A533 Gr B steel generally increase with increasing strain rate, while the ductility decreases or shows little effect. However, some data suggest a reversal in the yield and tensile strength behavior with strain rate in the region of the normal LWR operating temperatures.

3.1.2.2 Wrought Austenitic Stainless Steels

Type 304 Stainless Steel

Steichen and Ward reported a modest increase in the yield strength of Type 304 SS with increasing strain rate at 538°C (1000°F) over the range from 3×10^{-5} s^{-1} to 10 s^{-1}, with the value increasing from ~150 MPa (22 ksi) to ~170 MPa (25 ksi).[177] The uniform elongation decreased from ~17% to 11% over this same strain rate range, but the observed change in total elongation was minimal.

Iino studied the effect of strain rate on the tensile properties of Type 304 SS over strain rates from 10^{-6} to 10^{-1} s^{-1} and temperatures ranging from 77 to 1223 K (−196 to 950°C).[178] The tests were conducted in air at 25 to 950°C, dry ice vapor at −70 to 0°C, and various liquids, namely liquid nitrogen (−196°C), an ethanol-dry ice mixture (−78 to −25°C), ice water (0°C), water (25 to 99°C), and silicone oil (150°C). The results are summarized in Figs. 41 and 42. In the temperature range of interest to LWRs (100 to 300°C), the yield stress increases slightly with increasing strain rate, the ultimate tensile strength decreases, and the ductility as measured by the elongation to failure is unaffected or decreases slightly.

Huang et al. studied the strain-rate dependence of the tensile deformation behavior of Type 304 SS sheet in the temperature range of −80 to 160°C.[179] They found that deformation behavior results from the competition of two strengthening mechanisms. At low temperatures, the strain-induced transformation of unstable austenite to martensite predominates, and the strain-rate sensitivity is proportional to the transformation rate. At the higher end of the range of temperatures studied, slip predominates and the strain-rate sensitivity decreases with increasing strain.

Iino et al. subsequently conducted room-temperature tensile tests on smooth and notched cylindrical Type 304 SS specimens at strain rates ranging from 10^{-7} to 10^{3} s^{-1}.[180,181] They found that the yield strength increased with strain rate over this range, while the ultimate tensile strength decreased slightly to a strain rate of 10^{-1} s^{-1} and then again slowly increased. The uniform elongation also generally decreased with increasing strain rate (Fig. 43). Also plotted is the apparent magnetic permeability, as measured by a magnetic permeability meter on the curved side surface of the uniformly elongated gauge region of the fractured smooth specimen. An increase in permeability is associated with an increase in the martensite formed during deformation.

Marschall et al. tested A358 (Type 304 SS) piping material at a strain rate of 4×10^{-4} s^{-1} at room temperature, 150°C, and 288°C, and conducted additional tests at 288°C at strain rates of 1 and 10 s^{-1}.[182] They observed a modest decrease in ultimate tensile strength, a modest increase in yield strength, and little change in elongation with increasing strain rate at 288°C (Fig. 44).

Figure 45 presents results of an Avesta Sheffield report (reproduced by Nordberg)[183] showing the variation of room-temperature tensile flow stress with strain rate at 0.2 and 2.0% strain for Type 304 SS. As shown, the flow stress increases monotonically with increasing strain rate.

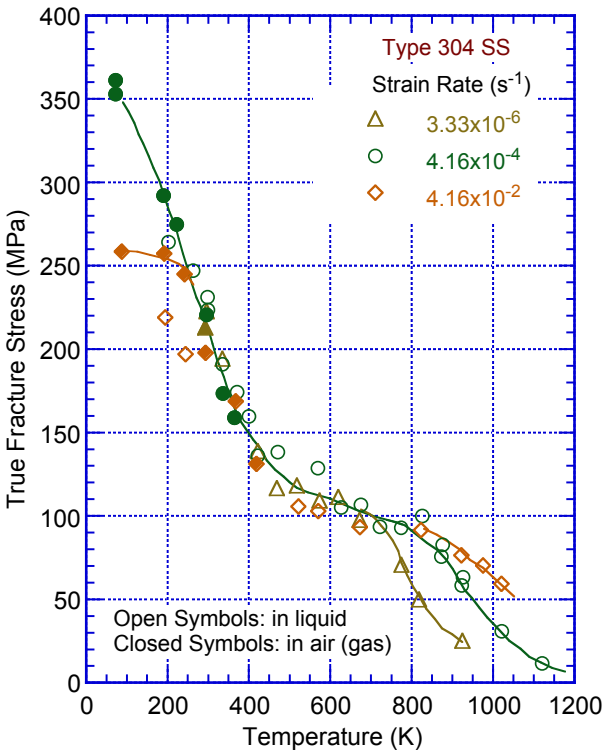

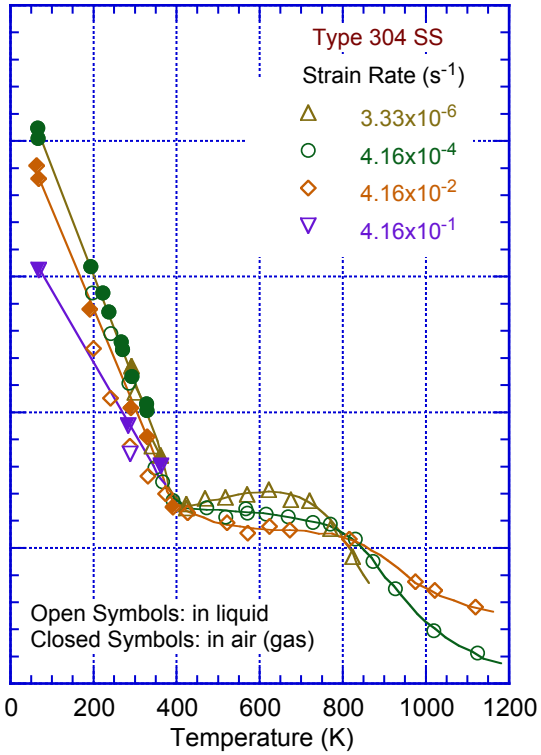

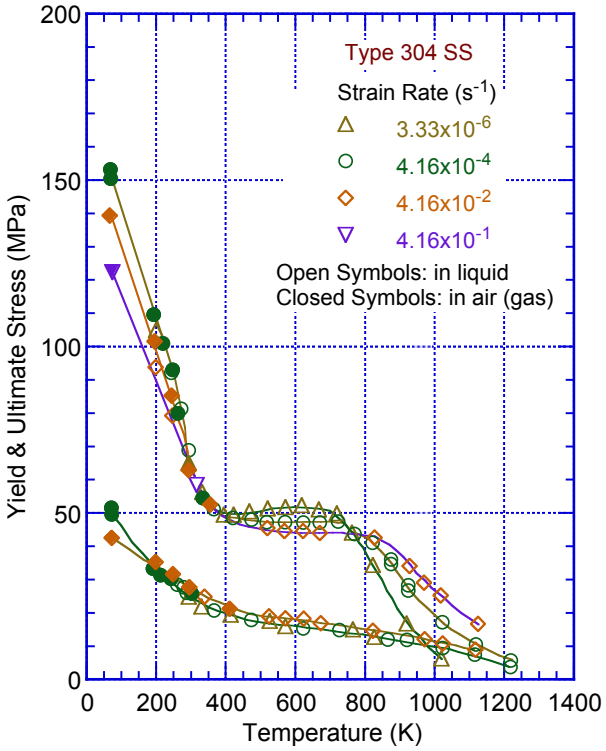

Figure 41.
Temperature and strain-rate dependence of yield strength (σ_y), ultimate tensile strength (UTS), true ultimate tensile strength (σ_u), and true fracture stress (σ_f) for Type 304 SS (Ref. 178).

Kundu and Chakraborti also conducted a room-temperature tensile test on solution annealed Type 304 SS at strain rates ranging between 5×10^{-4} and 1×10 s^{-1}.[184] They found that with increasing strain rate, the yield strength increased and tensile strength decreased (Table 8), and

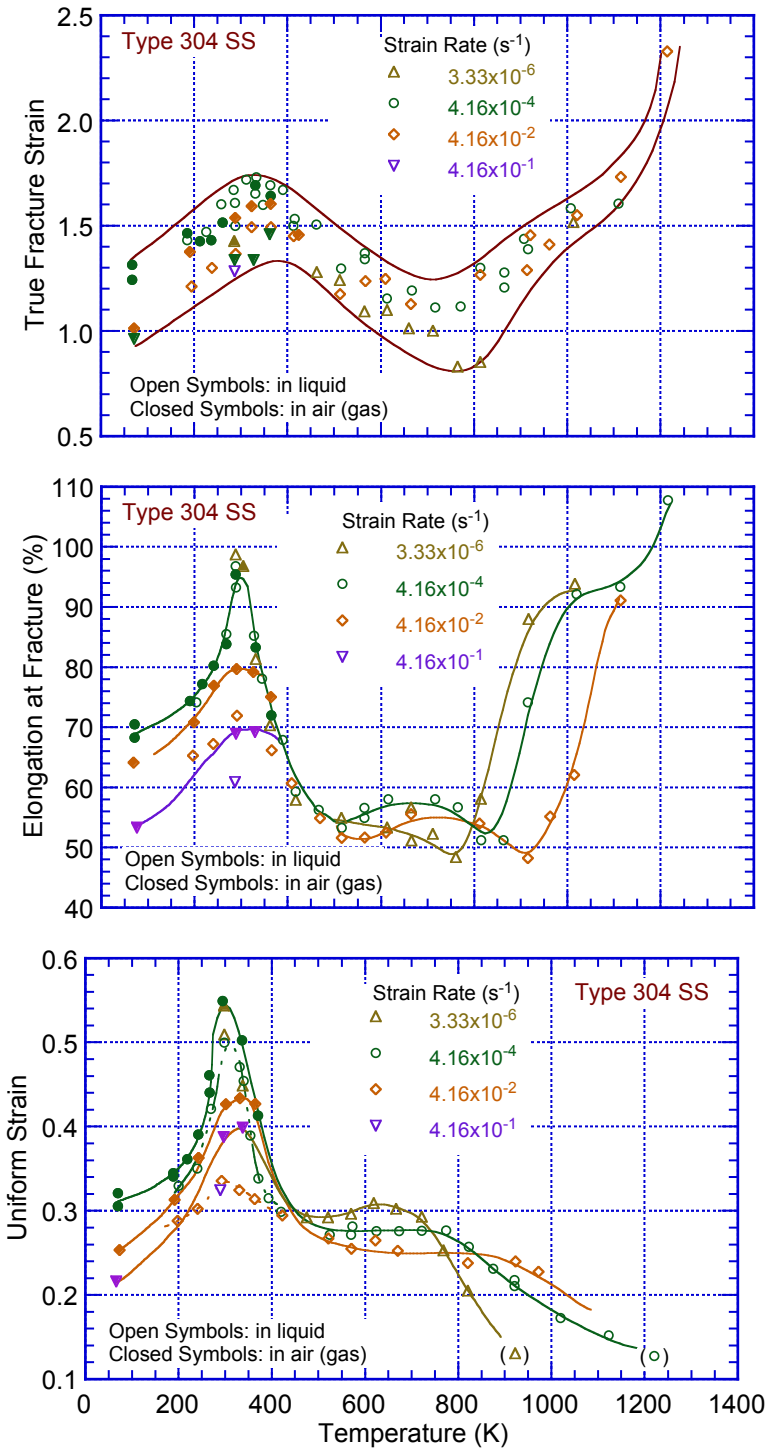

Figure 42. Temperature and strain-rate dependence of uniform strain (ε_u), elongation to fracture (e_f), and true fracture strain (ε_f) for Type 304 SS (Ref. 178).

both maintained a power–law relationship with strain rate. The decrease in tensile strength with increasing strain rate was attributed to the lesser amount of deformation-induced martensite formation and a greater role of thermal softening over work hardening at higher strain rates.

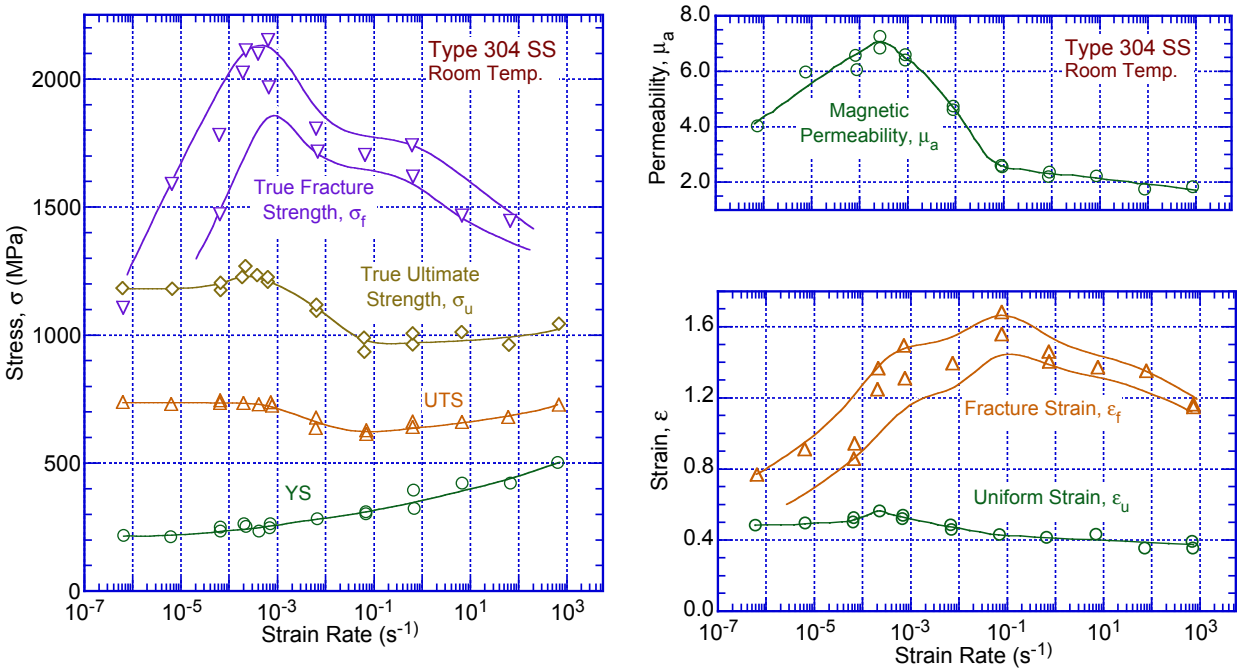

Figure 43. Variation of tensile and magnetic properties of Type 304 SS with strain rate at room temperature: (a) yield strength [σ_y], ultimate tensile strength [UTS], true ultimate tensile strength [σ_u], and true fracture strength [σ_f]; (b) uniform strain [ε_u], true fracture strain [ε_f], and apparent magnetic permeability at ε_u [μ_a] (Refs. 180,181).

Table 8. Room temperature tensile properties of solution annealed Type 304 steel at different strain rates (Ref. 184).

Initial Eng. Strain Rate (s^{-1})	0.2% Offset Y.S. (MPa)	Tensile Strength (MPa)	Ductility (% strain)[a]			Reduction of Area (%)	True Fracture Duct. (%)
			e_t	e_u	ε_u		
5×10^{-4}	268.0	672.1	108.3	99.6	74.0	85.4	192.6
1×10^{-3}	277.0	649.5	95.7	87.8	63.0	80.8	164.8
5×10^{-3}	283.0	628.5	75.0	66.5	51.0	78.70	154.5
1×10^{-3}	287.0	618.0	68.5	61.6	48.0	75.3	139.9
5×10^{-2}	291.4	611.2	61.3	56.8	45.0	75.0	138.6
1×10^{-1}	298.3	608.4	59.4	52.2	42.7	67.3	111.8
1×10^{-1}	298.3	608.4	59.4	52.2	42.7	67.3	111.8

[a] e_t = total engineering strain, e_u = uniform engineering strain, ε_u = uniform true strain.

Andrade-Campos et al. investigated the interdependencies between strain rate, plastic anisotropy, and strain hardening for Type 304 SS at room temperature in the strain range from 10^{-4} to 10^{-1} s^{-1} and found that changes in mechanical behavior with increasing strain rate depend strongly on the stability of the metastable austenite phase.[185] Similarly, Talonen et al. studied the effect of strain rate between 3×10^{-4} and 200 s^{-1} on the mechanical behavior and strain-induced phase transformation of Type 304 SS and found that this material shows significantly different behaviors at high strain rate as compared to quasi-static conditions.[186]

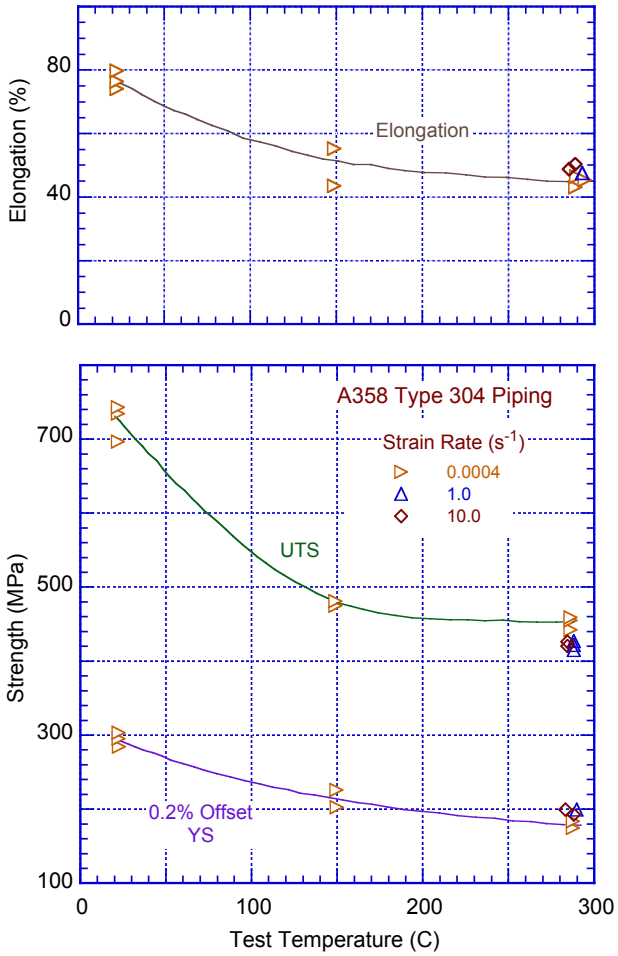

Figure 44.
Variation of tensile properties with temperature and strain rate for A358 (Type 304 SS) piping material (Refs. 182).

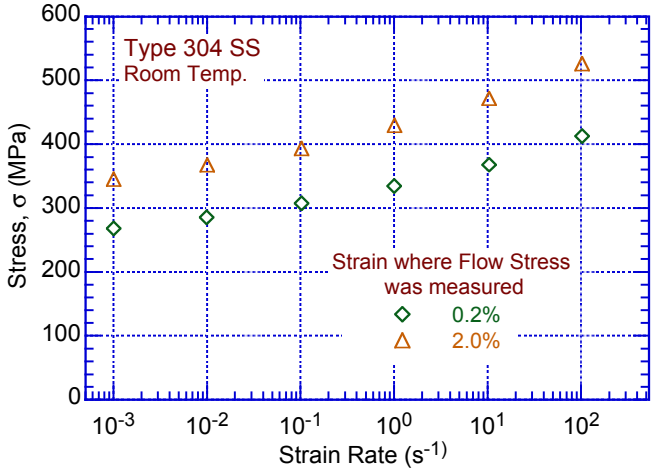

Figure 45.
Variation of room-temperature tensile flow stress at 0.2 and 2.0% strain with strain rate for Type 304 SS (Ref. 183).

These observations are also confirmed by Rodriguez-Martinez et al.,[187] who studied the martensitic transformation in Type 304 SS under tensile loading at room temperature over a range of strain rates. Their data (Fig. 46) indicates a clear increase in flow stress with increasing strain rate from 10 s^{-1} to 100 s^{-1}. They concluded that plastic deformation is the dominant mechanism responsible for the martensitic transformation phenomenon in this steel.

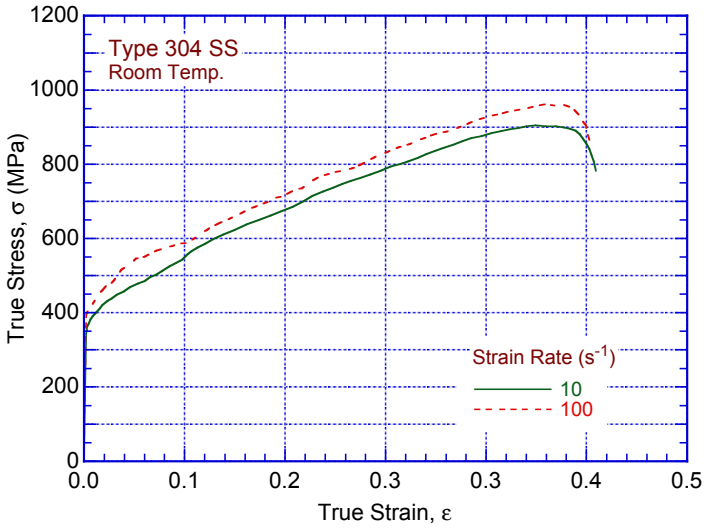

Figure 46.
True stress-true strain behavior of Type 304 SS at room temperature for two different strain rates (Ref. 187).

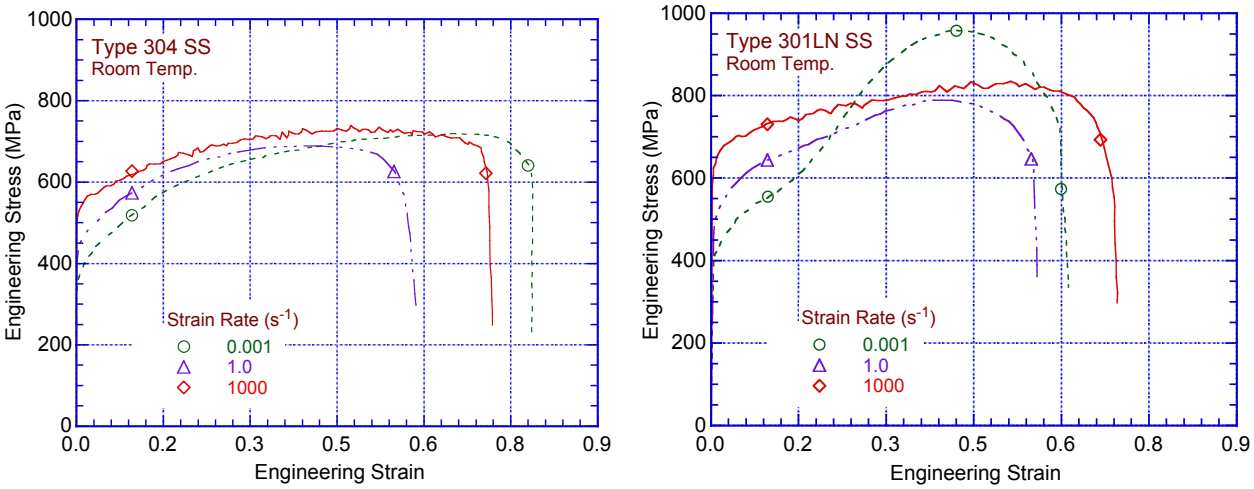

Figure 47. Room-temperature engineering tensile stress-strain curves at various strain rates for (a) Type 304 (EN 1.4301-2B) and (b) Type 301LN (EN 1.4318-2B) SS (Ref. 188).

The results of Kuokkala et al.[188] from room-temperature tests conducted at strain rates of 10^{-3}, 1, and 10^{3} s^{-1} on Types 304 and 301LN austenitic SSs again indicate that the yield stress increases with increasing strain rate (Fig. 47). However, the effect of strain rate on the ultimate tensile strength and the uniform and total elongations are not clear-cut.

In summary, for Type 304 SS, the yield stress and flow stress are generally found to increase with increasing strain rate, the ultimate tensile strength tends to decrease, and the ductility decreases or shows little change.

The effect of strain rate on the tensile properties of solution annealed and irradiated Type 304 stainless steel has also been investigated by Fish and Hunter.[189] The tests were conducted on specimens irradiated at 385-388°C in the Experimental Breeder Reactor-II (EBR-II) (fast neutrons) to fluences of 8.8-10.3 x 10^{22} n/cm^2 and tested at room temperature, 232, and 371°C (450 and 700°F). Their results, as summarized in Fig. 48, indicate that the tensile strength of the irradiated material increases modestly with strain rate at all three test temperatures.[42] The

uniform elongation also increases with strain rate for the room temperature tests but remains relatively insensitive to strain rate at the higher temperatures.

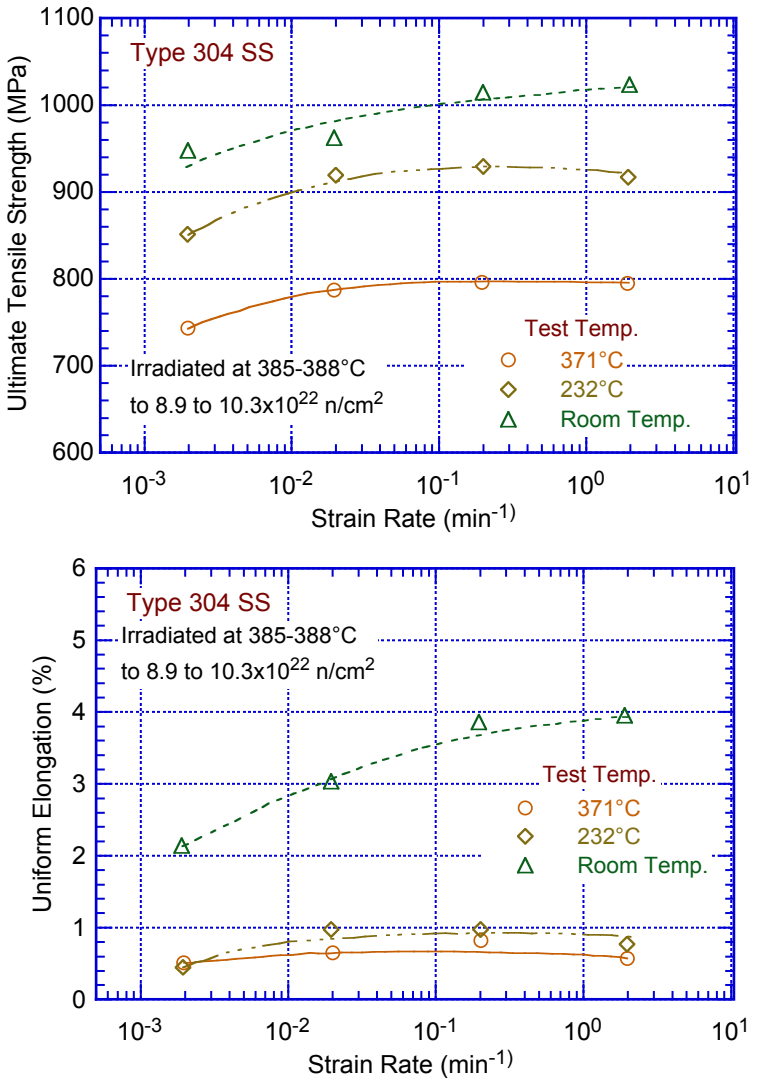

Figure 48. Effect of strain rate on the tensile properties of solution-annealed Type 304 stainless steel irradiated at 385-388°C in EBR-II to fluences of 8.8 to 10.3 x 10^{22} n/cm^2 and tested at RT, 232, and 371°C (450 and 700°F) (Ref. 42).

Types 304L and 304LN Stainless Steels

Semiatin and Holbrook investigated the isothermal plastic flow behavior of annealed Type 304L SS in uniaxial compression and torsional modes of deformation over a range of temperatures and strain rates.[190] In uniaxial compression, they found that high rates of strain hardening, which persist to large strains (≥0.7) at cold-working temperatures, occur only at small values of strain (≤0.2) at hot-working temperatures because of the influence of dynamic softening processes. The effect of deformation heating on flow behavior, which occurs primarily at high strain rates, was most significant at cold-working temperatures. Deformation heating was observed to result in flow stress maxima and flow softening. A method of estimating high strain rate, isothermal flow curves in such instances was derived. Shear stress–shear strain curves

derived from torsion tests exhibited dependences on temperature and strain rate similar to those observed in compression data. In contrast to the compression curves, however, the shear stress–shear strain curves showed lower rates of strain-hardening at room temperature, 4°C, 800°C, and (for high strain rates) 1,000°C. The choice of definition for calculating effective stress-strain from the torsion data could not be modified to bring the two types of data into coincidence. Only a structure-sensitive explanation could be invoked to explain the difference. Room-temperature tensile tests were conducted at constant true strain rates of 0.01 and 3.5 s^{-1}. Compression tests at 400, 800, and 1,000°C were conducted at constant true strain rates of 0.009 and 10 s^{-1}. For compression tests at 1,200°C, the nominal true strain rate was 10.2 s^{-1} for the first 60% of the total deformation, after which it dropped off sinusoidally to zero.

Stout and Follansbee reported the results of room-temperature uniaxial tension and compression tests conducted on Type 304L SS at strain rates between 10^{-4} s^{-1} and 10^{4} s^{-1}.[191] In addition, multiaxial experiments were performed at a strain rate of 10^{-3} s^{-1}. Strain-rate sensitivity was found to follow a thermal activation law over the entire range of strain rates studied.

Lichtenfeld et al. investigated the effect of strain rate on the stress-strain behavior of Type 304L SS at room temperature at strain rates ranging from 1.25×10^{-4} s^{-1} to 400 s^{-1}.[192] They observed an increase in yield strength with increasing strain rate, but the effects on ultimate tensile strength and uniform elongation were somewhat variable (Table 9 and Figs. 49 and 50). The material was found to transform readily with strain, with martensite nucleating on slip bands and at slip band intersections. The observed variations in ductility and strength with strain rate were explained in terms of the competition between hardening from the martensitic transformation and positive strain rate sensitivity, and softening due to deformational heating.

Table 9. Room-temperature tensile properties of temper-rolled Type 304L SS at different strain rates. Stated values are averages for three tests (Ref. 192).

Strain Rate (s^{-1})	0.2% Yield Strength (MPa)	Ultimate Tensile Strength (MPa)	Uniform Elongation (%)
1.25 x 10-4	300 ± 3	755 ± 0	59.1 ± 0.7
1.25 x 10-3	307 ± 5	714 ± 8	59.4 ± 0.6
1.25 x 10-2	328 ± 2	654 ± 5	44.2 ± 0.8
0.125	351 ± 0	646 ± 2	42.1 ± 0.3
1.25	361 ± 5	658 ± 4	42.7 ± 0.4
10	382 ± 6	673 ± 1	45.7 ± 0.4
100	438 ± 11	699 ± 1	45.5 ±0.6
400	480 ± 11	738 ± 4	45.9 ± 0.9

Antoun et al. conducted uniaxial compression tests on Type 304L SS at strain rates of 10^{-3}, 10^{-2}, and 10^{-1} s^{-1} and temperatures ranging from room temperature to 1093°C.[193] They observed only a very slight increase in flow stress with increasing strain rate at room temperature and 204°C and an unexpected decrease with increasing strain rate at 427 and 538°C. At higher temperatures, the flow stress increased more substantially with increasing strain rate.

Ishikawa et al. (1988) tested Type 304N thin-walled tubular specimens in torsion at room temperature and strain rates of 10^{-3} to 103 s^{-1}.[194] Their results, as reproduced by Norberg,[183] are shown in Fig. 51. The flow stress at $2\gamma^{p} = 2\%$, where γ^{p} is the principal shear strain, increases with increasing strain rate over the range.

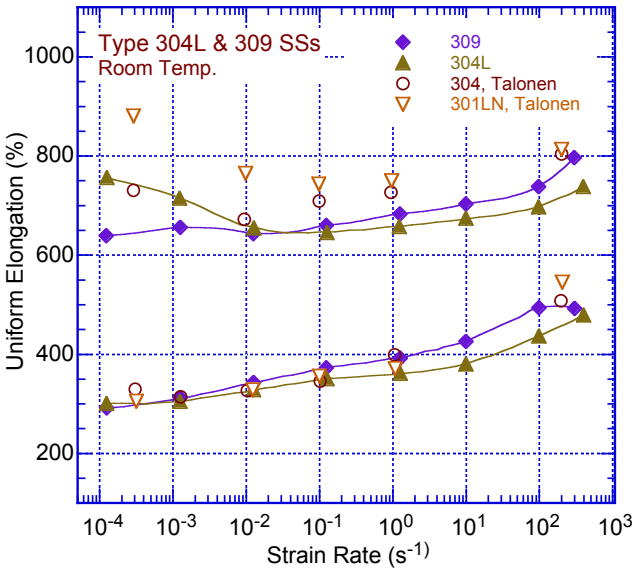

Figure 49.
Variation of 0.2% offset yield strength and ultimate tensile strength with strain rate for Types 304L and 309 SSs (Ref. 186,192).

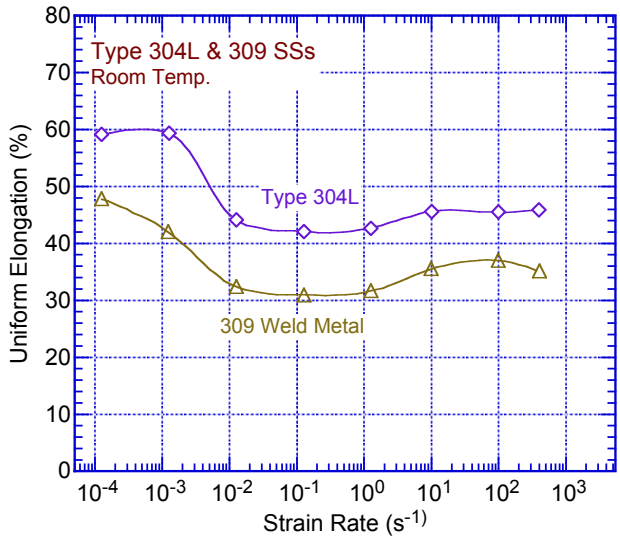

Figure 50.
Variation of uniform elongation with strain rate for Types 304L and 309 SSs (Ref. 192).

Prasad and Jonnalagadda[195] conducted dynamic compression loading experiments on Type 304LN SS at room temperature at strain rates ranging from 10^{-3} to 4800 s^{-1}; they found that the dynamic behavior was strongly affected by strain rate. The flow stress was found to increase with increasing strain rate at any specific accumulated strain, and the flow stress of Type 304LN SS was greater than that of Type 304L under both quasi-static (10^{-3} s^{-1}) and dynamic strain rates. The work hardening rate was found to decrease with increasing strain rate and accumulated strain, and the strain-rate sensitivity at a constant strain decreased linearly with increasing true strain.

In summary, the yield stress and flow stress are generally found to increase with increasing strain rate for Types 304L, 304N, and 304LN SSs, similar to the behavior observed for Type 304 SS. However, one researcher observed an unexpected decrease in flow stress with increasing strain rate at 427 and 538°C. As for Type 304 SS, the ultimate tensile strength tends to decrease, and the ductility decreases or shows little change.

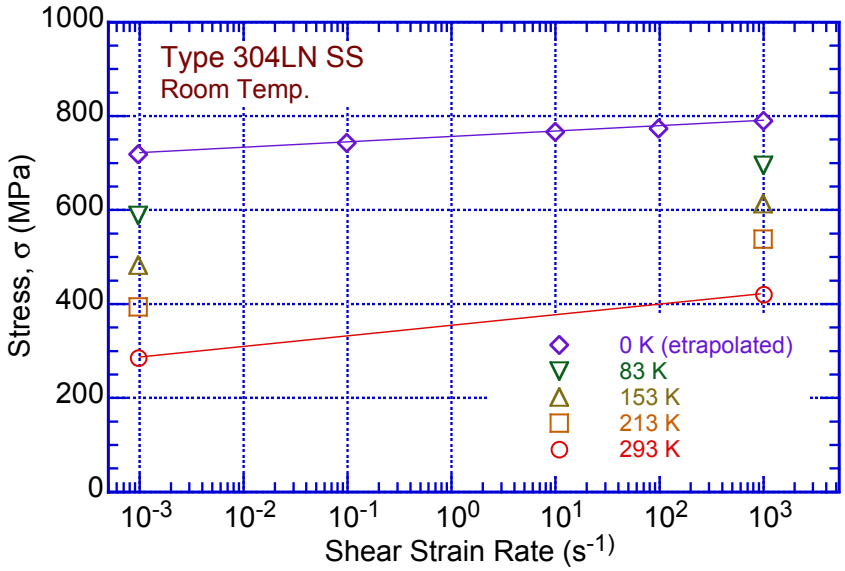

Figure 51. Room-temperature flow stress at $2\gamma^p = 2\%$, where γ^p is the principal shear strain, as a function of strain rate for Type 304N SS (Ref. 194 as modified by 183).

Type 316 Stainless Steel

Fahr conducted tensile tests at room temperature on 20% cold-worked Type 316 SS and at 650°C on annealed Type 316 SS (Table 10).[196] The tests were conducted at four different test machine crosshead speeds of 0.002, 0.02, 0.2, and 2.0 in./min; the actual strain rates are not reported. However, if it is assumed that all the strain was accumulated over the 1-in. gage section of the test specimens employed, upper values of strain rate can be calculated, namely, 3.3×10^{-5}, 3.3×10^{-4}, 3.3×10^{-3}, and 3.3×10^{-2} s^{-1}, respectively. At room temperature, the yield strength was found to be relatively insensitive to strain rate over the range tested, the elongation decreased only slightly, and the ultimate tensile strength increased slightly. At 650°C, the yield strength increased slightly with increasing strain rate, the elongation decreased slightly, and the ultimate tensile strength increased more significantly (≈20 %).

Varin studied the influence of temperature and strain rate on the plastic flow and ductility of an ultrafine-grained (grain size of about 2 μm) Type 316 SS in the temperature range of −196 to 950°C.[197] The temperature dependence of the yield (0.2% offset) and flow stresses exhibits three stages: (1) a decrease in stress with increasing temperature up to about 227°C (500K); (2) a plateau at which the stress is almost independent of temperature up to about 527°C (800K); and (3) a continuous drop in stress above 527°C (800 K). The flow stress was observed to increase with increasing initial strain rate over the range from 4.4×10^{-5} to 4.4×10^{3} s^{-1}. The percentage total elongation shows a minimum at about 900K or 627°C ($\epsilon f \approx 20\%$) followed by a ductility peak at about 1,150K or 887°C (ϵf ~120%) and a subsequent abrupt drop, at a nominal strain rate of about 2×10^{-4} s^{-1}. In general, at high temperatures total elongation of ultrafine-grained Type 316 SS increases with decreasing strain rate, emphasizing the increased importance of grain boundary sliding for maximum ductility. Microstructural studies of the fracture zone in tensile specimens show the existence of micro-cracks near grain boundary and triple point carbides at the temperature corresponding to the ductility minimum. Based on mechanical testing results and microstructural studies, it is suggested that the ductility peak mainly arises from a significant contribution from grain boundary sliding.

Table 10. Effect of strain rate on the tensile properties of Type 316 SS at room temperature and 650°C (Ref. 196).

Crosshead Speed (in./min)	Strain Rate[a] (s^{-1})	Yield Strength (MPa)	Tensile Strength (MPa)	Uniform Elongation (%)	Total Elongation (%)
20% cold-worked material tested at room temperature					
0.002	3.3×10^{-5}	1087	1094	1.9	13.1
0.02	3.3×10^{-4}	1020	1102	6.7	14.1
0.2	3.3×10^{-3}	1043	1108	2.1	12.5
2.0	3.3×10^{-2}	1112	1131	3.9	10.0
Annealed material tested at 650°C					
0.002	3.3×10^{-5}	119	392	22.7	36.6
0.02	3.3×10^{-4}	119	449	31.0	38.3
0.2	3.3×10^{-3}	117	466	31.3	37.1
2.0	3.3×10^{-2}	145	474	28.6	34.0

[a]Calculated rate assuming strain was accumulated over the 1-in. gage section of the test specimens.

Samuel et al. studied the effects of aging on the strain rate sensitivity of Type 316 SS at 650°C (923K).[198] They found that serrated flow associated with dynamic strain aging in this material can be suppressed by aging for 5000 h at 650°C, apparently because of the precipitation of chromium carbides and the accompanying depletion of chromium and carbon from the grain boundaries, which are preferential sites for dynamic strain aging. A plot of the strain rate dependence of the ductility of this alloy in the as-received (unaged) condition at 650°C (923K) is shown in Fig. 52. Both the uniform and total elongation, increase with increasing strain rate.

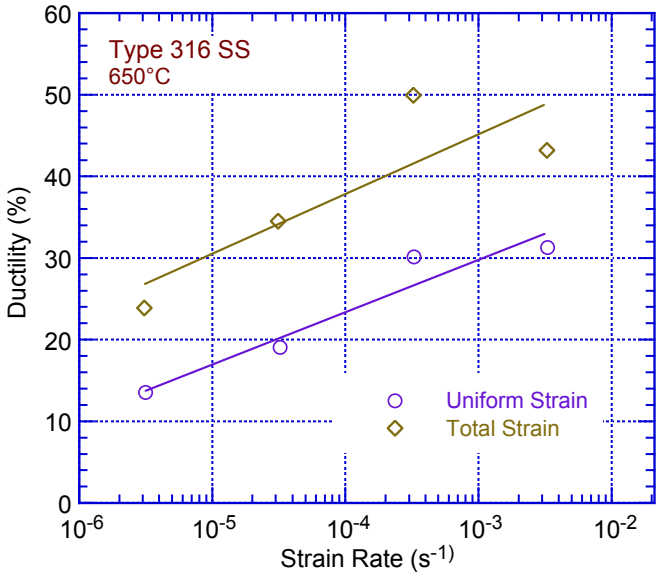

Figure 52.
Ductility (uniform and total elongations) of as-received Type 316 SS at 650°C (923 K). Plot of $\ln(\sigma_y)$ versus 1/T at four different strain rates for A533 Gr B steel (Refs. 170,198).

Morris has studied dynamic strain aging in a Ti-modified Type 316 SS with a 0.22% titanium addition to reduce elevated-temperature ductility loss after irradiation.[199] Tensile tests were conducted at 300, 500, and 700°C and strain rates of 0.002 to 10 min^{-1} (3.3×10^{-5} to 0.17 s^{-1}). He observed that the flow stress showed exhibited a somewhat variable dependence on strain rate and temperature, as shown in Figs. 53-55.

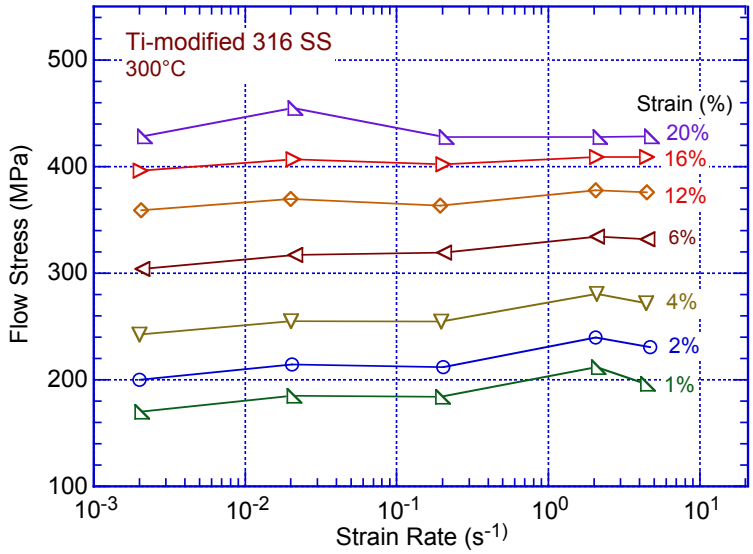

Figure 53.
Flow stress as a function of strain rate for titanium-modified (0.22% Ti) Type 316 SS at 300°C (Ref. 199).

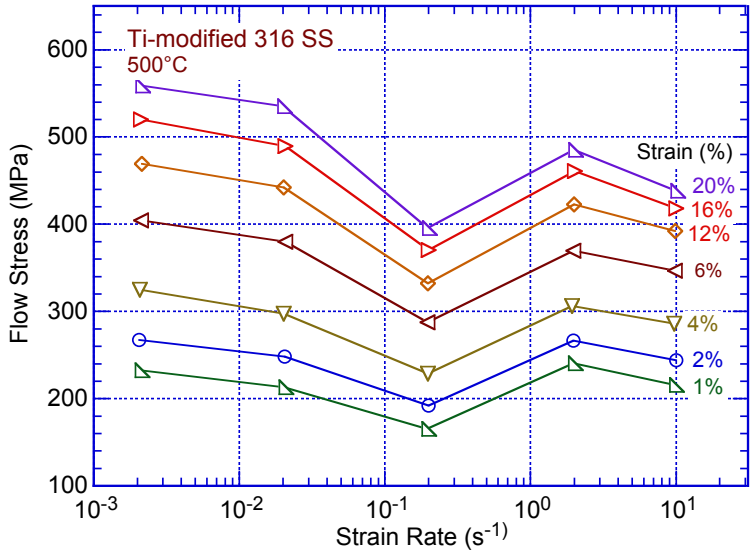

Figure 54.
Flow stress as a function of strain rate for titanium-modified (0.22% Ti) Type 316 SS at 500°C (Ref. 199).

In summary, the data of Fahr[196] indicate that the yield and ultimate tensile strengths of Type 316 SSI increase with increasing strain rate at 650°C, while the effect on the ductility is relatively small. Subsequent research indicates variable results, with Samuel et al. [198] observing an increase in ductility with increasing strain rate at 700°C.

Types 316L and 316LN Stainless Steel

The Steel Construction Institute of the U.K. summarized the results of a series of room-temperature tensile tests conducted at various strain rates on Type 316L SS.[200] As shown in Fig. 56, the flow stress at 0.2 and 1.0% strain increased with increasing strain rate over strain rates ranging from 10^{-4} to 10 s^{-1}.

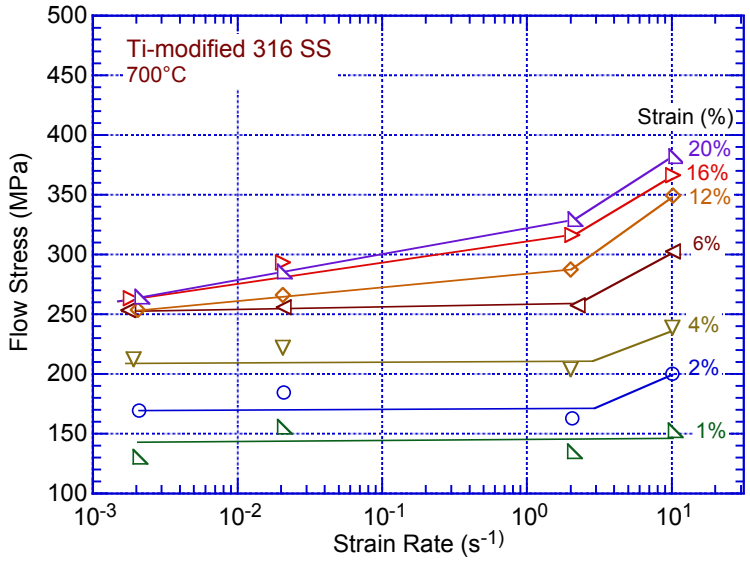

Figure 55.
Flow stress as a function of strain rate for titanium-modified (0.22% Ti) Type 316 SS at 700°C (Ref. 199).

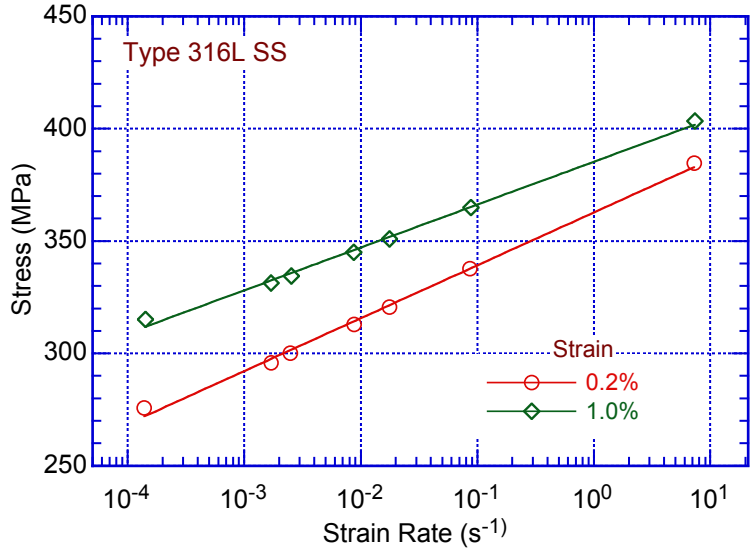

Figure 56.
Variation of flow stress at 0.2% and 1.0% strain for Type 316L SS tested in tension at room temperature (Ref. 201 reproduced in 183).

Hagström and Lindh-Ulmgren conducted compression tests on Type 316L SS at −80, −30, and +20°C and strain rates of 10^{-2} to 10 s^{-1}.[201] Their room-temperature results are shown in Fig. 57 as a plot of flow stress at 5% and 10% strain versus strain rate. Again, the flow stress increases monotonically with strain rate.

Hong and Lee conducted tensile and low-cycle fatigue tests on 17% cold-worked Type 316L SS over the temperature range of 20 to 750°C and strain rates of 1×10^{-4} to 1×10^{-2} s^{-1}.[202] They observed changes in the tensile properties associated with dynamic strain aging, particularly over the temperature range from 250 to 600°C (Fig. 58). The indicated crosshead speeds of 0.2, 2, and 20 mm/min correspond to strain rates of 10^{-4}, 10^{-3}, and 10^{-2} s^{-1}, respectively. The strain rate sensitivity in Fig. 58(c) is defined as $d\sigma/d(\ln \dot{\varepsilon})$, where $\dot{\varepsilon}$ is the true strain rate. The dynamic strain hardening stress in Fig. 58(d) is defined as the difference between true ultimate tensile strength and 0.2% yield strength.

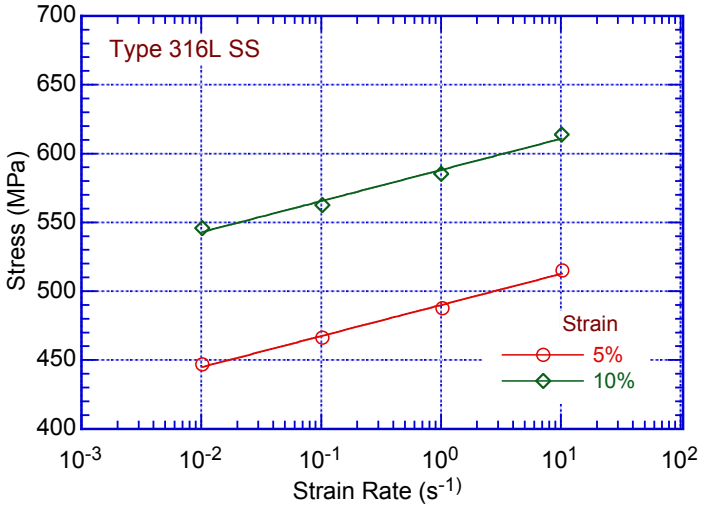

Figure 57.
Variation of flow stress at 5% and 10% compressive strain for Type 316L SS tested at room temperature (Ref. 201 reproduced in 183).

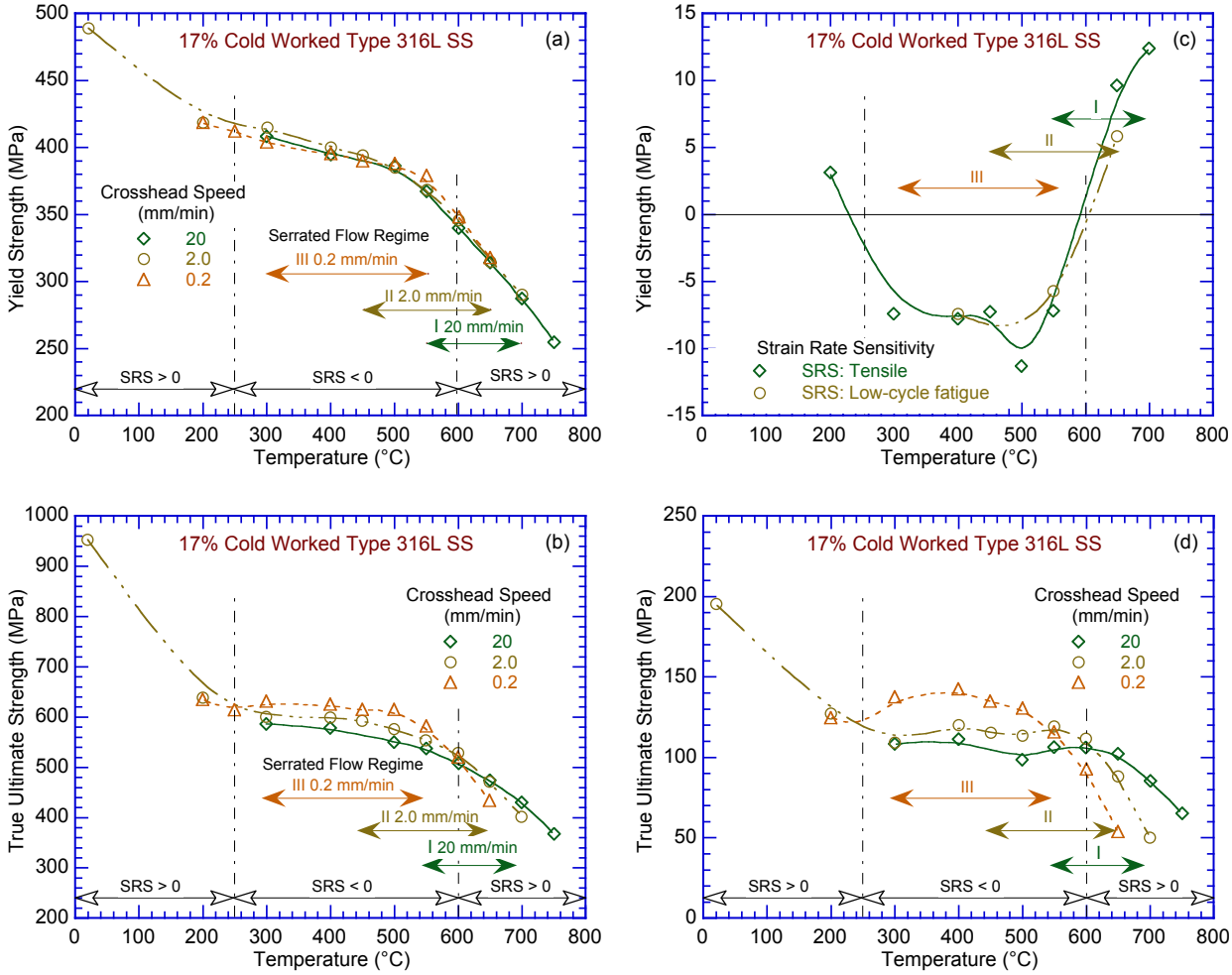

Figure 58. Variation of tensile properties for 17% cold-worked Type 316L SS with temperature for three different strain rates. The temperature regions in which serrated flow is observed in the stress strain curves for the three different strain rates is indicated by the blue bars (Ref. 202).

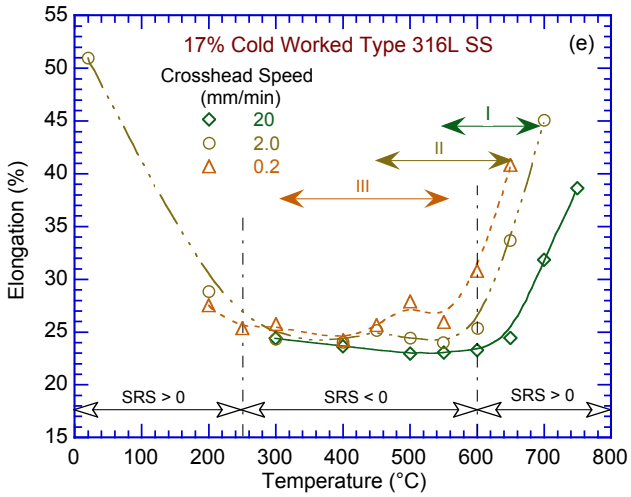

Figure 58. (Contd.)

Lee et al. investigated the dynamic mechanical properties of biomedical 316L SS under strain rates ranging from 1×10^3 s^{-1} to 5×10^3 s^{-1} and temperatures between 25°C and 800°C.[203] The results (Fig. 59) indicate that the flow stress, work-hardening rate, strain-rate sensitivity, and thermal activation energy are all significantly dependent on the strain, strain rate, and temperature. For a constant temperature, the flow stress, work-hardening rate, and strain-rate sensitivity increase with increasing strain rate, while the thermal activation energy decreases. Catastrophic failure occurred only for the specimens deformed at a strain rate of 5×10^3 s^{-1} and temperatures of 25°C or 200°C.

Choudhary performed tensile tests on Type 316LN SS at strain rates ranging from 3.16×10^{-5} to 3.16×10^{-3} s^{-1} over the temperature range of 300 to 1,123K (27 to 850°C) to examine the effects of temperature and strain rate on tensile deformation and fracture.[204] The variations of flow stress/strength values, work hardening rate, and tensile ductility with respect to temperature exhibited three distinct temperature regimes. The steel exhibited distinct low- and high-temperature serrated flow regimes and anomalous variations in terms of plateaus/peaks in flow stress/strength values and work hardening rate, negative strain rate sensitivity, and ductility minima at intermediate temperatures. The fracture mode remained transgranular. At high temperatures, the dominance of dynamic recovery was reflected in the rapid decrease in flow stress/strength values, work hardening rate, and increase in ductility with increasing temperature and decreasing strain rate. As shown in Fig. 60, his data indicate that, over the temperature range of interest for LWR applications (373 to 573K or 100 to 300°C), the normalized ultimate tensile strength (tensile strength/elastic modulus at temperature) deceases somewhat with increasing strain rate, while the yield strength, shows little variation. The uniform elongation decreases slightly with increasing strain rate, while the reduction of area shows a somewhat mixed behavior (Fig. 61).

In summary, most researchers observe an increase in flow stress with increasing strain rate for Types 316L and 316LN SSs, but there is some indication of a reversal in the strain rate effect on the ultimate tensile strength at temperatures on the order of 300 to 500°C. Elongation and reduction of area also appear to increase somewhat with increasing strain rate, though for cold-worked material the opposite effect has been observed.

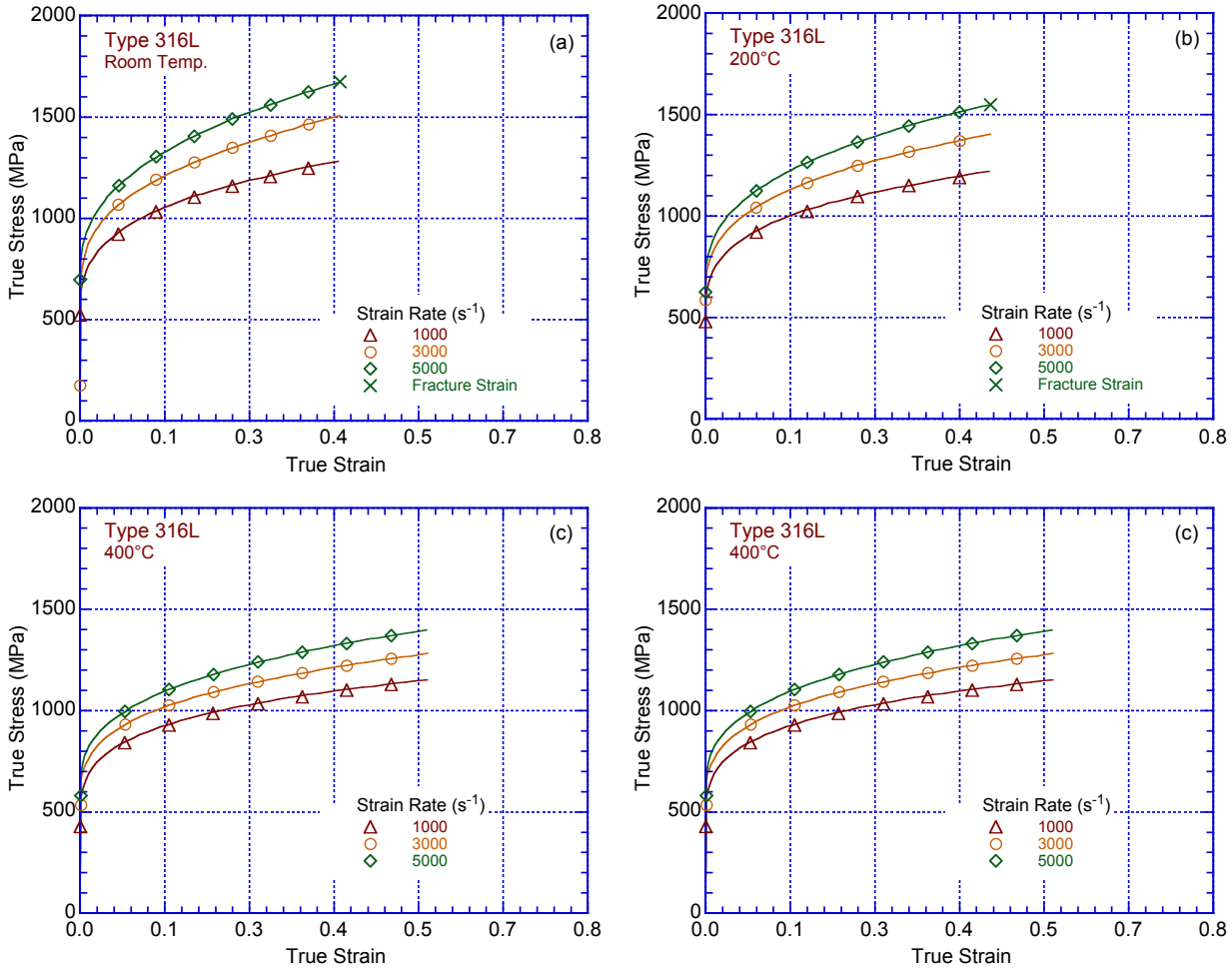

Figure 59. True stress-strain curves for Type 316L SS deformed at different strain rates and temperatures of (a) 25°C, (b) 200°C, (c) 400°C, and (d) 800°C (Ref. 203).

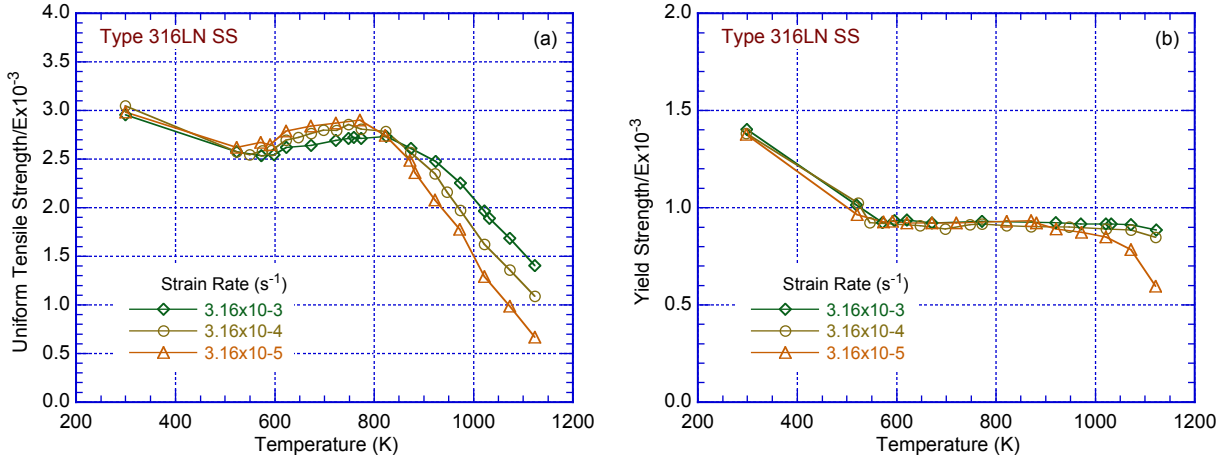

Figure 60. Variation of (a) normalized tensile strength and (b) normalized yield strength with temperature at three different strain rates for Type 316LN SS (Ref. 204).

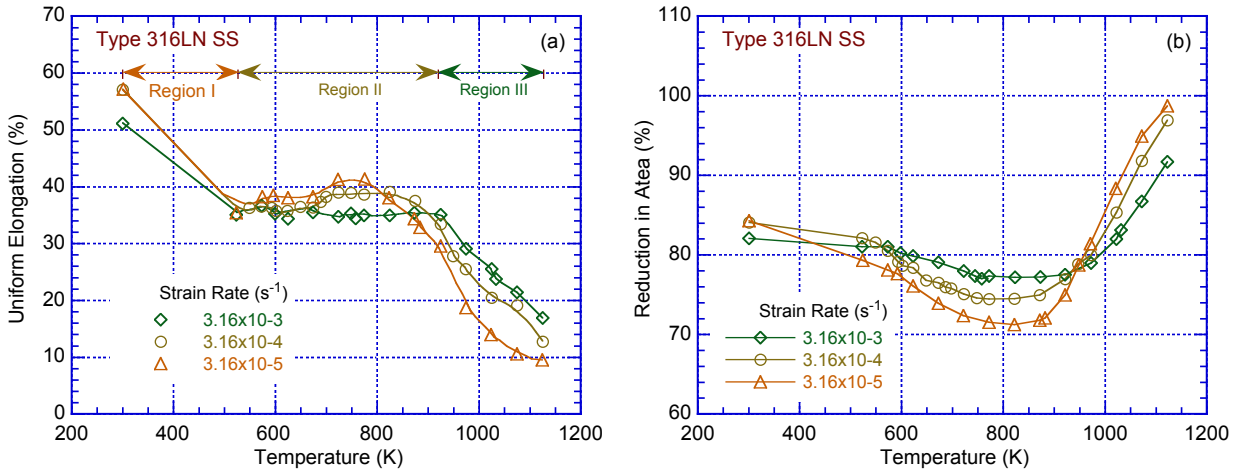

Figure 61. Variation of (a) uniform elongation and (b) reduction in area with temperature at three different strain rates for Type 316LN SS (Ref. 204).

Austenitic Stainless Steel Welds

Steichen and Ward carried out tensile tests on Type 308 SS shielded metal arc weld metal specimens taken from 60-mm-thick Type 304 SS plate.[177] The tests were conducted at temperatures from 316 to 649°C and strain rates from 3×10^{-5} to 10 s^{-1}. They found that the tensile properties varied considerably with the weld location (Table 11). They also observed that the weld metal had significantly higher yield strength and approximately one-half the ductility of the Type 304 SS base metal, but the ultimate tensile strengths of the two materials were nearly identical. Minor variations in strength and ductility with increasing strain rate were noted over the entire range of test temperatures, but these variations were considered to be largely within the range of normal data scatter. An exception to this pattern was an apparent small but continuous increase in the yield strength of the wrought Type 304 base metal with increasing strain rate. In addition, at 649°C, the yield and tensile strengths of the weld metal increased somewhat with increasing strain rate up to 10^{-2} s^{-1} and then leveled off. Similarly, the elongation decreased with increasing strain rate over the same range, and the reduction of area decreased slightly as well (Figs. 62-64).

Table 11. Tensile properties of Type 308 SS weld metal for various weld locations at 427°C and a strain rate of 0.03 s^{-1} (Ref. 177).

Specimen Location	Stress (MPa)		Elongation (%)		Reduction of Area (%)
	0.2% Yield	Ultimate	Total	Uniform	
Near weld surface	292	449	28.8	25.1	52.4
16 mm below surface	339	447	20.6	17.1	49.6
25 mm below surface	360	463	22.3	18.8	47.1
Weld center	366	454	19.8	16.7	50.0

Marschall et al. conducted tensile tests at 288°C (550°F) and a range of strain rates on submerged-arc (SA) girth weld specimens taken from an American Society for Testing and Materials (ASTM) A358, Type 304 piping material.[182] The welds employed the gas tungsten arc (GTA) process; the next two passes used the shielded-metal arc (SMA) process; and the

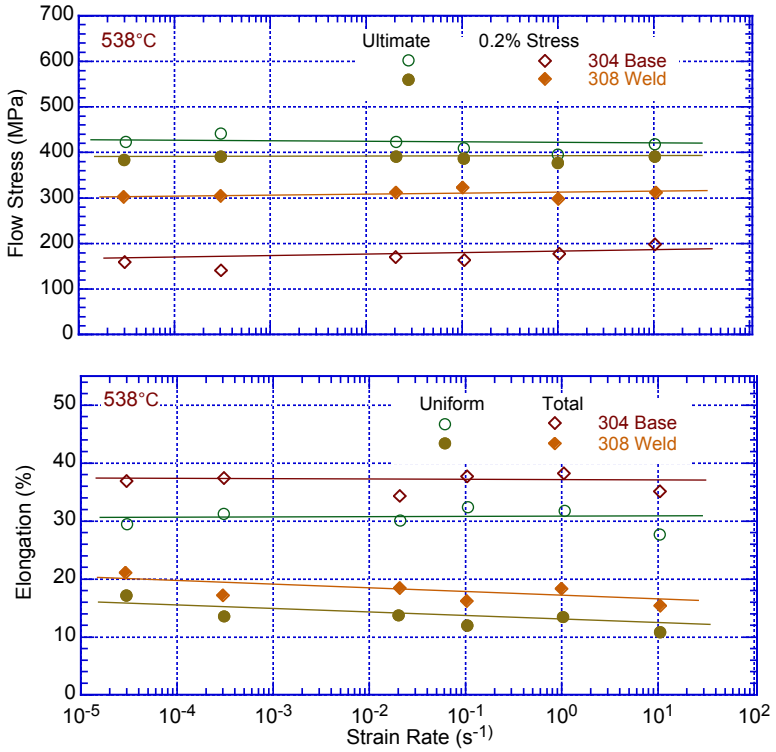

Figure 62. Effect of strain rate on the tensile properties of Type 308 SS weld metal and Type 304 SS base metal at 538°C (Ref. 177).

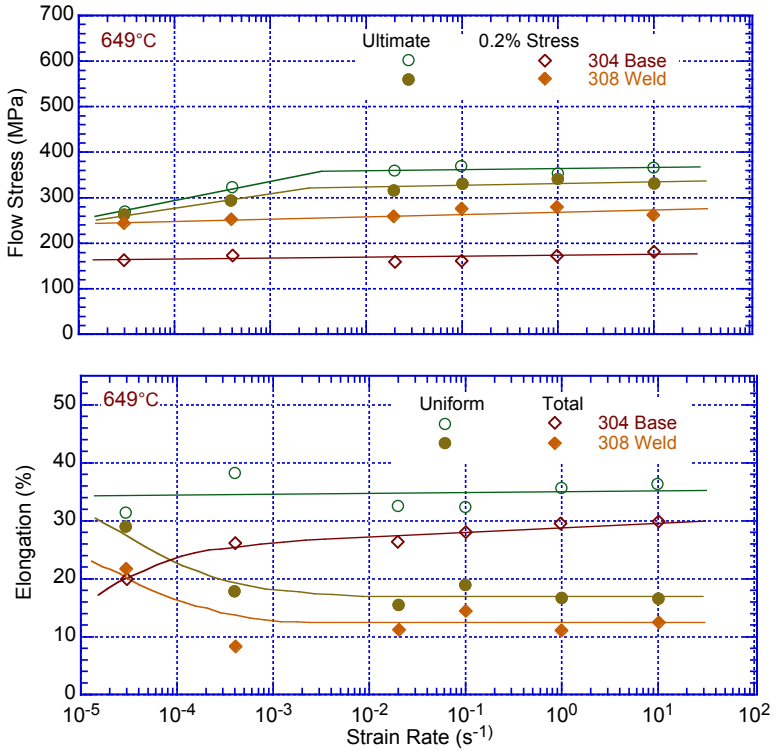

Figure 63. Effect of strain rate on the tensile properties of Type 308 SS weld metal and Type 304 SS base metal at 649°C (Ref. 177).

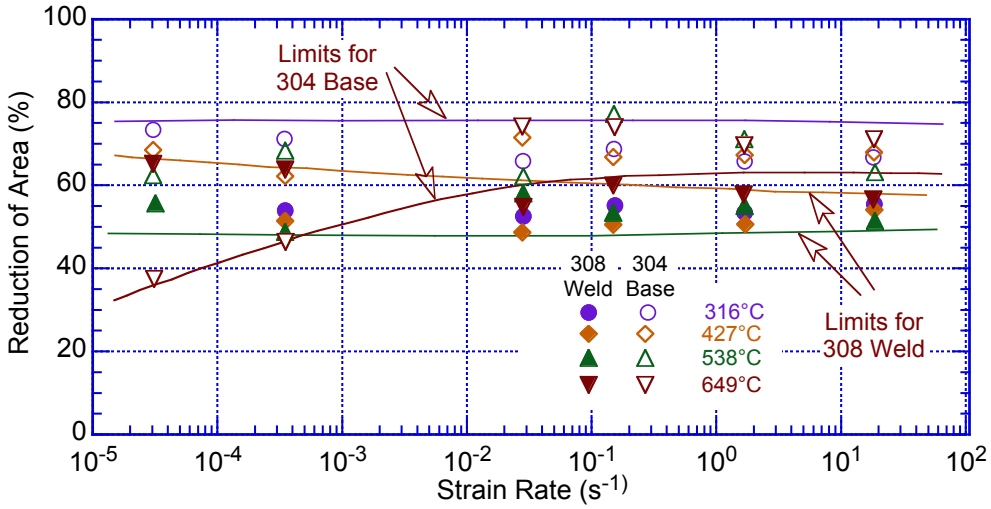

Figure 64. Effect of strain rate on the elevated-temperature reduction of area for Type 308 SS weld metal and Type 304 SS base metal (Ref. 177).

remaining passes used the SA process. The filler metal met specification SFA-5.9 (Class ER-308) for the GTA and SA welds and SFA-5.4 for the SMA weld. The weld material was found to exhibit a modest increase in the yield and tensile strengths with increasing strain rate (Fig. 65).

Figure 65.
True stress-true strain curves at 288°C (550°F) for a SA weld in a Type 304 SS pipe at several different strain rates (Ref. 182).

Lee and Tzeng studied the stress-strain response of Type 304L/308L SS SMA weld joints under compressive loading at strain rates ranging from 10^{-3} to 7.5×10^{3} s^{-1}.[205] The weld filler metal used was Type 308L SS, and the test specimens were taken from the weld joints to include the weld metal, the heat-affected zone, and the original base metal. The room-temperature stress-strain response of the composite specimen (Fig. 66) again shows a marked increase of flow stress with increasing strain rate. A similar strain-rate dependence was observed at test temperatures up to 500°C, though the flow stresses decreased with increasing temperature.[206] Similar tests were conducted on plasma-arc-welded Type 304L SS joints[207] and GTA-welded joints[208] at room temperature and the same strain-rate dependence of flow stress as observed.

In summary, the tensile data for Type 304/308 welds and Type 308 SS weld metal provide mixed results. Some researchers see a marked increase in flow stress with increasing strain rate, while others observe only a small effect. The elongation appears to decrease with increasing strain rate for the weld metal and remain roughly constant or increase slightly for the base metal. It should be noted, however, that none of these data were obtained in the temperature range of interest for LWRs.

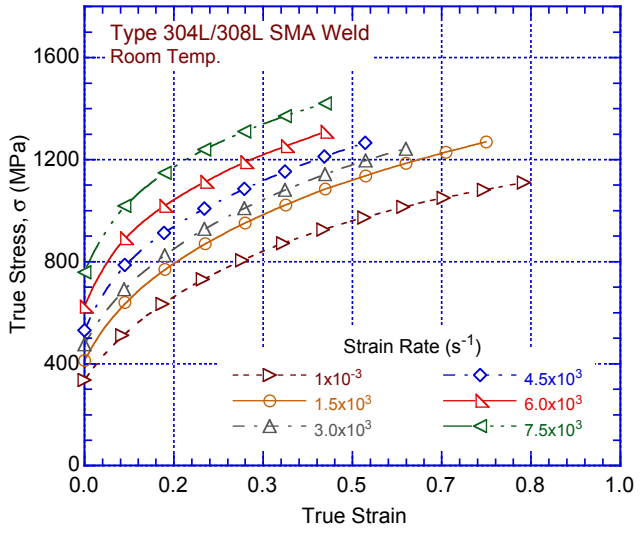

Figure 66.
True stress-true strain curves at room temperature for Type 304L/308L shielded-metal arc weld joints tested at several different strain rates (Ref. 205).

3.1.2.3 Cast Austenitic Stainless Steels (CASSs)

No literature data could be found on the effect of strain rate on the tensile properties of CF-3, CF-8, and CF-8M CASS materials.

3.1.2.4 Nickel Alloys

Alloy 600

Steichen and Ward[177] determined the tensile properties of annealed and thermally exposed Alloy 600 for test and exposure temperatures to 760°C (1400°F) and strain rates to 1.0 s^{-1}. The results indicate strength properties and ductility of annealed material are not greatly influenced by strain rate for temperatures to 538°C (1000°F). At the higher temperatures (649 and 760°C), strength properties substantially increase with strain rate. Ductility at these temperatures is controlled by fracture mode (transgranular versus intergranular) and dynamic recrystallization. Wu et al. performed compressive deformation tests on Alloy 600 at temperatures of 900 and 1150°C and strain rates ranging from 1 x 10^{-3} to 10 s^{-1}.[209] The observed flow stress varied significantly with strain rate, and the flow behavior was related to dynamic recrystallization and grain growth effects. Their results at 900C are shown in Fig. 67.

Thus, the data on the strain-rate effect on the flow stress of Alloy 600 indicate little effect of strain rate on the flow stress and ductility of Alloy 600 at temperatures up to 760°C and a strong effect on flow stress at higher temperatures.

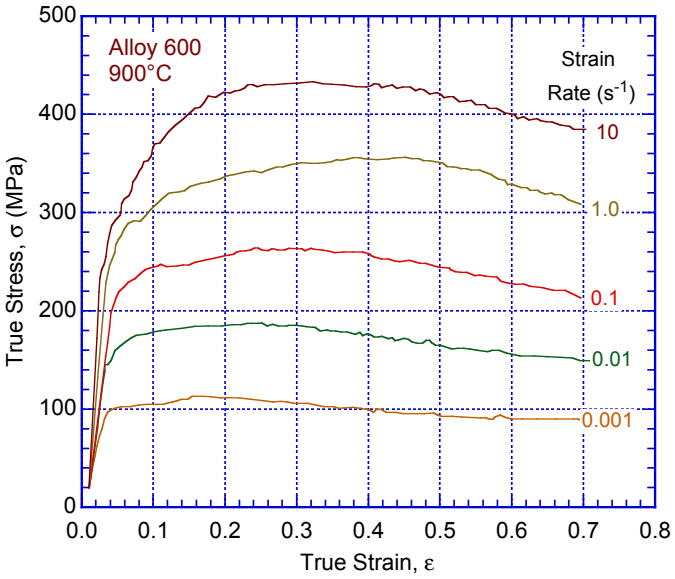

Figure 67.
Variation of true stress with true strain over a range of strain rates at 900°C for Alloy 600 (Ref. 209).

Alloy 690

Lee and Sun[210] and Lee et al.[211] have studied the plastic flow behavior of Alloy 690 at room temperature under compressive impact loading conditions. They observed that the compressive flow stress increased modestly with increasing strain rate in the range of 10^{-3} to 10^{-1} s^{-1} and a more dramatic increase at higher strain rates in the range of 2.3×10^3 to 8.3×10^3 s^{-1}. A summary of their findings is shown in Figs. 68 and 69. A sharp increase in the dependence of flow stress on strain rate is observed at strain rates greater than 10^{-3} s^{-1}. Lee et al. suggest that this increase is associated with a change in the rate-controlling mechanism from dislocation generation to mechanical twin formation.[211]

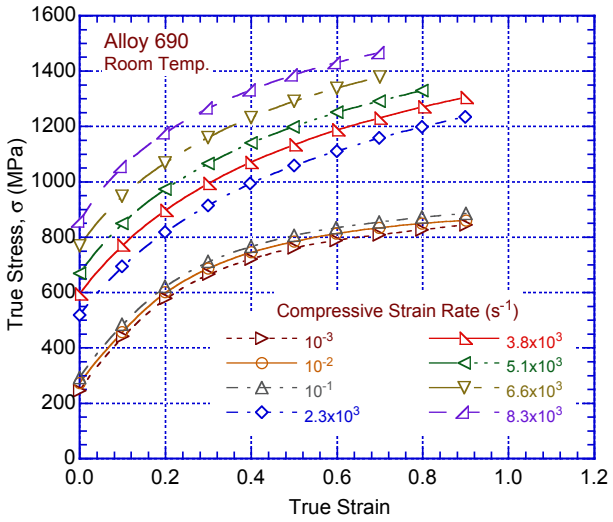

Figure 68.
Room-temperature true stress-true strain curves for Alloy 690 obtained at various strain rates under compressive loading (Ref. 210).

Hänninen et al.[212] (2005) studied dynamic strain aging and jerky flow phenomena in Alloys 600 and 690 by means of tensile tests at strain rates of 10^{-3} to 10^{-6} s^{-1} and at temperatures of 100 to 600°C. No remarkable difference in the DSA behavior of the two alloys was observed. The activation energies of DSA appearance were found to be 1.6 eV for both materials, which correspond closely to the activation energy of 1.76 eV for carbon, based on internal friction measurements.

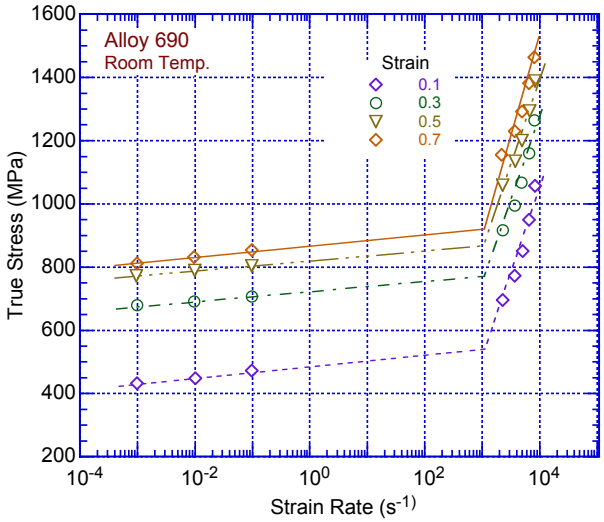

Figure 69.
Room-temperature dependence of flow stress at various strains on strain rate for Alloy 690 under compressive loading (Ref. 211).

Chen et al. investigated the high strain shear rate behavior of Alloy 690 alloy using the split Hopkinson torsional bar.[213,214] The shear strain rates were tested at 900, 1900, and 2600 s^{-1} and at temperatures of −100°C, 25°C, and 300°C, respectively. The dynamic shear behavior of Alloy 690 was found to be sensitive to strain rate and temperature. Both the flow stress and the fracture shear strain increased with increasing strain rate at a given temperature, and the fracture strain increased with increasing temperature at a given strain rate, while the flow stress decreased (Fig. 70). In addition, the strain rate sensitivity increased with increasing strain and strain rate but decreased with increasing temperature.

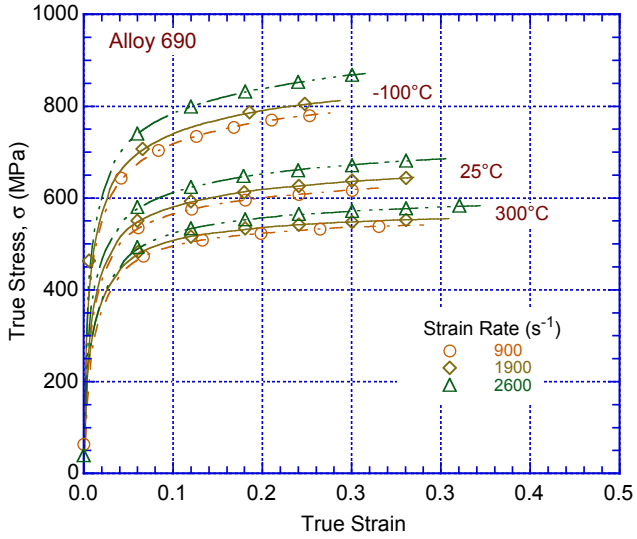

Figure 70.
Shear stress-strain curves of Alloy 690 deformed at different strain rates and temperatures (Refs. 213,214).

Guo et al. studied the deformation behavior of Alloy 690 at temperatures in the range of 950 to 1200°C and at strain rates from 0.001 to 10 s^{-1} by means of hot compression tests.[215] They observed a strong dependence of flow stress on strain rate, as shown in Fig. 71.

The tensile data for Alloy 690 therefore indicate an increase in flow stress with increasing strain rate over the entire temperature range from −100°C to 1200°C, though the magnitude of the effect appears to be temperature dependent.

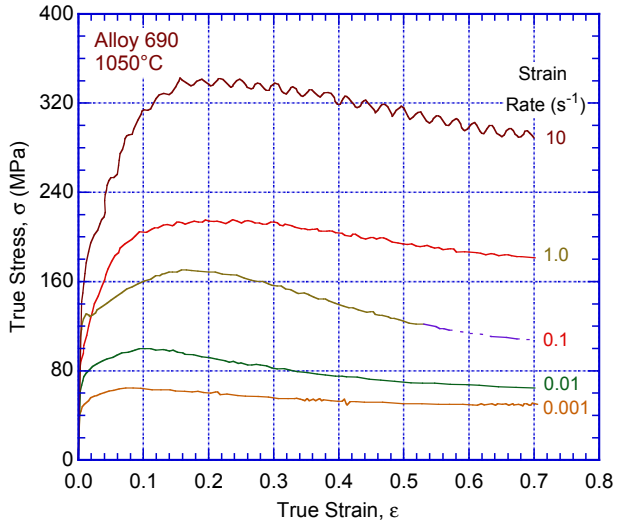

Figure 71.
True stress-true strain curves for Alloy 690 obtained from hot compression tests at 1050°C (Ref. 215).

3.1.3 Charpy Impact Properties

3.1.3.1 Carbon and Low-Alloy Steels

A508 Cl 3 and A533 Gr B Steels

The tensile data summarized above indicate that, for most of the structural alloys considered, the tensile ductility decreases with increasing strain rate. This behavior raises questions about the possibility of non-ductile behavior of these alloys under the moderately high strain rate loading conditions associated with seismic events. Perhaps the simplest measure of the ductility response of a material under high-loading-rate conditions is provided by Charpy impact test data. Ferritic alloys such as the A508 Cl 3 and A533 Gr B structural steels used in nuclear pressure vessel applications undergo a transition from ductile to brittle behavior under impact loading as the temperature is decreased. The associated ductile-to-brittle transition temperature (DBTT) is generally defined as the temperature at which the fracture energy under impact loading falls below 40 J (29.5 ft-lb) for a standard Charpy impact test. The brittle behavior of such materials at temperatures below the DBTT is clearly undesirable for nuclear applications, particularly under seismic loading conditions.

Tanguy et al. conducted a series of Charpy V-notch impact tests on A508 Cl 3 steel at impact velocities of 5 m/s, 500 μm/s, and 1 μm/s.[167] The results shown in Fig. 72 indicate that the greatest effect of impact velocity is on the upper shelf energy, which increases from ~155 J at a velocity of 1 μm/s to 220 J at 5 m/s. The effect of impact velocity on the DBTT is less clear, with the 40 J DBTT values ranging from approximately −100°C to −75°C (−150°F to −100°F) over this range of velocities. DBTT values in this range are well below anticipated temperatures for an operating or shutdown nuclear power plant. Bouchet et al published fracture toughness transition curves for both unirradiated and irradiated A508 Cl 3 steel (Fig. 73).[216] Their curves indicate a DBTT of approximately −40°C (−40°F) for the unirradiated material and 0°C (32°F) for the material irradiated to a fluence of 4.65×10^{19} n/cm^2 (>1 MeV). In addition, the upper shelf energy for the unirradiated material is noticeably higher.

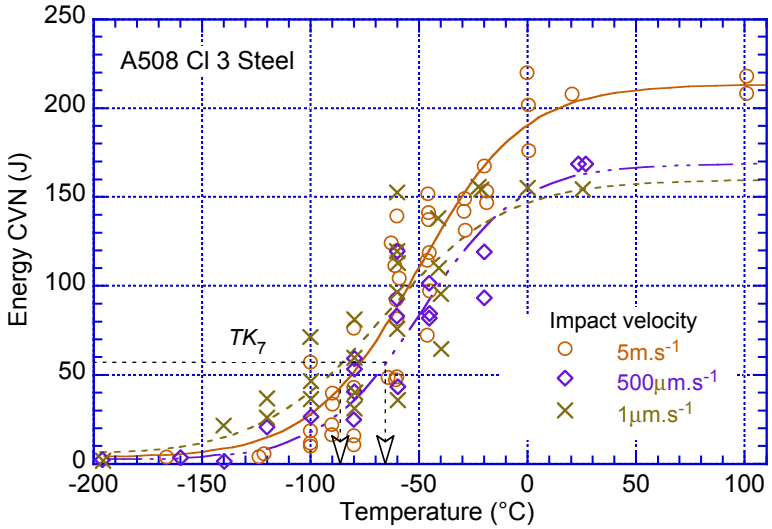

Figure 72. Charpy V-notch fracture toughness transition curves for A508 Cl 3 steel specimens tested at three different impact velocities (Ref. 167).

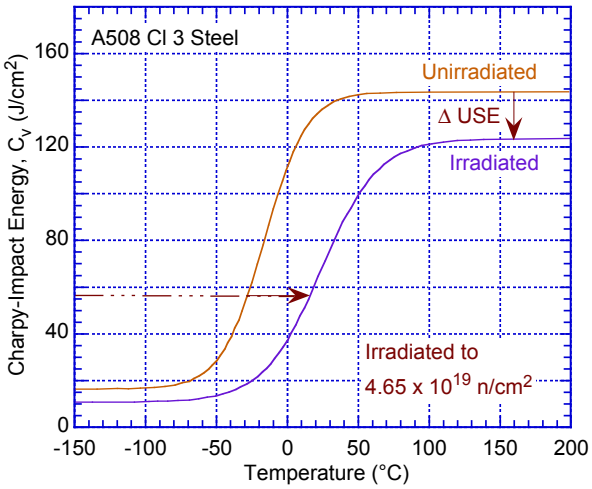

Figure 73. Charpy V-notch fracture toughness transition curves for A508 Cl 3 steel specimens in the unirradiated condition and after irradiation to a fluence of 4.65 × 10^{19} n/cm^2 (>1 MeV) (Ref. 216).

Hawthorne conducted both Charpy V-notch and dynamic tear tests on 12-in. thick plates of A533 Gr B steel before and after neutron irradiation.[217] Figure 74 shows the results of tests conducted on as-received material and material irradiated to a fluence of 2.8 × 10^{19} n/cm^2 (>1 MeV) at a temperature of 288°C (550°F). The DBTT for the unirradiated material is approximately −7°C (20°F), which places it below the range of concern for a NPP. However, the irradiated material exhibits a DBTT of approximately 104°C (220°F), which raises concerns about the susceptibility of this material to brittle fracture in a nuclear plant under cold standby or shutdown conditions. A qualitatively similar behavior is observed for weld-deposited material (Fig. 75); the DBTT increases from approximately −41°C (−42°F) for the unirradiated material to 110°C (230°F) for the material irradiated to a fluence of 2.5 × 10^{19} n/cm^2.

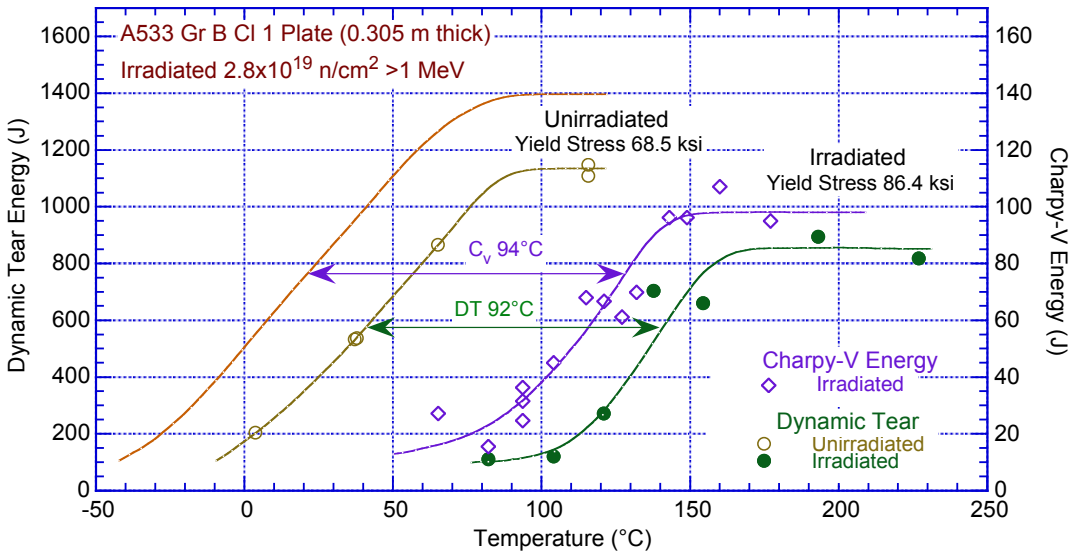

Figure 74. Charpy-V (Cv) and dynamic tear test data for a 12-in.-thick A533 Gr B Class 1 steel plate before and after 550°F (288°C) irradiation. All specimens were taken from the quarter thickness location and represent the transverse orientation (Ref. 217).

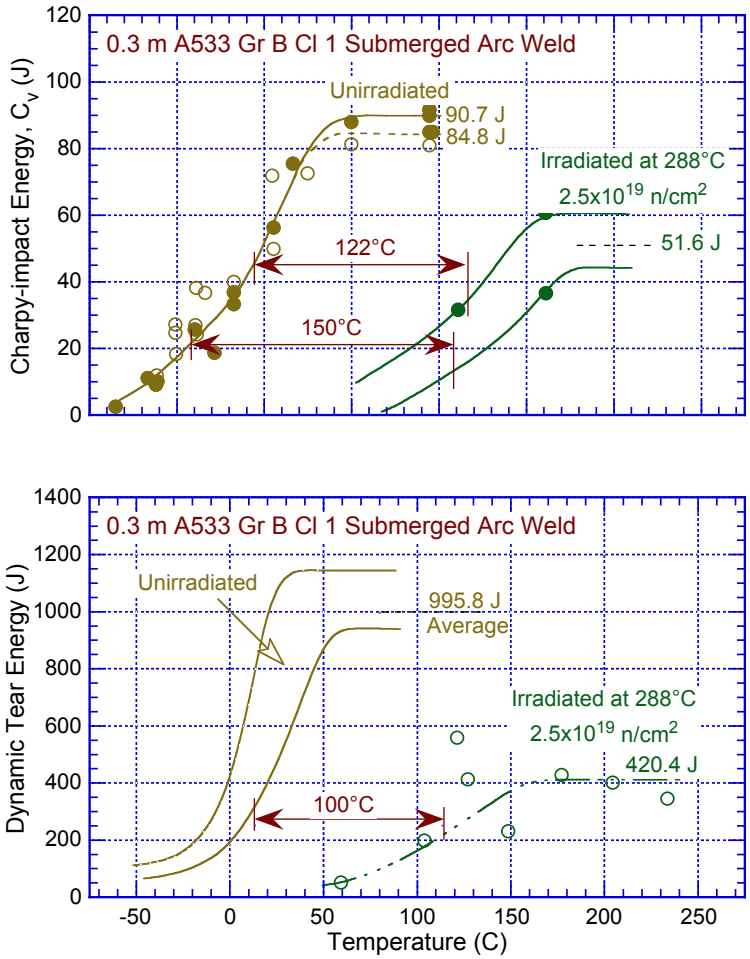

Figure 75.
Charpy-V (Cv) and dynamic tear test data for a 0.3 m-thick A533 Gr B Cl 1 SA weld deposit before and after 550°F (288°C) irradiation. Specimens were taken between the quarter- and half-thickness locations with their long dimension perpendicular to the welding direction. (Ref. 217).

Schubert et al. reported even higher DBTT values for A533 Gr B steel specimens irradiated at 150°C to a fluence of 1.0 × 10^{19} n/cm^2 (E >1 MeV).[218] They reported that this exposure increased the DBTT from 88°C (unirradiated) to 166°C (irradiated) for full-size specimens, from 120°C to 203°C for half-size specimens, and from 100°C to 170°C for one-third-size specimens.

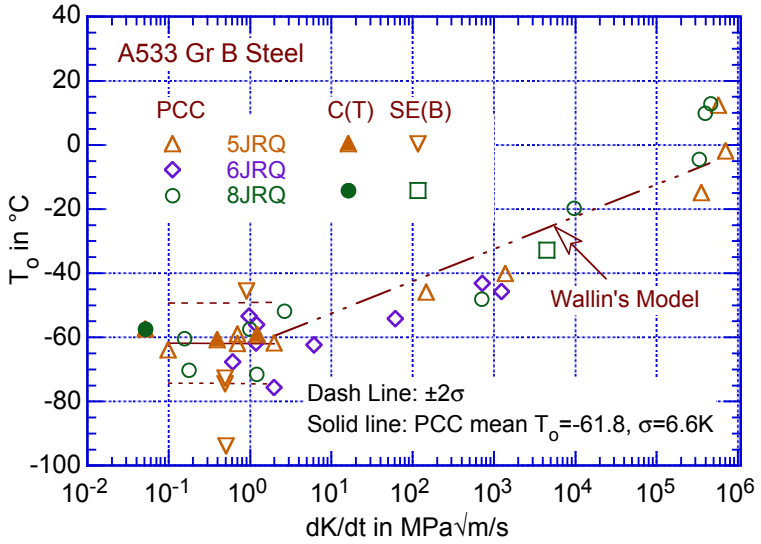

Figure 76.
Effect of loading rate on the DBTT of A533 Gr B steel (Ref. 219).

The International Atomic Energy Agency (IAEA) has coordinated an international program on the fracture toughness testing of nuclear pressure vessel steels.[219] The effect of loading rate on the DBTT was investigated for several steels, including A533 Gr B, as shown in Fig. 76. The data are for precracked Charpy specimens of various sizes, from Heat JRQ tested over a wide range of loading rates. The dashed curve shown in the figure represents the Wallin model.[220] A steady increase in transition temperature with increasing loading rate is clearly indicated.

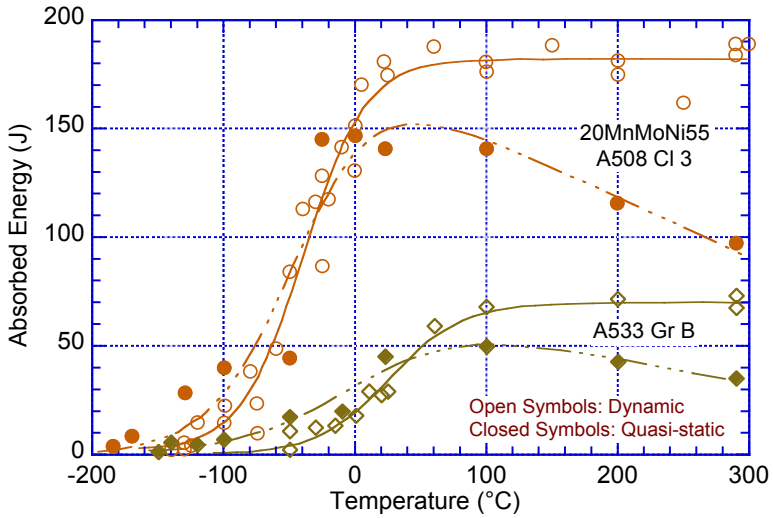

Figure 77. Effect of loading rate on the ductile-to-brittle Charpy transition curve for A508 Cl 3 (20MnMoNi55) and A533 Gr B (JSPS) pressure vessel steels (Ref. 176).

For all these results, it is noted that the strain rate imposed in a standard Charpy V-notch test is considerably higher than that anticipated for seismic loadings. However, Chaouadi and Puzzolante have showed that effect of loading rate on the DBTT in the case of A508 Cl 3 and

A533 Gr B pressure vessel steels is not great.[176] Fig. 77 shows the temperature dependence of absorbed energy in Charpy impact tests on these two steels conducted under dynamic and quasi-static loading conditions. As stated previously, the designation 20MnMoNi55 is the German specification for steel similar to A508 Cl 3 pressure vessel steel, and the JSPS material is a special heat of A533 Gr B steel provided by the JSPS Committee 129 for a series of round-robin tests on its ductile-to-brittle transition behavior. As shown in the figure, the difference between the dynamic and quasi-static DBTT for these two steels is relatively modest.

3.1.3.2 Austenitic Stainless Steels and Nickel Alloys

In general, a well-defined ductile-to-brittle transition is not observed for the austenitic SSs or nickel-base alloys. However, such behavior may be seen in duplex SSs and weldments or in material that has been subject to neutron irradiation. Figure 78 shows the ductile-to-brittle transition behavior of Type 308 SS filler metal in a specimen taken from a 12-in. Type 304 SS Schedule 100 pipe weldment.[221] The material was tested in the as-received condition and after aging for 7,700 or 10,000 h at 400°C. It is reasonable to assume that the DBTT for these materials is subject to the same loading rate effects as described above for the ferritic pressure vessel steels.

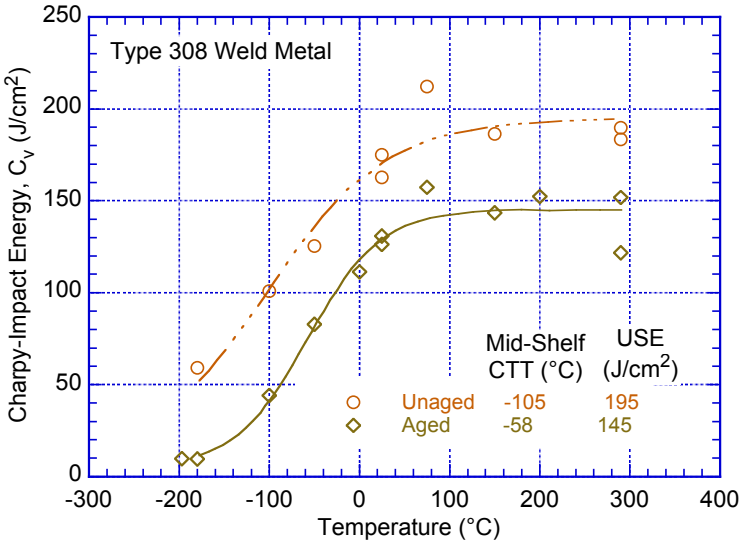

Figure 78.
Effect of thermal aging on the ductile-to-brittle transition temperature for Type 308 SS weld filler metal in the unaged condition and after aging for 7,700 h at 400°C (Ref. 221).

In summary, the Charpy impact data for A508 Cl 3 and A533 Gr B pressure vessel steels indicate either little effect or an increase in the DBTT with increasing loading rate. An increased loading rate also appears to increase the upper shelf energy somewhat for both steels. Neutron irradiation clearly increases the DBTT, and Type 308 SS weld filler metal appears to be increasingly susceptible to brittle fracture with elevated-temperature aging.

3.1.4 Fracture Toughness Properties

The fracture toughness of a material, as expressed by the critical stress intensity factor K_c (or, more specifically, K_{Ic} for mode I loading) provides a more quantitative means of measuring its resistance to brittle fracture than the DBTT. For ductile materials, the J-integral value, which is related to the energy release rate during crack extension, can instead be determined at the onset of stable crack extension to obtain the parameter J_{Ic} (or K_J) as a measure of the material's resistance to ductile crack initiation ("crack initiation toughness"). Another parameter that is commonly measured for ductile materials is the "ductile crack growth resistance," which is the J

value during stable crack growth and is commonly reported as a function of crack extension "a," in what is often referred to as the fracture toughness or J–R (J-integral/crack resistance) curve. Sometimes the slope of the J–R curve dJ/da is also reported as a function of crack extension.

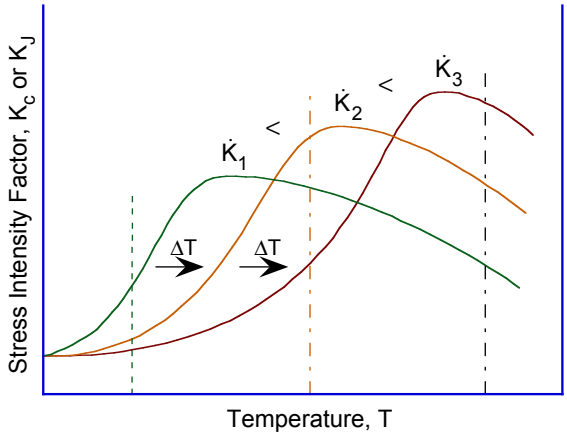

Figure 79.
General effect of loading rate on fracture toughness of most structural alloys (Ref. 222).

Fracture toughness is dependent on loading rate for many materials, including most structural alloys and increases with increasing loading rate, as illustrated in Fig. 79. Here, the linear elastic critical stress intensity factor for fracture, K_c, or alternatively, the J-integral critical stress intensity factor K_J, is schematically plotted as a function of temperature for three loading rates. For brittle behavior at temperature T_1, increasing the loading rate leads to a reduction in fracture toughness for most steels. For ductile behavior at temperature T_3, the initiation toughness increases for most steels with increasing loading rate. In the transition region at temperature T_2, increasing loading rate can lead to an increase in toughness if ductile behavior prevails, but a loading-rate-induced change in fracture mode is possible, leading to marked reduction of toughness at a given temperature.[222]

3.1.4.1 Carbon and Low-Alloy Steels

A508 Cl 3 and A533 Gr B Steels

Iwadate et al. conducted studies on the fracture toughness of A508 Cl 3 pressure vessel steel in the transition region using 25.4-mm- (1-in.-) thick compact tension (1T-CT) specimens.[223] They found that, as the strain or loading rate is increased, the fracture toughness-versus-temperature curves (and the DBTT) shift to higher temperatures, as shown in Fig. 80. They concluded that this behavior results from an elevation of the flow stress with increasing strain rate. It is also apparent from the figure that the data exhibit a considerable degree of scatter, and the scatter tends to increase with increasing temperature.

Kim and Kang[165] determined the crack initiation toughness (J_{Ic}) and crack growth resistance (dJ/da) of A508 Cl 3 steel at temperatures of 25–380°C and loading displacement rates 0.08, 0.5, and 3.0 mm/min. They found that, at room temperature and 380°C, J_{Ic} increased with increasing strain rate, but at intermediate temperatures the lowest loading rate resulted in the highest value of J_{Ic} (Fig. 81). The variance of dJ/da with temperature and loading displacement rate was mixed with no clear overall pattern (Fig. 82). They observed that both J_{Ic} and dJ/da decreased by about 30–40% at reactor operating temperatures. These behaviors were attributed to a DSA effect. At high loading rates, the minimum fracture toughness region shifted to higher temperatures.

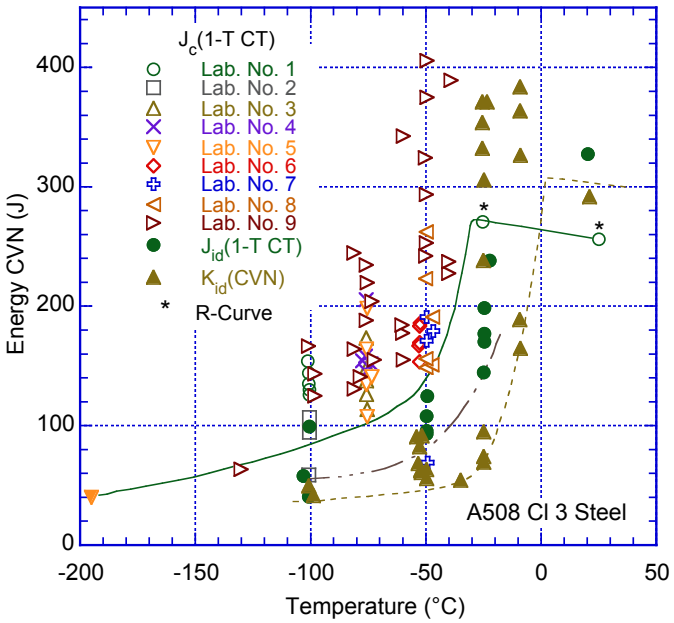

Figure 80. Fracture toughness versus temperature behavior for A508 Cl 3 steel. The three curves, from left to right, represent fits to data generated at strain rates of 1.6 MPa.m$^{1/2}$/s [static 1T-CT tests), 1.4 x 10^4 MPa.m$^{1/2}$/s (dynamic 1T-CT tests), and 6.5 x 10^5 MPa.m$^{1/2}$/s (instrumented Charpy tests), respectively (Ref. 223).

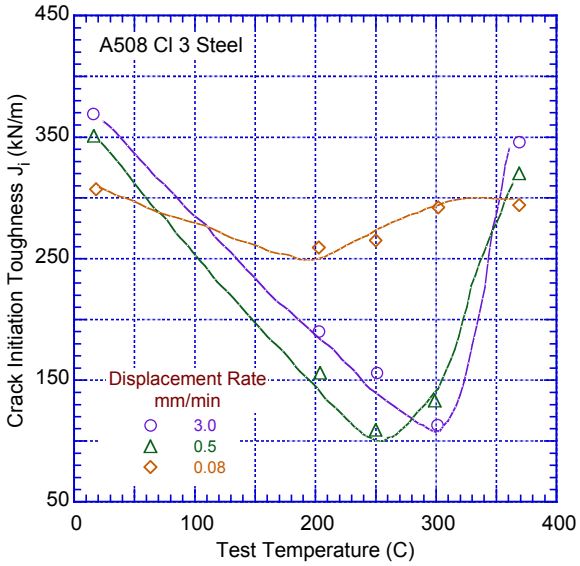

Figure 81.
Dependence of crack initiation toughness J_{Ic} on loading displacement rate and temperature for A508 Cl 3 pressure vessel steel (Ref. 165).

Chaoudi and Puzzolante[176] obtained crack resistance data at 25, 100, and 290°C using standard Charpy specimens for both the German 20MnMoNi55 steel (A508 Cl 3 pressure vessel steel) and the JSPS heat of A533 Gr B steel. The quasi-statically loaded specimens were subjected to three-point bend test at 0.1 mm/min, and the dynamic tests were conducted by using a standard Charpy impact machine with an impact velocity of 1.7 m/s. These loading rates correspond to approximately 1 and 105 kJm^{-2}s^{-1}, respectively. The resulting J versus crack extension, or J–R, curves shown in Figs. 83 and 84 clearly indicate that the crack resistance for both materials is significantly higher under dynamic loading conditions at both temperatures.

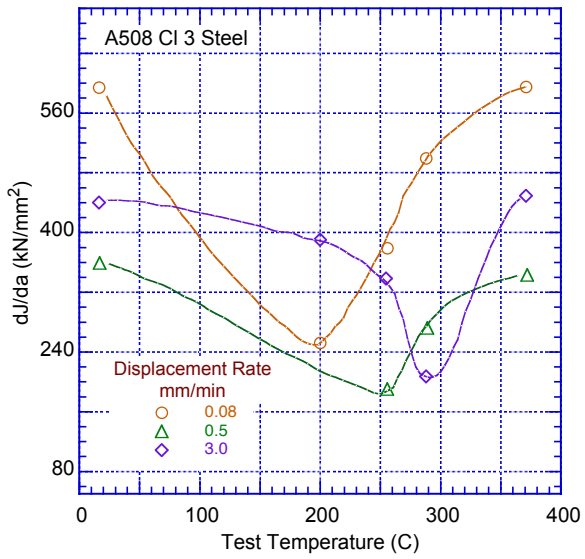

Figure 82.
Dependence of crack growth resistance dJ/da on loading displacement rate and temperature for A508 Cl 3 pressure vessel steel (Ref. 165).

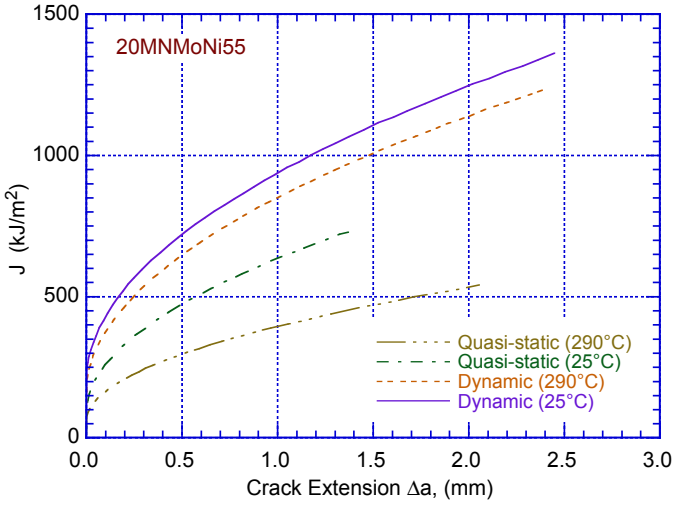

Figure 83.
Crack resistance behavior for the German 20MnMoNi55 steel at 25 and 290°C under both quasi-static and dynamic loading conditions (Ref. 176).

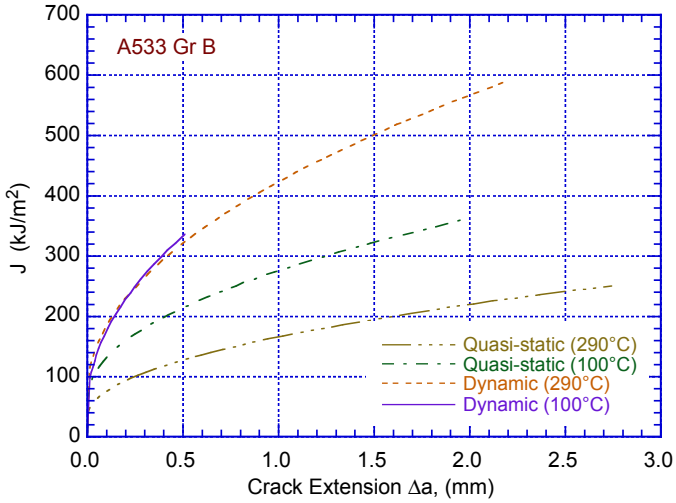

Figure 84.
Crack resistance behavior for the JSPS special heat of A533 Gr B steel at 25 and 290°C under both quasi-static and dynamic loading conditions (Ref. 176).

Mager[224] reproduced the data of Shabbits et al.[225] and Shabbits[226] on the fracture toughness of A533 Gr B steel (Fig. 85). Shabbits conducted fracture toughness tests under both static conditions and at a loading rate dK/dt of approximately 104 ksi·in$^{1/2}$. As shown in the figure, the dynamic fracture toughness values K_{Id} clearly fall at higher temperatures than the values determined under static conditions. The fracture toughness data of Landes[227] for A533 Gr. B steel, as adapted by Armstrong and Walley,[228] show a similar variation of static loading K_{IC}, dynamic loading K_{ID}, and crack arrest K_{IA} values at temperatures of 325K and below (Fig. 86). Again, the increased loading rate associated with dynamic loading results in a decrease in fracture toughness at a given temperature.

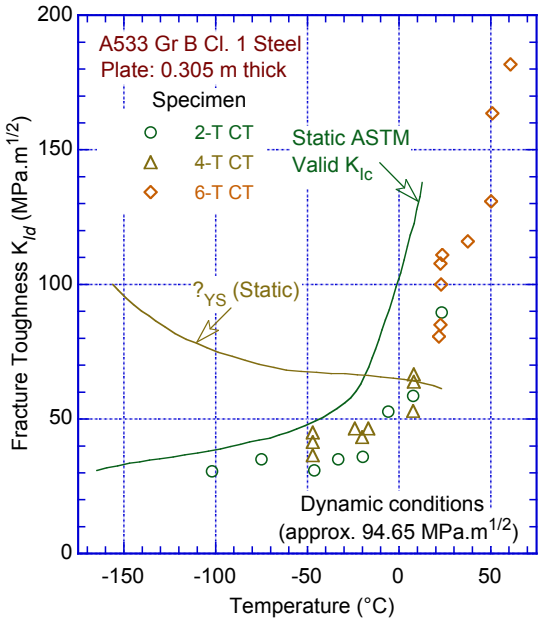

Figure 85.
Fracture toughness versus temperature behavior for A533 Gr B steel under both static (solid line) and dynamic (dK/dt of approx. 104 ksi·in$^{1/2}$) conditions (data points) (Ref. 225, 226 as reproduced in 224).

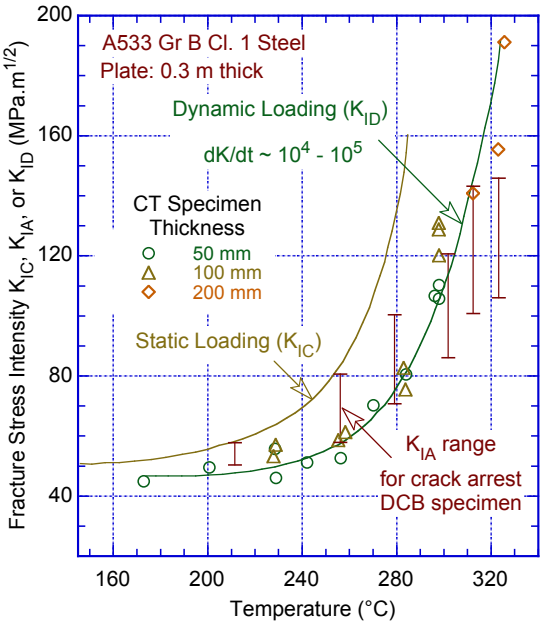

Figure 86.
Temperature dependence of static K_{IC}, dynamic K_{ID}, and crack arrest K_{IA} fracture toughness measurements for A533 Gr B steel (Ref. 227 as adapted by 228).

At higher temperatures, however, the dependence of strain rate on crack initiation fracture toughness appears to be mixed. Figure 87 shows the data of Jung and Murty[229] for A533 Gr B

steel on the dependence of crack initiation fracture toughness on temperature for three different strain rates. The variable behavior with strain rate is qualitatively similar to that for A508 Cl 3 steel as seen by Kim and Kang[165] and shown in Fig. 81.

The J-R ductile crack resistance curves of Koppenhoefer and Dodds for A533 Gr B steel are shown in Fig. 88.[230] The data plotted are from two different investigators and two different heats of material, both show a strong dependence of ductile crack resistance on loading rate.

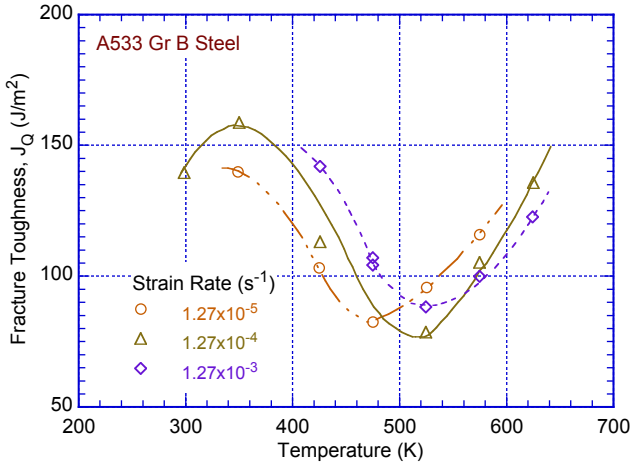

Figure 87.
Effect of temperature and strain rate on the crack initiation fracture toughness (here designated J_q) of A533 Gr B pressure vessel steel (Ref. 229).

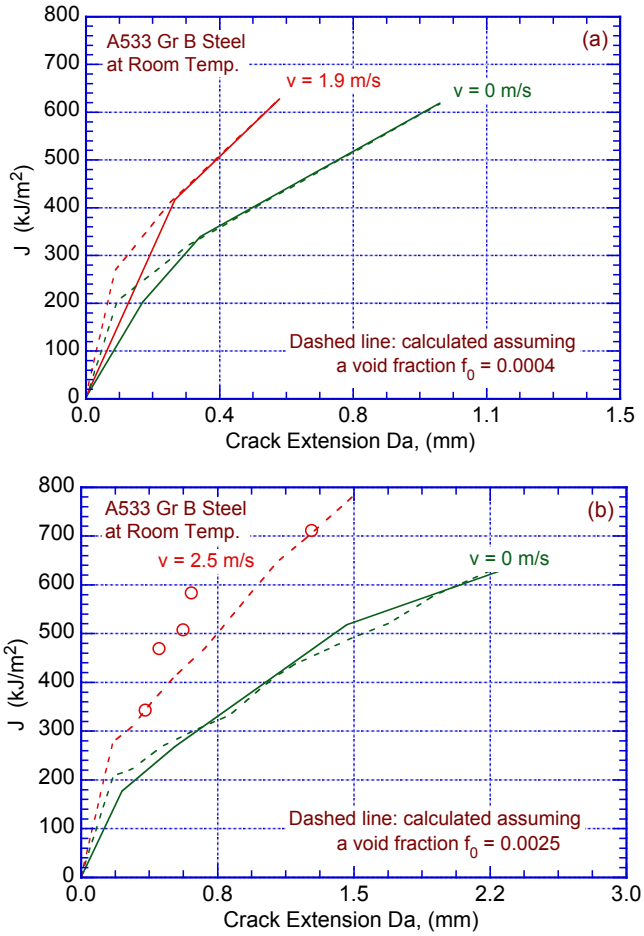

Figure 88.
Crack resistance behavior for two different heats of A533 Gr B pressure vessel steel at room temperature under both quasi-static and dynamic loading conditions. (a) shows the data of Wallin et al. (Ref. 231), and (b) shows the data of Joyce (Ref. 232). The dashed curves are calculated assuming a given void volume fraction f_o in the material that leads to ductile fracture (Ref. 230).

In general, the fracture toughness behaviors of A508 Cl 3 and A533 Gr B steels follow the behavior shown schematically in Fig. 79. However, a decrease in J_{Ic} with increasing strain rate has been observed by some researchers in the temperature range of interest for LWR applications (Figs. 81 and 86). The J-R curves generally show an increase in cracking resistance with increasing loading rate.

3.1.4.2 Types 304 and 316 Stainless Steels and their Weldments

Neutron irradiation can significantly decrease the fracture toughness of austenitic stainless steel and their weldments, and failure can occur without general yielding. Chopra[53] reviewed the literature on this effect over a range of experimental conditions, and Fig. 89 from his report shows a compilation of data on the effect of neutron irradiation under LWR conditions on the fracture toughness J_{Ic} of several wrought austenitic stainless steels as well as CF-8M cast duplex stainless steel. The tests were conducted in both air and boiling water reactor (BWR) coolant at temperature of 250–320°C. A similar effect is seen in the J–R curves for these alloys, as shown in Fig. 90 taken from Chopra's report.

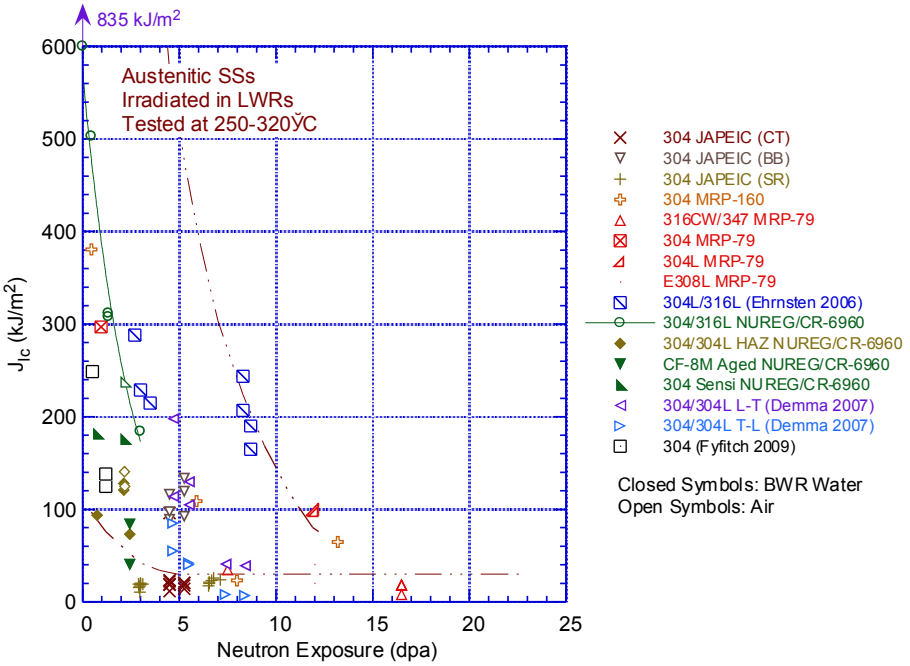

Figure 89. Change in fracture toughness, J_{Ic}, as as a function of neutron exposure for irradiated austenitic SSs. Dashed lines represent the scatter band for the fast reactor data on austenitic SSs irradiated at 350–450°C (662–843°F) (Ref. 39,42–44,47-52).

In a manner similar to that for the ferritic steels discussed above, loading rate also affects the fracture toughness of the austenitic SSs. Marschall et al. report the results of fracture toughness tests conducted on A376, Type 304 SS Schedule 120 pipe with 152 mm (6 in.) diameter.[233] Tests were conducted at 288°C under both quasi-static loading conditions and dynamic loading conditions at loading rates comparable to those associated with high-amplitude seismic events. The results shown in Fig. 91 again indicate an increase in fracture toughness associated with the higher loading rate. Similar tests were conducted on a SA girth weld specimen from an A358, Type 304 SS 406-mm (16-in.) diameter, Schedule 100 pipe with ER-

308 filler metal. As shown in Fig. 92, the higher loading rate results in an increase in fracture toughness, though the J values are appreciably lower than for the Type 304 SS base metal shown in Fig. 91.

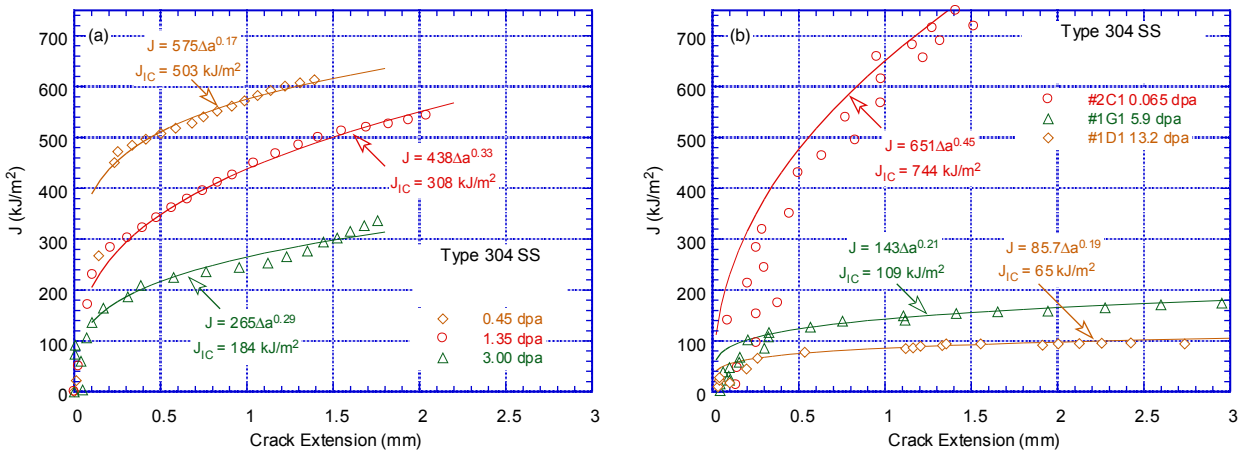

Figure 90. Change in fracture toughness, J_{IC}, as as a function of neutron exposure for SSs (Refs. 52,53).

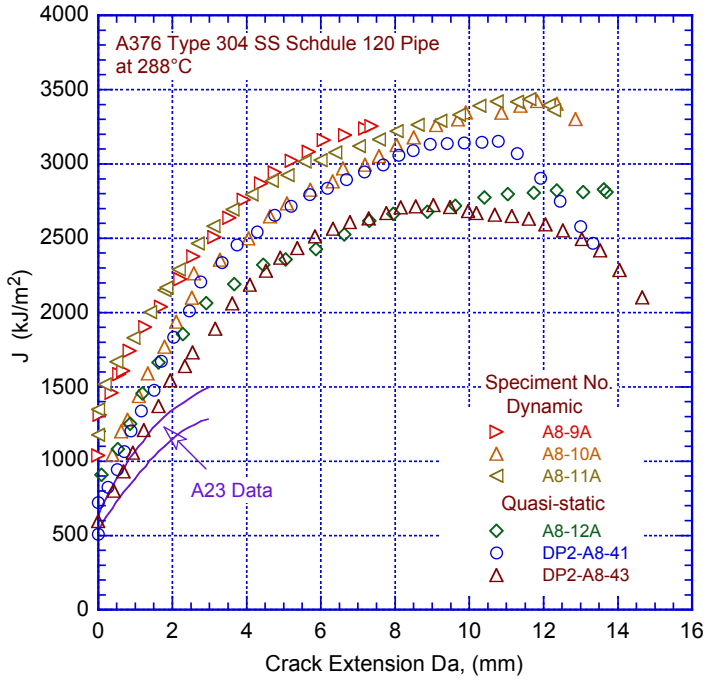

Figure 91.
Crack resistance behavior for A376, Type 304 SS Schedule 120 piping material at 288°C under both quasi-static and dynamic loading conditions (Ref. 233).

Nakajima et al. have investigated the effects of simulated BWR primary coolant on the fracture toughness of sensitized Type 304 SS at 98 and 288°C.[234] Their tests were conducted in water containing 0.2 and 8 ppm dissolved oxygen at displacement rates of 0.5, 0.01, and 0.001 mm/min. As shown in Fig. 93, the fracture toughness J increases with increasing displacement rate and with decreasing dissolved oxygen.

In a review of the fracture toughness behaviors of Types 304 and 316 SSs and their weldments, Mills compiled data from several investigators on the effect strain rate on fracture toughness

properties.[41] The result is shown in Fig. 94, in which the J_{Ic} and dJ/da values are summarized for these materials under static, semidynamic, and dynamic loading conditions. The semidynamic displacement rates correspond to ~600 mm/min, or crack initiation times of <0.5 s. In no case does increasing the loading rate exert a detrimental effect on fracture toughness properties, and in most instances the effect is slightly or even significantly (for one heat of Type 304 SS at 288°C) beneficial.

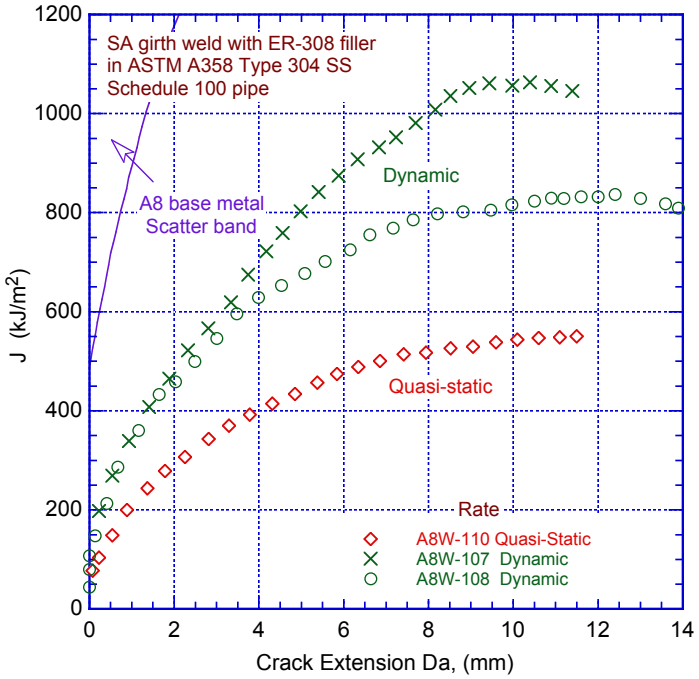

Figure 92.
Crack resistance behavior for an SA girth weld specimen from an A358, Type 304 SS 406-mm (16-in.) diameter, Schedule 100 pipe with ER-308 filler metal (Ref. 233).

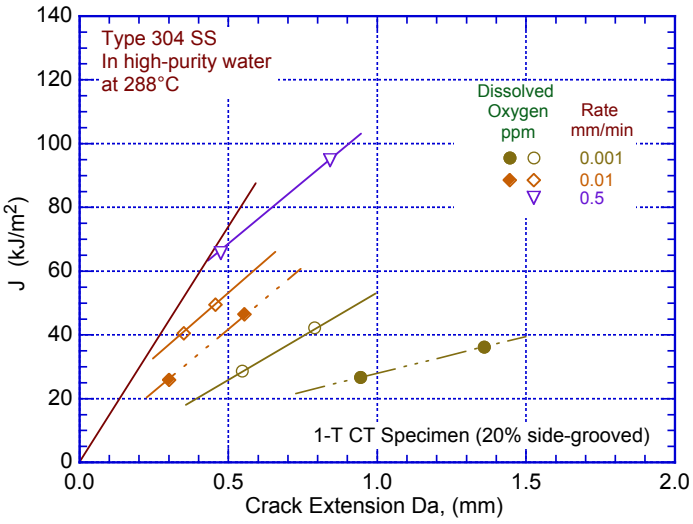

Figure 93.
Crack resistance behavior of sensitized Type 304 SS at 288°C in simulated BWR coolant with two dissolved oxygen levels at three different displacement rates (Ref. 234).

In summary, the fracture toughness data for Types 304 and 316 SSs generally indicate a beneficial effect of increasing loading rate on the crack resistance behavior of Types 304 and 316 SSs. However, the variability in the data indicates that the loading conditions of interest must be well-defined before these results can be reliably applied to a specific loading situation.

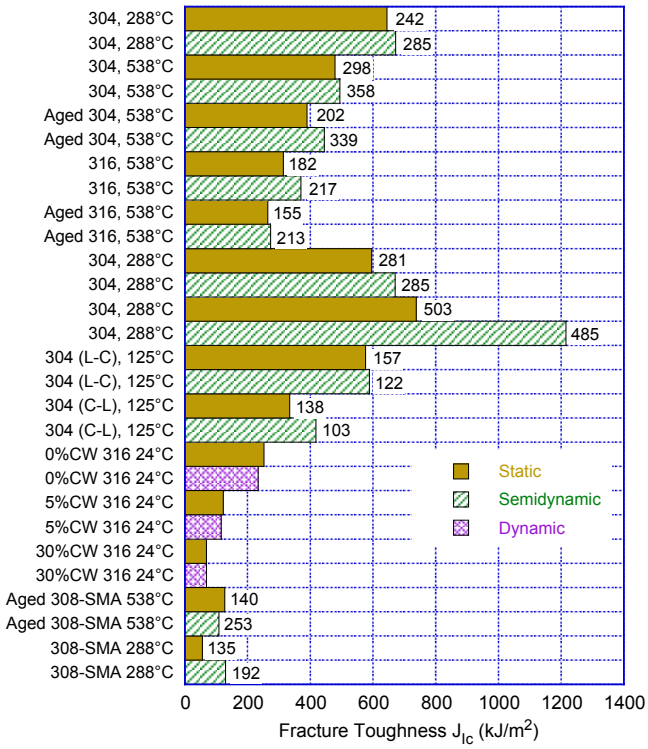

Figure 94.
Effect of strain rate on J_{Ic} and dJ/da (values of the latter parameter are given next to each bar in MPa) for Types 304 and 316 SSs and Type 308 SS weld metal under various conditions (Ref. 41).

3.1.4.3 Cast Austenitic Stainless Steels

The limited data in the literature on the effect of loading rate on the fracture toughness properties of CASS materials are somewhat inconsistent. Based on a comparison of the energy values measured with Charpy impact toughness tests and slow loading three-point bending tests, Devillers-Guerville et al.[235] concluded that the influence of loading rate on these parameters for CF-8M CASS materials is negligible. They attribute this to the large amount of austenitic phase, the fracture behavior of which they state to be insensitive to strain rate.

McConnell et al.[236] conducted fracture toughness tests on a high ferrite CF-3 material in the as-cast and aged conditions at three loading rates at room temperature and 300°C. The slowest loading rate was a quasi-static rate typical of J-integral testing. The second rate was approximately three orders of magnitude faster, and the highest rate was about one additional order of magnitude faster. For the as-cast material, they observed no significant variation in fracture toughness behavior with increasing strain rate either at room temperature or 300°C. However, for the room-temperature tests on aged material, increasing the loading rate resulted in an increase in J_c and a decrease in the slope, dJ/da, of the J–R curve.

Anzai et al.[237] likewise conducted fracture toughness tests on CF-3M material containing about 16% ferrite. The specimens were first aged for 1000h at 500°C to produce embrittlement and then tested at 0°C. They found that increasing the loading rate reduced the J value for crack initiation (J_c) and the slope of the J–R curve to about 18% of their values for quasi-static loading conditions (Fig. 95). Thus, they agree with McConnell et al.[236] that the slope of the J–R curve is decreased at faster loading rates, but the disagree about the effect on J_c values.

However, there is little or no data related to loading rate effects on the fracture toughness of CASS materials or austenitic SS welds, thermally aged for extended periods at temperatures between 300 and 370°C. The possible decrease in fracture toughness of such materials under

dynamic loading conditions at temperatures between room temperature and 100°C needs to be evaluated in the next phase of this program **(Information Gap 4)**.

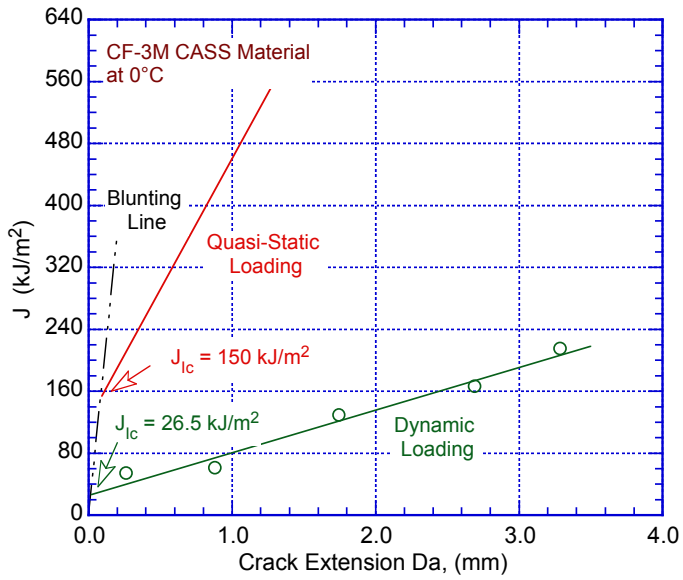

Figure 95.
Effect of loading rate on the J-R curve at 0°C for thermally aged CF-3M CASS materials (Ref. 237).

A recent study on low-temperature crack propagation for CASS CF-8 (Argonne Heat 68) material in PWR environments investigated the potential synergy between thermal and hydrogen embrittlement associated with decomposition of the ferrite at reactor temperatures.[238] The material was aged for 138,000 h (15.8 yr) at 350°C; measured ferrite content was 23%. Fracture toughness tests were conducted on 1-T CT specimens in air and PWR shutdown water chemistry (SWC) at 54°C. The results are shown in Fig. 40.[239] The specimens were either fatigue precracked in air at 54°C or fatigue-plus-SCC precracked in PWR water at 315°C. Note that one specimen that was precracked in PWR water at 315°C was inadvertently tested at elevated temperature of 315°C in PWR primary water chemistry. The updated lower-bound J–R curve developed at Argonne for CF-8 material containing 15–25% ferrite and tested at room temperature is also shown in the figure for comparison.[239]

The results indicate that at 54°C, the J-R curve data in air are bounded, with additional margin, by the updated lower-bound J-R curve. However, the J-R curve data for specimens precracked in air at 54°C and then tested in PWR (SWC) at 54°C are significantly below the lower-bound curve. These results show an apparent large effect of the coolant environment on fracture toughness. All material and test conditions are identical for the two sets of duplicate tests except that one was tested in air and the other in water. The specimens that were precracked in PWR water at 315°C and then tested in PWR water at 54°C or 315°C also show reduced fracture toughness relative to that in air, but the difference is less. The J–R curve data for the specimen that was cooled down to from 315°C and then tested at 54°C SWC are only marginally below the lower-bound J–R curve, and the data for the specimen that was precracked and tested at 315°C PWR primary water chemistry are slightly above the lower-bound curve.

The reason for the drastic reduction in fracture toughness in PWR SWC at 54°C relative to that in air at 54°C is not clear. Additional fracture toughness tests on thermally aged CASS CF-3 and CF-8 materials in air and LWR environments should be conducted to better understand the combined effects of hydrogen embrittlement and thermal embrittlement in LWR environments.

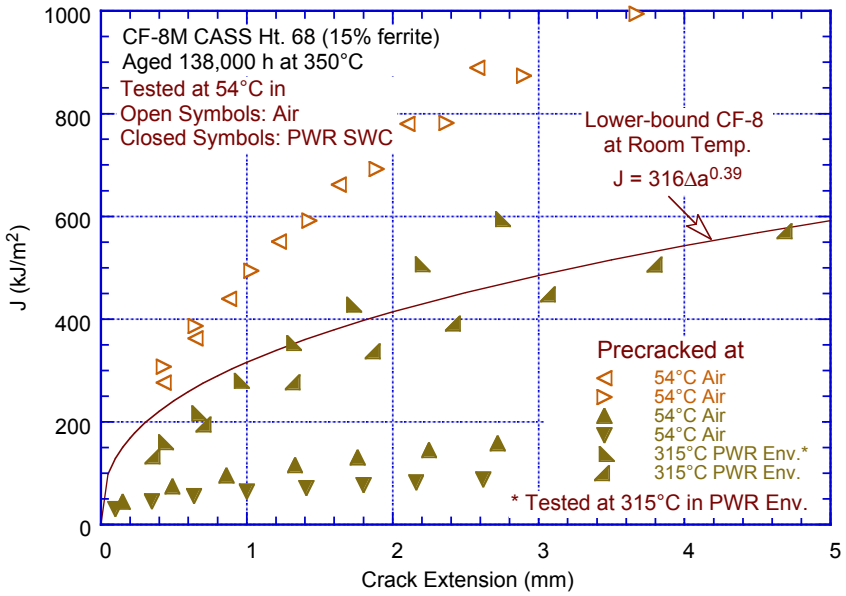

Figure 96. Fracture toughness J-R curve data for thermally aged Heat 68 of CF-8M plate at 54°C. The curve represent the lower bound curve at room temperature for static-cast CF-8 material (Ref. 239).

3.1.4.4 Nickel Alloys

Alloys 600 and 690

Mills and Brown determined the ductile J-R crack resistance behavior of Alloy 600 and its EN82H weld at 54°C to 338°C in air and hydrogenated water.[240] The material exhibited excellent fracture toughness under all test conditions, and the EN82H welds similarly displayed excellent toughness in both environments at the higher temperatures, but a dramatic degradation in toughness occurred in water at temperatures below 149°C, an effect attributed to hydrogen-induced intergranular cracking. Figure 97 shows the J–R curves for Alloy 600 for both environments. All results except for the dashed curve were obtained under quasi-static loading conditions (displacement rate = 0.05 mm/h). The data represented by the dashed curve were obtained at a faster loading rate of 300 mm/h, and an increase in fracture toughness with increased loading rate is apparent.

Brown and Mills conducted a similar set of experiments to determine the ductile J-R crack resistance behavior of Alloy 690 and its EN52 weld in air and hydrogenated water at 24 to 338°C.[241] Once again, both alloys exhibited excellent fracture toughness in air and in water at temperatures greater than 93°C. However, both materials experienced a dramatic loss of toughness in 54°C water, an effect again apparently associated with hydrogen-induced intergranular cracking. The effect of loading rate was investigated for Alloy 690 in a 54°C water environment, with displacement rates ranging from 0.005 to 305 mm/h. The results are shown in Fig. 98. The data for displacement rates in the range of 0.005 to 15 mm/h fall roughly on the same curve. However, increasing the displacement rate further to 305 mm/h produces a dramatic increase in the fracture toughness, and the J–R curve falls very near the curve for 149°C water. A similar, though somewhat less dramatic, effect of displacement rate for the EN52 welds was also observed.

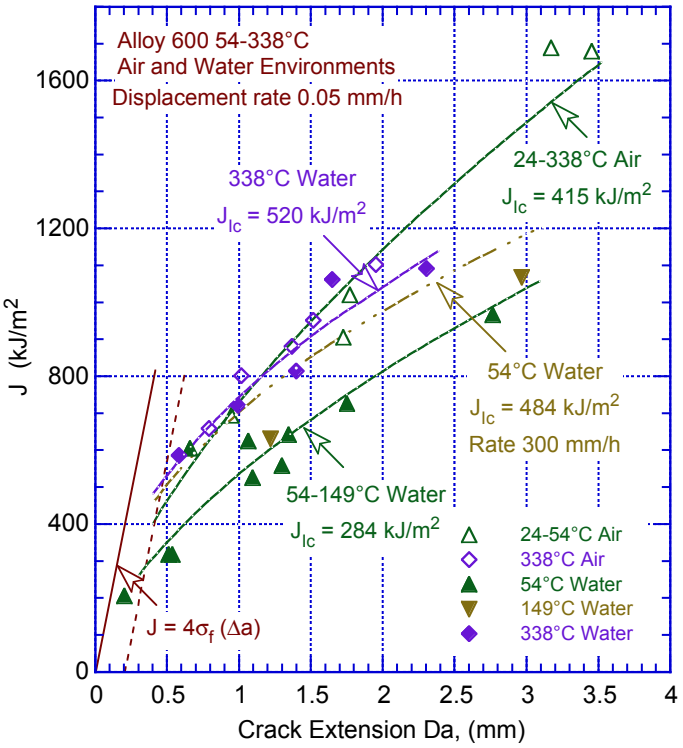

Figure 97.
J–R curves for Alloy 600 in air and water at temperatures of 54 to 338°C. All data were obtained under quasi-static loading conditions (displacement rate = 0.05 mm/h) except for the dashed curve, which represents results obtained at 300 mm/h (Ref. 240).

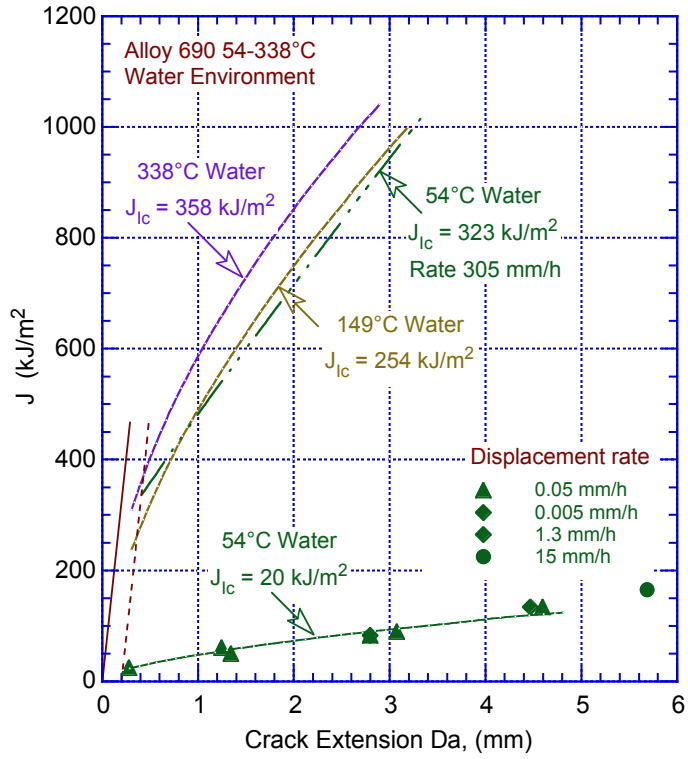

Figure 98.
J–R curves for Alloy 690 in a water environment at a temperature of 54°C and displacement rates of 0.005 to 305 mm/h. The J–R curves at 149 and 338°C obtained under quasi-static conditions are shown for comparison (Ref. 241).

As discussed earlier, a significant reduction in fracture toughness occurred at 54°C in an LWR environment relative to that in air for CF-8 CASS material aged for nearly 16 yr at 350°C. The

large decrease in fracture toughness in LWR SWC has been attributed to potential synergy between thermal embrittlement and hydrogen embrittlement associated with the decomposition of ferrite at reactor temperatures. In addition, similar studies on austenitic SS welds with relatively high ferrite content have not been conducted. The potential effect of reduced fracture toughness (or allowable flaw size) of nickel alloys, aged CASS materials, and austenitic SS welds in LWR SWC on the seismic design of reactor safety-related components have not been performed. Such evaluations need to be evaluated in the next phase of this program **(Information Gap 5)**.

3.1.5 Material Elastic Properties

The elastic modulus has been found to be strain-rate-sensitive for certain materials, including some polymers,[242,243] concrete,[244,245] and some several solder alloys.[246–248] However, in the studies summarized in the previous sections on the effects of strain rate on the tensile properties of structural alloys used in NPPs, none of the authors indicated that strain rate had any perceptible effect on elastic behavior. In addition, both Dinu et al.[113] and Levings and Sritharan[249] explicitly state that strain rate has no effect on the elastic modulus of specific structural alloys. A similar lack of strain-rate dependence is expected for the shear modulus and Poisson's ratio of these alloys.

3.2 Various Forms of Corrosion

This section will be completed in TLR-2.

3.3 Stress Corrosion Cracking in LWR Coolant Environments

This section will be completed in TLR-3.

3.4 Flaw Tolerance Evaluations Including Irradiation Effects

This section will be completed in TLR-4.

4. Summary

4.1 Seismic Design

Structural damage to NPPs occurs when the cumulative effects of ground acceleration exceed a certain threshold. The seismic loads on a structure are inertial loads generated by the deformation of the structure as it vibrates, and the seismic forces depend on the distribution of mass and stiffness throughout the structure. Because structures are typically designed to respond inelastically under vibration, the seismic forces also depend on the manner by which plasticity spreads through the structure, and these forces are typically amplified by resonance effects. In addition, the maximum vibratory accelerations of the SSE must take into account the characteristics of the underlying soil material in transmitting the earthquake-induced motions. Finally, damping effects within the structure must be taken into account.

The information needed for a seismic design includes (a) design ground response spectra, (b) in-structure response spectra, (c) acceleration time history, and (d) seismic anchor movements. The seismic design specifications include (a) the scope and boundaries of components to be seismically designed; (b) the applicable design and construction code; (c) the required seismic function (e.g., operability, leak tightness, and position retention) on the component or piping system; (d) the free-field seismic input for the design basis earthquake; (e) the in-structure seismic response spectra; and (f) the operating and design loading conditions concurrent with the seismic load.

The requirements for the acceptability of a component design by analysis are described in ASME Section III, Division 1 Subarticle NB-3210, “Design Criteria.” Alternatively, a design by rule approach as described in Subarticle NB/NC-3600 may be used for piping and piping components. The design methods in Section III Subarticle NB, NC, or NG for ASME Class 1, 2, and CS components also require a fatigue analysis as well as a fracture mechanics evaluation to prevent the likelihood of nonductile failure. The ASME Code fatigue analysis considers all transient loads, and for each load-cycle or load set pair, an individual fatigue usage factor is determined by the ratio of the number of cycles anticipated during the lifetime of the component to the allowable cycles.

4.2 Seismic Loading Rate Effects

4.2.1 Cyclic Deformation Behavior

In the temperature range of dynamic strain aging (200–370°C), some heats of carbon and low-alloy steels are sensitive to strain rate; with decreasing strain rate, the fatigue life may be unaffected, may decrease for some heats, or may increase for others. The cyclic stress–strain response of these steels varies with steel type, temperature, and strain rate. In general, they show initial cyclic hardening, followed by cyclic softening or a saturation stage at all strain rates. At high strain amplitudes, a secondary hardening stage is observed prior to fracture.

For the wrought austenitic SSs, the fatigue life is generally independent of strain rate at temperatures up to 400°C. During cyclic straining, austenitic SSs exhibit rapid hardening during the first 50–100 cycles; the extent of hardening increases with increasing strain amplitude and decreasing temperature and strain rate. The CASS CF-3, CF-8 and CF-8M generally show similar behaviors, though the cyclic-hardening behavior may be influenced by aging. The microstructural effects associated with cyclic loading for both ferritic and austenitic steels are discussed.

4.2.2 Tensile Properties

Literature data indicate that the yield and ultimate tensile strengths of A508 Cl 3 and A533 Gr B steel generally increase with increasing strain rate, while the ductility decreases or shows little effect. However, some data suggest a reversal in the yield and tensile strength behavior with strain rate in the region of the normal LWR operating temperatures. For Type 304, 304L, 304N and 304LN SSs, the yield stress and flow stress are generally found to increase with increasing strain rate, the ultimate tensile strength tends to decrease, and the ductility decreases or shows little change. Variable results have been obtained for Type 316 SS, but most researchers report an increase in flow stress with increasing strain rate for Types 316L and 316LN SSs. Elongation and reduction of area also appear to increase somewhat with increasing strain rate, though the opposite effect has been observed for cold-worked material. The tensile data for Type 304/308 welds and Type 308 SS weld metal show mixed results. Little effect of strain rate on the flow stress and ductility is reported for Alloy 600 at temperatures up to 760°C and marked increase in flow stress with increasing strain rate is seen at higher temperatures. The tensile data for Alloy 690 indicate an increase in flow stress with increasing strain rate over the entire temperature range from −100°C to 1,200°C, though the magnitude of the effect appears to be temperature dependent.

4.2.3 Fracture Behavior

The Charpy impact data for A508 Cl 3 and A533 Gr B pressure vessel steels indicate either little effect or an increase in the DBTT with increasing loading rate. An increased loading rate also appears to increase the upper shelf energy somewhat for both steels. Neutron irradiation clearly increases the DBTT, and Type 308 SS weld filler metal appears to be increasingly susceptible to brittle fracture with elevated-temperature aging.

The fracture toughness of A508 Cl 3 and A533 Gr B steels generally increases with increasing loading rate. However, a decrease in the crack initiation toughness J_{Ic} with increasing strain rate has been observed in few investigations in the temperature range of interest for LWR applications. The J–R curves generally show an increase in cracking resistance with increasing loading rate. The fracture toughness data for Types 304 and 316 SSs generally suggest a beneficial effect of increasing loading rate on the crack resistance. The limited data in the literature on the effect of loading rate on the fracture toughness properties of the CASS materials are somewhat inconsistent, and as-cast and aged material show different behaviors. Recent work on low-temperature crack propagation for CASS CF-8 material in PWR environments investigated the potential synergy between thermal and hydrogen embrittlement associated with decomposition of the ferrite at reactor temperatures, and a large effect of the coolant environment on fracture toughness was observed. For Alloy 600, a dramatic degradation in fracture toughness is observed in hydrogenated water at temperatures below 149°C, an effect attributed to hydrogen-induced intergranular cracking. This behavior is similar to that observed for aged CF-8 material in LWR SWC. At higher temperatures in the same environment, the fracture toughness increases with increasing loading rate. A qualitatively similar behavior is observed for Alloy 690.

4.2.4 Elastic Properties

No strain-rate dependence is observed for the elastic properties of NPP structural alloys.

4.3 Information Gaps

Five information gaps were identified in this work, as follows:

1. The possible impact of (a) current material condition, (b) loading rates associated with typical seismic events and with low-level seismic fatigue cycles (e.g., magnitudes associated with seismic accelerations between 0.01 g and OBE) on reactor component design needs to be investigated for at least two components, one from reactor core internal components and the other from primary pressure boundary piping (Section 2.4).
2. The cumulative effect of elastic strain cycling on material microstructure and the resulting effect on fracture properties of reactor structural materials needs to be examined (Section 3.1.1.2).
3. The reason for the reversed strain rate dependence (i.e., decrease in yield and flow stress with increase in strain rate) at 400°C and its potential impact on seismic design of safety-related structures and components needs to be determined (Section 3.1.2.1).
4. The possible decrease in fracture toughness of CASS materials and austenitic SS welds thermally aged at 300 to 370°C and tested under dynamic loading conditions at temperature between room temperature and 100°C needs to be investigated (Section 3.1.4.3).
5. The potential effect of reduced fracture toughness of Alloys 600 and 690, aged CASS CF-3 and CF-8 materials, and austenitic SS welds in LWR SWC on the seismic design of reactor safety-related components needs to be determined (Section 3.1.4.4).

References

1. Andersen, P.L., F.P. Ford, K. Gott, R.L. Jones, P.M. Scott, T. Shoji, R.W. Staehle, and R.L. Tapping, "Expert Panel Report on Proactive Materials Degradation Assessment," NUREG/CR-6923, BNL-NUREG-77111-2006, Nuclear Regulatory Commission, Washington, DC, 2007.

2. NRC (Nuclear Regulatory Commission), "Summary of Technical Information and Agreements from Nuclear Management and Resources Council Industry Reports Addressing License Renewal," NUREG-1557, Washington, DC, Dec. 2010. Available at http://www.osti.gov/scitech/biblio/392805.

3. NRC, Generic Aging Lessons Learned (GALL) Report, NUREG-1801, Rev. 2, Washington, DC, Dec. 2010.

4. Lian, T., "EPRI Materials Degradation Matrix," Rev. 3, Electric Power Research Institute, Palo Alto, CA, May 2013.

5. Busby, J.T., "Light Water Reactor Sustainability Materials Aging and Degradation Pathway Technical Program Plan," ORNL/LTR-2012/327, Rev. 0, U.S. Department of Energy, Washington DC, Sept. 2012.

6. Gott, K., "Databases of Operationally Induced Damage," *Proc. 15th Intl. Conf. on Environmental Degradation of Materials in Nuclear Power Systems—Water Reactors*, J. T. Busby, G. Ilevbare, and P. L. Andresen, eds., The Minerals, Metals & Materials Society, Warrendale, PA, pp. 1829–1841, 2011.

7. Ekstrom, P., K. Gott, and B. Brickstad, "Conditions for Long Term Operation of Nuclear Power Plants in Sweden," *Proc. 15th Intl. Conf. on Environmental Degradation of Materials in Nuclear Power Systems—Water Reactors*, J. T. Busby, G. Ilevbare, and P. L. Andresen, eds., The Minerals, Metals & Materials Society, Warrendale, PA, pp. 13–24, 2011.

8. IAEA (International Atomic Energy Agency), "Assessment and Management of Aging of Major Nuclear Power Plant Components Important to Safety: PWR Vessel Internals," IAEA-TECDOC-1557, Vienna, June 2007.

9. IAEA, , , "Aging Management for Nuclear Power Plants, Safety Guide No. NS-G-2.12, Safety Standards, Vienna, 2009.

10. IAEA, "Plant Life Management for Long Term Operation of Light Water Reactors–Principles and Guidelines," Technical Reports Series No. 448, Vienna, 2006.

11. IAEA, "Proactive Management of Aging for Nuclear Power Plants," Technical Reports Series No. 62, Vienna, 2009.

12. Jones, D.A., *Principles and Prevention of Corrosion*, Prentice Hall, 2nd ed., 1996.

13. Revie, R.W., ed., *Uhlig's Corroion Handbook*, J. Wiley and Sons, Inc., 2nd ed., 2000.

14. Saji, G., B. Timofeev, and V.A. Yurmanov, “Review of Corrosion Experience with Aged Components in Russia NPPs,” *Proc. 14th Intl. Conf. on Environmental Degradation of Materials in Nuclear Power Systems—Water Reactors*, American Nuclear Society, Lagrange Park, IL, pp. 1511–1524, 2009.

15. Berg, H.-P., “Corrosion Mechanisms and Their Consequences for Nuclear Power Plants with Light Water Reactors,” *Reliability and Risk Analysis: Theory and Applications*, 2 (4), Dec. 2009.

16. Macdonald, D.D., “The Point Defect Model for the Passive State,” *J. Electrochem. Soc.*, 139 (12), 3434–3449, Dec. 1992.

17. Newman, R., “Pitting Corrosion of Metals,” *The Electrochemical Society Interface*, 33–38, Spring 2010.

18. EPRI (Electric Power Research Institute), “A Method to Predict Cavitation and the Extent of Damage in Power Plant Piping,” EPRI TR-103198-T2, Palo Alto, CA, Dec. 1993.

19. NRC, “Recent Experience with Degradation of Reactor Pressure Vessel Head,” NRC Information Notice 2002–11, March 12, 2002.

20. NRC, “Through–Wall Circumferential Cracking of Reactor Pressure Vessel Head Control Rod Drive Mechanism Penetration Nozzles at Oconee Nuclear Station, Unit 3,” NRC Information Notice 2001–05, Washington, DC, April 30, 2001.

21. Hunt, E.S., “Boric Acid Corrosion Guidebook, Revision 1: Managing Boric Acid Corrosion Issues at PWR Power Stations,” EPRI Report 1000975, Electric Power Research Institute, Palo Alto, CA, Nov. 2001.

22. Czajkowski, C., “Boric Acid Corrosion of Ferritic Reactor Components,” NUREG/CR-2827, Nuclear Regulatory Commission, Washington, DC, July 1982.

23. Westinghouse, “Degradation of Reactor Coolant System Pressure Boundary Resulting from Boric Acid Corrosion,” Westinghouse letter NS-NRC-87-3260 to the NRC, dated October 15, 1987.

24. O’Neill, A.S., and J.F. Hall, “Boric Acid Corrosion of Carbon and Low-Alloy Steels Pressure-Boundary Components,” EPRI NP-5985, Electric Power Research Institute, Palo Alto, CA, Aug. 1988.

25. Ouellette, C.E., “B&W Boric Acid Corrosion Research and the Wastage and Inspection Procedures for RCS Leakage,” BAW-2126, B&W Nuclear Service Company, Lynchburg, VA, Dec. 1990.

26. Johnson, C.J., “Stagnant Water and Microbiologically Induced Corrosion in Cooling Water Systems,” EPRI Report TR-101541, Chapter 12, 1993.

27. EPRI, “Recommendations for an Effective Flow-Accelerated Corrosion Program (NSAC-202L-R4),” EPRI 3002000563, Palo Alto, CA, Nov. 2013.

28. EPRI, “Flow-Accelerated Corrosion in Power Plants, EPRI TR-106611-R1, Palo Alto, CA, Aug. 1998.

29. EPRI, “Investigations into Flow-Accelerated Corrosion at Low Temperatures,” EPRI Report 1013474, Electric Power Research Institute, Palo Alto, CA, Nov. 2006.

30. EPRI Report 1013013, “An Evaluation of Flow-Accelerated Corrosion in the Bottom Head Drain Lines of Boiling Water Reactors,” Electric Power Research Institute, Palo Alto, CA, March 2006.

31. Garud, Y.S., “Issues and Advances in the Assessment of Flow Accelerated Corrosion,” *Proc. 14th Intl. Conf. on Environmental Degradation of Materials in Nuclear Power Systems—Water Reactors*, American Nuclear Society, Lagrange Park, IL, pp. 962–972, 2009.

32. Wu, P.C. “Erosion/Corrosion-Induced Pipe Wall Thinning in U. S. Nuclear Power Plants,” NUREG-1344, Nuclear Regulatory Commission, Washington, DC, April 1989. Available at http://www.osti.gov/scitech/biblio/6152848.

33. Chopra, O.K. and G.L. Stevens, “Effects of LWR Coolant Environments on the Fatigue Life of Reactor Materials, Draft Report for Comment,” NUREG/CR-6909 Rev 1, ANL-12/60, March 2014.

34. Bruemmer, S.M., et al., “Critical Issue Reviews for the Understanding and Evaluation of Irradiation-Assisted Stress Corrosion Cracking,” EPRI TR-107159, Electric Power Research Institute, Palo Alto, CA, 1996.

35. Scott, P., “A Review of Irradiation Assisted Stress Corrosion Cracking,” *J. Nucl. Mater.,* 211, 101–122, 1994.

36. Was, G.S., and P.L. Andresen, “Stress Corrosion Cracking Behavior of Alloys in Aggressive Nuclear Reactor Core Environments,” *Corrosion,* 63, 19–45, 2007.

37. Andresen, P.L., F.P. Ford, S.M. Murphy, and J.M. Perks, “State of Knowledge of Radiation Effects on Environmental Cracking in Light Water Reactor Core Materials,” *Proc. 4th Intl. Symp. on Environmental Degradation of Materials in Nuclear Power Systems—Water Reactors*, NACE, Houston, TX, pp. 1.83–1.121, 1990.

38. Bruemmer, S.M., E.P. Simonen, P.M. Scott, P.L. Andresen, G.S. Was, and J.L. Nelson, “Radiation-Induced Material Changes and Susceptibility to Intergranular Failure of Light-Water-Reactor Core Internals,” *J. Nucl. Mater.* 274, 299–314, 1999.

39. Herrera, M.L., et al., “Evaluation of the Effects of Irradiation on the Fracture Toughness of BWR Internal Components,” *Proc. ASME/JSME 4th Intl. Conf. on Nucl. Eng. (ICONE-4)*, Vol. 5, A. S. Rao, R. M. Duffey, and D. Elias, eds., American Society of Mechanical Engineers, New York, pp. 245–251, 1996.

40. Mills, W.J., “Fracture Toughness of Irradiated Stainless Steels Alloys,” *Nucl. Technol.*, 82, 290–303, 1988.

41. Mills, W.J., “Fracture Toughness of Type 304 and 316 Stainless Steels and Their Welds,” *Intl. Mater. Rev.* 42, 45–82, 1997.

42. Xu, H., and S. Fyfitch, “Materials Reliability Program: A Review of Radiation Embrittlement for Stainless Steels (MRP-79),” Rev. 1, EPRI Report 1008204, Electric Power Research Institute, Palo Alto, CA, Sept. 2004.

43. Ehrnsten, U., K. Wallin, P. Karjalainen-Roikonen, S. van Dyck, and P. Ould, “Fracture Toughness of Stainless Steels Irradiated to ~9 dpa in Commercial BWRs,” *Proc. 6th Intl. Symp. on Contribution of Materials Investigations to Improve the Safety and Performance of LWRs*, Vol. 1, Fontevraud 6, French Nuclear Energy Society, SFEN, Fontevraud Royal Abbey, France, pp. 661–670, Sept. 18–22, 2006.

44. Carter, R.G., and R.M. Gamble, “Assessment of the Fracture Toughness of Irradiated Stainless Steel for BWR Core Shrouds,” *Fontevraud 5 Intl. Symp., Contribution of Materials Investigation to the Resolution of Problems Encountered in Pressurized Water Reactors*, Avignon, France, Sept. 25, 2002.

45. O’Donnell, I.J., H. Huthmann, and A.A. Tavassoli, “The Fracture Toughness Behaviour of Austenitic Steels and Weld Metal Including the Effects of Thermal Aging and Irradiation,” *Intl. J. Pressure Vessels Piping* 65 (3), 209–220, 1996.

46. Kim, C., R. Lott, S. Byrne, M. Burke, and G. Gerzen, “Embrittlement of Cast Austenitic Stainless Steel Reactor Internals Components,” *Proc. 6th Intl. Symp. on Contribution of Materials Investigations to Improve the Safety and Performance of LWRs*, Vol. 1, Fontevraud 6, French Nuclear Energy Society, SFEN, Fontevraud Royal Abbey, France, Sept. 18–22, 2006.

47. Demma, A., R. Carter, A. Jenssen, T. Torimaru, and R. Gamble, “Fracture Toughness of Highly Irradiated Stainless Steels in Boiling Water Reactors,” *Proc. 13th Intl. Conf. on Environmental Degradation of Materials in Nuclear Power Systems–Water Reactors*, T.R. Allen, P.J. King, and L. Nelson, eds., Canadian Nuclear Society, Toronto, Canada, Paper No. 114, 2007.

48. Fyfitch, S., H. Xu, A. Demma, R. Carter, R. Gamble, and P. Scott, “Fracture Toughness of Irradiated Stainless Steel in Nuclear Power Systems,” *Proc. 14th Intl. Conf. on Environmental Degradation of Materials in Nuclear Power Systems—Water Reactors*, American Nuclear Society, Lagrange Park, IL, 2009.

49. Fyfitch, S., H. Xu, K. Moore, and R. Gurdal, “Materials Reliability Program: PWR Internals Material Aging Degradation Mechanism Screening and Threshold Values (MRP-175),” EPRI Report 1012081, Dec. 2005.

50. EPRI, Materials Reliability Program, “Fracture Toughness Testing of Decommissioned PWR Core Internals Material Samples (MRP-160),” EPRI Report 1012079, Sept. 2005.

51. Chopra, O.K., and A.S. Rao, "A Review of Irradiation Effects on LWR Core Internal Materials - Neutron Embrittlement," *J. Nucl. Mater.* 412, 195–208, 2011.

52. Chopra, O.K., and W.J. Shack, “Crack Growth Rates and Fracture Toughness of Irradiated Austenitic Stainless Steels in BWR Environments,” NUREG/CR-6960, ANL-06/58, March 2008.

53. Chopra, O.K., “Degradation of LWR Core Internal Materials Due to Neutron Irradiation,” NUREG/CR-7027, Dec. 2010.

54. Andresen, P.L. “Emerging Issues and Fundamental Processes in Environmental Cracking in Hot Water,” *Proc. Research Topical Symposium on Environmental Cracking, Corrosion/07*, NACE, 2007.

55. Bruemmer, S.M., “New Issues Concerning Radiation-Induced Material Changes and Irradiation-Assisted Stress Corrosion Cracking in Light-Water Reactors,” *Proc. Tenth Intl. Symp. on Environmental Degradation of Materials in Nuclear Power Systems—Water Reactor*, Paper No. 0008V, NACE, Houston, TX, 2001.

56. Edwards, D., E. Simonen, and S. Bruemmer, “Radiation-Induced Segregation Behavior in Austenitic Stainless Steels: Fast Reactor versus Light Water Reactor Irradiations,” *Proc. 13th Intl. Conf. on Environmental Degradation of Materials in Nuclear Power Systems—Water Reactors*, T.R. Allen, P.J. King, and L. Nelson, eds., Canadian Nuclear Society, Toronto, Canada, Paper No. P0139, 2007.

57. Fyfitch, S., H. Xu, P. Scott, L. Fournier, and A. Demma, “Criteria for Initiation of Irradiation-Assisted Stress Corrosion Cracking in Stainless Steels in PWR Systems,” *Proc. 14th Intl. Conf. on Environmental Degradation of Materials in Nuclear Power Systems—Water Reactors*, American Nuclear Society, Lagrange Park, IL, 2009.

58. Jenssen, A., J. Stjarnsater, and R. Pathania, "Crack Growth Rates of Irradiated Commercial Stainless Steels in BWR and PWR Environments," *Proc. 15th Intl. Conf. on Environmental Degradation of Materials in Nuclear Power Systems—Water Reactors*, J.T. Busby, G. Ilevbare, and P.L. Andresen, eds., The Minerals, Metals & Materials Society, Warrendale, PA, pp. 1229–1240, 2011.

59. Jenssen, A., and L.G. Ljungberg, “Irradiation Assisted Stress Corrosion Cracking: Post Irradiation CERT Tests of Stainless Steels in a BWR Test Loop,” *Proc. Seventh Intl. Symp. on Environmental Degradation of Materials in Nuclear Power Systems—Water Reactor*, G. Airey et al., eds., NACE, Houston, TX, pp. 1043–1052, 1995.

60. Jenssen, A., and L.G. Ljungberg, “Irradiation Assisted Stress Corrosion Cracking of Stainless Alloys in BWR Normal Water Chemistry and Hydrogen Water Chemistry,” *Proc. Sixth Intl. Symp. on Environmental Degradation of Materials in Nuclear Power Systems—Water Reactors*, R. E. Gold and E. P. Simonen, eds., Minerals, Metals & Materials Society, Warrendale, PA, pp. 547–553, 1993.

61. Chopra, O.K., and A.S. Rao, "A Review of Irradiation Effects on LWR Core Internal Materials–IASCC Susceptibility and Crack Growth Rates of Austenitic Stainless Steels," *J. Nucl. Mater.,* 409, 235–256, 2011.

62. NRC (Nuclear Regulatory Commission), “Domestic Licensing of Production and Utilization Facilities*,”* Code of Federal Regulations, Title 10, Energy, Part 50, (10 CFR Part 50), Washington, DC.

63. NRC, “Appendix A to Part 50—General Design Criteria for Nuclear Power Plants,” (10 CFR Part 50).

64. Office of the *Federal Register*, National Archives and Records Administration,“Appendix A to Part 50—General Design Criteria for Nuclear Power Plants,*”* (10 CFR 50), Washington, DC.

65. Campbell, K.W., and Y. Bozorgnia, "A Ground Motion Prediction Equation for the Horizontal Component of Cumulative Absolute Velocity on the PEER-NGA Strong Motion Database," *Earthquake Spectra*, 26 (3), 635–650, Aug. 2010.

66. EPRI, “A Criterion for Determining Exceedance of the Operating Basis Earthquake,” EPRI NP-5930, Electric Power Research Institute, Palo Alto, CA, 1988.

67. Office of the *Federal Register*, National Archives and Records Administration, “Appendix J to Part 50—Primary Reactor Containment Leakage Testing for Water-Cooled Power Reactors,” (10 CFR 50), Washington, DC.

68. ASME (American Society of Mechanical Engineers), “Section XI. Rules for Inservice Inspection of Nuclear Power Plant Components,” The ASME Boiler and Pressure Vessel Code, 2004 edition as approved in 10 CFR 50.55a, ASME Boiler and Pressure Vessel Code, New York, NY.

69. Huang, C.T., W.D. lwan, K.R. Jaquay and N.C. Chokshi, "Analytical study of frequency effects on seismic margins," *Trans. of the 14th Int. Conf. on Structural Mechanics and Reactor Technology (SMiRT 14)*, Lyon, France, Paper K13/5, 1997.

70. Machida, H., "Effect of Dispersion of Seismic Load on Integrity of Nuclear Power Plant Piping," *Trans. of the 16th Int. Conf. on Structural Mechanics and Reactor Technology (SMiRT 16)*, Washington DC, Paper # 1116, 2001.

71. DeGrassi, G., J. Nie and C. Hofmayer. "Seismic Analysis of Large-Scale Piping Systems for the JNES/NUPEC Ultimate Strength Piping Test Program,” NUREG/CR-6983, 2008.

72. Shao, L.C., A.J. Murphy, N. Chokshi, P-T. Kuo and T.Y. Chang, "Seismic responses and resistance of age degraded structures and components," *Nucl. Eng. Des.,* 181, 3–15, 1998.

73. Zhang, T., F.W. Brust, D.J. Shim, G. Wilkowski, J. Nie and C. Hofmayer, "Analysis of JNES Seismic Tests on Degraded Piping," NUREG/CR-7015, 2010.

74. U.S. NRC, "A Performance-Based Approach to Define the Site-Specific Earthquake Ground Motion," Regulatory Guide 1.208, Washington, DC, March 2007.

75. Office of the *Federal Register*, National Archives and Records Administration "Appendix S to Part 50–*Earthquake Engineering Criteria for Nuclear Power Plants*," (10 CFR 50), Washington, DC.

76. Nicholas, T., "Material Behavior at High Strain Rates," in Impact Dynamics, J. A. Zukas, et al. eds., John Wiley & Sons, New York, 277-332, 1982.

77. Zener, C., and J. H. Hollomon, “Effect of Strain Rate upon Plastic Flow of Steel,” *J. Appl. Phys.*, 15, 22–32, 1944.

78. Rittel, D., and Z.G. Wang, “Thermo-Mechanical Aspects of Adiabatic Shear Failure of AM50 and Ti6Al4V Alloys,” *Mech. Mater.*, 40, 629–635, 2008.

79. Marchand, A., and J. Duffy, “An Experimental Study of the Formation Process od Adiabatic Shear Bands in a Structural Steel,” *J. Mech. Phys. Solids*, 36 (3), 251–283, 1988.

80. Rittel, D., Z.G. Wang, and M. Merzer, “Adiabatic Shear Failure and Dynamic Stored Energy of Cold Work,” *Phys. Rev. Lett.*, 96, 2006.

81. Rittel, D., P. Landau, and A. Venkert, “Dynamic Recrystallization as a Potential Cause for Adiabatic Shear Failure,” *Phys. Rev. Lett.*, 101, 2008.

82. Osovski, S., D. Rittel, P. Landau, and A. Venkert, “Microstructural Effects on Adiabatic Shear Band Formation,” *Scripta Meterialia*, 66, 9–12, 2012.

83. Osovski, S., Y. Nahmany, D. Rittel, P. Landau, and A. Venkert, “On the Dynamic Character of Localized Failure,” *Scripta Meterialia*, 67, 693–695, 2012.

84. Osovski, S., D. Rittel, and A. Venkert, “The Respective Influence of Microstructural and Thermal Softening on Adiabatic Shear Localization,” *Mech. Mater.*, 56, 11–22, 2013.

85. Roy, H., S. Sivaprasad, S. Tarafder and K.K. Ray, "Cyclic fracture behaviour of 304LN stainless steel under load and displacement control modes," *Fatigue Frac. Eng. Mat. Struct.*, 35 (2), 108–113, 2012.

86. Office of the *Federal Register*, National Archives and Records Administration, “Appendix B to Part 50—Quality Assurance Criteria for Nuclear Power Plants and Fuel Reprocessing Plants,” (10 CFR 50), Washington, DC.

87. Office of the *Federal Register*, National Archives and Records Administration, “Codes and Standards,” (10 CFR 50.55a), Washington, DC.

88. ASME, “Section III, Rules for Construction of Nuclear Facility Components, Division 1, Subsection NB, Class 1 Components,” ASME Boiler and Pressure Vessel Code, American Society of Mechanical Engineers, New York, NY.

89. ASME Code Section III, *Rules for Construction of Nuclear Facility Components, Division 1, Subsection NB, Class 1 Components*, ASME Boiler and Pressure Vessel Code, American Society of Mechanical Engineers, New York, NY.

90. NRC, "Quality Group Classifications and Standards for Water-, Steam-, and Radioactive-Waste-Containing Components of Nuclear Power Plants," Regulatory Guide 1.26, Washington, DC.

91. NRC, "Design, Fabrication, and Materials Code Case Acceptability, ASME Section III," Regulatory Guide 1.84, Washington, DC.

92. NRC, "ASME Code Cases Not Approved for Use," Regulatory Guide 1.193, Washington, DC.

93. Stevenson, J.D., “Historical International Development od Seismic Design and Analysis of Nuclear Power Plant Structures, Systems, and Components over the Last 60 Years,” OECD Nuclear Energy Agency, Nov. 19, 2010. Available at https://www.oecd-nea.org/nsd/csni/ia.

94. Lockheed Aircraft Corporation and Holmes & Narver, Inc., “Nuclear Reactors and Earthquakes,” TID-7024 prepared for the U.S. Atomic Energy Commission, Washington, DC, Aug. 1963.

95. Andrews, A., and P. Folger, “Nuclear Power Plant Design and Seismic Safety Consideration,” CRS 7-5700 R41805, Congressional Research Service, Library of Congress, Washington, DC, Jan. 12, 2012.

96. NRC, “Design Response Spectra for Seismic Design of Nuclear Power Plants,” Regulatory Guide 1.60, Rev. 2,Washington, DC, July 2014.

97. NRC, "Seismic Design Classification," Regulatory Guide 1.29, Washington, DC.

98. NRC, "Damping Values for Seismic Design of Nuclear Power Plants," Regulatory Guide 1.61, Washington, DC.

99. NRC, “Combining Modal Responses and Spatial Components in Seismic Response Analysis," Regulatory Guide 1.92, Washington, DC.

100. ASME, “Non-Mandatory Appendix N, ASME Code Section III, Boiler and Pressure Vessel Code, Section III, Division 1, Dynamic Analysis Methods,” New York, NY.

101. Newmark, N.M., and W.J. Hall, “Seismic Design Criteria for Nuclear Reactor Facilities,” *Proc. of Fourth World Conf. on Earthquake Engineering*, Vol. 2, pp. B4-37 to B4-50, Santiago, Chile, Jan. 1969.

102. Clarke, R., "Introduction to IBC Seismic Forces," University of West Indies, St. Augustine. Available at http://richardpclarke.tripod.com/seismicload1.pdf, Sept. 2014.

103. NIST (National Institute of Standards and Technology), U.S. Deptartment of Commerce, “Soil-Structure Interaction for Building Structures,” GCR 12-917-21, Gaithersburg, MD, Sept. 2012.

104. Veletsos, A.S., and N.M. Newmark, “Effect of Inelastic Bebavior on the Responseof Simple Systems to Earthquake Motions,” *Proc. Second World Conference on Earthquake Engineering (2WCEE)*, July 11–18, 1960. Available at http://nisee.berkeley.edu/elibrary/getpkg?id=S30595 (accessed Nov. 2014).

105. NRC, Rev. 1, “Damping Values for Seismic Design of Nuclear Power Plants,” Regulatory Guide 1.61, Washington, DC, March 2007.

106. NRC, “Standard Review Plan for the Review of Safety Analysis Reports for Nuclear Power Plants: LWR Edition,” NUREG-0800, Washington, DC, June 1987.

107. NRC, “Identification and Characterization of Seismic Sources and Determination of Safe Shutdown Earthquake Ground Motion,” Regulatory Guide 1.165, Washington, DC, March 1997.

108. Newmark, N.M., J.A. Blume, and K.K. Kapur, “Design Response Spectra for Nuclear Power Plants,” American Society of Civil Engineers (ASCE) Structural Engineering Meeting, San Francisco, April 1973, (ADAMS Accession No. ML13207A044).

109. Newmark, N.M., J.A. Blume, and K.K. Kapur, “Seismic Design Spectra for Nuclear Power Plants,” *Journal Power Div., ASCE*, pp. 287–303, November 1973, (ADAMS Accession No. ML13207A045).

110. Newmark, N.M., Consulting Engineering Services, “A Study of Vertical and Horizontal Earthquake Spectra,” Urbana, IL, USAEC Contract No. AT(49-5)-2667, WASH-1255, April 1973, (ADAMS Accession No. ML13203A235).

111. John A. Blume & Associates, “Recommendations for Shape of Earthquake Response Spectra,” San Francisco, California, USAEC Contract No. AT(49-5)-3011, WASH-1254, San Francisco, CA, Feb. 1973, (ADAMS Accession No. ML13203A236).

112. NRC, “Development of Floor Design Response Spectra for Seismic Design of Floor-Supported Equipment or Components,” Regulatory Guide 1.122, Washington, DC, Feb. 1978.

113. Dinu, F., A. Stratan, and D. Dubina, "Influence of Strain Rate on the Weld Detailing Behaviour in MR Connections," in *Behaviour of Steel Structures in Seismic Areas: Proceedings of the Fourth International Conference STESSA 2003*, Federico M. Mazzolani, ed., June 9–12, pp. 835–840, Naples, Italy, 2003.

114. Kurobane, Y., K. Ogawa, and C. Veda, "Kobe Earthquake Damage to High-Rise Ashiyama Apartment Buildings: Brittle Tensile Fracture of Box Section Columns," in *Tubular Structures VII*, I. Farkas and K. Jarmai, eds., Miskolc, pp. 277–284, Balkema, Rotterdam, Netherlands, August 28–30, 1996.

115. Kohzu, I., and K. Suita, "Single or Few Excursions Failure of Steel Structural Joints Due to Impulsive Shocks in the 1995 Hyogoken-Nanbu Earthquake," *Proc. 11th World Conference on Earthquake Engineering*, Acapulco, Mexico, Paper 412, June 26–28, 1996.

116. Gioncu, V., "Influence of Strain Rate on the Behaviour of Steel Members," in Behaviour of Steel Structures in Seismic Areas: *Proc. of the Third International Conference STESSA*, Montreal, Canada, Federico M. Mazzolani and Robert Tremblay, eds., pp. 19–26, 2000.

117. Chang, K.-C., and G.C. Lee, ”Strain Rate Effect on Structural Steel under Cyclic Loading.” *J. Eng. Mech.*, 113 (9), 1292–1301,1987. Available at http://dx.doi.org/10.1061/(ASCE)0733-9399(1987)113:9(1292).

118. Uang, C.M., and D.M. Bordad, "Dynamic Testing of Full-Scale Steel Moment Connections," *Proc. 11th World Conference on Earthquake Engineering*, Acapulco, Mexico, Paper 407, June 26–28, 1996.

119. Nakashima, M., K. Suita, K. Morisako, and Y. Marioka, "Tests of Welded Beam-Column Subassemblies I. Global Behaviour, II. Detailed Behaviour," *J. Struct. Eng.*, 124 (11), 1236–1252, 1998.

120. Antaki, G.A., “Pipeline and Pipeline Engineering,” p. 238, Marcel Dekker, Inc., New York, NY, 2003.

121. Wiessner, C.S., and M. MacGillivray, "Loading Rate Effects on Tensile Properties and Fracture Toughness of Steel," 1999. Available at http://www.twi-global.com/technical-knowledge/published-papers/loading-rate-effects-on-tensile-properties-and-fracture-toughness-of-steel-april-1999/.

122. Chopra, O. K., and W. J. Shack, "Effects of Material and Loading Variables on Fatigue Life of Carbon and Low–Alloy Steels in LWR Environments," in *Trans. of 13th Int. Conf. on Structural Mechanics in Reactor Technology (SMiRT 13)*, Vol. II, M. M. Rocha and J. D. Riera, eds., Escola de Engenharia – Universidade Federal do Rio Grande do Sul, Porto Alegre, Brazil, pp. 551–562, 1995.

123. Chopra, O. K., and W. J. Shack, "Evaluation of Effects of LWR Coolant Environments on Fatigue Life of Carbon and Low–Alloy Steels," in *Effects of the Environment on the Initiation of Crack Growth*, ASTM STP 1298, W. A. Van Der Sluys, R. S. Piascik, and R. Zawierucha, eds., American Society for Testing and Materials, Philadelphia, pp. 247–266, 1997.

124. Chopra, O. K., and W. J. Shack, "Effects of LWR Coolant Environments on Fatigue Design Curves of Carbon and Low-Alloy Steels," NUREG/CR-6583, ANL-97/18, Feb. 1998.

125. Abdel–Raouf, H., A. Plumtree, and T. H. Topper, "Effects of Temperature and Deformation Rate on Cyclic Strength and Fracture of Low–Carbon Steel," in *Cyclic Stress–Strain Behavior–Analysis, Experimentation, and Failure Prediction*, ASTM STP 519, American Society for Testing and Materials, Philadelphia, pp. 28–57, 1973.

126. Lee, B. H., and I. S. Kim, "Dynamic Strain Aging in the High–Temperature Low–Cycle Fatigue of SA 508 Cl. 3 Forging Steel," *J. Nucl. Mater*. **226**, 216–225, 1995.

127. Terrell, J. B., "Fatigue Life Characterization of Smooth and Notched Piping Steel Specimens in 288°C Air Environments," NUREG/CR–5013, EM–2232 Materials Engineering Associates, Inc., Lanham, MD, May 1988.

128. Amzallag, C., P. Rabbe, G. Gallet, H.–P. Lieurade, "Influence des Conditions de Sollicitation Sur le Comportement en Fatigue Oligocyclique D'aciers Inoxydables Austénitiques," *Memoires Scientifiques Revue Metallurgie*, pp. 161–173, March 1978.

129. Jaske, C. E., and W. J. O'Donnell, "Fatigue Design Criteria for Pressure Vessel Alloys," *Trans. ASME J. Pressure Vessel Technol.* **99**, 584–592, 1977.

130. Chopra, O. K., "Effects of LWR Coolant Environments on Fatigue Design Curves of Austenitic Stainless Steels," NUREG/CR-5704, ANL-98/31, arch 1999.

131. Chopra, O. K., "Mechanism and Estimation of Fatigue Crack Initiation in Austenitic Stainless Steels in LWR Environments," NUREG/CR-6787, ANL-01/25, July 2002.

132. Hayashi, M., K. Enomoto, T. Saito, and T. Miyagawa, "Development of Thermal Fatigue Testing with BWR Water Environment and Thermal Fatigue Strength of Austenitic Stainless Steels," *Nucl. Eng. Des*. **184**, 113–122, 1998.

133. Shack, W. J., and W. F. Burke, "Fatigue of Type 316NG SS," in *Environmentally Assisted Cracking in Light Water Reactors, Semiannual Report*, October 1989–March 1990, NUREG/CR–4667 Vol. 10, ANL–91/5, pp. 3–19, March 1991.

134. Pellissier–Tanon, A., J. L. Bernard, C. Amzallag, and P. Rabbe, "Evaluation of the Resistance of Type 316 Stainless Steel Against Progressive Deformation," in *Low–Cycle Fatigue and Life Prediction*, ASTM STP 770, C. Amzallag, B. N. Leis, and P. Rabbe, eds., American Society for Testing and Materials, Philadelphia, pp. 69–80, 1982.

135. Kanasaki, H., R. Umehara, H. Mizuta, and T. Suyama, "Fatigue Lives of Stainless Steels in PWR Primary Water," *Trans. 14th Intl. Conf. on Structural Mechanics in Reactor Technology (SMiRT 14)*, Lyon, France, pp. 473–483, 1997.

136. Tsutsumi, K., H. Kanasaki, T. Umakoshi, T. Nakamura, S. Urata, H. Mizuta, and S. Nomoto, "Fatigue Life Reduction in PWR Water Environment for Stainless Steels," in *Assessment Methodologies for Preventing Failure: Service Experience and Environmental Considerations*, PVP Vol. 410-2, R. Mohan, ed., American Society of Mechanical Engineers, New York, pp. 23–34, 2000.

137. Chopra, O. K., and J. L. Smith, "Estimation of Fatigue Strain–Life Curves for Austenitic Stainless Steels in Light Water Reactor Environments," in *Fatigue, Environmental Factors, and New Materials*, PVP Vol. 374, H. S. Mehta, R. W. Swindeman, J. A. Todd, S. Yukawa, M. Zako, W. H. Bamford, M. Higuchi, E. Jones, H. Nickel, and S. Rahman, eds., American Society of Mechanical Engineers, New York, pp. 249–259, 1998.

138. Chopra, O. K., "Estimation of Fracture Toughness of Cast Stainless Steels during Thermal Aging in LWR Systems," NUREG/CR-4513, Rev. 1, ANL-93/22, May 1994.

139. Slama, G., P. Petrequin, and T. Mager,, "Effect of Aging on Mechanical Properties of Austenitic Stainless Steel Castings and Welds," in *Assuring Structural Integrity of Steel Reactor Pressure Boundary Components, SMiRT Post Conference Seminar 6*, Monterey, CA, 1983.

140. Mughrabi, H., Dislocations and Properties of Real Material, Book No. 323, The Inst. of Metals, London, pp. 244–262, 1985.

141. Laird, C., Chapter 27, in *Physical Metallurgy*, 4th ed., R.W. Cahn and P. Haasen eds., pp. 2293–2397, Elsevier Science, 1996.

142. Polak, J., Cyclic Deformation, Crack Initiation, and Low-Cycle Fatigue, in *Comprehensive Structural Integrity*, Vol. 4.01, I. Milne, R.O. Ritche, and B. Karihallo, eds., Elsevier, Amsterdam, pp. 1–39, 2003.

143. Weidner, A., J. Man, W. Skrotzki, and J. Polak, "Slip Localization and Dislocation Structure at Early Stages of Fatigue Damage in Austenitic Stainless Steel (316L)," *International Conference on Fatigue*, ICF12, Ottawa, 2009.

144. Hull, D., in *Introduction to Dislocations*, Pergamon Press, Oxford, 1965.

145. Basinski, S. J., Z. S. Basinski, and A. Howie, "Early Stages of Fatigue in Copper Single Crstal," *Phil. Mag*. 19 (161), 899–924, 1969.

146. Grosskreutz, J. C, "The Mechanisms of Metal Fatigue (I)," *Phys. Stat. Sol.,* 47, 11–31, 1971.

147. McGrath, J. T., and W.J. Bratina, "Dislocation Structures in Fatigued Iron-Carbon Alloys," *Phil. Mag.* 12 (120), 1293–1305, 1965.

148. Weissmann, S., A. Shrier, and V. Greenhut, "Dislocation Substructure and Extension of Fatigue Life in Metal Crystals," *Trans. Am. Soc. Metals,* 59, 709, 1966.

149. Feltner, E., and C. Laird, "The Role of Slip Charater in Steady State Cyclic Stress Strain Behavior," *Trans. Metall. Soc. A.I.M.E., 245,* 1372, 1969.

150. Feltner, E., and C. Laird, "Cyclic Stress-Strain Response of F.C.C. Metals and Alloys – I Phenomenological Experiments," *Acta Metall.,* 15, 1621, 1967.

151. Abdel-Raouhf. H., P.P. Benham, and A. Plumtree, "Mechanical Behavior and Substructure of Strain Cycled Iron," *Can. Met. Q.,* 10, 87, 1971.

152. Pham, M.S., C. Solenthaler, K.G.F. Janssens, and S.R. Holdsworth, "Dislocation Structure Evolution and its Effect on Cyclic Deformation Response of AISI 316L Stainless Steel," *Mater. Sc. Eng*., 528, 3261–3269, 2011.

153. Chopra, O.K., and C.V.B. Gowda, "Substructural Development during Strain Cycling of Alpha-iron," *Phil. Mag.* 30 (3), 583–591, 1974.

154. Segall, R.L., Lattice Defects in Fatigued Metals, in *Electron Microscopy and Strength of Crystals*, Interscience, NY, 515, 1963.

155. Manjoine, M.J., "Influence of Strain Rate and Temperature on Yield Stress of Mild Steel," *J. of Applied Mechanics*, 66 (11), 211–218, 1944.

156. Wright, R.N., and W.J. Hall, "Loading Rate Effects in Structural Steel Design," *J. Struct. Div.*, 90 (55), 11–37, 1964.

157. Nagaraja Rao, N., M. Lohrmann, and L. Tall, "Effect of strain rate on the yield stress of structural steel," *ASTM J. Mat.*, 1 (1), Publication No. 293, Fritz Laboratory Reports, Paper 1684, March 1966.

158. Kaneta, K., I. Kohzu, and K. Fujimara, "On the Strength and Ductility of Steel Structural Joints Subjected to High-Speed Monotonic Tensile Loading," in *8th European Conference on Earthquake Engineering*, Lisbon, September 12–17, 1986.

159. Soroushian, P. and K.B. Choi, "Steel Mechanical Properties at Different Strain Rates, *J. Struct. Eng.*, 113 (11), 863–872, 1987.

160. Fujimoto, M., T. Naruba, and S. Sasaki, "Strength and Deformation Capacity of Steel Brace under High-Speed Loading," in *9th World Conference on Earthquake Engineering*, Tokyo, Vol. IV, pp. 139–144, August 2–9, 1988.

161. Kassar, M. and W.W. Wu, "Effect of Strain Rate on Material Properties of Sheet Steels," *J. Struct. Eng.*, 118 (11), 3136–3150, 1992.

162. Obata, M., Y. Goto, S. Matsura, andH. Fujiwara, Ultimate Behavior of Tie Plates at High-Speed Tension, *J. Struct. Eng.*, 122 (4), 416–422, 1996.

163. Campbell, J. D. and W.G. Ferguson, "The temperature and strain-rate dependence of the shear strength of mild steel," *Phil. Mag.*, 21 (169), 63–82, 1970.

164. Campbell, J.D., A.M. Eleiche, and M. C. Tsao. “Strength of Metals and Alloys at High Strains and Strain Rates,” in *Fundamental Aspects of Structural Alloy Design*, R.I. Jaffee and B. A. Wilcox, eds., Plenum, NY, pp. 545–561, 1977.

165. Kim, I. S. and S.S. Kang, “Dynamic Strain Aging in SA508-Class 3 Pressure Vessel Steel,” *Int. J. Pres. Vessels Piping*, 62, 123–129, 1995.

166. Tanguy, B., R. Piques, L. Laiarinandrasana, and A. Pineau, “Mechanical Behavior of A508 steel based on Double Nonlinear Viscoplastic Constitutive Equation,” in *EUROMAT 2000, Advances in Mechanical Behaviour, Plasticity and Damage*, D. Miannay, P. Costa, D. François, A. Pineau, eds., Elsevier, pp. 499–504, 2000.

167. Tanguy, B, J. Besson, R. Piques, and A. Pineau, “Ductile to Brittle Transition of an A508 Steel Characterized by Charpy Impact Test. Part-I: Experimental Results,” *Eng. Fract. Mech.*, 72, 49–72, 2005.

168. Wu, X.Q. and I.S. Kim, “Effects of Strain Rate and Temperature on Tensile Behavior of Hydrogen-Charged SA508, Cl. 3 Pressure Vessel Steel,” *Mat. Sci. Eng.*, 48, 309–318, May 2003.

169. Xu, S., X. Q. Wu, E. H. Han, and W. Ke, “Effects of dynamic strain aging on mechanical properties of SA508 class 3 reactor pressure vessel steel, *J. Mater. Sci.*, 44 (11), 2882–2889, 2009.

170. Bonora, N. and P.P. Milella, "Strain Rate and Temperature Effect in Ductile Failure Process: Characterization and Modeling Using Continuum Damage Mechanics,” Final Report to E.O.A.R.D., London, Contract No. F61775-99-WE066, July 2000.

171. Milella, P.P., “On the Dependence of the Yield Strength of Metals on Temperature and Strain Rate: The Mechanical Equation of the Solid State,” in *Shock Compression of Condensed Matter–2001*, CP 620, M.D. Furnish, N.N. Thadhani, and Y. Hone, eds., American Institute of Physics, College Park, MD, pp. 642–645, 2002.

172. Milella, P.P., "Temperature and Strain Rate Dependence of Mechanical Behavior of Body-Centered Cubic Structure Materials", *TMS Fall Meeting '98*, Chicago, IL, pp. 11–15, Oct. 1998.

173. Kanninen, M.F., et al., “Heavy Section Steel Technology Semiannual Progress Report for April-September 1987,” NUREG CR/4219, Vol. 4, No. 2, 1987.

174. Steichen, J.M., and J.A. Wiliams, “Effect of Strain Rate and Temperature on the Tensile Properties of Irradiated ASTM A533-B Steel,” *J. Nucl. Mater.*, 57, 303–311, Sept. 1975.

175. Solomos, G., C. Albertini, K. Labibes, V. Pizzinato, and B. Viaccoz, “Strain rate effects in nuclear steels at room and higher temperatures,” *Nucl. Eng. Des.*, 229 (1-2), 139–149, 2004.

176. Chaouadi, R. and J. L. Puzzolante, “Loading Rate Effect on Ductile Crack Resistance of Steels Using Precracked Charpy Specimens,” *Int. J. Pres. Vessels Piping*, 85, 752–761, 2008.

177. Steichen, J.M. and A.L. Ward, “High Strain Rate Tensile Properties of Type 308 SMA Weld Metal,” *Welding Research Supplement*, 130-s to 135-s, April 1975.

178. Iino, Y., “Tensile Properties of Type 304 Stainless Steel in Temperature Range 77 to 1223K and Strain Rate Range 10^{-6} to 10^{-1} s^{-1},” *Bull. Japan Soc. Mech. Eng.*, 29, 355–361, 1986.

179. Huang, G.L., D.K. Matlock, and G. Krauss, "Martensite Formation, Strain Rate Sensitivity, and Deformation Behavior of Type 304 Stainless Steel Sheet," *Met. Trans. A*, Vol. 20A, pp. 1239–1246, 1989.

180. Iino, Y., J. Svejcar, I. Dlouhý, and M. Forejt, “Effect of strain rate 10^{-4} to 10^{3} s^{-1} on room temperature tensile properties and notched plastic zone of type 304 stainless steel,” in *17th European Conference on Fracture 2008: Multilevel Approach to Fracture of Materials*, Components and Structures, pp. 773–779, 2008.

181. Iino, Y., J. Svejcar, I. Dlouhý, and M. Forejt, “Effect of strain rate 10^{-7} to 10^{-4} s^{-1} on room temperature tensile properties and notched plastic zone of type 304 stainless steel,” in *18th European Conference on Fracture 2010: Fracture of Materiále and Structures from Micro to Macro Scale*, pp. 1–8, 2010.

182. Marschall, C.W., M.P. Landow, G.M. Wilkowski, and A.R. Rosenfield, "Comparison of Static and Dynamic Strength and J-R Curves of Various Piping Materials from the IPIRG-1 Program," *J. Press. Vessels Piping*, Vol. 62, pp. 49–58, 1995.

183. Nordberg, H., "Note on the Sensitivity of Stainless Steels to Strain Rate," AvestaPolarit Research Foundation Research Report No. 04.0-1, March 2004.

184. Kundu, A and P.C. Chakraborti, “Effect of Strain Rate on Quasistatic Tensile Flow Behaviour of Solution Annealed 304 Austenitic Stainless Steel at Room Temperature,” *J. Mater. Sc.*, 45 (20), 5482–5489, Oct. 2010.

185. Andrade-Campos, A., F. Teixeira, U. Krupp, F. Barlat, E.F. Rauch, and J.J. Gracio, “Effect of Strain Rate, Adiabatic Heating, and Phase Transformation Phenomena on the Mechanical Behaviour of Stainless Steel," *Strain*, Vol. 46, pp. 283–297, 2010.

186. Talonen, J., P. Nenonen, G. Pape, and H. Hänninen, “Effect of Strain Rate on the Strain-Induced Martensite Transformation and Mechanical Properties of Austenitic Stainless Steels,” *Metal Mater. Trans. A*, 36A, 421–432, 2005.

187. Rodriguez-Martinez, J.A., R. Pesci, and A. Rusinek, “Experimental Study on the Martensitic Transformation in AISI 304 Steel Sheets Subjected to Tension under Wide Ranges of Strain Rate at Room Temperature,” *Mater. Sci. Eng.*, 528, 5974–5982, July 2011.

188. Kuokkala, V.T., S. Curtze, M. Isakov, and M. Hokka, “Dynamic Thermo-Mechanical Response of Austenite Containing Steels,” *Proc. of the Society for Experimental Mechanics Series*, Tom Proulx, ed., pp. 337-342, Uncasville, CT, June 13-16, 2011. Available at http://what-when-how.com/dynamic-behavior-of-materials/dynamic-thermo-mechanical-response-of-austenite-containing-steels-dynamic-behavior-of-materials/.

189. Fish, R.L., and C.W. Hunter, “Tensile Properties of Fast Reactor Irradiated Type 304 Stainless Steel,” *Irradiation Effects of Radiation on the Microstructure and Properties of Metals*, ASTM STP 611, American Society for Testing and Materials, pp. 119–138, 1976.

190. Semiatin, S.L., and J.H. Holbook, "Plastic Flow Phenomenology of 304L Stainless Steel," *Met. Trans. A*, 14 (8), 1681–1695, Aug. 1983.

191. Stout, M.G. and P.S. Follansbee, "Strain Rate Sensitivity, Strain Hardening, and Yield Behavior of 304L Stainless Steel," *J. Eng. Mater. Technol.,* 108 (4), 344–353, Oct. 1986.

192. Lichtenfeld, J., J.A. Vab Tyne, and M.C. Mataya, "Effect of strain rate on stress-strain behavior of alloy 309 and 304L austenitic stainless steel," *Metall. Mater.*, 37 (1), 147–161, Jan. 2006.

193. Antoun, B., J. Korellis, and B. Song, “Techniques for Testing 304L Stainless Steel over a Wide Range of Temperatures,” *Proc. of the 2007 Experimental and Applied Mechanics SEM Annual Conference and Exposition*, Springfield, MA, June 3–6, 2007.

194. Ishikawa, K., S. Tanimura, and T. Fukunaga, "Strain Rate and Temperature Effects on the Strength of 304N Stainless Steel (SUS 304N) (In Japanese)." *J. Soc. Mater. Sci. Japan*, **37** (432), 1410–1415, 1988.

195. Prasad, S.V. and K.N. Jonnalagadda, "Mechanical behavior of SS 304LN at High Strain Rates in Compression," Chapter 13 in *Dynamic Behavior of Materials*, Vol. 1: *Proc. of the 2012 Annual Conference on Experimental and Applied Mechanics,* Vijay Chalivendra, Bo Song, and Daniel Casem, eds., Costa Mesa, CA, pp. 101–108, June 11–14, 2012.

196. Fahr, D., "Analysis of Stress Strain Behavior of Type 316 Stainless Steel," ORNL-TM-4292, Oak Ridge National Laboratory, November 1973.

197. Varin, R., "The Effects of Temperature and Strain Rate on the Plastic Flow and Ductility of Ultrafine-Grained Type 36 Austenitic Stainless Steel," *Mat. Sci. Eng.*, 94, 93–107, Oct. 1987.

198. Samuel, K.G., S.L. Manan, and P. Rodriguez, "Effect of Aging on the Strain Rate Sensitivity and Serrated Flow of a Type 316 Stainless Steel at 923 K," *Scripta Metall. Mater.*, 26, 685-689, 1992.

199. Morris, J.G., "Dynamic Strain Aging in a Ti-Modified 316 Stainless Steel," *Mater. Sci. Eng.*, 7, 296–301, 1971.

200. Steel Construction Institute (U. K.), "Design Guide for Stainless Steel Blast Walls," 1998.

201. Hagström, J. and E. Lindh-Ulmgren, "Materialegenskaper vid höga töjningshastigheter (in Swedish)," SIMR Report IM-2000-006, 2000.

202. Hong, S-G and S-B Lee, "The Tensile and Low-Cycle Fatigue Behavior of Cold Worked 316L Stainless Steel: Influence of Dynamic Strain Aging," *Intl. J. Fatigue*, 26, 899–910, 2004.

203. Lee, W-S, T-H Chen, C-F Lin, and W-Z Luo, "Dynamic Mechanical Response of Biomedical 316L Stainless Steel as Function of Strain Rate and Temperature," *Bioinorg. Chem. Appl.*, 2011, 1, Article ID 173782, 2011.

204. Choudhary, B. K., "Influence of Strain Rate and Temperature on Tensile Deformation and Fracture Behavior of Type 316L(N) Austenitic Stainless Steel," *Metall. Mater. Trans.*, 45A, 302–316, 2014.

205. Lee, W-S and F-T Tzeng, "Mechanical Properties of 304L Stainless Steel SMAW Joints under Dynamic Impact Loading," *J. Mater. Sci.*, 40, 4839–4847, 2005.

206. Lee, W-S, C-F Lin, and B-T Chen, "Tensile Properties and Microstructural Aspects of 304L Stainless Steel Weldments as a Function of Strain Rate and Temperature," *Proc. of the Institution of Mechanical Engineers*, Part C, pp. 439–451, May 2005.

207. Lee, W-S, C-F Lin, C-Y Liu, and C-W Cheng, "The Effects of Strain Rate and Welding Current Mode on the Dynamic Impact Behavior of Plasma-Arc Welded 304L Stainless Steel Weldments," *Met. Trans.*, 35A, 1505–1515, 2004.

208. Lee, W-S, C-F Lin, C-Y Liu, and F-T Tzeng, "Impact Properties of 304L Stainless Steel GTAW Joints Evaluated by High Strain Rate of Compression Test," *J. Nucl. Mater.*, 335 (3), 335–344, 2004.

209. Wu, H-Y, F-J Zhu, S-C Wang, W-R Wang, C-C Wang, and C-H Chiu, "Hot Deformation Characteristics and Strain-Dependent Constitutive Analysis of Inconel 600 Superalloy," *J. Mater. Sci.*, 47, 3971–-3981, 2012.

210. Lee, W-S, and T-N Sun, "Plastic Flow Behaviour of Inconel 690 Super Alloy Under Compressive Impact Loading," *Mat. Trans.*, 45 (7), 2339-2345, 2004.

211. Lee, W-S, C-Y. Liu, and T.N. Sun, "Behavior of Inconel 690 Super Alloy Evaluated by Impact Test," *J. Mater. Process. Technol.*, 153, 219–225, 2004.

212. Hänninen, H., M. Ivanchenko, Y. Yagodzinskyy, V. Nevdacha, U. Ehrnstén, and P. Aaltonen, "Dynamic Strain Aging of Ni-Base Alloys Inconel 600 and 690," *Proc. 12th International Conf. on Environmental Degradation of Materials in Nuclear Power System–Water Reactors*, T.R. Allen, P.J. King, and L. Nelson, eds., The Minerals, Metals & Materials Society, 2005.

213. Chen, T-H., C-K. Tsai, and T-H. Fang, "Dynamic Shear Characteristic and Fracture Feature of Inconel 690 Alloy under Different High Strain Rates and Temperatures," *Advan. Mat. Sci. Eng*., 2013, 1–5, Article ID 382503, 2013.

214. Chen, T. H., T. H. Fang, and T. C. Cheng, "High Strain Rate Shear Characteristic and Fracture Feature of Inconel 690 Alloy," *Proc. 2013 Conf. on Innovation, Communication, and Engineering (ICICE 2013)*, T. H. Meen, S. D. Prior, and D. K. T. Lam., eds., Qingdao, Shandong, China, pp. 15–18, Oct. 26–Nov. 1, 2013.

215. Guo, S., D. Li, H. Pen, Q. Guo, and J. Hu, “Hot Deformation and Processing Maps of Inconel 690 Superalloy,” *J. Nucl. Mater.*, 410, 52–58, 2011.

216. Bouchet, C., B. Tanguy, J. Besson, and S. Bugat, “Prediction of the Effects of Neutron Irradiation on the Charpy Ductile to Brittle Transition Curve of an A508 Pressure Vessel Steel,” *Comput. Mater. Sci.,* 32, 294–300, 2005.

217. Hawthorne, J.R., “Postirradiation Dynamic Tear and Charpy-V Performance of 12-in. Thick A533-B Steel Plates and Weld Metal,” *Nucl. Eng. Design*, 17, 116–130, 1971.

218. Schubert, L.E., A.S. Kumar, S.T. Rosinski, and M.L. Hamilton, “Effect of Specimen Size on the Impact Properties of Neutron Irradiated A533B Steel,” *J. Nucl. Mater.*, 225, 231–237, 1995.

219. IAEA, Master Curve Approach to Monitor Fracture Toughness of Reactor Pressure Vessels in Nuclear Power Plants, IAEA-TECDOC-1631, International Atomic Energy Agency, Vienna, 2009.

220. Wallin, K., “Effect of Strain Rate on the Fracture Toughness Reference Temperature T0 for Ferritic Steels,” *Recent Advances in Fracture*, The Minerals, Metals & Materials Society, 1997.

221. Gavenda, D.J., W.F. Michaud, T.M. Galvin, W.F. Burke, and O.K. Chopra, “Effects of Thermal Aging on Fracture Toughness and Charpy-Impact Strength of Stainless Steel Pipe Welds,” NUREG/CR-6428, ANL-95-47, U.S. Nuclear Regulatory Commission, Washington, DC, May 1996.

222. Wiessner, C.S., and M. MacGillivray, “Loading Rate Effects on Tensile Properties and Fracture Toughness of Steel,” 1999. Available at http://www.twi-global.com/technical-knowledge/published-papers/loading-rate-effects-on-tensile-properties-and-fracture-toughness-of-steel-april-1999/.

223. Iwadate, T., M. Kusuhashi, and Y. Tanaka, “Effect of Strain Rate on Small Specimen Fracture Toughness in the Transition Region,” in *Fracture Mechanics: Twenty-Fourth Volume*, ASTM STP 1207, J. Landes, D. McCabe, and J. Boulet, eds., American Society for Testing and Materials, Philadelphia, PA, pp. 325–341, 1994.

224. Mager, T.R., “Fracture Toughness Properties of Heavy Section A533, Grade B, Class 1 Steel Plate and Submerged Arc Weldment,” *Nucl. Eng. Des.*, 17, 76–90, 1971.

225. Shabbits, W.O., W.H. Pryle, and E.T. Wessel, “Heavy Section Fracture Toughness Properties ofA533, Grade B, class 1 Steel Plate and Submerged Arc Weldment,” WCAP-7414, Westinghouse Electric Co. LLC, Pittsburgh, PA, Dec. 1969.

226. Shabbits, W.O., “Dynamic Fracture Toughness Properties of Heavy Section A533, Grade B, Class 1 Steel Plate,” WCAP 7623, Westinghouse Electric Co. LLC, Pittsburgh, PA, Dec. 1970.

227. Landes, J.D., “Fracture Mechanics and the Nuclear Industry,” *Metall. Trans. A*, 21A, 1097–1104, 1990.

228. Armstrong, R.W. and S.M. Walley, “High Strain Rate Properties of Metals and Alloys,” *Int. Mater. Rev.*, 53, 105–128, 2008.

229. Jung, Y.H. and K.L. Murty, “Effect of Temperature and Strain Rate on Upper Shelf Fracture Behavior of A533 Class 1 Pressure Vessel Steel,” in *Fracture Mechanics: Nineteenth Symp.*, ASTM STP 969, American Society for Testing and Materials, Philadelphia, 392-401, 1988.

230. Koppenhoefer, K.C. and R.H. Dodds, “Numerical Investigation of Loading Rate Effects on Pre-Cracked Charpy V-Notch Specimens,” University of Illinois Report UILU-ENG-97-2008, Aug. 1997.

231. Wallin, K., Valo, M. Rintamaa, R., Torronen, K. and Ahlstrand, R., Characteristics of the IAEA Correlation Monitor Material for Surveillance Programs, Radiation Embrittlement of Nuclear Reactor Pressure Vessel Steels: An International Review (Third Volume), ASTM STP 1011, American Society of Testing and Materials, Philadelphia, pp. 91–111, 1989.

232. Joyce, J.A., Ductile to Brittle Toughness Transition Characterization of A533B Steel, NUREG/CR-5142, U.S. Nuclear Regulatory Commission, Washington, DC, 1988.

233. Marschall, C.M., M.P. Landow, and G.M. Wilkowski, “Loading Rate Effects on Strength and Fracture Toughness of Pipe Steels Used in Task 1 of the IPIRG Program,” NUREG/CR-6098, BMI-2175, Oct. 1993.

234. Nakajima, N., S. Shima, H. Nakajima, and T. Kondo, "The Fracture Toughness of Sensitized 304 Stainless Steel in Simulated Reactor Water," *Nucl. Eng. Des.*, 93, 95–106, 1986.

235. Devillers-Guerville, L., J. Besson, and A. Pineau, “Notch Fracture Toughness of a Cast Austenitic Stainless Steel: Modeling of Experimental Scatter and Size Effect,” *Nucl. Eng. Des.*, 168 (1–3), 211–225, 1997.

236. McConnell, P., W. Sheckherd, and D.M. Morris, “Properties of Thermally Embrittled Cast Duplex Stainless Steel.” *J. Mater. Eng.*, 11 (3), 227–236. 1989.

237. Anzai, H., J. Kuniya, and I. Masaoka, “Effect of 475°C Embrittlement on Fracture Resistance of Cast Duplex Stainless Steel, *Trans. Iron Steel Inst. Japan*, 28, 400–405, 1988.

238. Morra, M., "Program on Technology Innovation: Scoping Study of Low Temperature Crack Propagation for 182 Weld Metal in BWR Environments and for Cast Austenitic Stainless Steel in PWR Environments (Rev. 1)," EPRI 1020957, Electric Power Research Institute, Palo Alto, CA, May 2010.

239. Chopra, O.K., "Effects of Thermal Aging and Neutron Irradiation on Crack Growth Rate and Fracture Toughness of Cast Stainless Steels and Austenitic Stainless Steel Welds," NUREG/CR-7185, ANL-14/10, to be published.

240. Mills, W.J., and C.M. Brown, “Fracture Toughness of Alloy 600 and an EN82H Weld in Air and Water,” *Metall. and Mater. Trans. A*, 32A, 1161–1174, 2001.

241. Brown, C.M. and W.J. Mills, "Fracture Toughness of Alloy 690 and EN52 Welds in Air and Water," *Metall. and Mater. Trans. A*, 33A, 1725–1735, 2002.

242. Zhou, Y and P.K. Mallick, “Effects of Temperature and Strain Rate on the Tensile Behavior of Unfilled and Talc-Filled Polypropylene,” *Part I: Experiments, Polymer Engineering and Science*, 42 (12), 2449–2460, Dec. 2002.

243. Jacob, G.C., M. Starbuck, J.F. Fellers, S. Simunovic, and R.G. Boeman, “Strain Rate Effects on the Mechanical Properties of Polymer Composite Materials,” Published online in Wiley InterScience (www.interscience.wiley.com).

244. Wakabayashi, M., T. Nakamura, N Yoshida, and S. Iwai, “Dynamic Loading Effects on the Structural Performance of Concrete and Steel Materials and Beams,” *Proc. Seventh World Conference on Earthquake Engineering*, Vol. 6, Istanbul, Turkey, pp. 271–278, Sept. 8–12, 1980.

245. Zhang, X., G. Ruiz, R.C. Yu, E. Poveda, R. Porras, “Strain Rate Effect on the Compressive Behaviour of High-Strength Concrete,” *Anales de Mecánica de la Fractura*, 28 (1), 107–112, 2011.

246. Shi, X.Q., W. Zhou, H.L.J. Pang, and Z.P. Wang, “Effect of Temperature and Strain Rate on Mechanical Properties of 63Sn/37Pb Solder Alloy,” *ASME J. Electronic Packaging*, 121 (3), 179–185, 1999.

247. Xu, L., K.E. Tan, and J.H.L. Pang, “Strain-Rate Effects on Mechanical Properties for SAC387 and SAC105-Y Solder,” *Proc. Second Electronics System-Integration Technology Conference, 2008*, ESTC 2008, Greenwich, U.K., Sept. 1–4, pp. 845–850, 2008.

248. Pang, J.H.L., *Lead Free Solder: Mechanics and Reliability*, pp. 25–27, Springer Science+Business Media, New York, 2012.

249. Levings, J., and S. Sritharan, “Effects of Cold Temperature and Strain Rate on the Stress-Strain Behavior of ASTM A706 Grade 420(60) Steel Reinforcement,” *J. Mater. Civ. Eng.*, 24 (12), 1441–1449, 2012.